



Space Structures and Systems Laboratory  
Aerospace and Mechanical Engineering Department

# Nonlinear Modal Analysis of Conservative and Nonconservative Aerospace Structures

Thesis submitted in fulfillment of the requirements for the degree of  
Doctor in Engineering Sciences

by

**Ludovic Renson, Ir.**

February 2014



---

### **Author's Contact Details**

Ludovic RENSON, Ir.  
Space Structures and Systems Laboratory  
Structural Dynamics Research Group  
Aerospace and Mechanical Engineering Department  
University of Liège

1 Chemin des chevreuils  
4000 Liège  
Belgium

Office phone: +32 (0)4 366 4854  
Email: l.renson@ulg.ac.be

---



---

### **Members of the Examination Committee**

Olivier BRULS (President of the Committee)  
Professor - Université de Liège  
Email: O.Bruls@ulg.ac.be

Gaëtan KERSCHEN (Supervisor)  
Professor - Université de Liège  
Email: G.Kerschen@ulg.ac.be

Alan R. CHAMPNEYS  
Professor - University of Bristol (UK)

Greg DIMITRIADIS  
Professor - Université de Liège

Jean-Claude GOLINVAL  
Professor - Université de Liège

Ludovic NOELS  
Professor - Université de Liège

Giuseppe REGA  
Professor - Sapienza Università di Roma (IT)

Rodolphe SEPULCHRE  
Professor - University of Cambridge (UK)

Cyril TOUZÉ  
Professor - École Nationale Supérieure de Techniques Avancées  
(FR)

---



# Preface

The concept of nonlinear normal modes (NNMs) provides a solid and rigorous theoretical framework for the analysis of the nonlinear oscillations of mechanical systems. If NNMs have been studied since more than fifty years, it is only very recently that contributions dealing with their numerical calculation have been reported in the literature. Although these methods pave the way for the application of NNMs to more complex systems, they have not yet reached the necessary maturity. In this context, the purpose of this research is (i) to further investigate the performance of an existing method for computing the NNMs of conservative systems and (ii) to propose two new methods for the computation of NNMs of nonconservative systems.

The first contribution of this thesis is to calculate the NNMs of a real-life aerospace structure, the SmallSat spacecraft developed by EADS Astrium. An algorithm that combines an advanced shooting method with the pseudo-arclength continuation technique is utilized. We show that the NNMs provide a very useful interpretation of the strongly nonlinear dynamics of the spacecraft. One specific contribution is to numerically reproduce with great fidelity several interactions between modes with noncommensurate linear frequencies that were observed experimentally.

The second original contribution of this thesis is to develop two new methods for computing the NNMs of damped systems. The first method solves the partial differential equations (PDEs) governing the geometry of the NNM. The PDEs are recognized as hyperbolic, and it is shown that they require appropriate numerical treatments including specific boundary conditions. The proposed method combines a streamline upwind Petrov-Galerkin finite-element formulation with a resolution strategy based on annular domains to grow sequentially the manifold. The algorithm is demonstrated using a wide variety of systems ranging from two-degree-of-freedom to multi-degree-of-freedom nonlinear systems with linear and nonlinear damping. The applicability of the algorithm to complex real-life structures is demonstrated using a full-scale aircraft. The second method presented in this work computes a NNM as a collection of trajectories defined with boundary value problems (BVPs). The method has the distinctive advantage that it does not rely on a parameterization of the NNM. It is demonstrated on two-degree-of-freedom examples featuring linear and nonlinear damping.



# Acknowledgments

*This doctoral dissertation is the result of several years of research at the University of Liège and would have been unachievable without the involvement of a number of people.*

*I would like to express my gratitude to my advisor Professor Gaëtan Kerschen for his constant enthusiasm during the course of this research. Thank you for your support and patience, I could not have asked for better guidance.*

*I am pleased to acknowledge the members of my thesis committee who provided regular feedback about my work. I also thank my colleagues of the Space Structures and Systems Laboratory for the friendly working atmosphere and for the numerous fruitful discussions we had. In particular, I would like to thank Luc Masset for his precious help in Matlab. More generally, I am thankful to my colleagues of the Aerospace and Mechanical Engineering Department and, especially, to Geoffrey Deliège with whom I had a lot of helpful discussions about the finite element method.*

*I am grateful to Professor Cyril Touzé for hosting me in the Unité de Mécanique at ENSTA ParisTech. Thank you for your warm welcome and for the help you provided in developing the ideas in this thesis.*

*A special thank also goes to my parents, my sister and, foremost, to Marie. Your encouragements throughout these years have been motivating.*



# Contents

<b>Introduction</b>	<b>1</b>
<b>1 The Concept of Nonlinear Normal Modes</b>	<b>5</b>
1.1 Introduction . . . . .	6
1.2 Definitions of NNMs . . . . .	6
1.2.1 Rosenberg’s Definition . . . . .	6
1.2.2 Shaw and Pierre’s Definition . . . . .	7
1.3 Fundamental NNM Properties . . . . .	8
1.3.1 Frequency-Energy Dependence . . . . .	9
1.3.2 Internal Resonances . . . . .	9
1.3.3 Bifurcations and Stability . . . . .	11
1.3.4 Forced Response . . . . .	13
1.4 Calculation of NNMs . . . . .	14
1.4.1 NNMs Defined as Periodic Solutions . . . . .	15
1.4.2 NNMs Defined as Two-Dimensional Invariant Manifolds . . . . .	19
1.5 Analytical Approximation of Shaw and Pierre’s Invariant Manifold . . . . .	24
1.5.1 Approximation using Polynomial Series Expansion . . . . .	24
1.5.2 Application to a 2DOF example . . . . .	26
1.6 Numerical Resolution of the Manifold-Governing PDEs . . . . .	36
1.6.1 A Galerkin-Based Approach . . . . .	36

---

1.6.2	A Transport Method . . . . .	37
1.7	Concluding Remarks . . . . .	38
<b>2</b>	<b>Nonlinear Dynamics and Undamped NNMs of a Full-Scale Spacecraft</b>	<b>41</b>
2.1	Introduction . . . . .	42
2.2	The SmallSat Spacecraft Structure . . . . .	42
2.2.1	Finite Element Modeling of the Underlying Linear Satellite . . . . .	44
2.2.2	Reduced-Order Modeling . . . . .	45
2.3	Modeling of the WEMS Nonlinearities . . . . .	47
2.4	Direct Numerical Integration and Numerical Continuation . . . . .	52
2.5	Nonlinear Modal Analysis of the SmallSat . . . . .	55
2.6	Concluding Remarks . . . . .	66
<b>3</b>	<b>A Finite Element Approach to Compute NNMs of Nonconservative Systems</b>	<b>69</b>
3.1	Introduction . . . . .	70
3.2	The Manifold-Governing PDEs . . . . .	71
3.3	Computation of NNMs Using the Finite Element Method . . . . .	73
3.3.1	Initial Domain and First Guess . . . . .	74
3.3.2	Domain Correction Using a Mesh-Moving Technique . . . . .	76
3.3.3	Streamline Upwind Petrov-Galerkin (SUPG) . . . . .	78
3.3.4	Domain Prediction . . . . .	81
3.4	Extension to Nonconservative Systems . . . . .	81
3.5	Discussion . . . . .	83
3.5.1	Comparison with the Transport Method . . . . .	83
3.5.2	Hyperbolicity . . . . .	84
3.6	Conclusions . . . . .	87

---

<b>4</b>	<b>Numerical Demonstration of the Proposed Algorithm</b>	<b>89</b>
4.1	Introduction . . . . .	90
4.2	2DOF System With Geometric Nonlinearities . . . . .	90
4.2.1	Conservative Case . . . . .	91
4.2.2	Nonconservative Case . . . . .	97
4.3	Cantilever Beam With Nonlinear Boundary Conditions . . . . .	99
4.3.1	Conservative Case . . . . .	99
4.3.2	Nonconservative Case . . . . .	101
4.4	Two Coupled Van Der Pol Oscillators . . . . .	103
4.5	A Full-Scale Aircraft . . . . .	107
4.6	Conclusions . . . . .	112
<b>5</b>	<b>Application to More Complex Damping Models</b>	<b>113</b>
5.1	Introduction . . . . .	114
5.2	Lyapunov-Based Domains . . . . .	114
5.2.1	A Case Study . . . . .	114
5.2.2	Definition of New Domain Boundaries . . . . .	117
5.2.3	Computing Lyapunov Functions . . . . .	117
5.2.4	The Modified Algorithm for NNM Computation . . . . .	119
5.3	Revisiting the 2DOF System with Regularized Friction . . . . .	122
5.4	Conclusions . . . . .	126
<b>6</b>	<b>Computation of Damped NNMs Using Boundary Value Problems</b>	<b>127</b>
6.1	Introduction . . . . .	128
6.2	A Boundary Value Approach . . . . .	129
6.2.1	The 2DOF System With Cubic Spring . . . . .	131
6.2.2	The 2DOF System With Regularized-Coulomb Friction . . . . .	135

---

6.3 Conclusions . . . . .	139
<b>Conclusions</b>	<b>140</b>
<b>A Bifurcation Analysis</b>	<b>145</b>

# Introduction

Modal analysis is central in the study of linear vibrating systems and is arguably the most popular tool in structural dynamics. It is based on the concept of linear normal modes (LNMs). Each LNM is an intrinsic structural property which represents the synchronous vibration of the structure at resonance. It is characterized by three modal parameters, namely the modal shape (i.e., the structural deformation), the natural frequency and the damping ratio. One remarkable mathematical property of LNMs is that there exist orthogonality relations between them. The first consequence is the principle of *invariance* which states that if the motion is initiated on one specific LNM, it remains on this mode while all other modes remain quiescent for all time. The second consequence is the principle of *modal superposition*, i.e., free and forced oscillations of the system can be expressed as a linear combination of LNMs. They have thus the interesting property of uncoupling the equations of motions, i.e., they allow describing large-scale structures in terms of lower-order and simpler systems. One of the first applications of LNMs was thus model reduction with, for instance, the well-known Craig-Bampton method. Another remarkable feature of LNMs is that they can be determined either from a mathematical model by solving an eigenvalue problem (theoretical modal analysis) [51] or from experimental data using techniques developed for more than 50 years (experimental modal analysis) [45]. This duality is extensively used for finite element model updating and validation of real-world systems. Nowadays, it is fair to say that modal analysis is a mature field. It has, for instance, become an integral part of certification processes in the aerospace industry.

With continual interest in expanding the performance envelope of engineering systems, aerospace structures are designed to be lighter and more flexible introducing, e.g., large-amplitude vibrations and reinforcing the presence of nonlinear components or materials. For instance, the recourse to carbon-fiber composite materials is frequent but their dynamical behavior can substantially deviate from linearity. In addition, the growing importance of interconnections between sub-components leads to interfaces with complex behavior. An accurate modeling of their dynamics requires apprehending damping mechanisms which often go beyond the simplistic linear viscous assumption. They can be described, for instance, using nonlinear hysteresis models. Clearly, in this context, linearity is an idealization, an exception to the rule.

Classical modal analysis is however based on the assumption of linear behavior and can actually fail in the presence of nonlinear phenomena. Any attempt to apply traditional

methods results, at best, in a suboptimal design. The development of a nonlinear analog to linear modal analysis is thus an active research area. In this context, the concept of nonlinear normal modes (NNMs) has proved to offer solid theoretical foundations for interpreting the dynamics of nonlinear systems. Pioneered in the 1960s [136–138], NNMs are regarded as the direct extension of LNMs to nonlinear systems providing a clear conceptual relation between both concepts. In particular, despite they possess new properties peculiar to nonlinear systems, NNMs are still viewed as intrinsic structural properties and represent the structural deformation in the vicinity of the nonlinear resonance [157]. For this reason, similarly to their linear analog, NNMs were mainly used to interpret the system's response to harmonic excitation and for the purpose of nonlinear model reduction (e.g., in [2, 97]).

Interestingly, among the wide variety of nonlinearity sources, the NNM literature mainly focused on localized stiffness nonlinearities [50, 157] and on distributed (geometrical) nonlinearities [2, 151]. In this conservative framework, the first numerical method addressing NNM computation was presented in [147]. Later, more advanced approaches were developed as, e.g., in [5]. In the same direction, an effective computational method was developed at the University of Liège in M. Peeters' PhD dissertation [50, 119, 120]. The method was not only applied to academic examples but also to an industrial structure, the Morane Saulnier MS-760 Paris aircraft [74]. In the 1990s, the concept of NNM was extended to nonconservative systems [144, 145]. Using analytical methods, NNMs were calculated for systems including linear and nonlinear damping [92, 145, 153]. More recently, different interpretations of the definition of NNMs led to several numerical methods for computing them [9, 13, 91, 126].

## Motivation

Even if effective numerical tools for NNM computation are becoming available, the current practice in industry is still to ignore nonlinearities, arguably because their analysis is regarded as impractical.

The first objective of this doctoral thesis is to demonstrate that addressing and interpreting the dynamics of real-life systems using NNMs is within reach. To this end, the dynamics of a spacecraft, the SmallSat satellite developed by EADS Astrium, is investigated. The NNMs of the spacecraft are computed using advanced numerical techniques, and their ability to clarify the complicated dynamics of the structure is examined.

The second objective of this work is to propose an effective algorithm for computing the NNMs of general nonconservative systems. This is a central step for uncovering the role played by damping and understanding further the dynamics of real-life structures. Damping is present in all structures and is responsible for the limited response of the system at resonance. It thus plays a key role in structural integrity. However, damping also introduces additional complexity and makes difficult any attempt to accurately predict the

behavior of the system. For instance, nonlinear damping can introduce hardening or softening behavior [24, 98]. Although the theoretical framework for NNMs of nonconservative systems exists, computing them is a challenging task.

The purpose of this doctoral thesis is thus to progress further in the development of a practical nonlinear modal analysis in structural dynamics and, in particular, in aerospace engineering. To this end, the present manuscript is divided into six chapters as follows.

Chapter 1 introduces the concept of NNMs and briefly discusses their fundamental properties. The contributions present in the technical literature are briefly reviewed, and a particular attention is given to the computational method used in Chapter 2. The rest of the chapter is then devoted to the concept of NNMs for nonconservative systems. Their definition as two-dimensional invariant manifolds in phase space is discussed, and the different mathematical formulations existing in the literature are presented. The approach proposed by Shaw and Pierre which describes NNMs using partial differential equations (PDEs) is further investigated in this work. After briefly reviewing the existing numerical methods, the motivation for developing a novel algorithm is evidenced.

Chapter 2 investigates the nonlinear dynamics of the SmallSat spacecraft. A detailed finite element model of the satellite is built, and an experimentally-identified model of the nonlinear isolation device is incorporated into the model. The satellite presents a rich dynamics including jumps, high-frequency content, and modal interactions. Some of the phenomena observed experimentally are evidenced numerically using time integration and continuation methods. An additional bifurcation analysis also reveals the existence of quasiperiodic regimes of motion. Finally, the NNMs are computed and the behavior of several modes exhibiting nonlinear modal interactions and energy localization is discussed in great detail. Overall, very good qualitative agreement between experimental and numerical results is noticed.

Chapter 3 develops a novel method for computing the NNMs of nonconservative systems. The algorithm is based on a discretization of the manifold-governing PDEs using finite element techniques. The theoretical basis of the method as well as its different steps are described in detail. The method allows computing NNMs as invariant manifold for both conservative and nonconservative systems and directly addresses the limitations exhibited by the earlier contributions.

Chapter 4 demonstrates the accuracy and effectiveness of the proposed method using four examples of increasing complexity. First, a two-degree-of-freedom (2DOF) system demonstrates the general applicability of the method. A cantilever beam with nonlinear boundary conditions is then considered to show the effectiveness of the method for mechanical systems with increased dimensionality. The third example considers the presence of nonlinear damping in a 2DOF system composed of two coupled Van der Pol oscillators. Finally, a preliminary analysis of the NNMs of a full-scale aircraft shows that the method can deal with large-scale systems.

Chapter 5 addresses the computation of NNMs for systems possessing more complex

damping models. It is shown that the finite-element-based method developed in Chapter 3 requires numerically-robust boundaries for the computational domain. This is achieved using domains defined with Lyapunov functions. The improved algorithm is illustrated using a two-degree-of-freedom system with regularized Coulomb friction.

Chapter 6 investigates an alternative method for the computation of damped NNMs. The two-dimensional manifold is computed as a one-parameter family of trajectories calculated through a boundary value problem. The method does not rely on a predefined parameterization, which overcomes an important assumption in the description of NNMs proposed by Shaw and Pierre. The approach is illustrated with two different two-degree-of-freedom systems possessing a cubic spring and regularized Coulomb friction, respectively.

Finally, conclusions regarding the completed research and the contributions to nonlinear modal analysis are drawn. The perspectives of the present work are discussed.

# Chapter 1

## The Concept of Nonlinear Normal Modes

---

### Abstract

This chapter introduces the concept of nonlinear normal modes (NNMs) and briefly discusses their fundamental properties. The contributions present in the technical literature are briefly reviewed, and a particular attention is given to the concepts exploited in the following chapters. The computational method used in Chapter 2 is presented. The rest of the chapter is then devoted to the concept of NNMs for nonconservative systems. Their definition as two-dimensional invariant manifolds in phase space is discussed. The approach proposed by Shaw and Pierre which describes NNMs using partial differential equations is further investigated in this work.

---

## 1.1 Introduction

The objective of this first chapter is to acquaint the reader with the concept of nonlinear normal modes (NNMs). The two main definitions of NNMs are given in Section 1.2. The fundamental properties of NNMs are discussed in Section 1.3. Section 1.4 follows with a brief review of existing methods for NNM calculation. A particular emphasis is placed on the methods exploited and developed in this thesis. The continuation algorithm used in Chapter 2 is presented in Section 1.4.1, and the mathematical formulation of NNMs for nonconservative systems is presented in Section 1.4.2. The approach of Shaw and Pierre, which forms the basis for the developments of Chapter 3, is detailed in Section 1.5. The corresponding numerical methods are discussed in Section 1.6. Finally, conclusions are drawn in Section 1.7 and underline some of the remaining challenges that are addressed in the present thesis.

## 1.2 Definitions of NNMs

The theoretical foundations which serve as the cornerstone of NNMs developments were laid down by Lyapunov and Poincaré. In his *center theorem* and under some regularity assumptions, Lyapunov stated that for a finite-dimensional Hamiltonian system whose linearized system possesses purely imaginary eigenvalues with non-commensurate ratios (non-resonance condition), there exist  $N$  families of periodic solutions [72, 100]. At low energy, the periodic solutions of each family are in the neighborhood of a linear normal mode (LNM) of the linearized system. These  $N$  families define  $N$  NNMs that can be regarded as the nonlinear extensions of the  $N$  LNMs of the underlying linear system.

### 1.2.1 Rosenberg's Definition

Based on these theoretical developments, the concept of NNMs was pioneered in the 1960s by Rosenberg [138]. Regarded as a rigorous extension of LNMs to nonlinear systems, NNMs were initially defined as *a vibration at unison* of the system, i.e., as synchronous oscillations [136–138]. The definition suggests that all degrees of freedom (DOFs) move with the same frequency, reach their extreme values and cross zero at the same time. During a NNM motion, each coordinate  $i$  ( $i \neq k$ ) can thus be expressed as a function  $x_i = \hat{x}_i(x_k)$  of a master coordinate  $x_k$ . These functions are referred to as the modal curves and are a priori nonlinear. In the particular case where  $\hat{x}_i(x_k) = c_i x_k$  with the  $c_i$ 's constant, the modal curves form straight lines. Similarly to a linear system, there thus exists a constant relation between all the coordinates of the system, and the NNM is said *similar*.

Rosenberg's approach was further developed by Rand [130–133], Manevitch and Mikhlin [101],

and the reader is referred to [106, 155, 157] for more comprehensive reviews about the early developments.

As illustrated in [119, 120], Rosenberg's definition might appear as too restrictive under some circumstances. An extended definition considering NNMs as *non-necessarily synchronous* periodic oscillations was recently proposed in [94]. This definition allows accounting for the presence of new resonance phenomena (see Section 1.3.2) and is attractive when targeting the computation of NNMs [75, 120]. This extended definition is the approach considered in Chapter 2 of this thesis.

## 1.2.2 Shaw and Pierre's Definition

In the 1990s, Shaw and Pierre proposed an alternative definition that provides an elegant extension of NNMs to nonconservative systems. Based on geometric arguments, they defined an NNM as a two-dimensional invariant manifold in phase space [144, 145]. In particular, they defined *a normal mode of motion for the non-linear, autonomous system as a motion which takes place on a two-dimensional invariant manifold in the system's phase space. This manifold has the following properties: it passes through a stable equilibrium point of the system and, at that point, it is tangent to a plane which is an eigenspace of the system linearized about that equilibrium* [145].

This approach generalizes the property of invariance of LNMs to nonlinear systems, and NNMs are understood as the direct foliation of the two-dimensional linear eigenspaces spanned by the LNMs of the linearized system. Figure 1.1 illustrates this concept and presents the invariant manifold of the first (in-phase) NNM of a 2DOF system (described in Figure 1.2). At the origin, the curved surface that represents the NNM is tangent to a LNM. In Rosenberg's framework, the invariant manifold is paved by the collection of periodic orbits.

Shaw and Pierre's definition is more general than Rosenberg's definition because it is applicable to both conservative and nonconservative systems. The definition is also the common denominator to several mathematical formulations describing the NNMs of damped systems (cf. Section 1.4.2).

The approach of Shaw and Pierre was applied for both continuous [17, 143, 146] and discrete mechanical systems [144, 145], and enjoyed many applications in different contexts, e.g., in piecewise-linear systems [27, 65], in rotating systems [96, 122], aeroelastic pitch-plunge models [42] and, more generally, in nonconservative systems [145, 163].

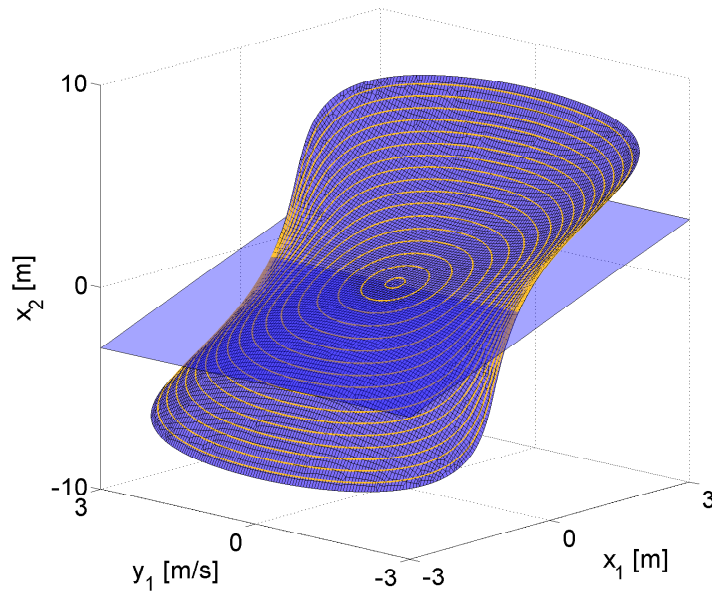


Figure 1.1: NNM as two-dimensional invariant manifold for the conservative 2DOF system (1.1). The periodic orbits (in orange) pave the surface of the manifold.

### 1.3 Fundamental NNM Properties

NNM properties are illustrated using the 2DOF system pictured in Figure 1.2. The equations of motion governing the dynamics are

$$\begin{aligned}\ddot{x}_1 + (2x_1 - x_2) + 0.5x_1^3 &= 0, \\ \ddot{x}_2 + (2x_2 - x_1) &= 0.\end{aligned}\tag{1.1}$$

This seemingly simple system presents nevertheless a majority of the generic characteristics of NNMs. Moreover, although system (1.1) is conservative, the properties discussed herein also apply to NNMs of nonconservative systems (as we shall see in the next chapters). Finally, we will show that, despite NNMs possess new properties peculiar to nonlinear systems, they also have a clear conceptual relation to LNMs.

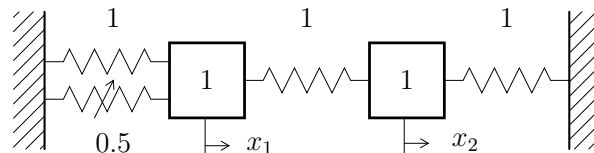


Figure 1.2: Schematic representation of the 2DOF system example.

### 1.3.1 Frequency-Energy Dependence

A general feature of nonlinear systems is the frequency-energy dependence of their oscillations. An appropriate graphical depiction of NNMs is thus a frequency-energy plot (FEP) where a NNM is represented by a family of points, drawn at the minimal period of the periodic motion and at an energy equal to the conserved total energy during the motion. A branch, represented by a solid line, is a family of NNM motions possessing the same qualitative features (e.g., the in-phase NNM motions of a 2DOF system). The FEP of system (1.1) is presented in Figure 1.3 and was computed using the shooting method described in Section 1.4.1. The backbone of the plot is formed by two branches, which represent in-phase (bottom) and out-of-phase (top) synchronous NNMs. The FEP clearly shows that nonlinear modal parameters depend on vibrational energy:

- The frequency of both the in-phase and out-of-phase NNMs increases with the energy level, which reveals the hardening characteristic of the system.
- The modal curves, i.e., the curve drawn in the configuration space defined by the displacements  $x_1(t)$  and  $x_2(t)$ , change for increasing energies. They are illustrated with the insets in Figure 1.3. As energy increases, the straight line becomes curved as a sign of the nonlinear relationship which exists between  $x_1$  and  $x_2$ .
- The out-of-phase modal curve evolves toward an horizontal line as the NNM tends to localize the energy in the first mass. This localization phenomenon is generic in nonlinear systems [11, 77, 157] and can occur even for perfectly symmetric systems (see, e.g., [50]).

### 1.3.2 Internal Resonances

A salient feature of nonlinear systems is that NNMs may interact during a general motion of the system. In the presence of these interactions, NNMs with well-separated fundamental frequencies can exchange energy. These couplings, often referred to as modal interactions or internal resonances, possess no linear counterpart and are realized thanks to the presence of harmonics in the response of the system. Modal interactions have been studied extensively in the literature (see, e.g., the monograph [108]). A case of particular interest is when the linear natural frequencies are commensurate or nearly commensurate [16, 77, 87, 108]. As a consequence, an harmonic of the lowest-frequency mode coincides with the fundamental frequency of another NNM which leads to an interaction.

Due to the frequency-energy dependence of NNMs, it was further shown that such interactions can also develop between modes with non-commensurate linear frequencies. It is for instance the case of system (1.1) which possesses a ratio of  $\sqrt{3}$  between its linear natural frequencies. Figure 1.4 presents the FEP of system (1.1) when NNM computation is carried out at higher energy levels. A loop, termed *tongue*, appears in the continuity

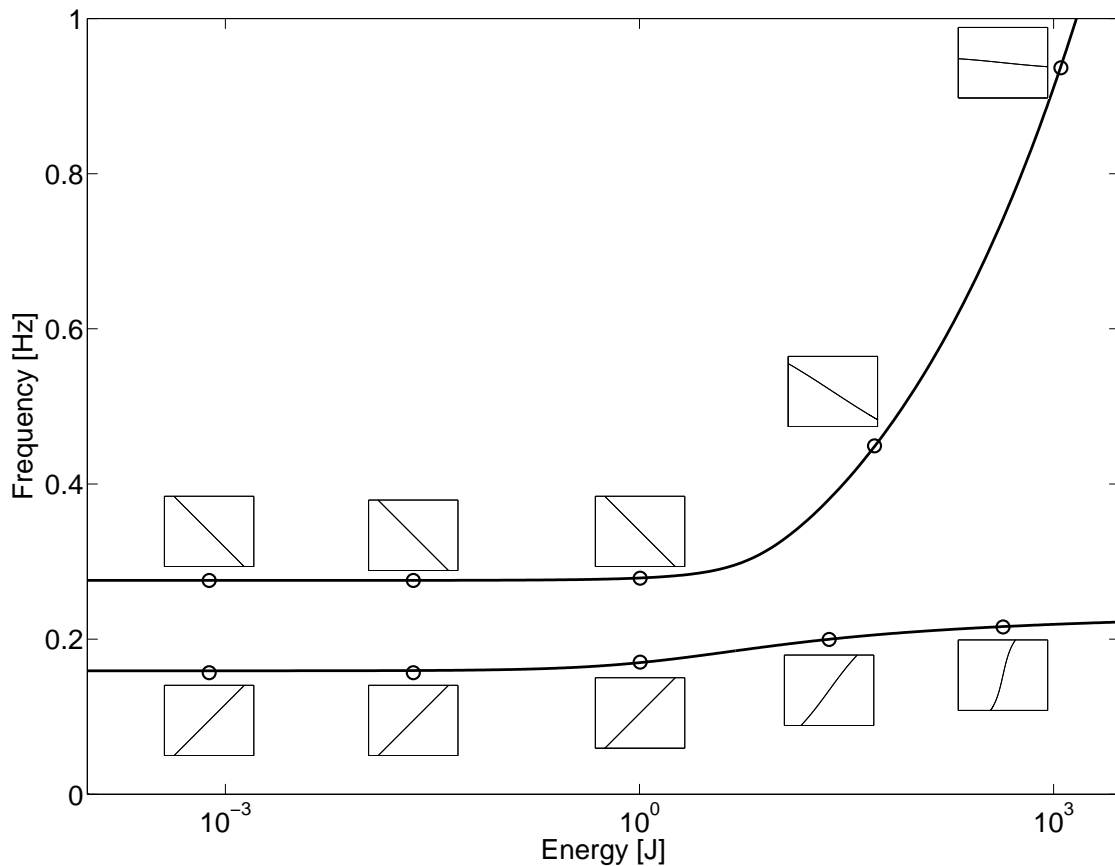


Figure 1.3: Frequency-energy plot of system (1.1). NNM motions depicted in the configuration space are inset. The horizontal and vertical axes in these plots are the displacements of the first and second DOFs, respectively; the aspect ratio is set so that increments on the horizontal and vertical axes are equal in size to indicate whether or not the motion is localized to a particular DOF.

of the backbone branch. To thoroughly understand this resonance mechanism, the out-of-phase NNM branch is represented in the FEP at the third of its frequency. This is relevant, because a periodic solution of period  $T$  is also periodic with period  $3T$ . The resulting branch is pictured in dashed lines. It turns out that a smooth transition from the in-phase to the out-of-phase mode occurs on the tongue. This transition is also depicted in Figure 1.5 where the evolution of the configuration space and of the Fourier coefficients is shown for several points on the tongue or in its vicinity. Starting from NNM motion (a), an in-phase motion characterized by two perceptible harmonic components is observed. From (a) to (d), the relative importance of the third harmonics grows, as clearly confirmed by the motion in the configuration space. Moving from (d) to (e) corresponds to a drastic qualitative change in the dynamics. First, the first harmonic has completely disappeared for both oscillators. Second, the signs of the coefficients of the

third harmonics are opposite. Overall, this means that an out-of-phase motion with a three times as large frequency is realized. Eventually, through a 3:1 internal resonance, the motion ends up on the out-of-phase mode. From (f) to (h), the relative importance of the third harmonic diminishes, and a motion qualitatively similar to that at (a) is observed. However, the configuration space of NNM (h) reveals the presence of a fifth harmonics, which is a precursor to the gradual development of another tongue along which a 5:1 interaction takes place. Following the same reasoning, it can be shown this simple two-degree-of-freedom system exhibits a countable infinity of interactions (2:1, 4:1, 5:1, etc.). This was confirmed numerically in [75].

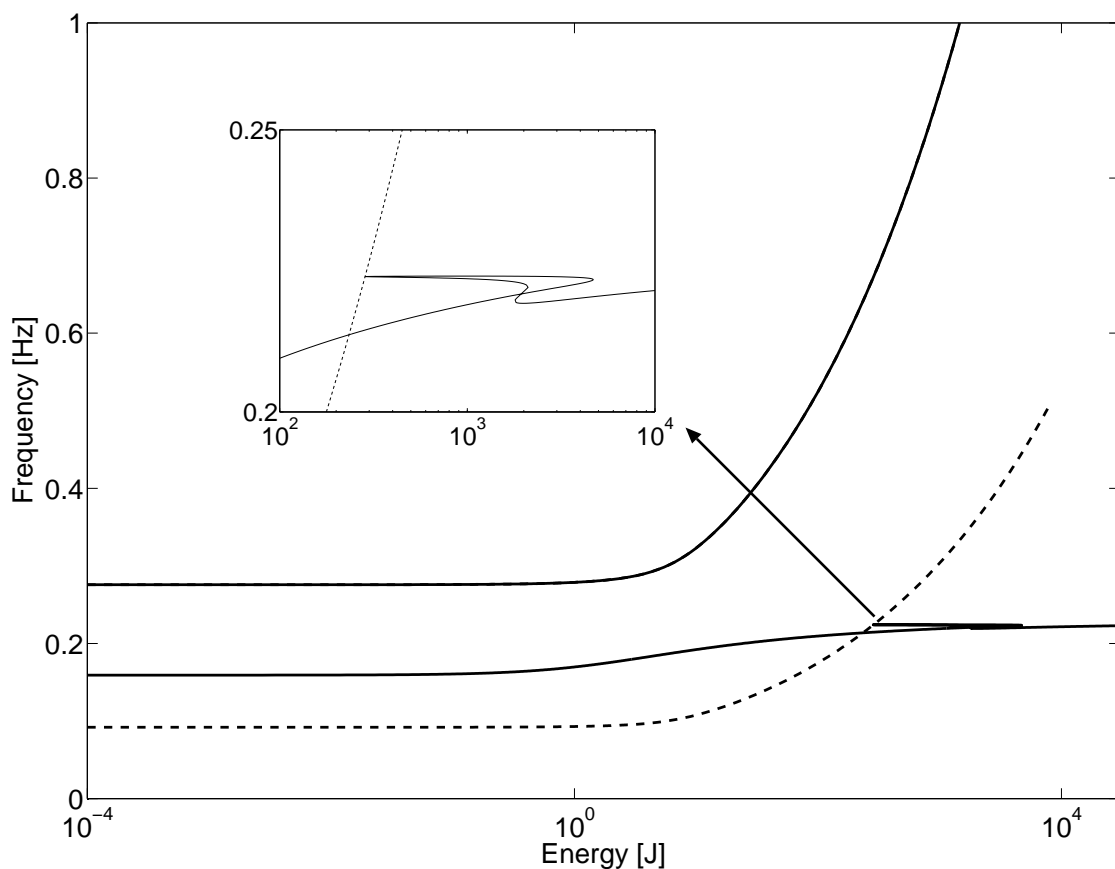


Figure 1.4: Frequency-energy plot of system (1.1). — — —: out-of-phase NNM represented at the third of its fundamental frequency.

### 1.3.3 Bifurcations and Stability

A third fundamental property of NNMs is that their number may exceed the number of DOFs of the system. Due to mode bifurcations, not all NNMs can be regarded as the

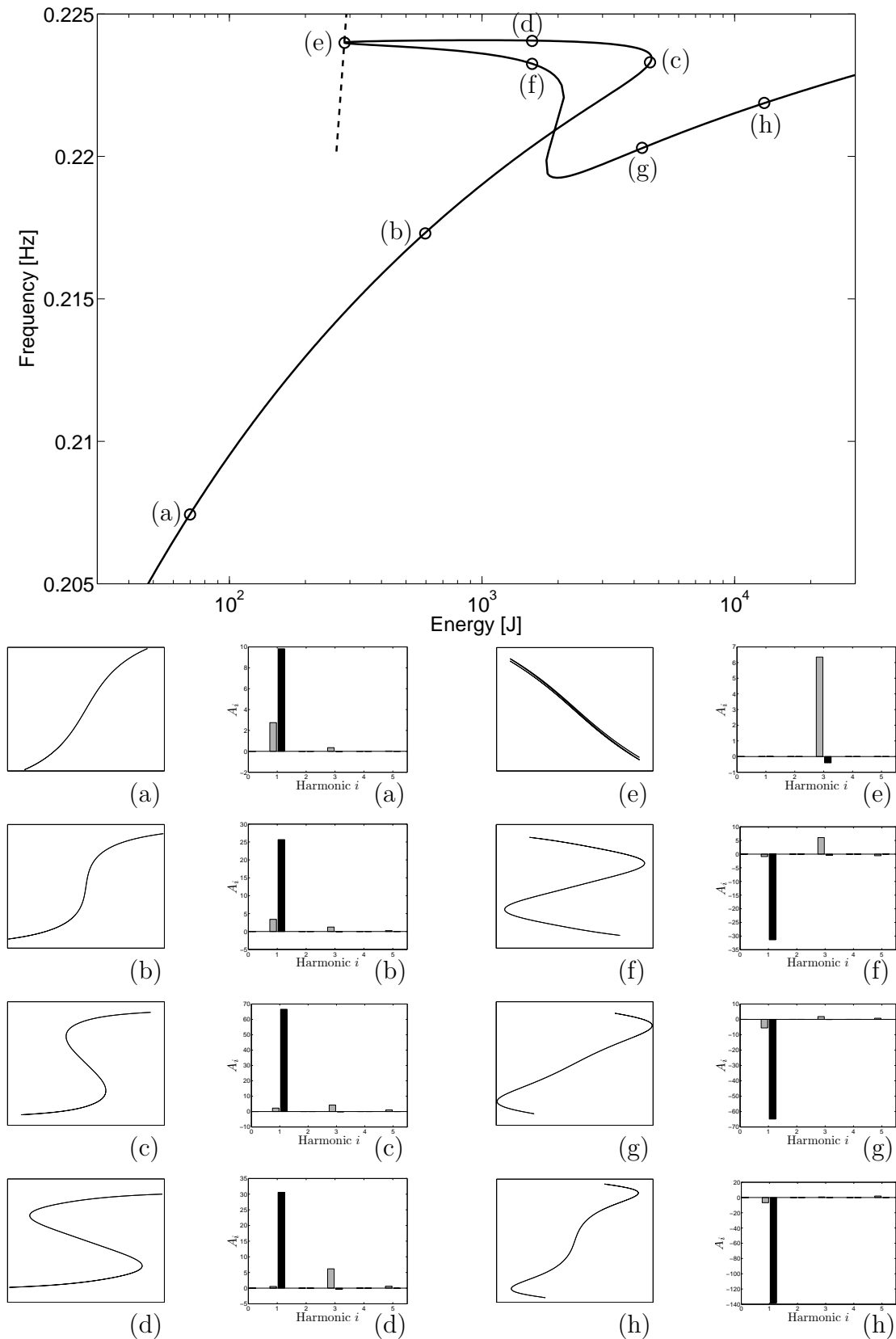


Figure 1.5: Internally resonant NNMs (3:1 resonance). Top plot: close-up of the tongue in the frequency-energy plot. Bottom plots: configuration space (horizontal axis:  $x_1$ ; vertical axis:  $x_2$ ) and Fourier coefficients of a series containing cosine terms only (grey:  $x_1$ ; black:  $x_2$ ).

nonlinear continuation of a LNM. One example is displayed in Figure 1.6 where a new branch of NNMs emerges from the main curve through a (symmetry-breaking) bifurcation. Such new families of NNMs, which cannot be considered as the extension of any LNM, were reported for numerous systems [50, 55, 73, 140, 155].

The concept of bifurcations is interrelated with the concept of stability, because a change in stability occurs through a bifurcation. Therefore, another important characteristic of NNMs is that they can be stable or unstable, which is in contrast to linear theory where all modes are neutrally stable. In this context, instability means that small perturbations of the initial conditions that generate the NNM motion lead to the elimination of the periodic oscillation. Unstable NNMs are not physically realizable.

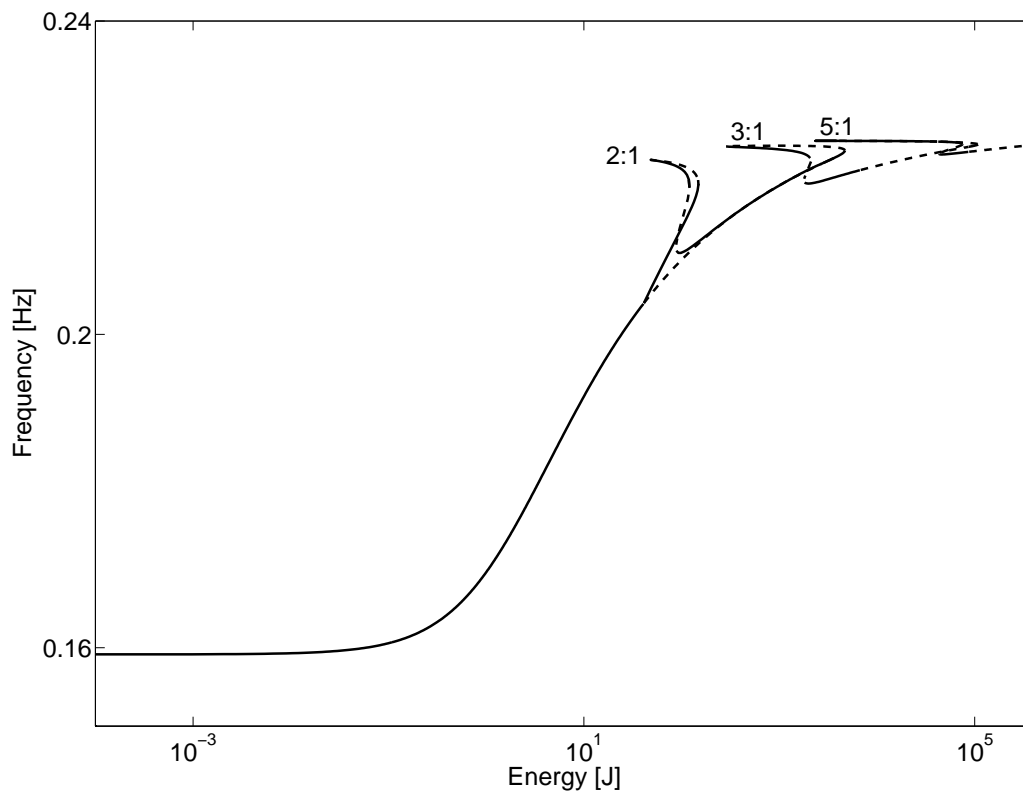


Figure 1.6: Frequency-energy plot for the 2DOF system (1.1) including NNM stability. Stable – and unstable – – oscillations.

### 1.3.4 Forced Response

Akin to their linear counterpart, NNMs reflect the structural deformation in the vicinity of resonance [157]. NNMs have therefore been used to interpret the system's response

to harmonic excitation. This property is illustrated in Figures 1.7(a, b) which present the response of the first and second mass of system (1.1) for several stationary harmonic excitations of increasing amplitude (from 0.002 N to 0.2 N). The backbone curve of the first NNM (in dashed line) perfectly predicts the forced resonance of the system. Thanks to this property, NNMs were extensively used for nonlinear model reduction [2, 13, 97, 114, 123, 125, 128, 149, 152].

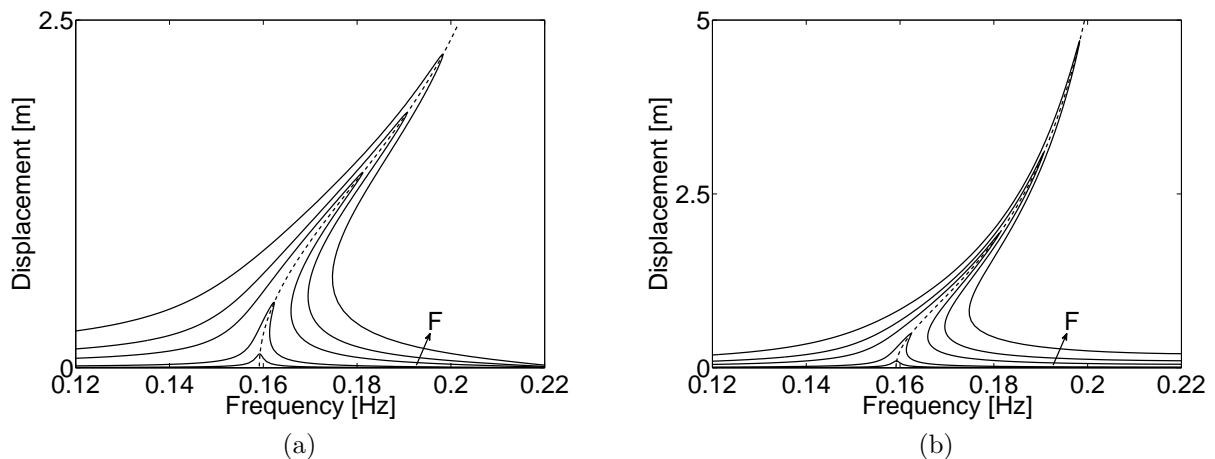


Figure 1.7: Response (—) of the 2DOF system to harmonic forcing computed using continuation methods and for increasing forcing amplitudes  $F$  (from 0.002 N to 0.2 N). The backbone curve traced by the first NNM (---).

## 1.4 Calculation of NNMs

The first constructive technique for NNM calculation, also known as the energy-based formulation, dates back to Rosenberg's work [137, 138] and expresses NNMs as modal curves in the configuration space. This approach was applied and further developed by Manevitch and Mikhlin [101], by Rand [130], and Vakakis et al. [76, 157]. In the 1970s, Rand studied NNMs in [130, 131, 133, 134], and, in particular, he studied their stability in [132]. Since then, many other contributions addressed NNM calculation using various analytical techniques. Among others, one can note the multiple scales method [49, 86, 87, 104, 111, 162] and the complex normal-form method presented by Lamarque and Jézéquel [64]. More recently, a real normal-form method was presented in [151, 153, 154]. The harmonic balance method was also employed (e.g., in [20, 110]) but, in view of the increasing complexity of higher-order expansions, analytical treatments are often limited to a single harmonic. The periodic solutions of a NNM were viewed as special geodesics on a Riemannian manifold in [170], and they were approximated using analytic series. Shaw and Pierre also established a polynomial series expansion for approximating the geometry

of the two-dimensional invariant manifold describing a NNM [145]. More recently, the complex averaging method which proposes an elegant formalism to calculate NNMs was developed by Manevitch [102].

This review is nonexhaustive, and we refer the reader to the book of Vakakis et al. [157] for a review of the developments before the 1990s and to the recent reviews of Mikhlin et al. [6, 106].

### 1.4.1 NNMs Defined as Periodic Solutions

On the one hand, analytical methods have the advantage to provide an explicit expression for NNMs which allows gaining insight into the system's dynamics. On the other hand, such techniques are in essence limited to low-dimensional, weakly nonlinear systems or regimes of motion. Numerical methods were introduced in order to address these limitations. In this context, considering NNMs as periodic oscillations of an autonomous nonlinear system is appealing, because effective algorithms for the numerical continuation of periodic orbits are well-established [33, 40, 107, 141].

One of the first contributions to NNM computation was presented by Slater in [147]. The proposed computational procedure directly integrates the governing equations of motion over one period using a numerical algorithm (e.g., Runge-Kutta or Newmark). In order to compute isolated NNM motions, initial conditions were modified using an optimization algorithm that minimizes a cost function representing the lack of periodicity of the current iterate. The energy was then gradually increased with the previously computed NNM motion as an initial guess for the next NNM.

Most recent algorithms still employ this two-step procedure where isolated periodic solutions are first computed and then varied to progressively obtain the complete NNM branch. However, more sophisticated continuation methods are employed. For instance, the method developed by Cochelin et al. [5, 29] combines harmonic balance and the asymptotic numerical continuation. The latter is a semi-analytical continuation technique that is based on a power series expansion of the unknowns in terms of a control parameter [28]. The approach considered herein uses an alternative algorithm that was proposed in [120]. Its structure is presented in Figure 1.8. The two-step method combines a shooting method for computing isolated periodic solutions and a pseudo-arclength continuation method for tracing out the entire family of periodic solutions corresponding to a NNM.

The application of these methods is often limited to low-dimensional and/or academic examples [117, 162], and contributions for large and complex systems are rare. We can however cite the work of Kerschen et al. who computed NNMs for an aircraft modeled with more than 500 DOFs [74] paving the way for application of the NNM concept to real-life structures.

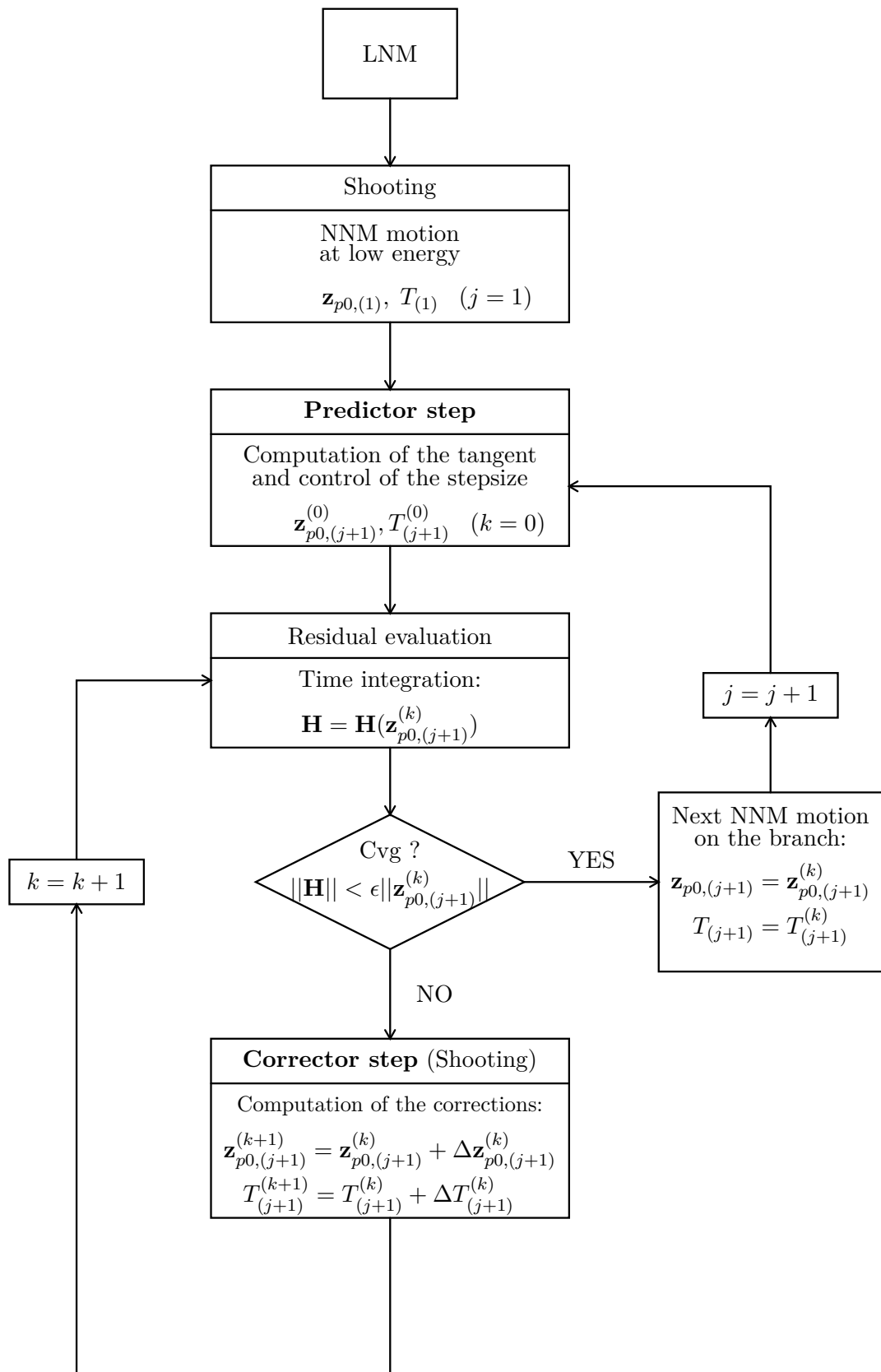


Figure 1.8: Algorithm for NNM computation.

## Shooting Method

The free response of discrete mechanical systems with  $N$  DOFs is considered, assuming that continuous systems have been spatially discretized. The ordinary differential equations of motion are

$$\mathbf{M}\ddot{\mathbf{x}}(t) + \mathbf{K}\mathbf{x}(t) + \mathbf{f}_{\text{nl}}(\mathbf{x}(t)) = 0 \quad (1.2)$$

where  $\mathbf{M}$  and  $\mathbf{K}$  are the mass and stiffness matrices, respectively;  $\mathbf{x}$  and  $\dot{\mathbf{x}}$  are the displacement and acceleration vectors, respectively;  $\mathbf{f}_{\text{nl}}$  is the nonlinear restoring force vector.

The equations of motion of system (1.2) can be recast into state space form

$$\dot{\mathbf{z}} = \mathbf{g}(\mathbf{z}) \quad (1.3)$$

where  $\mathbf{z} = [\mathbf{x}^* \quad \dot{\mathbf{x}}^*]^*$  is the  $2N$ -dimensional state vector, and  $(\cdot)^*$  denotes the transpose operation, and

$$\mathbf{g}(\mathbf{z}) = \begin{pmatrix} \dot{\mathbf{x}} \\ -\mathbf{M}^{-1} [\mathbf{K}\mathbf{x} + \mathbf{f}_{\text{nl}}(\mathbf{x})] \end{pmatrix} \quad (1.4)$$

is the vector field. The solution of this dynamical system for initial conditions  $\mathbf{z}(0) = \mathbf{z}_0 = [\mathbf{x}_0^* \quad \dot{\mathbf{x}}_0^*]^*$  is written as  $\mathbf{z}(t) = \mathbf{z}(t, \mathbf{z}_0)$  in order to exhibit the dependence on the initial conditions,  $\mathbf{z}(0, \mathbf{z}_0) = \mathbf{z}_0$ . A solution  $\mathbf{z}_p(t, \mathbf{z}_{p0})$  is a periodic solution of the autonomous system (1.3) if  $\mathbf{z}_p(t, \mathbf{z}_{p0}) = \mathbf{z}_p(t + T, \mathbf{z}_{p0})$ , where  $T$  is the minimal period.

The NNM computation is carried out by finding the periodic solutions of the governing nonlinear equations of motion (1.3). In this context, the shooting method is a popular numerical technique which solves the two-point boundary-value problem defined by the periodicity condition

$$\mathbf{H}(\mathbf{z}_{p0}, T) \equiv \mathbf{z}_p(T, \mathbf{z}_{p0}) - \mathbf{z}_{p0} = \mathbf{0}. \quad (1.5)$$

$\mathbf{H}(\mathbf{z}_0, T) = \mathbf{z}(T, \mathbf{z}_0) - \mathbf{z}_0$  is called the shooting function and represents the difference between the initial and final state (at time  $T$ ) of the system. Using direct numerical time integration and the Newton-Raphson algorithm, the shooting method consists in finding, in an iterative way, the initial conditions  $\mathbf{z}_{p0}$  and the period  $T$  that realize a periodic motion.

The phase of the periodic solutions is not fixed. If  $\mathbf{z}(t)$  is a solution of the autonomous system (1.3), then  $\mathbf{z}(t + \Delta t)$  is geometrically the same solution in state space for any  $\Delta t$ . Hence, an additional condition  $h(\mathbf{z}_{p0}) = 0$ , termed the phase condition, has to be specified in order to remove the arbitrariness of the initial conditions.

In summary, an isolated NNM motion is computed by solving the augmented two-point boundary-value problem defined by

$$\begin{cases} \mathbf{H}(\mathbf{z}_{p0}, T) = 0 \\ h(\mathbf{z}_{p0}) = 0 \end{cases} \quad (1.6)$$

## Continuation of Periodic Solutions

Due to the frequency-energy dependence, the modal parameters of an NNM vary with the total energy. An NNM family, governed by equations (1.6), therefore traces a curve, termed an NNM branch, in the  $(2N + 1)$ -dimensional space of initial conditions and period  $(\mathbf{z}_{p0}, T)$ . Starting from the corresponding LNM at low energy, the computation is carried out by finding successive points  $(\mathbf{z}_{p0}, T)$  of the NNM branch using methods for the numerical continuation of periodic motions (also called path-following methods). The space  $(\mathbf{z}_{p0}, T)$  is termed the continuation space.

Different methods for numerical continuation have been proposed in the literature. The so-called pseudo-arclength continuation method is used herein.

Starting from a known solution  $(\mathbf{z}_{p0,(j)}, T_{(j)})$ , the next periodic solution  $(\mathbf{z}_{p0,(j+1)}, T_{(j+1)})$  on the branch is computed using a predictor step and a corrector step.

### Predictor step

At step  $j$ , a prediction  $(\tilde{\mathbf{z}}_{p0,(j+1)}, \tilde{T}_{(j+1)})$  of the next solution  $(\mathbf{z}_{p0,(j+1)}, T_{(j+1)})$  is generated along the tangent vector to the branch at the current point  $\mathbf{z}_{p0,(j)}$

$$\begin{bmatrix} \tilde{\mathbf{z}}_{p0,(j+1)} \\ \tilde{T}_{(j+1)} \end{bmatrix} = \begin{bmatrix} \mathbf{z}_{p0,(j)} \\ T_{(j)} \end{bmatrix} + s_{(j)} \begin{bmatrix} \mathbf{p}_{z,(j)} \\ p_{T,(j)} \end{bmatrix} \quad (1.7)$$

where  $s_{(j)}$  is the predictor stepsize. The tangent vector  $\mathbf{p}_{(j)} = [\mathbf{p}_{z,(j)}^* \ p_{T,(j)}]^*$  to the branch defined by (1.6) is solution of the system

$$\begin{bmatrix} \frac{\partial \mathbf{H}}{\partial \mathbf{z}_{p0}} \Big|_{(\mathbf{z}_{p0,(j)}, T_{(j)})} & \frac{\partial \mathbf{H}}{\partial T} \Big|_{(\mathbf{z}_{p0,(j)}, T_{(j)})} \\ \frac{\partial h}{\partial \mathbf{z}_{p0}}^* \Big|_{(\mathbf{z}_{p0,(j)})} & 0 \end{bmatrix} \begin{bmatrix} \mathbf{p}_{z,(j)} \\ p_{T,(j)} \end{bmatrix} = \begin{bmatrix} \mathbf{0} \\ 0 \end{bmatrix} \quad (1.8)$$

with the condition  $\|\mathbf{p}_{(j)}\| = 1$ . This normalization can be taken into account by fixing one component of the tangent vector and solving the resulting overdetermined system using the Moore-Penrose matrix inverse; the tangent vector is then normalized to 1.

### Corrector step

The prediction is corrected by a shooting procedure in order to solve (1.6) in which the variations of the initial conditions and the period are forced to be orthogonal to the predictor step. At iteration  $k$ , the corrections  $\mathbf{z}_{p0,(j+1)}^{(k+1)} = \mathbf{z}_{p0,(j+1)}^{(k)} + \Delta \mathbf{z}_{p0,(j+1)}^{(k)}$ ,  $T_{(j+1)}^{(k+1)} = T_{(j+1)}^{(k)} + \Delta T_{(j+1)}^{(k)}$  are computed by solving the linear system

$$\begin{bmatrix} \frac{\partial \mathbf{H}}{\partial \mathbf{z}_{p0}} \Big|_{(\mathbf{z}_{p0,(j+1)}^{(k)}, T_{(j+1)}^{(k)})} & \frac{\partial \mathbf{H}}{\partial T} \Big|_{(\mathbf{z}_{p0,(j+1)}^{(k)}, T_{(j+1)}^{(k)})} \\ \frac{\partial h}{\partial \mathbf{z}_{p0}}^* \Big|_{(\mathbf{z}_{p0,(j+1)}^{(k)})} & 0 \\ \mathbf{p}_{z,(j)}^* & p_{T,(j)} \end{bmatrix} \begin{bmatrix} \Delta \mathbf{z}_{p0,(j+1)}^{(k)} \\ \Delta T_{(j+1)}^{(k)} \end{bmatrix} =$$

$$\begin{bmatrix} -\mathbf{H}(\mathbf{z}_{p0,(j+1)}^{(k)}, T_{(j+1)}^{(k)}) \\ -h(\mathbf{z}_{p0,(j+1)}^{(k)}) \\ 0 \end{bmatrix} \quad (1.9)$$

where the prediction is used as initial guess, i.e.,  $\mathbf{z}_{p0,(j+1)}^{(0)} = \tilde{\mathbf{z}}_{p0,(j+1)}$  and  $T_{(j+1)}^{(0)} = \tilde{T}_{(j+1)}$ . The last equation in (1.9) corresponds to the orthogonality condition for the corrector step. This iterative process is carried out until convergence is achieved.

### Sensitivity Analysis

Each shooting iteration involves the time integration of the equations of motion to evaluate the current shooting residue  $\mathbf{H}(\mathbf{z}_{p0}^{(k)}, T^{(k)}) = \mathbf{z}_p^{(k)}(T^{(k)}, \mathbf{z}_{p0}^{(k)}) - \mathbf{z}_{p0}^{(k)}$ . As evidenced by equation (1.9), the method also requires the evaluation of the  $2N \times 2N$  Jacobian matrix

$$\frac{\partial \mathbf{H}}{\partial \mathbf{z}_0}(\mathbf{z}_0, T) = \left. \frac{\partial \mathbf{z}(t, \mathbf{z}_0)}{\partial \mathbf{z}_0} \right|_{t=T} - \mathbf{I} \quad (1.10)$$

where  $\mathbf{I}$  is the  $2N \times 2N$  identity matrix.

An effective method for determining  $\partial \mathbf{z}(t, \mathbf{z}_0)/\partial \mathbf{z}_0$  is to use sensitivity analysis which consists in differentiating the equations of motion (1.3) with respect to the initial conditions  $\mathbf{z}_0$  which leads to

$$\frac{d}{dt} \left[ \frac{\partial \mathbf{z}(t, \mathbf{z}_0)}{\partial \mathbf{z}_0} \right] = \left. \frac{\partial \mathbf{f}(\mathbf{z})}{\partial \mathbf{z}} \right|_{\mathbf{z}(t, \mathbf{z}_0)} \left[ \frac{\partial \mathbf{z}(t, \mathbf{z}_0)}{\partial \mathbf{z}_0} \right] \quad (1.11)$$

with

$$\frac{\partial \mathbf{z}(0, \mathbf{z}_0)}{\partial \mathbf{z}_0} = \mathbf{I} \quad (1.12)$$

since  $\mathbf{z}(0, \mathbf{z}_0) = \mathbf{z}_0$ . Hence, the matrix  $\partial \mathbf{z}(t, \mathbf{z}_0)/\partial \mathbf{z}_0$  at  $t = T$  can be obtained by numerically integrating over  $T$  the initial-value problem defined by the linear ordinary matrix differential equations (1.11) with the initial conditions (1.12). The solution of equations (1.11) is computed together with the solution of the nonlinear equations of motion in a single numerical simulation. At a periodic solution, the matrix  $\partial \mathbf{z}_p(T, \mathbf{z}_{p0})/\partial \mathbf{z}_{p0}$  is the so-called monodromy matrix. Its eigenvalues, the Floquet multipliers, allow to perform a stability analysis of the NNM motions.

### 1.4.2 NNMs Defined as Two-Dimensional Invariant Manifolds

We now consider more general equations of motion

$$\mathbf{M} \ddot{\mathbf{x}}(t) + \mathbf{C} \dot{\mathbf{x}}(t) + \mathbf{K} \mathbf{x}(t) + \mathbf{f}_{nl}(\mathbf{x}(t), \dot{\mathbf{x}}(t)) = 0 \quad (1.13)$$

where  $\mathbf{M}$ ,  $\mathbf{C}$ , and  $\mathbf{K}$  are the mass, damping, and stiffness matrices, respectively;  $\mathbf{x}$ ,  $\dot{\mathbf{x}}$ , and  $\ddot{\mathbf{x}}$  are the displacement, velocity, and acceleration vectors, respectively;  $\mathbf{f}_{nl}$  is the nonlinear

restoring force vector. There is no specific assumption on the damping matrix  $\mathbf{C}$  which can have both symmetric (nonconservative) and skew-symmetric (conservative) contributions. The linear damping needs not to be proportional. The system of equation (1.13) is transformed into its first-order form

$$\dot{\mathbf{z}} = \mathbf{g}(\mathbf{z}) = \begin{pmatrix} \dot{\mathbf{x}} \\ -\mathbf{M}^{-1} [\mathbf{C}\dot{\mathbf{x}} + \mathbf{K}\mathbf{x} + \mathbf{f}_{\text{nl}}(\mathbf{x}, \dot{\mathbf{x}})] \end{pmatrix} = \begin{pmatrix} \mathbf{y} \\ \mathbf{f}(\mathbf{z}) \end{pmatrix}, \quad (1.14)$$

where the term  $\mathbf{f}$  represents all the inertia-normalized (linear and nonlinear) elastic and dissipative forces in the equations of motion.

### Shaw and Pierre Formulation

In the presence of damping, oscillations are generally traveling waves because there exists a phase lag between the DOFs of the system. In the general damping case, the linear theory resorts to complex LNMs to account for this lag. Shaw and Pierre demonstrated that a description of a mode using a displacement-velocity pair of coordinates is, in essence, similar to the complex approach. Hence, they proposed to parametrize the two-dimensional invariant manifold, or equivalently the NNM, using a single *master-pair* of state-space variables, a displacement  $x_k$  and a velocity  $y_k$ , the other variables being functionally related to the master pair. The approach to calculate NNMs was then inspired by the center manifold theory [25].

Writing the master coordinates as  $(u, v)$ , the remaining variables follow the constraint equations

$$\begin{aligned} x_i &= X_i(u, v), \\ y_i &= Y_i(u, v), \quad i = 1, \dots, N; \quad i \neq k. \end{aligned} \quad (1.15)$$

Similarly to the center manifold approach, the time dependence in the equations of motion is eliminated by asserting that the motion occurs on the invariant manifold. In this way, the time derivative of Equations (1.15) gives

$$\begin{aligned} \dot{x}_i &= \frac{\partial X_i}{\partial u} \dot{u} + \frac{\partial X_i}{\partial v} \dot{v}, \\ \dot{y}_i &= \frac{\partial Y_i}{\partial u} \dot{u} + \frac{\partial Y_i}{\partial v} \dot{v}, \end{aligned} \quad (1.16)$$

where  $\dot{u} = v$  and  $\dot{v} = f_k$ . Plugging these equations into (1.14) leads to a set of  $2N - 2$  partial differential equations (PDEs) that can be solved for the  $X_i$ 's and  $Y_i$ 's

$$\begin{aligned} Y_i(u, v) &= \frac{\partial X_i(u, v)}{\partial u} v + \frac{\partial X_i(u, v)}{\partial v} f_k, \\ f_i &= \frac{\partial Y_i(u, v)}{\partial u} v + \frac{\partial Y_i(u, v)}{\partial v} f_k, \end{aligned} \quad (1.17)$$

where  $i = 1, \dots, N$ ;  $i \neq k$ ,  $f_i = f_i(u, \mathbf{X}(u, v), v, \mathbf{Y}(u, v))$  are the components of  $\mathbf{f}$  (cf. Equation (1.14)) with  $\mathbf{X} = \{X_j : j = 1, \dots, N ; j \neq k\}$  and  $\mathbf{Y} = \{Y_j : j = 1, \dots, N ; j \neq k\}$ .

Around the system's equilibrium point, the manifold-governing PDEs (1.17) admit  $N$  solutions which are the extension of the  $N$  underlying LNMs [145]. After solving (1.17), the constraint equations (1.15) give a geometric description of a NNM in phase space. At the origin, each NNM is tangent to the linear eigenspace spanned by the corresponding LNM.

Substituting the  $X_i$ 's and  $Y_i$ 's in the ordinary differential equations governing the master coordinates  $x_k$  and  $y_k$ , the dynamics on the NNM is obtained:

$$\begin{aligned} \dot{u} &= v, \\ \dot{v} &= f_k(u, \mathbf{X}(u, v), v, \mathbf{Y}(u, v)). \end{aligned} \quad (1.18)$$

Interestingly, the dynamics of the full system is reduced to the dynamics of a single-degree-of-freedom (SDOF) oscillator. These reduction capabilities were exploited for interpreting the dynamics of the system and for building reduced-order models, e.g., in [4, 21, 123, 125]. NNMs defined as invariant manifolds were also used in continuous [17, 111, 112, 143, 146], piecewise-linear [27, 65] and gyroscopic systems [96, 161]. This model reduction approach was latter extended to forced systems in [18, 67].

### Normal-Form Approach

The method of normal forms is a perturbation method comparable to the multiple-scales method [109] and whose foundations date back to Poincaré. It is only recently that the method was introduced in the context of NNMs of mechanical systems by Jézéquel and Lamarque [64]. Based on a block-diagonal complex form, the method was however opaque for structural dynamicists. With the distinctive advantage of keeping the form of an oscillator, a real normal-form transformation was proposed by Touzé et al. [153]. Furthermore, Touzé et al. demonstrated that the method is strictly equivalent to Shaw and Pierre's approach [153]. In a similar trend, Neild and Wagg presented a second-order normal form transformation [113]. Their approach presents an improved accuracy when simulating the system's behavior around the resonance [113].

The idea of normal-form transformations is to apply successive coordinate transformations to bring the equations of motion in their simplest form. Generally speaking, it extends the idea of uncoupling the equations of motion by removing the non-resonant nonlinear terms. If successful, the procedure reduces the dynamics of the full system to the dynamics of SDOF oscillators whose superposition is governed by the nonlinear transformation. Normal-form transformations thus extend the principle of superposition to nonlinear systems. This idea was discussed by Pellicano and Mastroddi in [121]. The transformation can however fail due to the generic presence of the so-called resonant terms.

Adapted from [153], Figure 1.9 illustrates the concept of the transformation. Around the

equilibrium point of the system (here, the origin), the linear modal displacements  $P_i$  and velocities  $Q_i$  define straight coordinates which span the phase space with a regular grid. After the calculation of the normal-form transformation, a set of curved coordinates, i.e., the *normal* coordinates  $(R_i, S_i)$ , is obtained. Each specific pair of these coordinates is attached to an invariant manifold which represents a NNM. In Figure 1.9, the invariant manifolds are represented by  $\mathcal{M}_1$  for  $(R_1, S_1) \neq 0$  and  $\mathcal{M}_2$  for  $(R_2, S_2) \neq 0$ . Using the *normal* coordinates, the phase space is no longer spanned by flat eigenspaces, but rather by curved invariant manifolds [153]. The method was used for the purpose of reduced-order

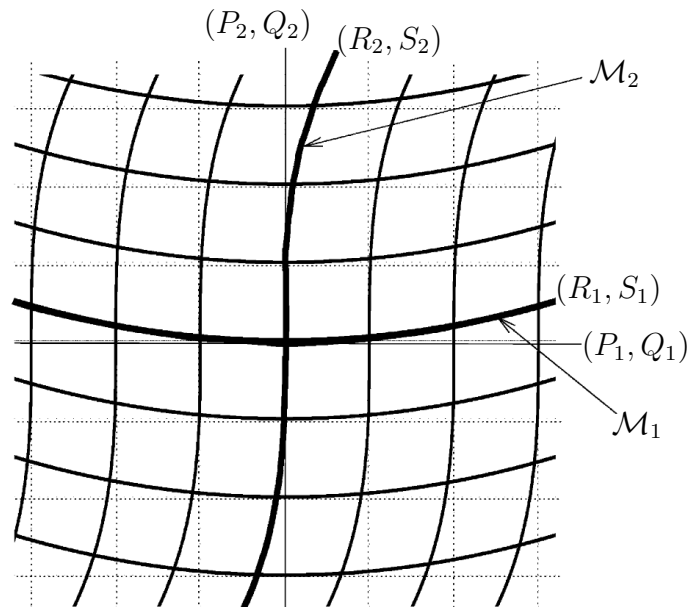


Figure 1.9: Illustration of the linear modal coordinates  $(P_i, Q_i)$  and the *normal* coordinates  $(R_i, S_i)$  associated with the normal-form transformation. The *normal* coordinates define the invariant manifolds  $\mathcal{M}_1$  and  $\mathcal{M}_2$  which represents the NNMs of the system. Picture taken and adapted from [153].

modeling and, in particular, most applications considered the reduction of geometrically nonlinear structures such as beams, plates, shells, etc. [2, 13, 151–153].

Although there exist different attempts to develop numerical normal-form methods (for instance using symbolic calculations [168, 169] or second-order formulations [113]), as of now, normal-form methods are mostly analytical techniques.

### Amplitude- and Phase-Dependent Modal Quantities

Another interesting approach was proposed by Bellizzi and Bouc, first for conservative systems [8] and then for nonconservative systems [9]. Similarly to Shaw and Pierre, the method defines a NNM motion in terms of a single pair of variables, here, an amplitude

and a phase variable  $(a(t), \psi(t))$ . The other coordinates are functionally related to this pair using the constraint relations

$$\begin{aligned}\mathbf{x}(t) &= a(t)\mathbf{X}(a(t), \phi(t)), \\ \dot{\mathbf{x}}(t) &= \mathbf{y}(t) = a(t)\mathbf{Y}(a(t), \phi(t)),\end{aligned}\tag{1.19}$$

where  $\mathbf{X}$  and  $\mathbf{Y}$  are vector functions representing the modal amplitude. A similar formalism as in Equations (1.15) is deliberately chosen to underline the parallel between both methods. Amplitude and phase variables are governed by a pair of ordinary differential equations governing the SDOF motion which takes place on the NNMs [9]:

$$\begin{aligned}\dot{\phi}(t) &= \Omega(a(t), \phi(t)), \\ \dot{a}(t) &= a(t)\xi(t)(a(t), \phi(t)).\end{aligned}\tag{1.20}$$

The scalar functions  $\Omega$  and  $\xi$  define the motion frequency and damping ratio, respectively. All together,  $\mathbf{X}$ ,  $\mathbf{Y}$ ,  $\Omega$  and  $\xi$  define the modal motion.

Plugging Equations (1.19)–(1.20) into the equations of motion and removing any explicit time dependence yields the set of PDEs

$$\begin{aligned}(\mathbf{X} + a\mathbf{X}_a)\xi + \mathbf{X}_\phi\Omega &= \mathbf{Y}, \\ \mathbf{M}(\mathbf{Y} + a\mathbf{Y}_a)\xi + \mathbf{M}\mathbf{Y}_\phi\Omega + \frac{1}{a}\mathbf{f}(a\mathbf{X}, a\mathbf{Y}) &= \mathbf{0}.\end{aligned}\tag{1.21}$$

The number of equations in (1.21) is lower than the number of unknowns by two. Additional normalization conditions are thus added to the set of PDEs.

Equations are then discretized using a Fourier-Galerkin projection similar in principle to [124] and finally solved using a classical Newton-Raphson procedure. This method was successfully applied to 2DOF conservative systems [8] and to 2DOF systems including linear or nonlinear damping [9]. In [117], the resolution strategy was improved to reduce the computational burden associated with the Fourier-Galerkin projection and applied to compute the NNMs of a clarinet-like musical instrument. In particular, the *method of lines*, where all but one dimensions are discretized using the finite difference method, was considered to solve NNM equations as an initial value problem.

## Complex Nonlinear Modes

In direct analogy with complex LNMs, complex nonlinear modes were introduced by Laxalde and Thouverez in [91]. The method uses generalized Fourier series to approximate NNM motions and derive a nonlinear eigenvalue problem. More precisely, the complex eigensolutions are written as [90, 91]:

$$\mathbf{x}(t) \approx \mathbf{x}(\eta, \tau) = \sum_{p=0}^{+\infty} \sum_{n=-\infty}^{+\infty} \hat{\mathbf{x}}_{p,n} e^{-p\eta + jn\tau}\tag{1.22}$$

where  $\tau = \omega t$  and  $\eta = \beta t$  are two new time scales referring to the oscillations and the envelope modulation (i.e., the nonconservative effects), respectively. Substituting Equation (1.22) into the equations of motion and using a Fourier-Galerkin projection, a complex eigenvalue problem is obtained:

$$\forall(p, n) \in [0, \dots, N_p] \times [-N_n, \dots, N_n], \quad (-p\beta + jn\omega)^2 \hat{\mathbf{x}}_{p,n} - \frac{\langle \mathbf{f}, \phi_{p,n} \rangle}{\|\phi_{p,n}\|^2} = 0 \quad (1.23)$$

where  $\langle \mathbf{f}, \phi_{p,n} \rangle$  denotes the inner product

$$\langle g, h \rangle = \frac{1}{2\pi} \int_{-\infty}^{+\infty} \int_0^{2\pi} g(\eta, \tau) h(\eta, \tau) d\tau d\eta \quad (1.24)$$

between  $\mathbf{f}$  and the set of basis functions  $\phi_{p,n}(\nu, \tau) = e^{-p\nu + jn\tau}$ . The nonlinear force vector  $\mathbf{f}$  is calculated in the time domain by reconstructing the displacement and velocity vectors with the given set of  $\{\hat{\mathbf{x}}_{p,n}\}$ . The nonlinear terms are then projected onto the generalized Fourier basis. In the algebraic system of equations (1.23), the number of unknowns exceeds the number of equation by two [91]. Similarly to the method in Section 1.4.2, the system is complemented by an additional mode normalization. A chosen control coordinate is considered, and the real and imaginary parts of one of its harmonics are used to define the modal amplitude  $q$  as

$$q = q^{\mathcal{R}} + jq^{\mathcal{I}}, \quad (1.25)$$

where  $j^2 = -1$ . Each eigenvector is accordingly normalized with respect to this modal amplitude, and the system is solved using Newton-like methods. A continuation algorithm is then used to evolve the nonlinear eigenvalue solutions for increasing modal amplitudes. Using an alternative normalization based on the kinetic energy, Krack et al. [79] recently used this method in the context of friction nonlinearities. Interestingly, the complex modal amplitude  $q$  actually represents the two-dimensional subspace on which the NNM motion takes place.

## 1.5 Analytical Approximation of Shaw and Pierre's Invariant Manifold

As illustrated in Sections 1.2 and 1.4.2, the concept of NNMs for damped systems has already enjoyed many contributions, which differ according to the mathematical interpretation of their definition as two-dimensional invariant manifold. In what follows, we focus on the approach presented by Shaw and Pierre, and we study the PDEs governing the manifold's geometry (Equations (1.17)).

### 1.5.1 Approximation using Polynomial Series Expansion

In general, the equations governing the geometry of the NNM are at least as difficult to solve as the original set of ordinary differential equations governing the system's dynamics.

However, as in the center manifold method [25] or in the general framework of invariant manifold calculation [54], the PDEs (1.17) allow an approximate solution in the form of a polynomial series expansion [145]:

$$\begin{aligned} X_i(u, v) &= a_{1i}u + a_{2i}v + a_{3i}u^2 + a_{4i}uv + a_{5i}v^2 \\ &\quad + a_{6i}u^3 + a_{7i}u^2v + a_{8i}uv^2 + a_{9i}v^3 + \dots, \\ Y_i(u, v) &= b_{1i}u + b_{2i}v + b_{3i}u^2 + b_{4i}uv + b_{5i}v^2 \\ &\quad + b_{6i}u^3 + b_{7i}u^2v + b_{8i}uv^2 + b_{9i}v^3 + \dots, \end{aligned} \quad (1.26)$$

where the coefficients  $a_{ji}$  and  $b_{ji}$  are the new unknowns and describe the geometry of the manifold. Substituting expressions (1.26) into the PDEs and gathering terms of like powers in  $u$  and  $v$ , a set of nonlinear coupled algebraic equations is obtained with, at cubic order,  $18(N - 1)$  equations for  $18(N - 1)$  unknown coefficients. As illustrated in [145], the first-order coefficients ( $a_{1i}, a_{2i}, b_{1i}, b_{2i}$ ) define the plane spanned by the corresponding LNM. The higher-order coefficients represent thus the deformation of this linear eigenspace under the effect of nonlinearity. In other words, any deviation from a flat surface is attributable to nonlinear effects. The linear coefficients can be obtained as in [145] or by the resolution of the linear eigenvalue problem as follows [148]. The general state-space form (1.14) of the equations of motion is linearized around the equilibrium of the system:

$$\dot{\mathbf{z}} = \begin{pmatrix} \mathbf{x} \\ \mathbf{y} \end{pmatrix} = \left[ \begin{array}{cc} \mathbf{0} & \mathbf{I} \\ \mathbf{K} + \frac{\partial \mathbf{f}}{\partial \mathbf{x}} & \mathbf{C} + \frac{\partial \mathbf{f}}{\partial \mathbf{y}} \end{array} \right] \mathbf{z} = \mathbf{A} \mathbf{z} \quad (1.27)$$

where  $\mathbf{A}$  is a linear operator which is assumed to have  $N$  distinct pairs of complex conjugate eigenvalues  $\lambda_m = \alpha_m \pm j\beta_m$ ,  $m = 1, \dots, N$  with their associated complex eigenvectors  $\mathbf{z}_m = \mathbf{z}_m^{\mathcal{R}} \pm j\mathbf{z}_m^{\mathcal{I}}$ . It can be shown that  $\mathbf{z}_m^{\mathcal{R}}$  and  $\mathbf{z}_m^{\mathcal{I}}$ ,  $\forall m$ , are linearly independent, and may constitute a new basis in the phase space [59], in which the equations of motion take the block-diagonal form. Focusing on a single-mode contribution, and applying a second coordinate transformation as suggested in [148], the complete coordinate transformation

$$\mathbf{z} = \begin{bmatrix} \mathbf{z}_m^{\mathcal{R}} & \mathbf{z}_m^{\mathcal{I}} \end{bmatrix} \begin{bmatrix} \beta_m & 0 \\ -\alpha_m & 1 \end{bmatrix} \begin{pmatrix} u_m(t) \\ v_m(t) \end{pmatrix} \quad (1.28)$$

gives all the coefficients  $a_{1i}$  and  $b_{1i}$  in the first column and  $a_{2i}$  and  $b_{2i}$  in the second column of the matrix product on the right-hand side of the equation. In the case of an undamped and non-gyroscopic system, there is no phase difference between the DOFs of the system and, at the linear level,  $a_{2i} = b_{1i} = 0$  and  $a_{1i} = b_{2i}$ . One should note that zeroth-order coefficients,  $a_{0i}$  and  $b_{0i}$ , can be introduced in the series expansion to account for the special cases where the nonlinearities shift the equilibrium position from the origin, or generate an additional equilibrium [145].

It was shown that solving the set of nonlinear algebraic equations can be carried out at very little cost as higher-order equations are linear in the lower-order coefficients. Therefore, starting from the results of the eigenvalue problem, the second-order coefficients are obtained through the resolution of a linear algebraic problem. Based on the linear

and second-order coefficients, third-order coefficients are obtained, and a similar procedure follows for higher-order coefficients.

A complete coordinate transformation from the modal space to the physical space (i.e.,  $(x_i, y_i)$ ) using a linear superposition of NNMs was proposed in [145]. As mentioned in [153], this transformation is erroneous because it omits the presence of nonlinear couplings between the NNMs as illustrated by the normal-form transformations [121]. Those coupling terms however vanish when the motion takes place on a single NNM, which shows that the invariance principle can be generalized to nonlinear systems.

## 1.5.2 Application to a 2DOF example

The NNMs of the 2DOF system (1.1) considered in Section 1.3 are now calculated using the polynomial expansion. Following Equations (1.14) to (1.17), we have:

$$\begin{cases} \dot{x}_1 = y_1 \\ \dot{x}_2 = y_2 \\ \dot{y}_1 = f_1(x_i, y_i) = -x_1 - (x_1 - x_2) - 0.5x_1^3 - c_1\dot{x}_1 - c_2(\dot{x}_1 - \dot{x}_2) \\ \dot{y}_2 = f_2(x_i, y_i) = -x_2 - (x_2 - x_1) - c_2\dot{x}_2 - c_3(\dot{x}_2 - \dot{x}_1) \end{cases} \quad (1.29)$$

where the  $c_i$ 's,  $i = 1, 2, 3$ , are the coefficients of the different viscous damping terms introduced in the original Equations (1.1). Using the first pair of state variables as the master pair, i.e.,  $(u, v) = (x_1, y_1)$ , the PDEs write

$$\begin{aligned} Y_2(u, v) &= \frac{\partial X_2(u, v)}{\partial u}v + \frac{\partial X_2(u, v)}{\partial v}f_1, \\ f_2 &= \frac{\partial Y_2}{\partial u}v + \frac{\partial Y_2}{\partial v}f_1. \end{aligned} \quad (1.30)$$

The slave coordinates  $X_2(u, v)$  and  $Y_2(u, v)$  are expanded up to the third and fifth orders according to Equations (1.26).

### Conservative Case

System (1.1) is first considered in the conservative case (i.e., the  $c_i$ 's are set to zero). Table 1.1 presents the coefficients obtained for the third-order expansion. Only 5 and 6 terms out of 18 are actually required to describe the in-phase and the out-of-phase NNMs, respectively. When analyzing the coefficients, it is observed that linear (first-order) coefficients clearly match the in-phase and out-of-phase motion describing the LNMs. Second-order coefficients are all zero because there is no quadratic nonlinearity in the system. The non-zero terms are characteristic of a synchronous motion where displacements  $u$  and  $X_2$  cancel out at the same values in the  $(u, v)$  plane. Similarly, velocities  $v$  and  $Y_2$  cancel out simultaneously when displacements are at their maximum values. Finally, Table 1.1 shows that the coefficient  $b_7$  is zero for the in-phase NNM whereas it is non-zero

Coeff.	In-phase NNM	Out-of-phase NNM	Coeff.	In-phase NNM	Out-of-phase NNM
$a_1$	1	-1	$b_1$	0	0
$a_2$	0	0	$b_2$	1	-1
$a_3$	0	0	$b_3$	0	0
$a_4$	0	0	$b_4$	0	0
$a_5$	0	0	$b_5$	0	0
$a_6$	0.1667	0.1923	$b_6$	0	0
$a_7$	0	0	$b_7$	0	0.2308
$a_8$	0.25	0.0577	$b_8$	0	0
$a_9$	0	0	$b_9$	0.25	0.0577

Table 1.1: Coefficients of the third-order polynomial expansion describing the manifold geometry in the conservative example.

Coeff.	In-phase NNM	Out-of-phase NNM	Coeff.	In-phase NNM	Out-of-phase NNM
$a_{15}$	0.0152	-0.0197	$b_{15}$	0	0
$a_{16}$	0	0	$b_{16}$	0.0455	-0.0302
$a_{17}$	-0.0682	-0.0173	$b_{17}$	0	0
$a_{18}$	0	0	$b_{18}$	-0.0909	-0.0198
$a_{19}$	0.0028	-0.0021	$b_{19}$	0	0
$a_{20}$	0	0	$b_{20}$	0.0028	-0.0021

Table 1.2: Coefficients for the fifth-order polynomial description of the manifold geometry in the conservative example.

for the out-of-phase NNM. An inspection of the analytical expressions demonstrates that this term is perfectly balanced for the in-phase NNM when linear stiffness coefficients are equal to 1 whereas it is strictly positive for the out-of-phase NNM (see [145]).

The polynomial expansion is then extended to fifth order. The coefficients are listed in Table 1.2. For this new expansion, the 18 lower-order coefficients do not need to be recalculated. The computation of the 22 new coefficients, i.e., 10 for the fourth-order terms and 12 for fifth-order terms, is also sequential. Similarly to quadratic coefficients, quartic coefficients are all zero as there is no even nonlinearity  $a_{10} = \dots = a_{14} = b_{10} = \dots = b_{14} = 0$ . The corrections brought by the fifth-order terms are also small as the coefficients are one or two orders of magnitude lower than cubic and linear coefficients. Furthermore, they are still characteristic of a synchronous motion.

Figure 1.10 illustrates the accuracy of the polynomial expansion for the first NNM. In particular, Figures 1.10(a, b) represent the slave coordinates  $X_2(u, v)$  and  $Y_2(u, v)$  for the third-order (light blue) and the fifth-order (dark blue) approximations. For conservative

systems, the “exact” manifolds can be computed using the numerical continuation technique developed in [120] by gathering in phase space all the computed periodic orbits. This reference manifold is plotted in orange for comparison with the series expansion. Around the origin and for a region of unit radius, the three surfaces are almost flat and appear similar. At higher amplitudes, the third- and fifth-order approximations deviate from the reference, but a good matching is preserved along the zero-velocity line and, to a slightly lesser extent, along the zero-displacement line. The larger discrepancies are observed at the corner of the domain, where the fifth-order approximation actually provides a worse approximation of the manifold than at third order.

In Figures 1.10(c – f), results accuracy is investigated using the system’s dynamics. Specifically, the equations governing the modal dynamics (i.e., the dynamics on the invariant manifold) are integrated over time using a fourth-order Runge-Kutta method. The modal time series are then projected back to the physical space using Equations (1.15). The initial conditions (ICs) in physical space are then considered for a second time integration of the full system of equations of motion (Equations (1.29)). The resulting time series are displayed in Figures 1.10(c – d) for intermediate-amplitude and in Figures 1.10(e – f) for high-amplitude ICs. Third- and fifth-order approximations are presented in the left and right columns, respectively. A more quantitative comparison of the time series is achieved using the normalized mean-square error (NMSE):

$$\text{NMSE}(x) = \frac{100}{S\sigma_{\tilde{x}}^2} \sum_{i=1}^S (\tilde{x}(i) - x(i))^2, \quad (1.31)$$

where  $x$  is the time series to be compared to the reference time series  $\tilde{x}$ ,  $S$  is the number of samples and  $\sigma_{\tilde{x}}^2$  is the variance of the reference time series. A NMSE value of 1% is commonly assumed to reflect excellent concordance between time series.

NMSE values for all ICs are reported in Table 1.3. Note that additional low-amplitude ICs are also considered. For low and intermediate ICs, the dynamics is in perfect agreement with the reference and the fifth-order expansion further improves the matching. Boivin et al. showed that, for systems where the lowest nonlinearity is of order  $Q$ , the dynamic is accurate to order  $(N' + Q - 1)$  where  $N'$  is the order of approximation of the invariant manifold. For general nonlinearities, this means that the approximation of the dynamics is accurate, at least, to one order higher than the manifold itself, and two orders higher in the case of purely odd nonlinearities [17, 18]. The accuracy generally decreases with the amplitude. For high ICs, a reasonable agreement is observed for the third-order expansion, but the approximation fails at fifth order. This confirms the previous visual inspections of the invariant manifold. This behavior is typical of series expansion methods for which the approximation is improved inside the convergence domain but may diverge faster outside the convergence domain when the expansion order is increased.

One should note that, although NMSE provides an objective indicator for comparing the times series, it has the disadvantage to penalize more frequency errors than amplitude errors (i.e., 1% of error in amplitude or frequency does not give similar NMSE values).

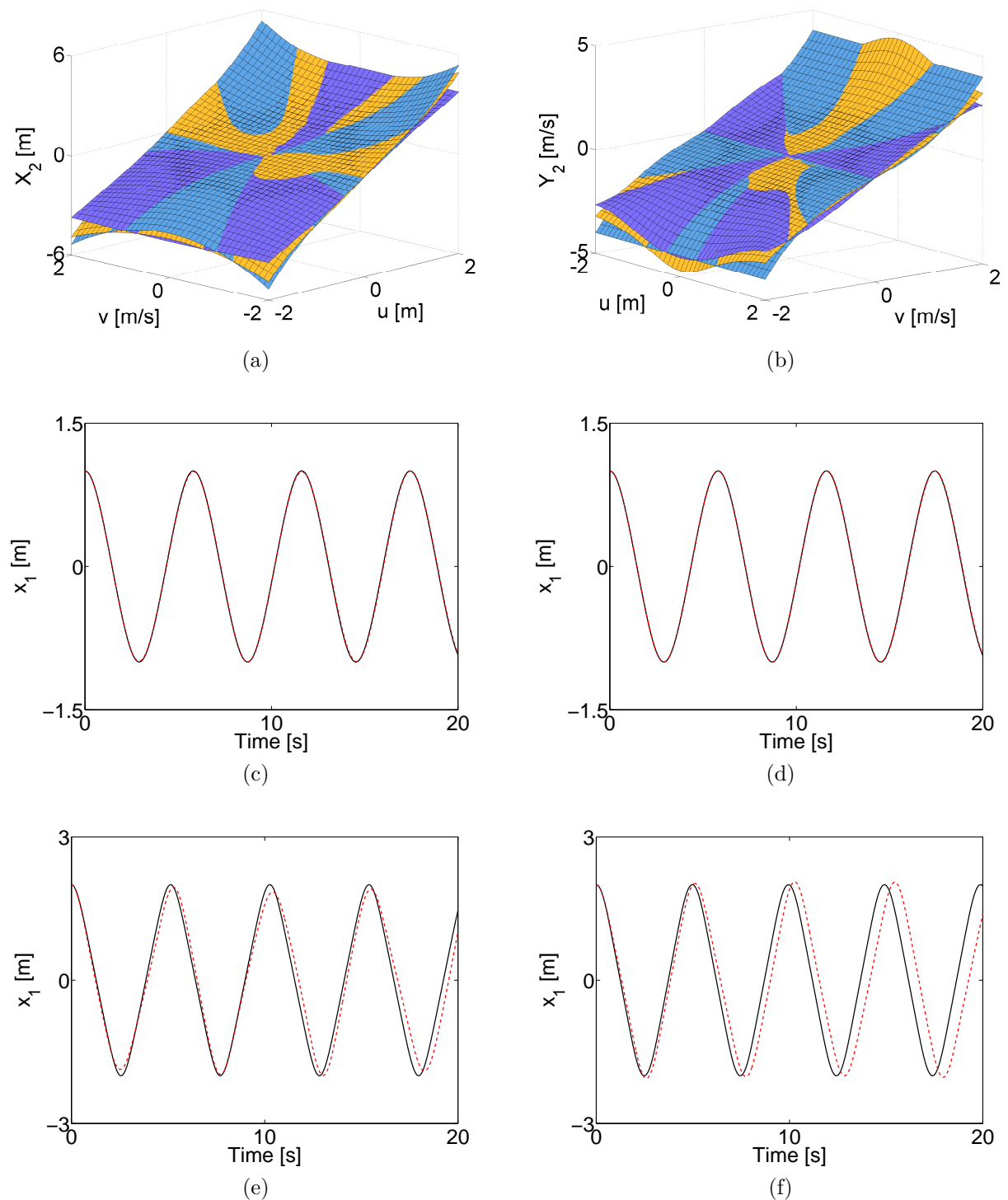


Figure 1.10: Validation of the polynomial expansion for the in-phase NNM. (a, b) Invariant manifold  $X_2$  and  $Y_2$  in phase space (light blue: 3<sup>rd</sup> order, dark blue: 5<sup>th</sup> order, and orange: numerical continuation). (c – d) Dynamics on the invariant manifold (black) and for the full system (red) with intermediate-amplitude ICs and third- and fifth-order approximations, respectively. (e – f) Dynamics with high-amplitude ICs.

Initial conditions	NMSE( $u(t)$ )[%]	NMSE( $v(t)$ )[%]	NMSE( $X_2(t)$ )[%]	NMSE( $Y_2(t)$ )[%]
<b>3<sup>rd</sup> order</b>				
$(u, v) = (0.1, 0)$	$10^{-10}$	$10^{-10}$	$10^{-10}$	$10^{-10}$
$(u, v) = (1, 0)$	$3 \times 10^{-2}$	$3 \times 10^{-2}$	$3 \times 10^{-2}$	$3 \times 10^{-2}$
$(u, v) = (2, 0)$	4	5	4	4
<b>5<sup>th</sup> order</b>				
$(u, v) = (0.1, 0)$	$10^{-11}$	$10^{-11}$	$10^{-11}$	$10^{-11}$
$(u, v) = (1, 0)$	$2 \times 10^{-10}$	$2 \times 10^{-10}$	$2 \times 10^{-10}$	$2 \times 10^{-10}$
$(u, v) = (2, 0)$	23	24	22	20

Table 1.3: Quantitative comparison between the conservative dynamics on the in-phase NNM and for the full system. Third- and fifth-order approximations are considered for low-, intermediate-, and high-amplitude initial conditions (0.1,0), (1,0), (2,0), respectively.

Initial conditions	NMSE( $u(t)$ )[%]	NMSE( $v(t)$ )[%]	NMSE( $X_2(t)$ )[%]	NMSE( $Y_2(t)$ )[%]
<b>3<sup>rd</sup> order</b>				
$(u, v) = (0.1, 0)$	$10^{-9}$	$10^{-9}$	$10^{-9}$	$10^{-9}$
$(u, v) = (1, 0)$	0.3	0.3	0.3	0.3
$(u, v) = (2, 0)$	5.8	5.5	49.8	48.5
<b>5<sup>th</sup> order</b>				
$(u, v) = (0.1, 0)$	$10^{-12}$	$10^{-12}$	$10^{-12}$	$10^{-12}$
$(u, v) = (1, 0)$	$6 \times 10^{-4}$	$6 \times 10^{-4}$	$7 \times 10^{-4}$	$8 \times 10^{-4}$
$(u, v) = (2, 0)$	1.6	1.4	6.7	9.0

Table 1.4: Quantitative comparison between the conservative dynamics on the out-of-phase NNM and for the full system. Third- and fifth-order approximations are considered for low-, intermediate-, and high-amplitude initial conditions (0.1,0), (1,0), (2,0), respectively.

Figure 1.11 presents the results for the out-of-phase NNM. Contrary to the in-phase NNM, the overall match between the approximations and the reference is less accurate. Both approximations of the invariant surface appear to be good at high velocity but for relatively small displacements. The fifth-order approximation improves the NNM approximation for all ICs considered (cf. Table 1.4). In Figure 1.11(e), there exists however a strong qualitative and quantitative difference between the dynamics of the reduced and full systems. It is explained by the rough approximation of the manifold in this region. At third order, harmonics arising from the cubic components in the expansion are present in the time series. At fifth order, these harmonics are removed by the fifth-order terms that all possess a negative sign.

Finally, the analysis of the conservative case is concluded by investigating the reproduction of the FEP using the reduced dynamics given by Equations (1.18). The FEPs are

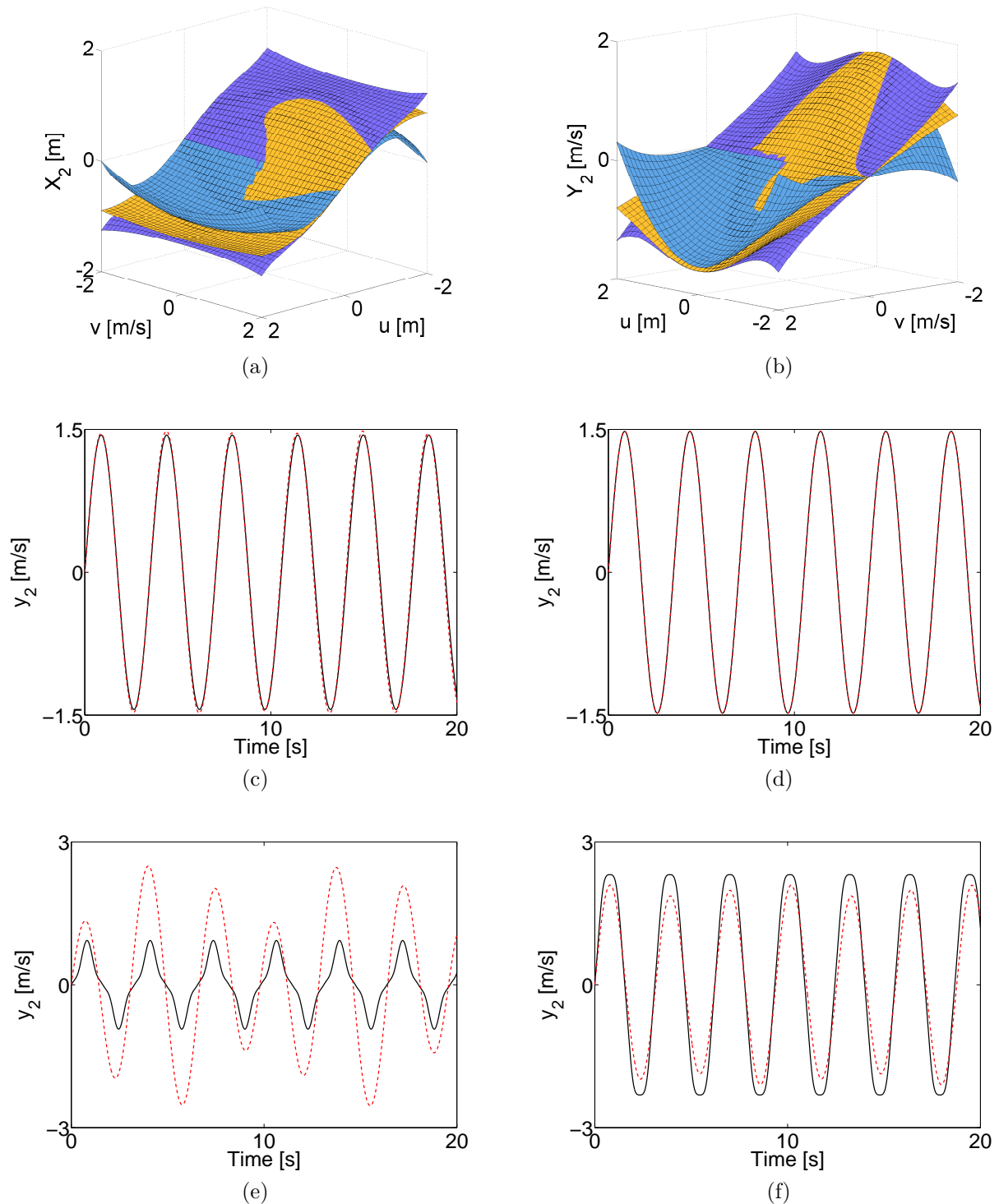


Figure 1.11: Validation of the polynomial expansion for the out-of-phase NNM. (a, b) Invariant manifold  $X_2$  and  $Y_2$  in phase space (light blue: 3<sup>rd</sup> order, dark blue: 5<sup>th</sup> order, and orange: numerical continuation). (c – d) Dynamics on the invariant manifold (black) and for the full system (red) with intermediate-amplitude ICs and third- and fifth-order approximations, respectively. (e – f) Dynamics with high-amplitude ICs.

computed using continuation with the frequency as parameter. The FEP for the in-phase and the out-of-phase NNM are given in Figures 1.12(a) and (b), respectively. The comparison with the curves computed in Section 1.3 (in black) confirms the previous observations. For the first NNM, the fifth-order expansion barely improves the accuracy for low amplitudes (i.e., energy) and fails at higher amplitudes. Conversely, for the second NNM, the fifth-order expansion increases the validity range of the expansion. Overall, the polynomial approximations of both modes remain however limited to weakly nonlinear regimes of motion.

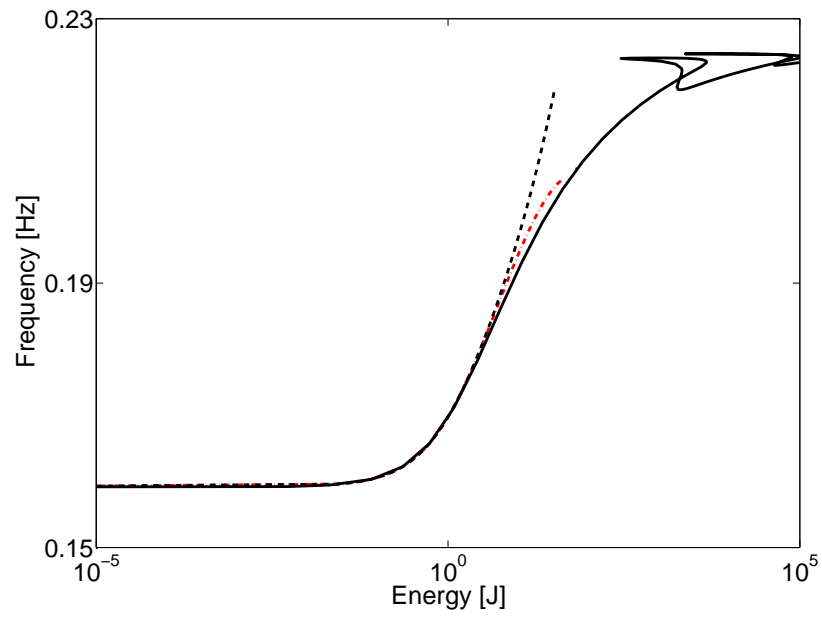
### Nonconservative Case

In this section, linear damping is introduced into the 2DOF system with the following parameters:  $c_1 = 0$  and  $c_{2,3} = 0.3$ . The coefficients describing the geometry of the manifolds at fifth order are given in Table 1.5. The findings are similar to the conservative case. In particular, in the absence of even nonlinearity, quadratic and quartic coefficients are all zero. Due to the non-proportionality of the damping, the linear coefficients defining the LNM have changed from the underlying conservative case. Moreover, the coefficients  $(a_9, a_{20}, b_9, b_{20})$  are non-zero which clearly indicates a phase difference between the two masses of the system. Finally, the strong character of the damping has only slightly affected the non-zero coefficients already present in the conservative case and the new coefficients are generally small.

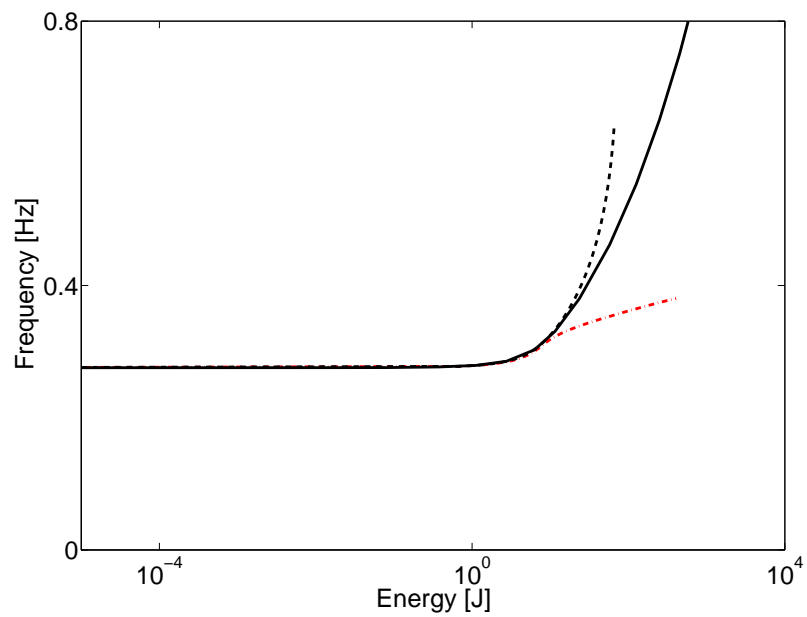
Coeff.	In-phase NNM	Out-of-phase NNM	Coeff.	In-phase NNM	Out-of-phase NNM
$a_1$	0.9471	-1.1056	$b_1$	0.1401	0.4599
$a_2$	-0.1386	-0.1550	$b_2$	0.9676	-0.9891
$a_6$	0.1554	0.0327	$b_6$	0.0531	0.2088
$a_7$	-0.0074	-0.0492	$b_7$	0.0244	0.1991
$a_8$	0.2191	-0.0110	$b_8$	0.0768	0.0821
$a_9$	-0.0627	-0.0187	$b_9$	0.2455	0.0324
$a_{15}$	0.0127	0.0089	$b_{15}$	0.0131	-0.0187
$a_{16}$	-0.0128	0.0129	$b_{16}$	0.0409	-0.0260
$a_{17}$	-0.0591	0.0116	$b_{17}$	0.0037	-0.0225
$a_{18}$	0.0101	0.0087	$b_{18}$	-0.0810	-0.0113
$a_{19}$	0.0018	0.0021	$b_{19}$	0.0104	-0.0030
$a_{20}$	-0.0065	0.0009	$b_{20}$	0.0052	-0.0008

Table 1.5: Coefficients of the fifth-order expansion describing in-phase and out-of-phase NNMs for the nonconservative system.

The accuracy of the approximation of the out-of-phase NNM is now discussed. The invariant manifolds calculated at the third (light blue) and fifth orders (dark blue) are compared



(a)



(b)

Figure 1.12: Frequency-Energy plot of the 2DOF system (1.1). (a) In-phase NNM; (b) out-of-phase NNM. Black: reference from the continuation of the full system of equations of motion, red and blue: third- and fifth-order expansions, respectively.

Initial conditions	NMSE( $u(t)$ )[%]	NMSE( $v(t)$ )[%]	NMSE( $X_2(t)$ )[%]	NMSE( $Y_2(t)$ )[%]
<b>3<sup>rd</sup> order</b>				
$(u, v) = (0.1, 0)$	$10^{-9}$	$10^{-9}$	$10^{-9}$	$10^{-9}$
$(u, v) = (1, 0)$	$3 \times 10^{-2}$	$10^{-2}$	$3 \times 10^{-2}$	$2 \times 10^{-2}$
$(u, v) = (2, 0)$	3.9	1.5	4.6	2.3
<b>5<sup>th</sup> order</b>				
$(u, v) = (0.1, 0)$	$10^{-9}$	$10^{-9}$	$10^{-9}$	$10^{-9}$
$(u, v) = (1, 0)$	$2 \times 10^{-4}$	$2 \times 10^{-4}$	$2 \times 10^{-4}$	$2 \times 10^{-4}$
$(u, v) = (2, 0)$	0.3	0.1	0.6	0.3

Table 1.6: Quantitative comparison between the nonconservative dynamics on the out-of-phase NNM and for the full system. Third- and fifth-order approximations are considered for low-, intermediate-, and high-amplitude initial conditions  $(0.1, 0)$ ,  $(1, 0)$ ,  $(2, 0)$ , respectively.

in Figure 1.13 to a reference manifold computed using the method developed in Chapter 3. Contrary to the conservative case, the invariant surface is almost flat throughout the domain, and its inclination confirms the nonproportional character of the damping. The overall aspect of the invariant manifold is well captured by both approximations. The larger discrepancies occur when the master displacement and velocity are maximum and of the same sign. However, using visual inspection, it is difficult to determine if the fifth-order approximation improves the third-order solution at higher amplitudes. The computation of time series for the full and reduced systems shows that there is in fact an improvement for all tested ICs. This is illustrated in Figures 1.13(c – f). The NMSE values of the time series are reported in Table 1.6. For ICs similar to the conservative case, the NMSE values appear smaller.

## Discussion

The analytical approach proposed by Shaw and Pierre [145] was considered in this section to obtain a description of a NNM as a polynomial series. The method is applicable to both conservative and nonconservative systems and proved to be accurate for low to intermediate vibration amplitudes. However, the method presents also some limitations. In particular, for a given vibration amplitude, the introduction of higher-order terms in the approximation does not guarantee an improvement of the results. The convergence domain of the expansion is *a priori* unknown. Moreover, increasing the expansion order reflects into additional analytical calculations and implementation efforts [123]. Finally, as for all series expansions, the choice of the expansion variables is critical. It was mentioned in [145] that the expansion can fail, for instance, in the case of localization. In this situation, some coefficients become too large indicating a failure of the series development. The expansion has thus to be considered in terms of other variables.

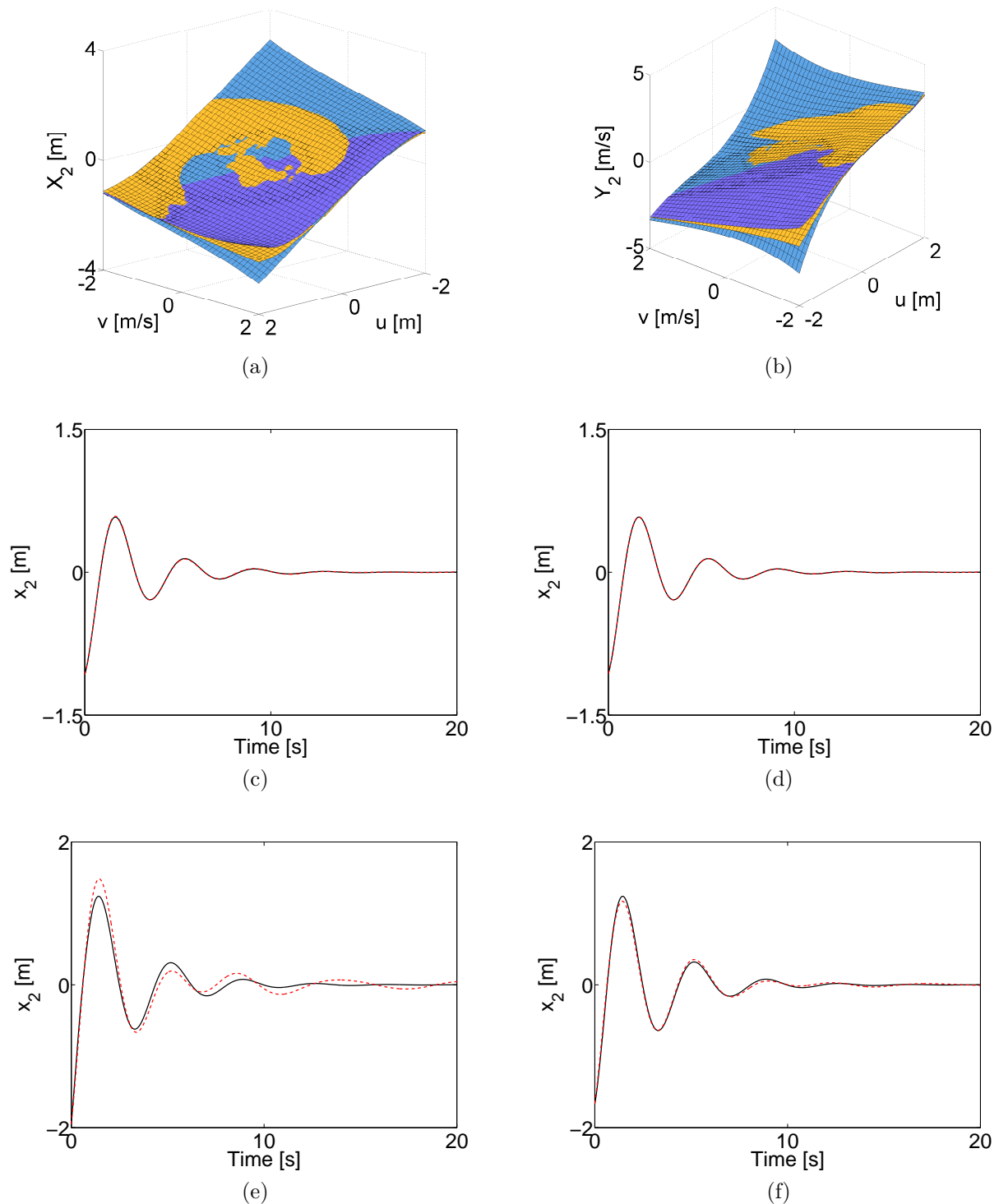


Figure 1.13: Validation of the polynomial expansion for the out-of-phase NNM. (a, b) Invariant manifold  $X_2$  and  $Y_2$  in phase space (light blue: 3<sup>rd</sup> order, dark blue: 5<sup>th</sup> order, and orange: method presented in Chapter 3). (c – d) Dynamics on the invariant manifold (black) and for the full system (red) with intermediate-amplitude ICs and third- and fifth-order approximations, respectively. (e – f) Dynamics with high-amplitude ICs.

## 1.6 Numerical Resolution of the Manifold-Governing PDEs

Numerical methods were introduced with the objective of addressing the limitations of analytical methods. This section briefly reviews the contributions existing in the literature.

### 1.6.1 A Galerkin-Based Approach

The first attempt to carry out numerical computation of PDEs (1.17) is that of Pesheck et al. [126]. Equations of motion were first written in modal space as

$$\ddot{\boldsymbol{\eta}} + \mathbf{Z}\dot{\boldsymbol{\eta}} + \boldsymbol{\Omega}\boldsymbol{\eta} = \hat{\mathbf{f}}(\boldsymbol{\eta}, \dot{\boldsymbol{\eta}}) \quad (1.32)$$

and where  $\boldsymbol{\eta}$  is the vector of normalized modal coordinates,  $\mathbf{Z}$  the modal damping matrix, and  $\boldsymbol{\Omega}$  the modal stiffness matrix.  $\hat{\mathbf{f}}(\boldsymbol{\eta}, \dot{\boldsymbol{\eta}})$  is the nonlinear force vector projected onto the linear modal basis. Following the same two-dimensional parameterization of the invariant surface as in Section 1.4.2, a pair of master variables  $(\eta_k, \dot{\eta}_k)$  is chosen and the remaining coordinates are described in terms of this pair. An additional transformation into polar coordinates is used to define the master pair into amplitude  $a$  and phase  $\phi$  variables:

$$\eta_k = a \cos \phi, \quad \dot{\eta}_k = a\omega_k \sin \phi. \quad (1.33)$$

The constraint relations are

$$\eta_i = P_i(a, \phi), \quad \dot{\eta}_i = Q_i(a, \phi), \quad i = 1, \dots, N; \quad i \neq k. \quad (1.34)$$

The manifold-governing PDEs are

$$\begin{aligned} Q_i &= \frac{\partial P_i}{\partial a} a \tilde{f}_k \sin \phi + \frac{\partial P_i}{\partial \phi} (\omega_k + \tilde{f}_k \cos \phi), \\ -2\zeta_i \omega_i Q_i - \omega_i^2 P_i + \hat{f}_i &= \frac{\partial Q_i}{\partial a} a \tilde{f}_k \sin \phi + \frac{\partial Q_i}{\partial \phi} (\omega_k + \tilde{f}_k \cos \phi), \end{aligned} \quad (1.35)$$

where  $\tilde{f}_k = -\left(\frac{\hat{f}_k}{a\omega_k} + 2\zeta_k \omega_k \sin \phi\right)$  and  $i = 1, \dots, N; \quad i \neq k$  [126]. The phase-amplitude formulation allows to approximate the functional  $P_i$  and  $Q_i$  with double expansion series

$$P_i(a, \phi) = \sum_{l=1}^{N_a} \sum_{m=1}^{N_\phi} C_i^{l,m} T_{l,m}(a, \phi), \quad Q_i(a, \phi) = \sum_{l=1}^{N_a} \sum_{m=1}^{N_\phi} D_i^{l,m} U_{l,m}(a, \phi), \quad (1.36)$$

where the functions  $T_{l,m}$  and  $U_{l,m}$  are global shape functions. They can be split into amplitude (i.e., polynomial) and phase (i.e., harmonic) contributions as

$$T_{l,m}(a, \phi) = L_l(a) \cos((m-1)\phi), \quad U_{l,m}(a, \phi) = L_l(a) \sin(m\phi) \quad (1.37)$$

and where  $L_l(a)$  are orthogonal polynomial functions [126]. Introducing Equations (1.36) into the PDEs (1.35) and using a Galerkin projection [126] based on the individual shape functions gives the discretized system

$$\int_{a,\phi} U_{p,q} \left[ -a \sum_{l,m} D_i^{l,m} U_{l,m} + \sum_{l,m} C_i^{l,m} \frac{\partial T_{l,m}}{\partial a} \tilde{f}_k a^2 \sin \phi + \sum_{l,m} C_i^{l,m} \frac{\partial T_{l,m}}{\partial \phi} (a\omega_k + \tilde{f}_k \cos \phi) \right] da d\phi = 0, \quad (1.38)$$

$$\int_{a,\phi} T_{p,q} \left[ 2\zeta_i \omega_i a \sum_{l,m} D_i^{l,m} U_{l,m} + \omega_i^2 a \sum_{l,m} C_i^{l,m} T_{l,m} - a \hat{f}_i + \sum_{l,m} D_i^{l,m} \frac{\partial U_{l,m}}{\partial a} \tilde{f}_k a^2 \sin \phi + \sum_{l,m} D_i^{l,m} \frac{\partial U_{l,m}}{\partial \phi} (a\omega_k + \tilde{f}_k \cos \phi) \right] da d\phi = 0, \quad (1.39)$$

where  $p = 1, \dots, N_a$  and  $q = 1, \dots, N_\phi$ . Eventually, the set of  $2(N-1)N_a N_\phi$  highly-coupled and highly-nonlinear algebraic equations is solved using Newton-like methods. Pesheck's method clearly eliminates a number of problems associated with the local polynomial approximation of the manifold. In particular, the accuracy of the results is now only reduced to a computational effort and guaranteed in the computational domain.

The method was at first computationally too demanding. The formulation was thus improved by considering simpler (linear) shape functions along  $a$  [123]. The method was simultaneously generalized to consider piecewise-linear nonlinearities [65] and forced systems [67]. Interestingly, to the best of our knowledge, the method was applied to damped systems only in a single study [96].

## 1.6.2 A Transport Method

More recently, Blanc et al. [13] proposed a new method for solving the manifold-governing PDEs. Using a similar modal and polar coordinate transformations as Pesheck et al., the PDEs were written as a transport problem:

$$\begin{aligned} \mathbf{V} \nabla P_i &= Q_i, \\ \mathbf{V} \nabla Q_i &= \hat{f}_i - \omega_i^2 P_i, \quad i = 1, \dots, N; \quad i \neq k, \end{aligned} \quad (1.40)$$

where  $\nabla$  is the gradient operator and  $\mathbf{V} = (\dot{a}, \dot{\phi})$  a velocity vector with:

$$\dot{a} = -\frac{f_k \sin \phi}{\omega_k}, \quad \dot{\phi} = \omega_k - \frac{f_k \cos \phi}{a\omega_k}. \quad (1.41)$$

To solve the transport PDEs in a domain  $(a, \phi) \in ]0, A[ \times ]0, 2\pi[$ , boundary conditions (BCs) are imposed along the zero-phase boundary and are iteratively modified to obtain

the continuity of the manifold:  $P_i(a, 0) = P_i(a, 2\pi)$  and  $Q_i(a, 0) = Q_i(a, 2\pi) \forall i \neq k$  [13]. Suitable BCs are also specified at the boundary  $a = A$ .

For a 2DOF system, the problem of finding the suitable BCs at  $\phi = 0$  was written as a minimization problem [13]:

$$J(P_0, Q_0) = \frac{1}{2} \int_0^A [(P(a, 2\pi) - P_0)^2 + (Q(a, 2\pi) - Q_0)^2] da \quad (1.42)$$

where  $P_0 = P(a, 0)$ ,  $Q_0 = Q(a, 0)$  and where  $P(a, 2\pi)$  and  $Q(a, 2\pi)$  are the solution of the transport problem for  $(P_0, Q_0)$  as initial conditions. Note that the index  $i$  was omitted as, for a 2DOF system, there is only one unknown displacement and velocity field.

The transport problem was solved on a regular grid over the domain and using an off-centered finite difference (FD) scheme which starts at  $\phi = 0$  and progresses toward increasing values of  $\phi$  [13]. At a phase line  $n$ , the partial derivative of  $P$  (similarly of  $Q$ ) in the amplitude direction was:

$$\left(\frac{\partial P}{\partial a}\right)(a_m, \phi_n) \approx \frac{P_n^m - P_n^{m-1}}{\delta a} \quad \text{if } V_a^{n,m} > 0, \quad (1.43)$$

$$\left(\frac{\partial P}{\partial a}\right)(a_m, \phi_n) \approx \frac{P_n^{m+1} - P_n^m}{\delta a} \quad \text{if } V_a^{n,m} < 0, \quad (1.44)$$

at point  $(a_m, \phi_n)$ . The choice of the discretization according to the direction of the velocity is classical for transport problems. We refer to [13] for additional details about the discretization scheme.

Eventually, the Jacobian matrix of the optimization problem was obtained by the method of the adjoint state [13, 99] and the problem was solved using a Newton-like method. Interestingly, the first guess of the solution was determined using an asymptotic approximation of the invariant manifold [153].

Thanks to its solid theoretical foundations, the method accurately computes the geometry of the invariant manifolds defining NNMs. Obtained NNMs were then used for the purpose of building reduced-order models. However, in the absence of shape functions (as in the Galerkin-based approach), the method does not have a direct interpolation basis for computing the dynamics on the invariant manifold. Such basis was computed *a posteriori* by fitting the collection of points of the FD discretization. As of now, the method is not applicable to nonconservative systems and has to be extended, as discussed in [13]. In particular, the definition of appropriate BCs at  $a = A$  appears problematic.

## 1.7 Concluding Remarks

NNMs offer a solid and useful theoretical framework for addressing the nonlinear dynamics of engineering structures. Their properties allow, for instance, to observe the evolution of

the frequency of a mode as the energy of initial conditions varies, and thus to determine whether a mode is nonlinear or not. NNMs can also explain nonlinear phenomena that are unexplainable from a linear viewpoint as, e.g., modal interactions. Finally, NNMs are also interesting for practicing engineers because they have a clear conceptual relation with LNMs. In particular, among other things, NNMs represent the structural deformation at resonance.

In the conservative framework, the definition of NNMs as *non-necessarily synchronous* periodic oscillations is particularly appealing when targeting their computation. Although there now exist sophisticated methods to compute NNMs, their application to complex, strongly nonlinear, real-life structures is not yet well-established. The algorithm combining shooting and pseudo-arclength continuation that was presented in Section 1.4.1 will address such a structure in Chapter 2, paving the way for a practical application of NNMs.

In the nonconservative framework, NNMs are viewed as two-dimensional invariant manifolds in phase space. This definition is the common denominator to several formulations for NNMs of damped systems (see Section 1.4.2). In Section 1.5.2, we focused on the approach presented by Shaw and Pierre, and we studied the PDEs governing the manifold's geometry. We believe that invariant objects play a key role in the study of dynamical systems, and that solving the PDEs to obtain the manifold's geometry will allow to progress in the theoretical understanding of NNMs. Moreover, this approach opens up new possibilities for developing geometrical methods to compute and interpret NNMs (as we shall see in Chapter 6). Finally, from a practical point of view, the constraint relations defining the NNM geometry offer a straightforward reduction of the system's dynamics.

The PDE solutions were first approximated analytically using polynomial series. The method is accurate only for weakly nonlinear regimes of motion and suffers from the generic issues of series expansions. In Section 1.6, the two existing contributions for numerically solving the PDEs governing NNMs were reviewed.

In conclusion, computing NNMs for nonconservative systems remains a challenging task. Although the mathematical framework exists, there is a need for computational methods that can accurately and effectively solve the corresponding set of PDEs when damping is present. Chapter 3 addresses this challenge and proposes a rigorous finite-element-based method for computing NNMs of general nonconservative systems.



## Chapter 2

# Nonlinear Dynamics and Undamped NNMs of a Full-Scale Spacecraft

---

### **Abstract**

This chapter investigates the dynamics of a real-life satellite structure possessing a strongly nonlinear component. Based on the results of a test campaign carried out in collaboration with EADS-Astrium and LMS, a mathematical model of the spacecraft is built for gaining additional insight into the nonlinear phenomena that were observed experimentally. Forced/unforced, damped/undamped numerical simulations are carried out using numerical continuation techniques and the nonlinear normal modes of the system are carefully analyzed.

---

## 2.1 Introduction

It is widely accepted that virtually all engineering structures are nonlinear, at least in certain regimes of motion. Even if the common industrial practice is to ignore nonlinearity, a recent trend is to consider or even utilize nonlinear components during the design process. Addressing nonlinearity is however a challenging task in view of the numerous phenomena that nonlinear systems can exhibit. The last decade witnessed important progress in this direction and more particularly in the analysis of nonlinear aerospace structures. Substantial efforts were made to address the numerical modeling of complex nonlinear aerospace structures (see, e.g., [93, 127]). Analysis using advanced numerical continuation techniques was also carried out in [78, 164].

Despite this increasing interest, very few studies attempted to numerically analyze and experimentally compare the dynamics of a real-life structure in strongly nonlinear regimes of motion. Additionally, there are very few contributions where nonlinear normal modes (NNMs) are computed to analyze the dynamics of large-scale systems. Consequently, most practicing engineers still view NNMs as a concept that is foreign to them.

To bridge this gap, this chapter is concerned with the study of the SmallSat spacecraft, which possesses a nonlinear component with multiple axial and lateral mechanical stops. A mathematical model of the satellite is identified using measurements collected during a typical qualification test campaign. A detailed finite element model of the underlying linear satellite is first built in Section 2.2 and reduced using the Craig-Bampton technique. The model identified experimentally for the nonlinear vibration isolation device is incorporated into the finite element model in Section 2.3. The nonsmooth nonlinearities in the model are regularized for facilitating the ensuing numerical simulations. Section 2.4 provides the numerical evidence of some of the phenomena observed experimentally. A bifurcation analysis then reveals the existence of quasiperiodic regimes of motion. Finally, Section 2.5 studies the dynamics of the spacecraft using NNMs. The nonlinear modal analysis of the SmallSat spacecraft is carried out, and several nonlinear modes exhibiting nonlinear modal interactions and energy localization are discussed in great detail. The direct correspondence with experimental observations demonstrates that NNMs provide a useful framework for addressing real-life systems. The conclusions of this chapter are drawn in Section 2.6.

## 2.2 The SmallSat Spacecraft Structure

The SmallSat structure was conceived by EADS-Astrium as a low-cost platform for small satellites in low earth orbits [139]. It is a monocoque tube structure which is 1.2 *m* in height and 1 *m* in width. It is composed of eight flat faces for equipment mounting purposes, creating an octagon shape, as shown in Figure 2.1(a). The octagon is manufactured using carbon-fiber-reinforced plastic by means of a filament winding process. The

structure thickness is 4 *mm* with an additional 0.25-*mm*-thick skin of Kevlar applied to both the inside and outside surfaces to provide protection against debris. The top floor is an 1-*m*<sup>2</sup> sandwich aluminum panel, with 25-*mm* core and 1-*mm* skins. The interface between the spacecraft and the launch vehicle is achieved via four aluminum brackets located around cut-outs at the base of the structure. The total mass including the interface brackets is around 64 *kg*.

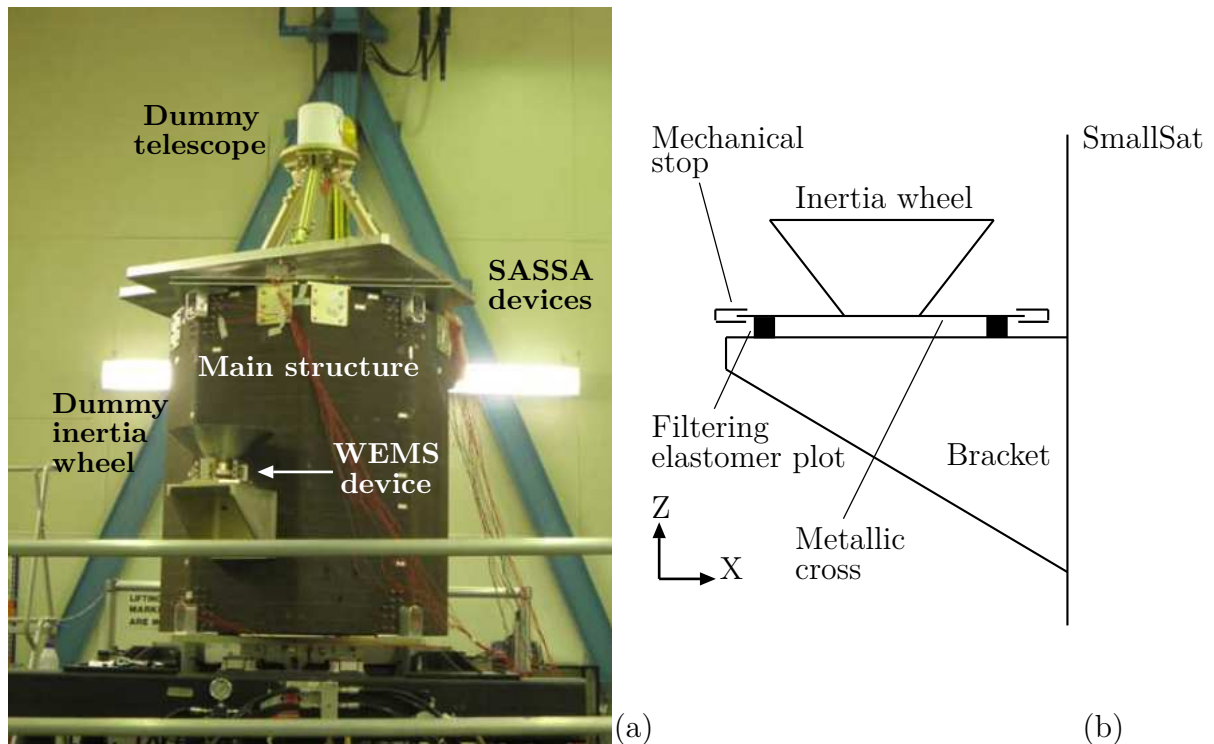


Figure 2.1: SmallSat spacecraft equipped with an inertia wheel supported by the WEMS and a dummy telescope connected to the main structure by the SASSA isolators. (a) Photograph; (b) schematic of the nonlinear vibration isolation device.

The spacecraft structure supports a dummy telescope mounted on a baseplate through a tripod; its mass is around 140 *kg*. The dummy telescope plate is connected to the SmallSat top floor by three shock attenuators, termed shock attenuation systems for spacecraft and adaptor (SASSAs) [22], whose dynamic behavior may exhibit nonlinearity. Besides, as depicted in Figure 2.1(b), a support bracket connects to one of the eight walls the so-called wheel elastomer mounting system (WEMS) which is loaded with an 8-*kg* dummy inertia wheel. The WEMS acts as a mechanical filter which mitigates high-frequency disturbances coming from the inertia wheel through the presence of a soft elastomeric interface between its mobile part, i.e., the inertia wheel and a supporting metallic cross, and its fixed part, i.e., the bracket and by extension the spacecraft. Moreover, the WEMS incorporates eight mechanical stops, covered with a thin layer of elastomer, and designed to limit the axial and lateral motions of the inertia wheel during launch, which gives rise to strongly nonlinear dynamical phenomena (cf. Section 2.3).

### 2.2.1 Finite Element Modeling of the Underlying Linear Satellite

A finite element model (FEM) of the SmallSat satellite created in the LMS-SAMTECH SAMCEF software is used in the present study to conduct numerical experiments. It comprises about 150,000 degrees of freedom (DOFs). The model idealizes the composite tube structure using orthotropic shell elements. The top floor, the bracket, and the wheel support are also modeled using shell elements. Boundary conditions are enforced at the base of the satellite through 4 clamped nodes. Proportional damping using the parameters provided by EADS-Astrium is also introduced in the model.

The typical frequency range of interest for spacecraft testing is between 5 and 100 Hz. Within this frequency interval, the model comprises 18 linear modes that can be classified into three groups of six modes, as listed in Table 2.1. The first group, between 8 Hz and 29 Hz, shows local WEMS motions. The corresponding modal shapes are depicted in Figure 2.2. Modes 1 and 2 show a concave trajectory of the WEMS about Y and X axes, respectively. Modes 3 and 5 correspond to a convex trajectory of the WEMS about Y and X axes, respectively. The fourth mode presents an in-plane rotation and extension of the WEMS cross. Only mode 6 combines a significant bracket deflection with a vertical WEMS motion. The second group, between 32 and 58 Hz, is composed of local SASSA modes including global deformation of the main structure. The last group comprises modes with local deformation of the main structure panels often combined with bracket deformation.

To monitor the integrity of the structure between each qualification run, low-level random data were acquired throughout the test campaign. Specifically, this was performed considering axial white-noise excitations filtered in 5 – 100 Hz and driven via a base acceleration of  $0.001 g^2/Hz$ . The low-level time series were exploited to identify the linear modal properties of the spacecraft, utilizing transmissibility functions (TFs) as no force measurement was available at the shaker-to-structure interface. This analysis is carried out using the frequency-domain subspace algorithm derived in reference [105]. The resulting estimates of the resonance frequencies of the spacecraft are also given in Table 2.1. We refer to [115] for more details about the experimental identification.

We note that a formal model updating process could not be achieved during the test campaign. Bringing the predictions of the model in very close quantitative agreement with the experimental results was therefore not the objective. Nonetheless, the good agreement in Table 2.1 between the natural frequencies predicted by the FEM and those identified experimentally together with the correct mode ordering confirm that the model should have satisfactory predictive capabilities.

Mode #	Model frequency [Hz]	Experimental frequency [Hz]
1	8.06	8.19
2	9.14	–
3	20.44	–
4	21.59	–
5	22.05	20.18
6	28.75	22.45
7	32.49	–
8	34.78	34.30
9	39.07	–
10	40.78	43.16
11	45.78	45.99
12	57.76	55.71
13	68.99	64.60
14	75.14	–
15	79.82	–
16	83.36	–
17	89.01	88.24
18	95.30	–

Table 2.1: Comparison between numerical and experimental natural frequencies. A dash means that the corresponding mode could not be identified during the test campaign.

## 2.2.2 Reduced-Order Modeling

Because the WEMS nonlinearities are spatially localized, condensation of the linear FEM can be effectively achieved using the Craig-Bampton reduction technique [7]. This leads to a substantial decrease in the computational burden without degrading the accuracy of the numerical simulations in the frequency range of interest. The Craig-Bampton method expresses the complete set of initial DOFs in terms of retained DOFs and internal vibration modes of the structure clamped on the retained nodes. To introduce the WEMS nonlinearities, the reduced-order model (ROM) is constructed by keeping one node on both sides of the lateral and axial mechanical stops. In total, eight nodes of the initial FEM possessing 3 DOFs each and 10 internal modes of vibration are kept; this reduced model possesses 34 DOFs and is termed ROM810. For local excitation of the WEMS, a second ROM, termed ROM910, is created with an additional node on the metallic cross.

The ROM accuracy is assessed by comparing its modal parameters with those of the original full-scale model. The deviation between the mode shapes is determined using the modal assurance criterion (MAC). MAC value ranges from 0 in the absence of correlation to 1 for a complete correspondence. The frequency deviations as well as the MAC of ROM810 are displayed in Figure 2.3. We observe a very good correlation for the first 18 modes which cover the frequency range of interest.

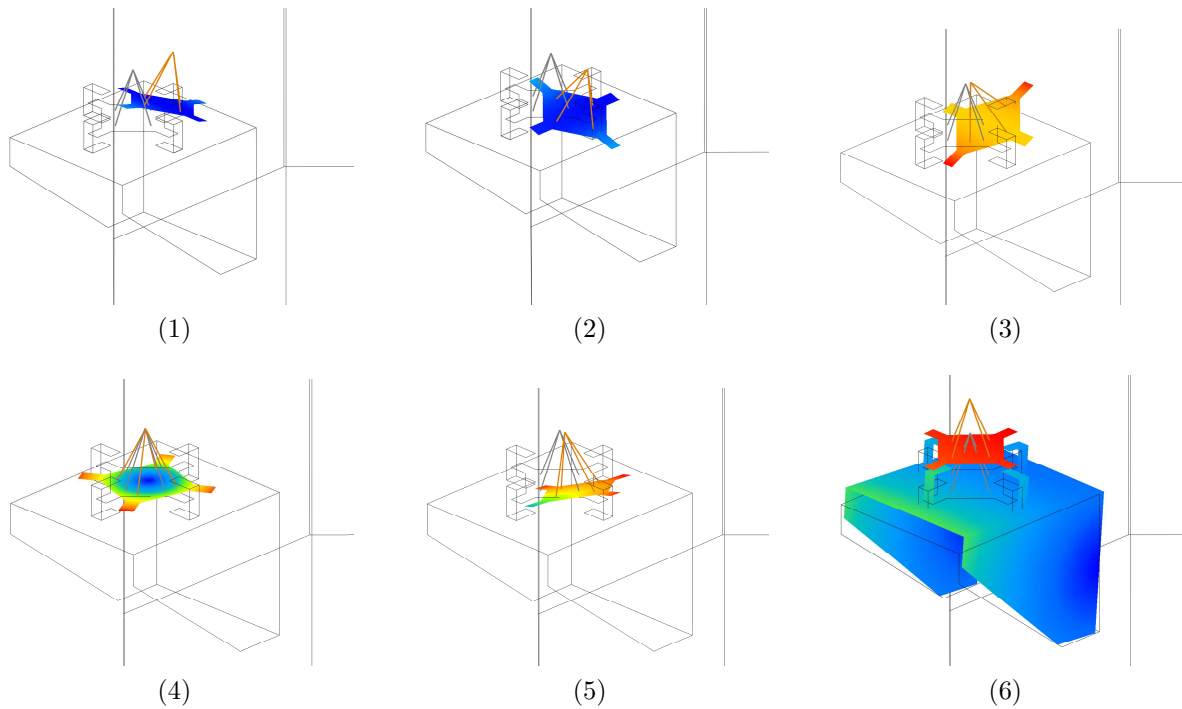


Figure 2.2: Close-up of the six first LNMs (local WEMS motion). (1 – 6) for LNM 1 to LNM 6, respectively.

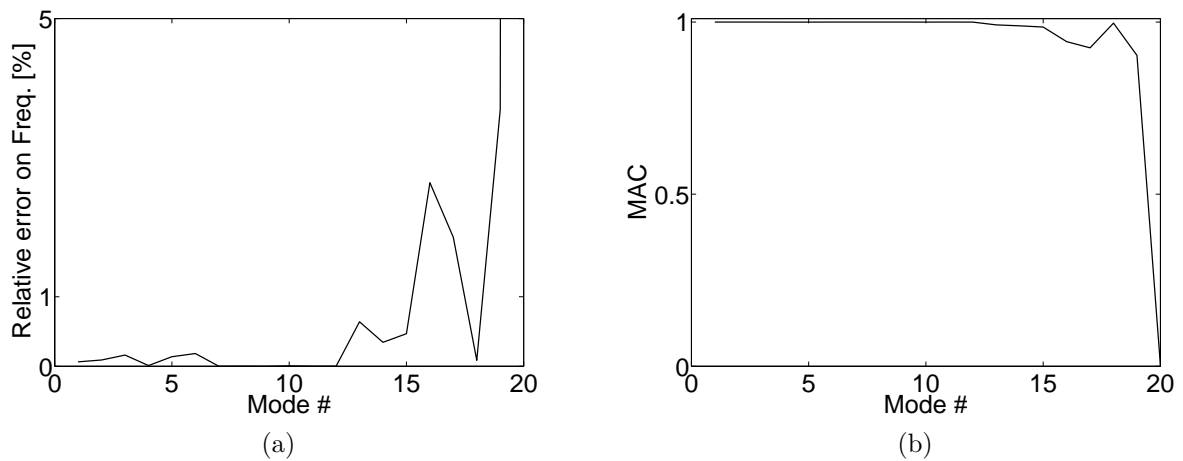


Figure 2.3: Relative error on frequencies and MAC between the ROM810 and the original model.

## 2.3 Modeling of the WEMS Nonlinearities

The identification of the SmallSat's nonlinear components is performed using measurements collected during a typical qualification test campaign which consisted of swept-sine base excitations applied to the spacecraft for different amplitude levels, sweep rates and directions. Two specific data sets measured under 0.6  $g$  and 1  $g$  axial loadings and for positive sweep rates of 2 and 4 octaves per minute, respectively, are exploited.

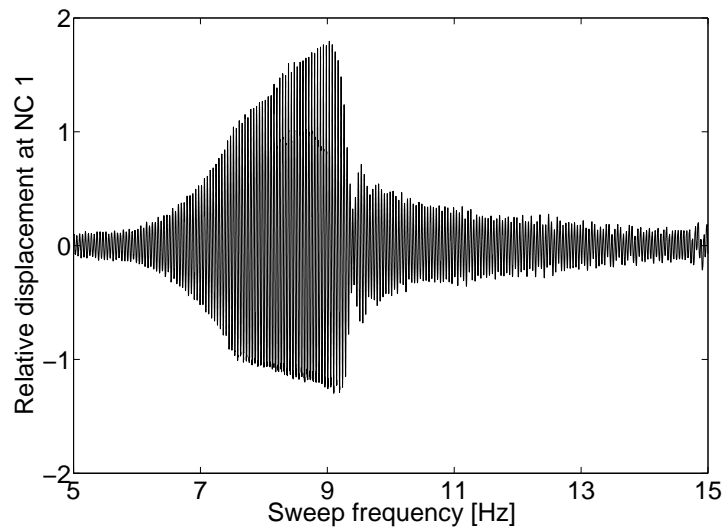
Across the structure, the WEMS appears as the strongest nonlinearity source. Figure 2.4(a) illustrates the axial relative displacement between the WEMS cross and its support for data measured at 1  $g$ . One remarks the clear skewness and nonsmoothness of the envelope of oscillations, which exhibits a sudden transition from large to small amplitudes of vibration, referred to as a jump phenomenon. This envelope also presents a significant asymmetry entailing larger amplitudes of motion in positive displacement, and a discontinuity in slope for negative displacements around 7.5  $Hz$ . Figure 2.4(b) shows the wavelet transform of the time series presented in Figure 2.4(a). The presence of a wideband frequency, including strong harmonics, confirms the strongly-nonlinear character of the WEMS. The presence of even harmonics and the sudden disappearance of the wideband content also indicates a nonsmooth character of the nonlinearity.

Figure 2.5 presents a simplified, yet relevant, modeling of the WEMS where the inertia wheel, owing to its important rigidity, is seen as a point mass. The four nonlinear connections (NCs) between the WEMS mobile and fixed parts are labeled NC1–4, respectively.

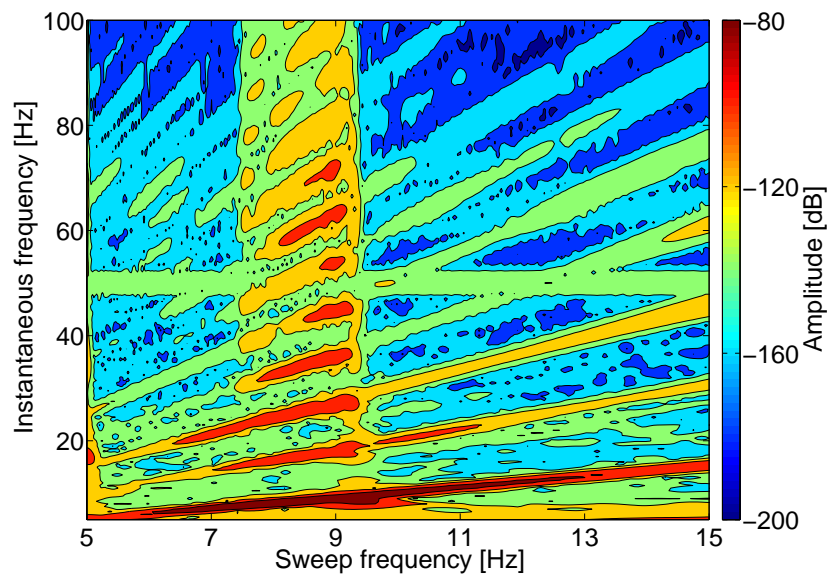
Once nonlinear components are located, the identification procedure addresses the characterization and the parameter estimation of the nonlinearity. Both steps are performed using the restoring force surface (RFS) method. Based exclusively on measured signals, the RFS was first introduced in [103] and is covered in great detail in the textbook [166]. It serves commonly as a parameter estimation technique. However, the RFS method is used beforehand in an unconventional manner for nonlinearity characterization purposes. The starting point is Newton's law of dynamics written for a specific degree of freedom located next to a nonlinear structural component, namely

$$\sum_{n=1}^N m_{i,n} \ddot{x}_n + f_i(\mathbf{x}, \dot{\mathbf{x}}) = p_i \quad (2.1)$$

where  $i$  is the DOF of interest,  $N$  the number of DOFs in the system,  $m_{i,j}$  the mass matrix elements,  $\mathbf{x}$ ,  $\dot{\mathbf{x}}$  and  $\ddot{\mathbf{x}}$  the displacement, velocity and acceleration vectors, respectively,  $\mathbf{f}$  the restoring force vector encompassing elastic and dissipative effects, and  $\mathbf{p}$  the external force vector. The key idea of the approach is to discard in Equation (2.1) all the inertia and restoring force contributions that are not related to the nonlinear component, as they are generally either unknown, e.g., the coupling inertia coefficients, or not measured, e.g., the rotational DOFs. If we denote by  $j$  another measured DOF located across the



(a)



(b)

Figure 2.4: Analysis of the relative displacement across the WEMS cross and its support. (a) Time series at 1  $g$ . (b) Wavelet transform of the relative displacement in (a).

nonlinear connection, Equation (2.1) is therefore approximated by

$$m_{i,i} \ddot{x}_i + f_i(x_i - x_j, \dot{x}_i - \dot{x}_j) \approx p_i. \quad (2.2)$$

If no force is applied to DOF  $i$ , a simple rearrangement leads to

$$f_i(x_i - x_j, \dot{x}_i - \dot{x}_j) \approx -m_{i,i} \ddot{x}_i. \quad (2.3)$$

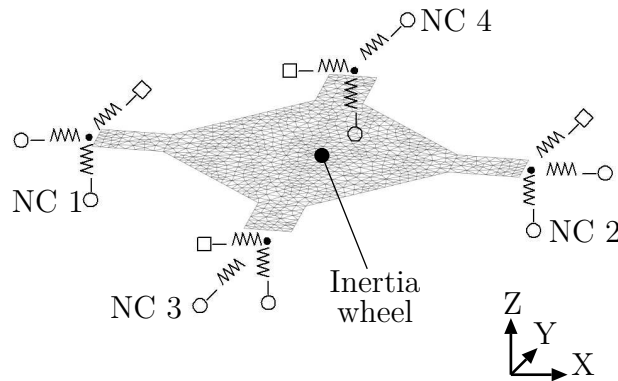


Figure 2.5: WEMS. Simplified modeling of the WEMS mobile part considering the inertia wheel as a point mass. The linear and nonlinear connections between the WEMS mobile and fixed parts are signaled by squares and circles, respectively.

Equation (2.3) shows that the restoring force of the nonlinear connection is approximately proportional to the acceleration at DOF  $i$ . Hence, by simply representing the acceleration signal, with a negative sign, measured at one side of the nonlinear connection as a function of the relative displacement and velocity across this connection, the nonlinearities can be conveniently visualized and an adequate mathematical model for their description can then be selected. This methodology was already successfully applied to the characterization of the nonlinearities at the wing tip of the MS-760 Morane Saulnier aircraft [74] and in the wing-to-payload interfaces of an F-16 aircraft [116].

To visualize the elastic nonlinearities of the WEMS device, a cross section along the axis where the velocity is zero of the restoring force surface defined by the triplets  $(x_{i,k} - x_{j,k}, \dot{x}_{i,k} - \dot{x}_{j,k}, -\ddot{x}_{i,k})$ , where  $k$  refers to the  $k$ -th sampled instant, can be drawn. Figures 2.6(a, b) show the plots corresponding to NC1 at 0.6  $g$  and 1  $g$ , respectively. These figures confirm the nonsmooth and asymmetric nature of the nonlinearities in the system. Visual inspection estimates the  $-Z$  clearance at around 1. The restoring force curve at 1  $g$  also reveals the activation of the  $+Z$  stop, beyond a relative displacement of about 1.5. For confidentiality, clearances are given through adimensionalised quantities.

Reference [115] demonstrates in detail that the axial equation of motion of the WEMS mobile part, i.e., the dummy inertia wheel and its metallic cross-shaped support, can be formulated explicitly by asserting that it behaves as a rigid body. Under this assumption, the NC stiffness curves are identifiable using the restoring force surface method (RFS). The restoring-force curves obtained for NC1 and NC2 are depicted in Figure 2.7(a, b), respectively. As qualitatively shown in Figure 2.6, it turns out that the WEMS modeling should account for combined nonsmooth and gravity-induced asymmetric effects. This leads us to select a trilinear model  $k_-$ ,  $k$  and  $k_+$  with dissimilar clearances  $a_-$  and  $a_+$  for the axial nonlinearities. For the lateral nonlinearities, a bilinear model  $k_{\pm}$  and  $k$  suffices, because there is only one clearance  $a_{\pm}$  per connection. A curve-fitting process, represented by the red curve in Figure 2.7(a, b), provides the unknown parameters for our

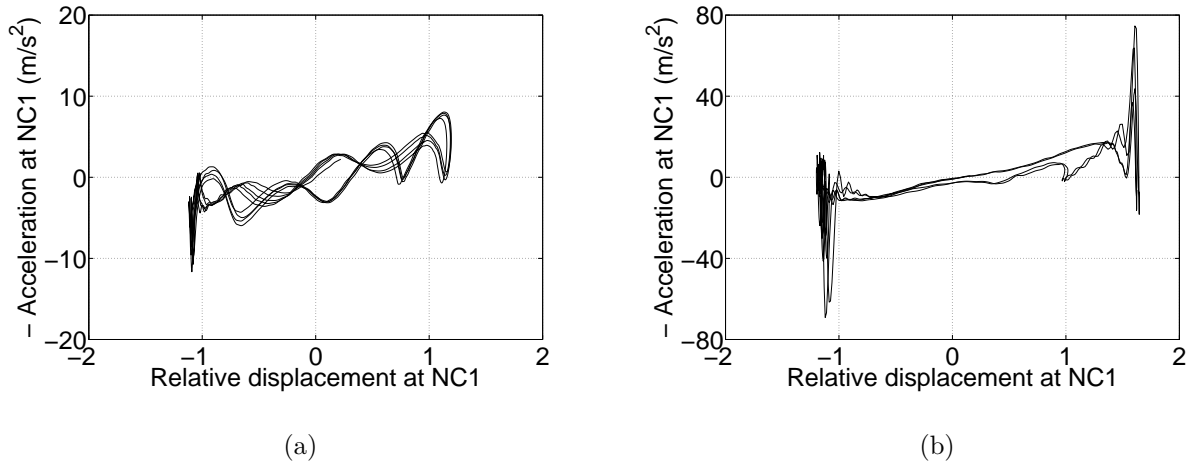


Figure 2.6: Nonlinearity characterization of the WEMS device using the restoring force surface method. (a) 0.6 *g*; (b) 1 *g*.

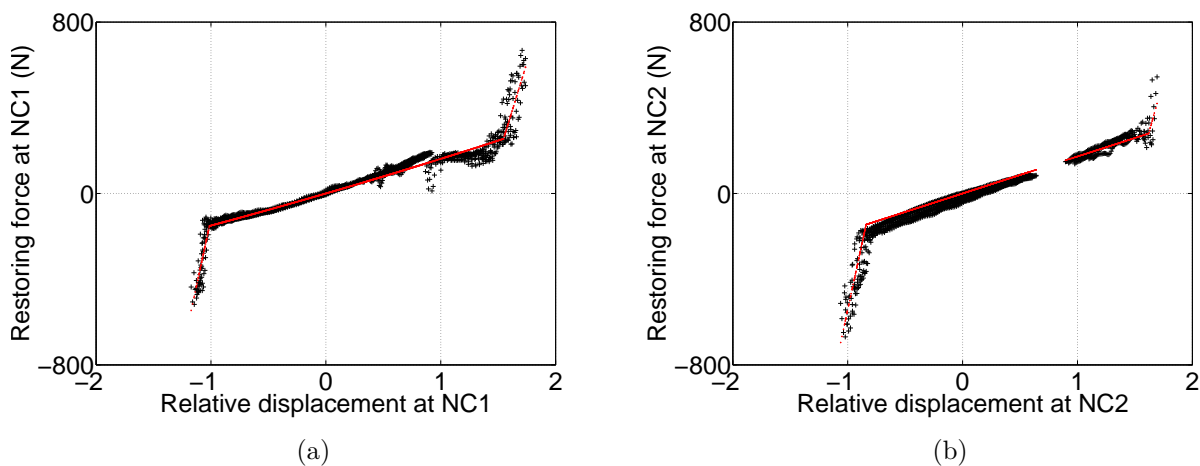


Figure 2.7: WEMS. (a, b) Experimental stiffness curve constructed using the RFS method (in black) and fitted with a trilinear model (in red) for NC1 and NC2, respectively.

piecewise-linear model (see Table 2.2). For confidentiality, stiffness coefficients are also given through adimensionalised quantities. Localized damping terms given by EADS-Astrium were also included in the FEM to account for the dissipation of the elastomer plots.

Finally, for facilitating the numerical investigations in the forthcoming sections, the continuity of the first derivative of the different restoring forces of the WEMS is enforced using regularization. This approach is also motivated by the stiffness curve in Figure 2.7(a), which reveals that the actual structural behavior is smoother than a piecewise-linear law. A local regularization using Hermite polynomials in the interval  $[a - \Delta, a + \Delta]$  is

Stiffness	NC1	NC2	NC4	NC3
Axial $k_Z$	8.30	9.21	9.18	10.03
Lateral $k_X$	1.31	1.31	0.69	0.69
Lateral $k_Y$	0.69	0.69	0.69	0.69
Axial $k_{+,Z}$	79.40	88.41	79.40	88.41
Axial $k_{-,Z}$	118.07	116.73	118.07	116.73
Lateral $k_{\pm,XY}$	40	40	40	40
Clearance				
Axial $a_{+,Z}$	1.55	1.62	1.59	1.59
Axial $a_{-,Z}$	1.01	0.84	0.93	0.93
Lateral $a_{\pm,XY}$	2	2	2	2

Table 2.2: Parameters of the WEMS nonlinear connections (adimensionalised for confidentiality).

considered where  $a$  and  $2\Delta$  are the clearance and the size of the regularization interval, respectively. The nominal interval considered throughout the paper is equal to 5% of the clearance size. As illustrated in Figure 2.8, the main advantage of this strategy is that it preserves the purely linear behavior of the restoring force outside the regularization interval.

The mathematical description of the nonlinear force is given by

$$f_{nl}(x) = \begin{cases} \text{sign}(x)(ka_+ + k_+(x - a_+)) & x \geq a_+ + \Delta_+ \\ p_+(t(x)) & a_+ + \Delta_+ > x > a_+ - \Delta_+ \\ kx & a_+ - \Delta_+ \geq x \geq -(a_- - \Delta_-) \\ p_-(t(x)) & -(a_- - \Delta_-) > x > -(a_- + \Delta_-) \\ \text{sign}(x)(ka_- + k_-(x - a_-)) & x \leq -(a_- + \Delta_-) \end{cases} \quad (2.4)$$

where  $x$  is the relative displacement between the two DOFs defining the NC. The parameters  $a_{\pm}$ ,  $k_{\pm}$ , and  $\Delta_{\pm}$  are positive scalars. The Hermite polynomials are defined as

$$p_{\pm}(t) = h_{00}(t)p_k + h_{10}(t)(x_{k+1} - x_k)m_k + h_{01}(t)p_{k+1} + h_{11}(t)(x_{k+1} - x_k)m_{k+1} \quad (2.5)$$

where  $p_k$  and  $p_{k+1}$  are the values of the restoring force at points  $x_k = \text{sign}(x)(a - \Delta)$  and  $x_{k+1} = \text{sign}(x)(a + \Delta)$ , respectively.  $m_k$  and  $m_{k+1}$  are the values of the restoring force derivative at the same  $x_k$  and  $x_{k+1}$  points; they correspond to the stiffness coefficients  $k_1$  and  $k_{\pm}$ , respectively. The local scaled abscissa is

$$t(x) = \frac{x - x_k}{x_{k+1} - x_k}. \quad (2.6)$$

The  $h_{ij}(t)$  functions are given by

$$h_{00}(t) = 2t^3 - 3t^2 + 1, \quad (2.7)$$

$$h_{10}(t) = t^3 - 2t^2 + t, \quad (2.8)$$

$$h_{01}(t) = -2t^3 + 3t^2, \quad (2.9)$$

$$h_{11}(t) = t^3 - t^2. \quad (2.10)$$

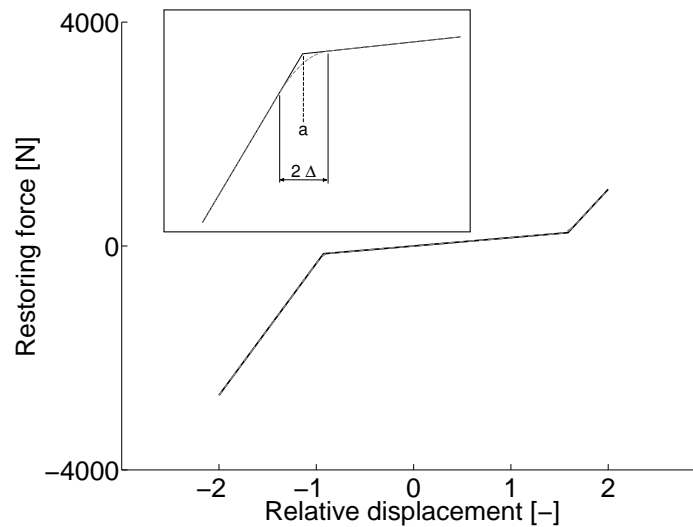


Figure 2.8: Axial WEMS nonlinearity modeling. True piecewise-linear (—) and regularized (---) restoring forces.

## 2.4 Direct Numerical Integration and Numerical Continuation

The reduced model ROM910 including the WEMS nonlinearities is now used to conduct numerical simulations. To this end, a swept-sine excitation with a sweep rate of 2 octaves per minute in the 5 – 90 Hz range is applied to the inertial wheel in the axial direction. The excitation amplitude is 140 N. Direct numerical integration of the equations of motion is carried out using Newmark’s algorithm. Figure 2.9(a) represents the axial displacement of the NC2 as a function of the excitation frequency. A main resonance peak which corresponds to mode 6 is located around 33 Hz. Because the corresponding linear natural frequency is 28.75 Hz, this nonlinear mode undergoes a substantial increase in frequency due to the frequency-energy dependence of nonlinear oscillations. The asymmetry, non-smoothness and skewness of the displacement envelope in the vicinity of the resonance peak are additional manifestations of the WEMS nonlinearities. A sudden transition from large to small amplitudes of vibration, referred to as a jump phenomenon, is also observed. After the jump, the satellite response quickly stabilizes to a low-amplitude response with almost no beating phenomenon; it is a sign of the presence of strong damping. The wavelet transform of the displacement signal is plotted in Figure 2.9(b). The amplitude of the wavelet transform is represented in logarithmic scale ranging from blue (low amplitude) to red (high amplitude). The presence of wideband frequency components around 30 Hz confirms the activation of nonsmooth nonlinearities in the neighborhood of the resonance. Their disappearance closely coincides with the jump phenomenon. Even harmonics in the wavelet transform are generated by the asymmetric modeling of the WEMS. The results

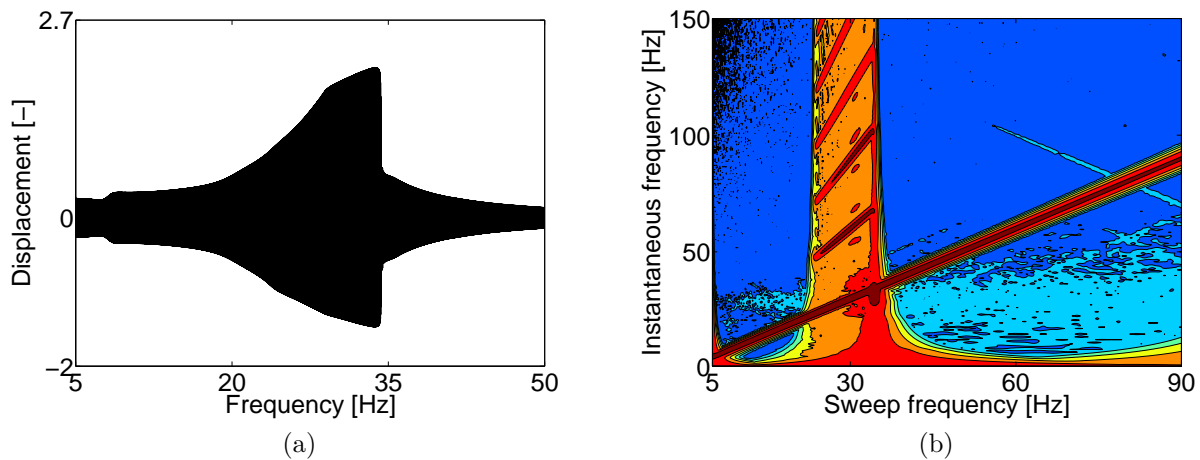


Figure 2.9: NC2-Z response to swept-sine excitation. (a) Displacement; (b) wavelet spectrum.

in Figure 2.9 therefore present a very good qualitative concordance with those observed experimentally for mode 1 in Figure 2.4.

In order to gain further insight into the experimental results, an algorithm for numerical continuation is employed to compute the system response to a 140 N stepped-sine forcing. A shooting technique for computing isolated periodic solutions is combined with pseudo-arclength continuation for tracking the evolution of the periodic solutions for increasing excitation frequencies [141]. Bifurcation analysis is performed using test functions based on the monodromy matrix [10, 85]. The theoretical concept are briefly presented in Appendix A. The results of numerical continuation are shown in Figure 2.10. They are superimposed on the time series of Figure 2.9(a) and provide an accurate estimation of the displacement envelope. Two limit point (LP) bifurcations give rise to a change in stability of the periodic solutions. The bifurcation mechanism is illustrated in Figure 2.11(a). The eigenvalues of the monodromy matrix, i.e., the Floquet multipliers, are represented in the real-imaginary plane for several periodic solutions on either side of the bifurcation. The multiplier that crosses the unit circle through  $+1$  confirms that the periodic solutions have become unstable through a LP bifurcation. The upper LP coincides with the jump phenomenon and explains why there is a sudden transition between two stable attractors characterized by large and small amplitudes, respectively. This is a classical theoretical result in the literature, often illustrated using single-DOF oscillators, but these simulations show that it can also be observed during testing of real-life engineering structures.

Another objective of this section is to uncover nonlinear dynamical phenomena not encountered experimentally. Interestingly, the numerical continuation process highlights that the periodic solutions undergo two additional Neimark-Sacker bifurcations [10, 85]. In addition to changing the stability of the periodic solutions, this type of bifurcation

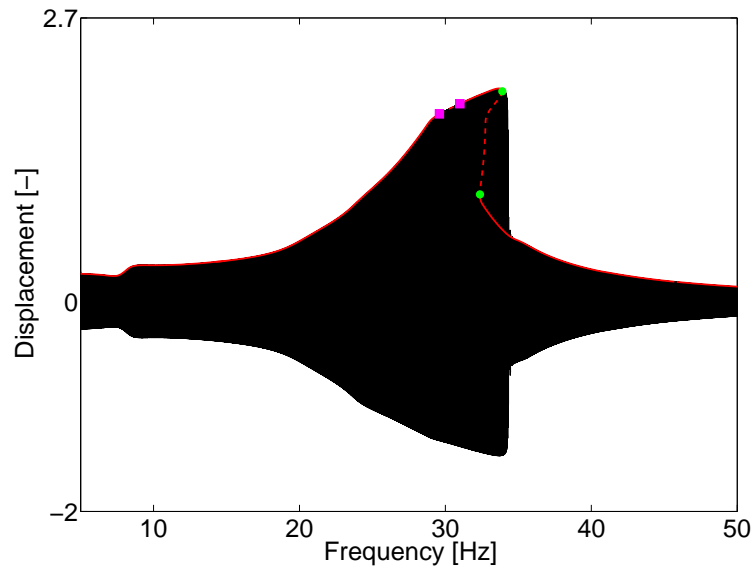


Figure 2.10: SmallSat displacement response at NC2-Z. The responses to swept-sine (direct simulations, 2 octaves per minute) and stepped-sine (numerical continuation) excitations are depicted in black and red, respectively. The red solid and dashed lines correspond to stable and unstable periodic solutions, respectively. Limit point and Neimark-Sacker bifurcations are pictured with green bullets (●) and magenta squares (■), respectively.

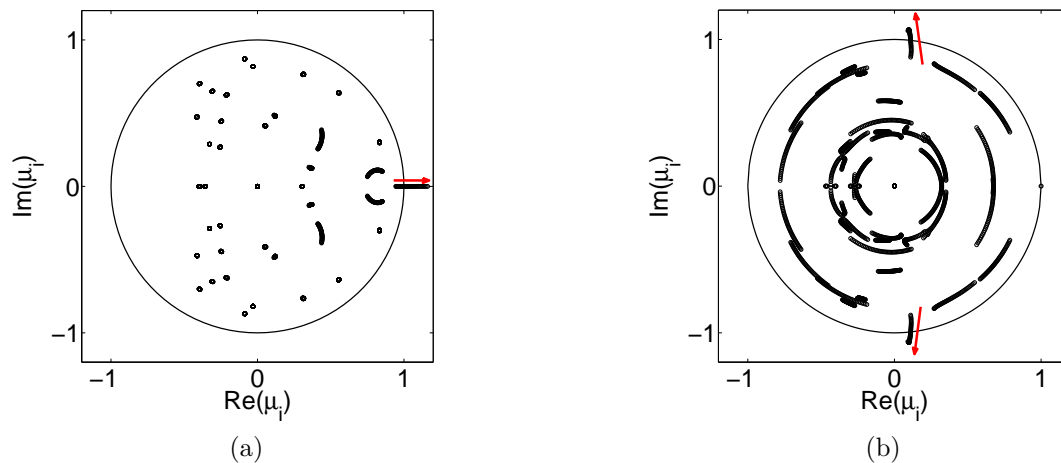


Figure 2.11: Evolution of the Floquet multipliers  $\mu_i$  for several periodic solutions along the continuation path. (a) Evolution across a LP bifurcation; (b) evolution across a NS bifurcation.

produces an emerging torus on which quasiperiodic (QP) motion may occur. Here, a pair of (complex conjugate) Floquet multipliers crosses simultaneously the unit circle as

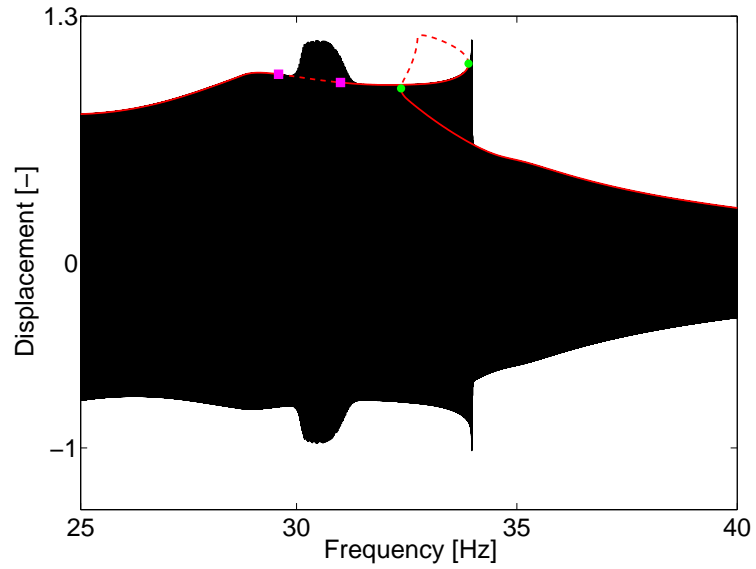
presented in Figure 2.11(b). Such QP motion was not present in the time series of Figure 2.9(a). However, numerical simulations for slower sweep rates, e.g., for a linear sweep rate of 10 Hz per minute as in Figure 2.12, show that QP motion can be observed. The envelope of the displacement signal increases rapidly after the first Neimark-Sacker bifurcation, and periodic motion degenerates into QP motion. After the second bifurcation, the QP motion is transformed into periodic motion, and the envelope decreases rapidly. There is a small delay between the first (second) bifurcation and the onset (disappearance) of QP motion; this delay is to be attributed to the transient character of the swept-sine excitation. Figure 2.12(b) shows that the time series associated with QP motion also exhibits asymmetric behavior with dominant positive displacements. Overall, this complex, inherently nonlinear dynamical behavior is of important practical significance, because, as displayed in Figure 2.12(a), the vibration amplitude associated with QP motion is as large as the amplitude close to the main resonance of the system.

## 2.5 Nonlinear Modal Analysis of the SmallSat

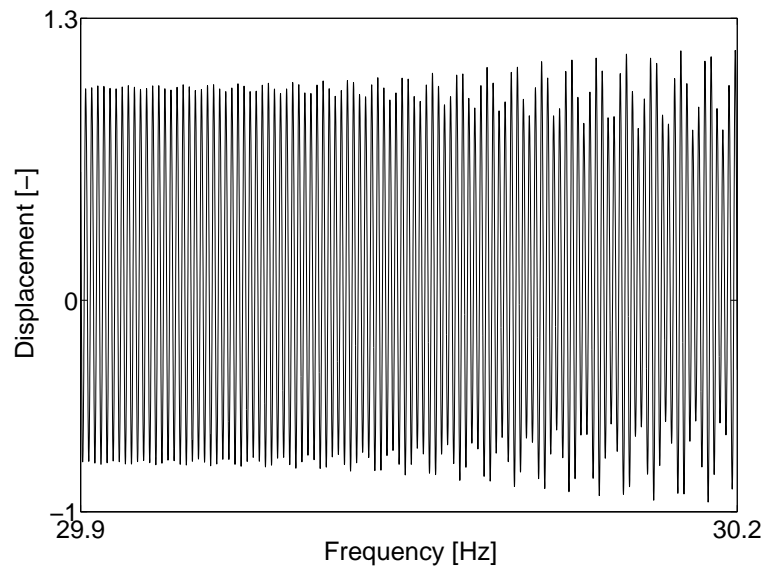
In Section 2.4, a nonconservative FEM was utilized to investigate the nonlinear phenomena observed during the test campaign of the SmallSat spacecraft. Because the damped dynamics can often be interpreted based on the topological structure and the bifurcations of the NNMs of the underlying conservative system [75], a detailed nonlinear modal analysis using the underlying conservative model is carried out herein. This approach is also a usual engineering practice because there is frequently a lack of knowledge about damping mechanisms present in the structure.

The computation algorithm for NNMs that was presented in Chapter 1 is applied to the ROM810 model. Unlike the previous application of the NNM theory to the full-scale aircraft [74], an interesting feature of the satellite is that almost every mode of the underlying linear system in the 0 – 100 Hz range involves motion of the nonlinear component. The exception is mode 9 for which the WEMS remains quiescent, as shown in Figure 2.13(a). This is confirmed by the constant natural frequency of NNM9 in the FEP of Figure 2.13(b). Modes 1, 5, 6, and 7 were found to exhibit particularly interesting dynamics and are described in this section.

The first linear normal mode (LNM1) corresponds to a local motion involving the WEMS. Its nonlinear counterpart is pictured in Figure 2.14. The FEP of NNM1 is formed by one main backbone to which one “tongue” is attached. At low energies, no mechanical stop is activated, and the NNM frequency remains identical to the natural frequency of LNM1. The corresponding modal shape is also identical to that of LNM1. Beyond a certain energy threshold, the relative displacements along X of nonlinear connections NC1 and NC2 enter into the regularization area of the piecewise-linear restoring forces. The NNM frequency rapidly increases due to the large difference between the stiffnesses of the elastomer plots and of the mechanical stops. When progressing along the backbone, harmonic components of the fundamental NNM oscillation frequency are created by the



(a)



(b)

Figure 2.12: Evidence of QP motion. (a) Displacement at NC1–Z and (b) close-up of the transition from periodic to QP motion. The responses to swept-sine (direct simulations) and stepped-sine (numerical continuation) excitations are depicted in black and red, respectively. Limit point and Neimark-Sacker bifurcations are pictured with green bullets (●) and magenta squares (■), respectively.

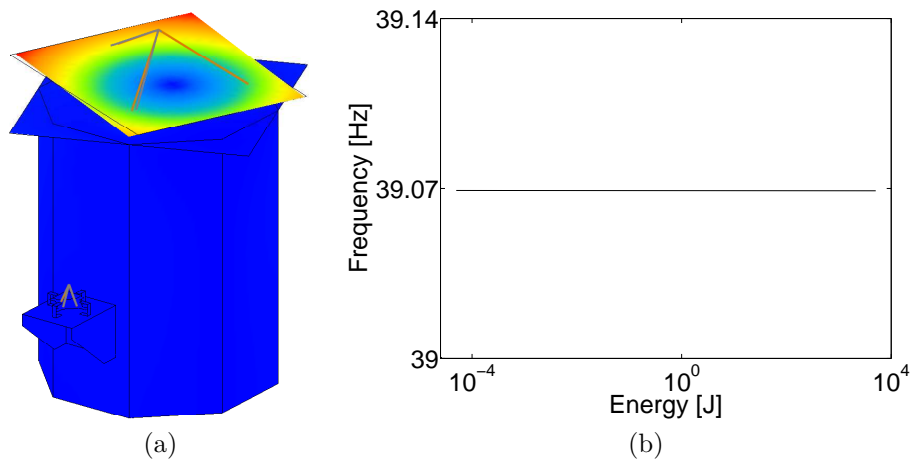


Figure 2.13: Mode 9. (a) Linear modal shape; (b) frequency-energy plot.

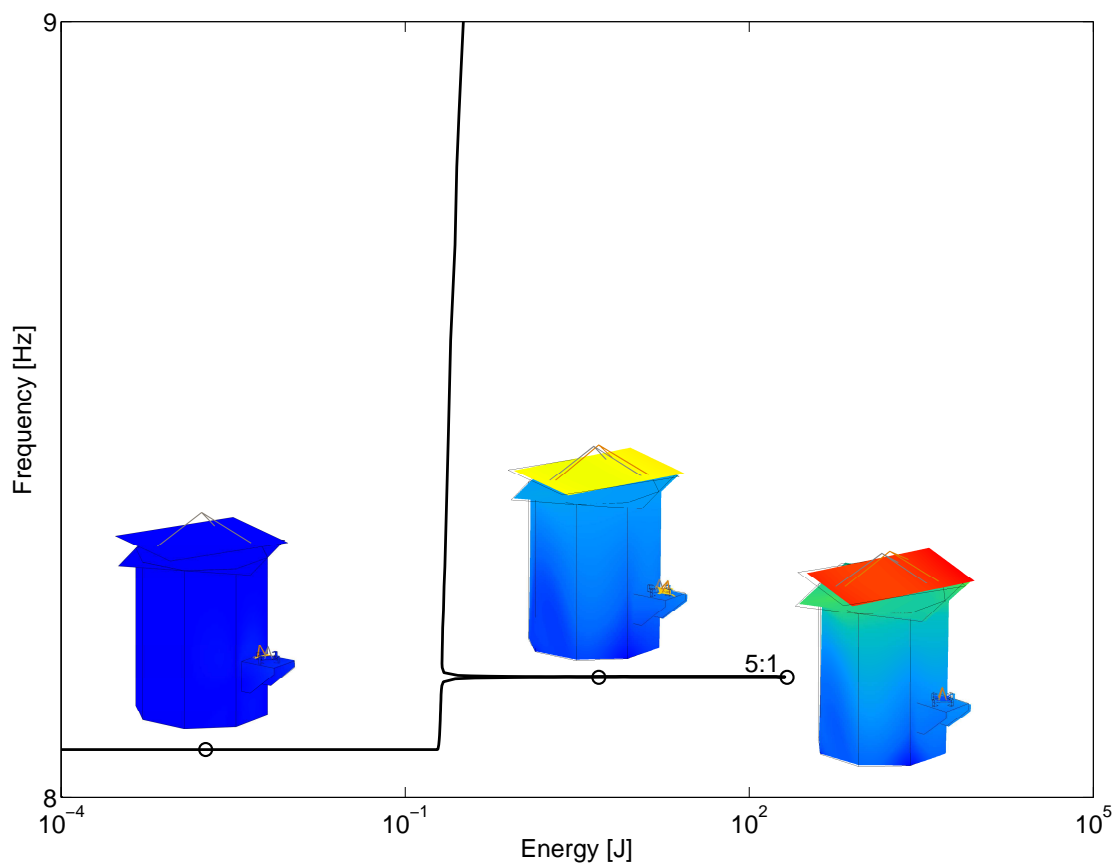


Figure 2.14: FEP of the first NNM with different modal shapes inset.

WEMS nonlinearities. Once one of these harmonics has a frequency close to the oscillation frequency of another NNM, a dynamic coupling between the two modes exists, and a tongue of internal resonance is produced. This is precisely what happens for the 5:1 internal resonance in Figure 2.14. As energy increases along this branch, the fifth harmonic becomes more important than the fundamental frequency. The modal shape located around the middle of the branch is a mixing between NNM1 and NNM10; it is a purely nonlinear mode with no linear counterpart. At the extremity, the sole fifth harmonic remains, which completes the transition to NNM10. Such internal resonances between NNMs were previously reported in the literature, see, e.g., [75, 94], also in the case of a two-degree-of-freedom vibro-impact system [95] and a full-scale aircraft [74]. They are therefore not further described herein. However, it is interesting to note that, due to nonlinearities, the excitation of a local mode can trigger the excitation of a more global mode involving instrument panel motion. This latter mode is characterized by a much larger modal mass and can potentially jeopardize structural integrity during launch.

Figure 2.15 presents the FEP of the fifth spacecraft NNM. The same findings as for NNM1 can be drawn from this FEP, namely a sudden increase in NNM frequency once mechanical stops are activated and the presence of internal resonances. One branch of 2:1 internal resonance with NNM11 and two 4:1 branches with NNM17 and 18 are generated due to the asymmetric modeling of the WEMS. Branches involving even harmonics were also observed for a system with cubic nonlinearity in [75], but, due to the symmetry of the restoring force, they were created through symmetry-breaking bifurcations. The existence of branches 15:1 and 120:1 is questionable, because the corresponding oscillation frequencies are outside the range of validity of ROM810.

What is particularly interesting with NNM5 is that its 2:1 interaction with NNM11 was observed experimentally. The experimental evidence is presented in the wavelet transform of Figure 2.16. At the NC4-Y sensor, the only visible frequency component is around 45-46 Hz despite the fact that the excitation frequency is twice smaller, a clear sign of an energy transfer between modes. An important remark is that it is not the experimental mode with a linear frequency of 22.45 Hz which is involved in the interaction, but rather the experimental mode with a linear frequency of 20.18 Hz (see Table 2.1). Due to the hardening effect of the WEMS, the frequency of this latter mode increases up to 22.5-23 Hz in Figure 2.16, which, in turn, triggers the excitation of the experimental mode possessing a linear frequency of 45.99 Hz. To the best of our knowledge, this is the first time that such an agreement between predictions and experiments is reported for an interaction between two modes of a real-life structure with noncommensurate linear natural frequencies.

A third local mode of the WEMS, NNM6, is presented in Figure 2.17. As for NNM5, there is a 2:1 modal interaction during which NNM6 interacts with NNM12 corresponding to an axial motion of the instrument supporting panel. Numerical evidence of this interaction is provided by analyzing the response at the instrument panel to swept-sine excitation in Figure 2.18(a). Damping is included in the numerical simulation. For a forcing amplitude of 20 N, the satellite presents several resonance peaks at frequencies equal to the

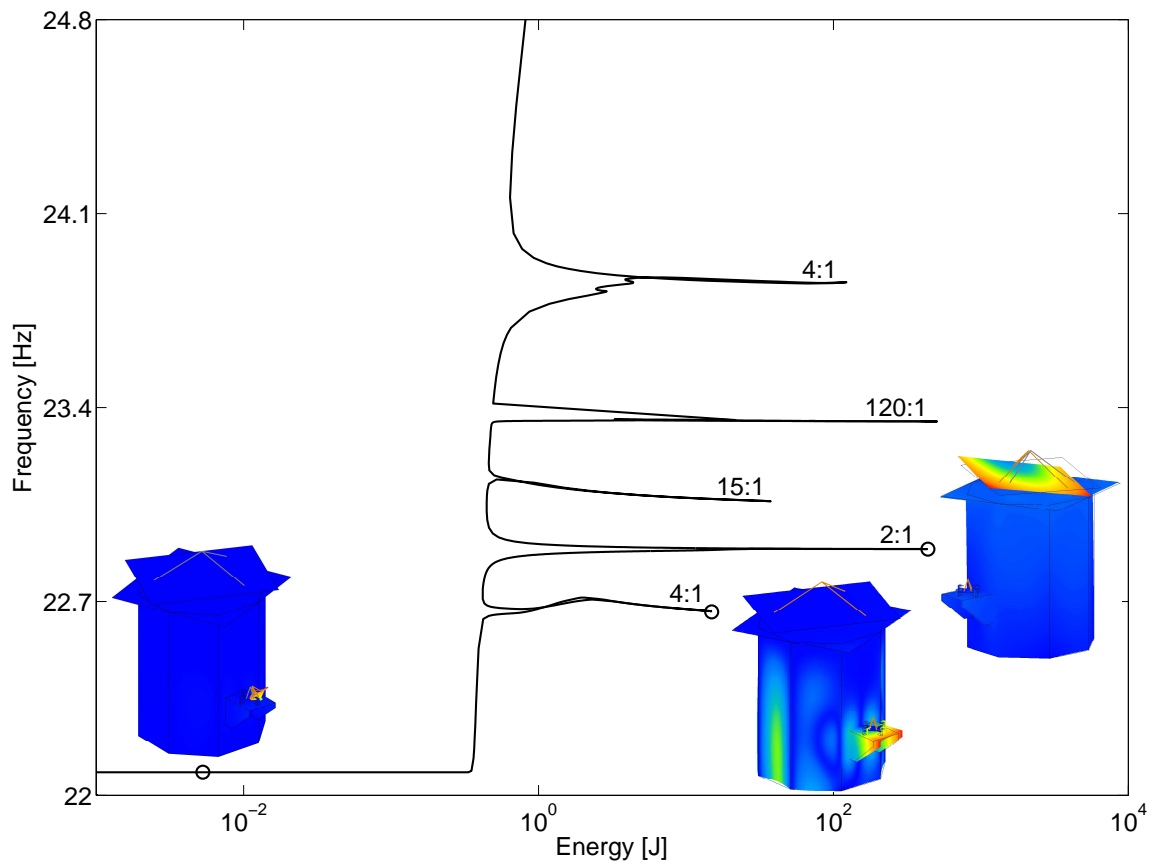


Figure 2.15: FEP of the fifth NNM with different modal shapes inset.

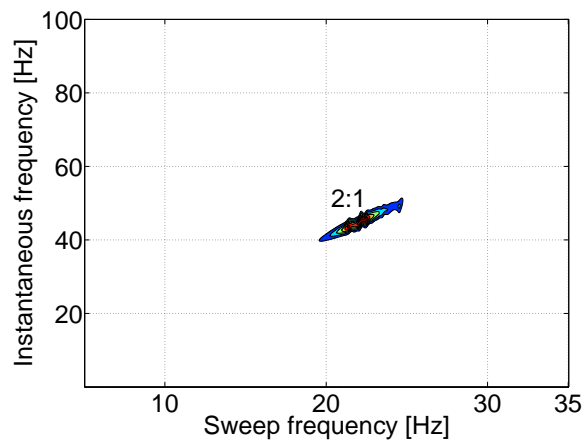


Figure 2.16: Wavelet transform of the experimental time series measured at NC4-Y (swept-sine excitation, 1g).

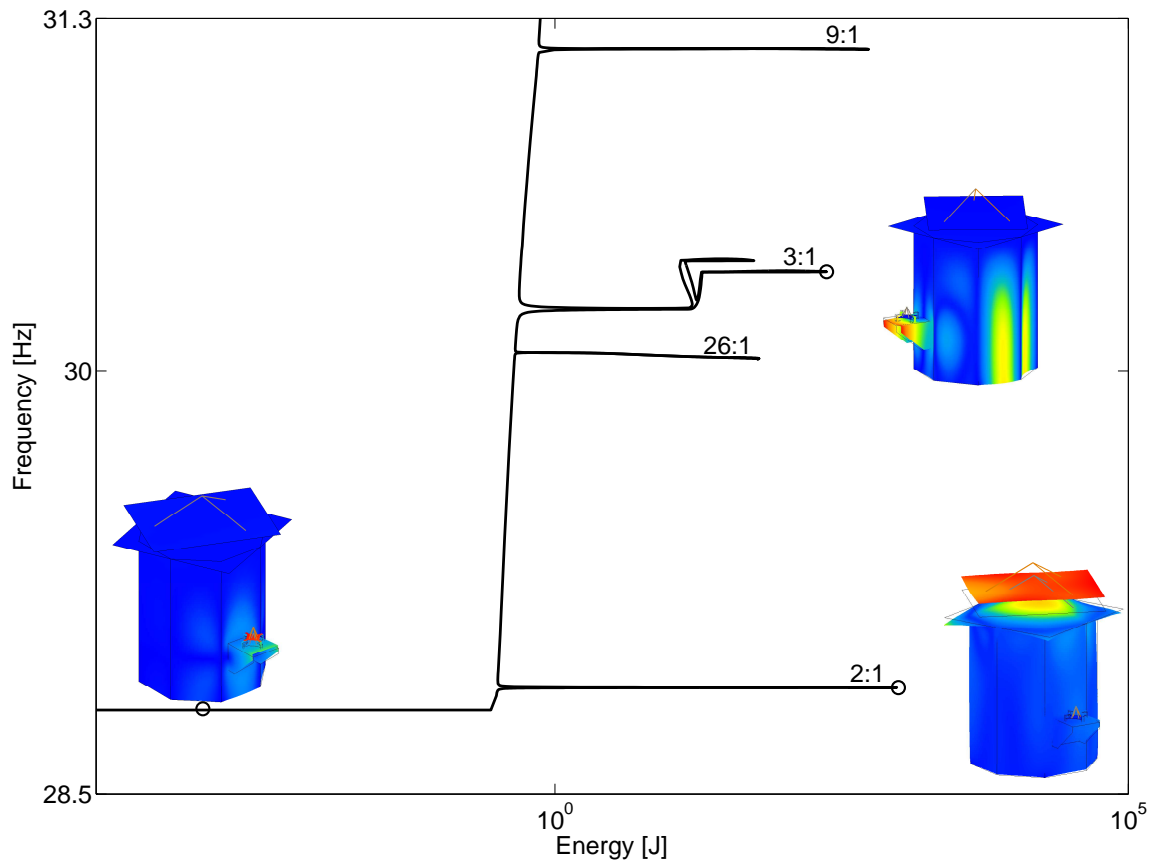


Figure 2.17: FEP of the sixth NNM with different modal shapes inset.

linear natural frequencies (see Table 2.1). For a forcing amplitude of 80 N, an additional resonance peak corresponding to an excitation frequency of 29 Hz can be observed. The presence of this resonance cannot be predicted by a linear analysis, because there is no linear mode possessing instrument panel motion below 32 Hz. It is therefore a nonlinear resonance during which the second harmonic of NNM6 characterized by a frequency close to 58 Hz excites NNM12. This, in turn, produces a large response at the instrument panel when the excitation frequency is in the vicinity of NNM6. Interestingly, this nonlinear resonance has an acceleration twice as large as the acceleration corresponding to the linear resonance of the panel at 58 Hz. We note that Figure 2.18(a) bears strong resemblance with Figure 2.18(b) where the phenomenon is experimentally observed in accelerations measured at the instrument panel. Further experimental evidence of the modal interaction is shown in the wavelet transform measured at NC4 in Figure 2.18(c). The excitation frequency, denoted by fund., is accompanied with higher harmonic components of comparable amplitudes. Specifically, a second harmonic ranging from 55 to 60 Hz is visible

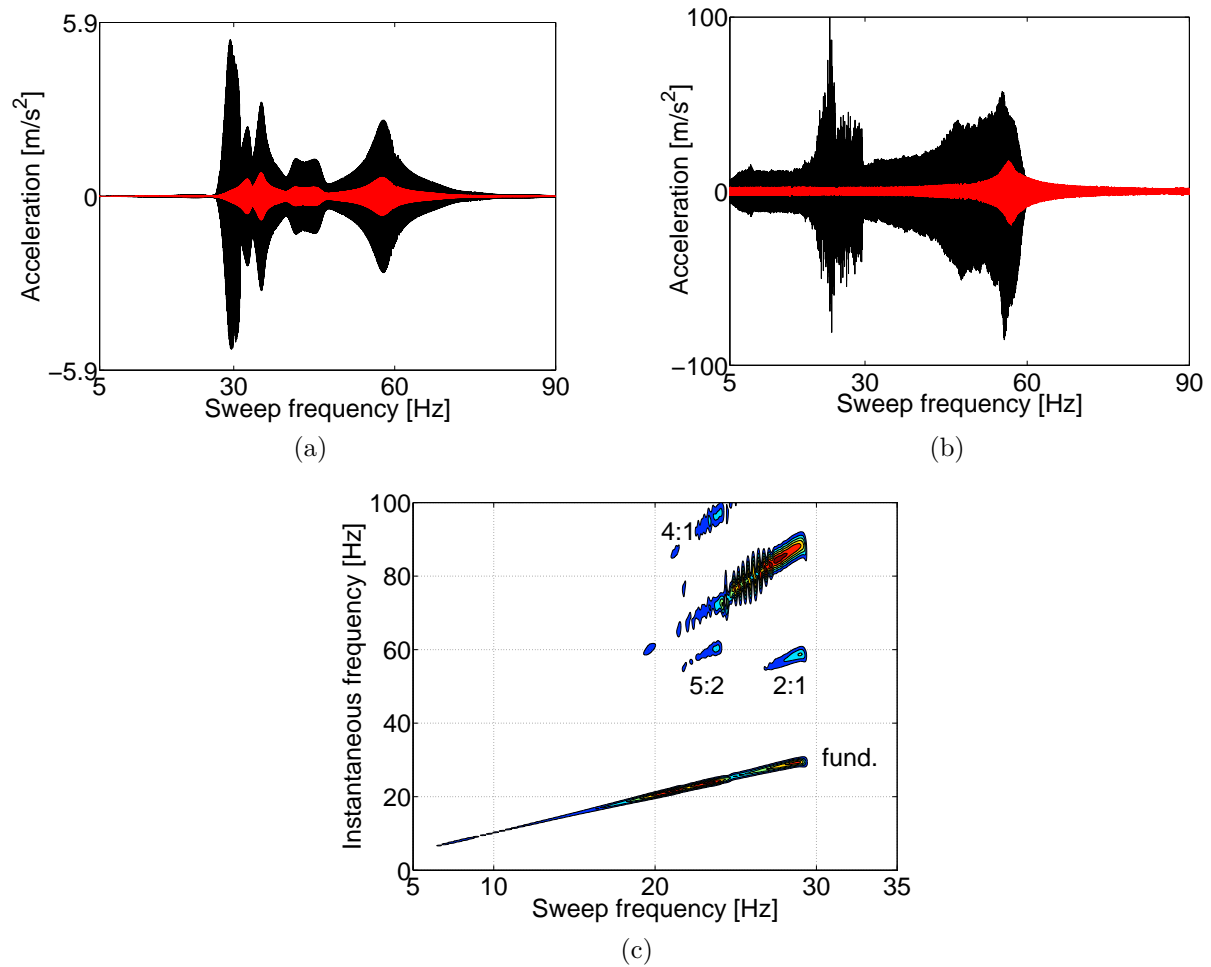
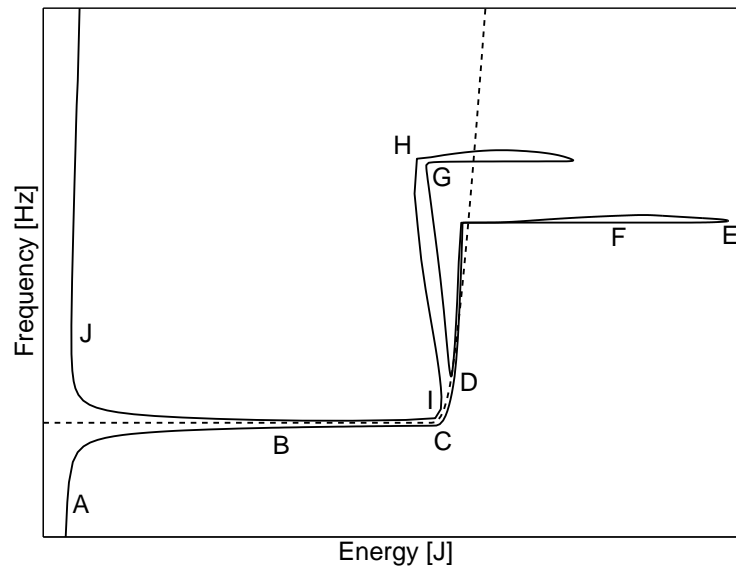


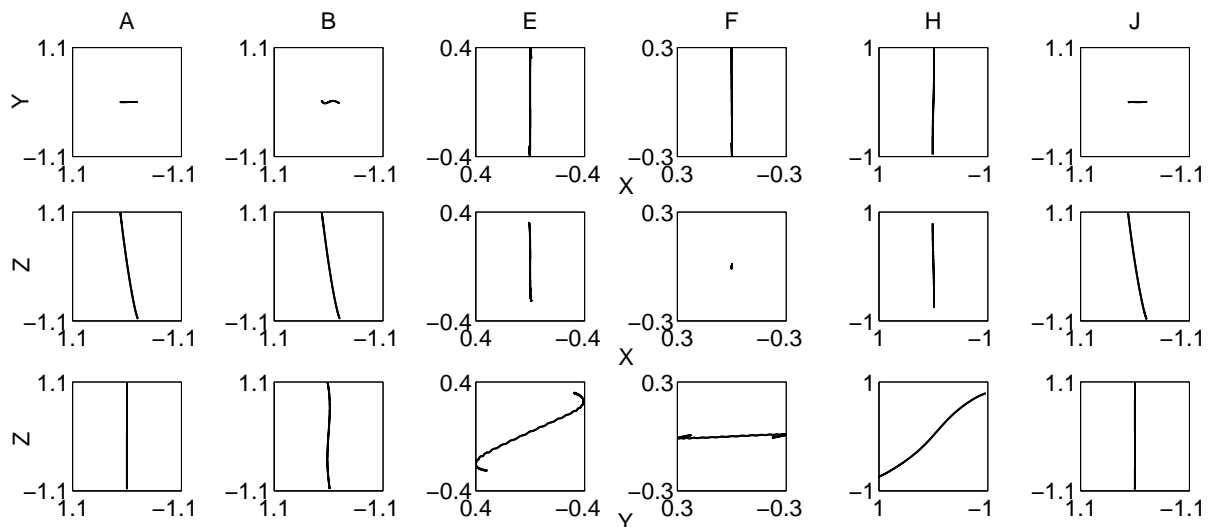
Figure 2.18: Numerical and experimental evidence of the 2:1 modal interaction between NNM6 and NNM12. (a) Acceleration at the instrument panel for a swept-sine excitation of 20 N (red) and 80 N (black) amplitude (direct numerical simulation); (b) raw experimental accelerations measured at the instrument panel at 0.1  $g$  (blue) and 1 $g$  (black). (c) wavelet transform of the relative displacement at NC4-Z (measured during the testing campaign).

when the excitation frequency approaches 30 Hz. There is no identified linear mode just below 30 Hz, but, due to the hardening effect of the WEMS, the linear frequency of 22.45 Hz increases substantially during nonlinear regimes of motion. The second harmonic then excites the experimental mode with a linear frequency of 55.71 Hz.

The 3:1 modal interaction presents a nonconventional topology compared to the other branches in the FEP of Figure 2.17. A close-up of the branch is shown in Figure 2.19 together with the backbone of NNM17 represented at the third of its fundamental frequency. The reason for this complex topology is that the dynamics has to evolve from NNM6, a mode with a predominant axial motion between the WEMS and the bracket



(a)



(b)

Figure 2.19: 3:1 interaction between NNM6 and NNM17. (a) Close-up of the internal resonance branch; (b) motion of the center of gravity of the WEMS cross.

activating a unique axial nonlinear connection, NC2-Z, to NNM17, a mode with lateral motion of the bracket activating two other nonlinear connections in the lateral direction, NC3-Y and NC4-Y. To understand this progression, the motion of the center of gravity of the WEMS cross is displayed in Figure 2.19. Clearly, the WEMS motion takes place in the XZ plane at points A and B, YZ plane at point E, Y direction at point F, YZ plane at

	NC2-Z (+,-)	NC3-Z (+,-)	NC4-Z (+,-)	NC3-Y (+,-)	NC4-Y (+,-)
A	(0,2.2)	(0,0)	(0,0)	(0,0)	(0,0)
B	(0,2.2)	(0,0)	(0,0)	(0,0)	(0,0)
C	(0,2.2)	(0,0.07)	(0,0)	(0,0)	(0,0)
D	(0,2.3)	(0,0.19)	(0,0)	(1.1,1.1)	(1.1,1.1)
E	(0,0)	(0,0)	(0,2.9)	(3.4,3.6)	(3.4,3.4)
F	(0,0)	(0,0)	(0,0)	(3,3)	(3,3)
G	(0,0)	(0,0)	(0,0)	(4,4)	(4,4)
H	(0,0)	(0,0)	(0,2.7)	(3.5,3.8)	(3.7,3.7)
I	(0,2.1)	(0,0)	(0,1.0)	(0,0)	(0,0)
J	(0,2.3)	(0,0)	(0,0)	(0,0)	(0,0)

Table 2.3: Activation of the nonlinear connections on the 3:1 interaction between NNM6 and NNM17. A zero value indicates that the mechanical stop is not activated. A value greater than one implies that the regularization interval is crossed. + and - correspond to positive and negative relative displacements, respectively.

point H and finally back to XZ plane at point J. In addition, Table 2.3 displays the nonlinear connections that are active at the considered points together with the penetration in the corresponding regularization intervals.

At point A on the backbone of NNM6, the WEMS and the bracket vibrates axially resulting in activation of NC2-Z for negative relative displacements. At point B on the internal resonance branch, the WEMS motion is not significantly affected, but lateral motion of the bracket in the Y direction is induced. The MAC between NNM6-B and LNM6 is 0.5, a clear sign of the departure from mode 6. At point C, the MAC between NNM6-C and LNM17 is 0.92 indicating that the transition to NNM17 is well initiated. A second axial connection (NC3-Z) is activated for negative relative displacements, but there is no visible frequency increase between points B and C. As indicated in Table 2.3, the reason is that the motion barely penetrates in the regularization interval of NC3-Z. Conversely, a sudden frequency increase, which closely follows the evolution of the backbone of NNM17, is observed between points C and D. This is a nonconventional behavior for an internal resonance branch. This occurs because the interaction with NNM17 generates lateral motion of the WEMS, which, in turn, activates two additional lateral connections, NC3-Y and NC4-Y. At point D, there are therefore 4 active connections. They have an important influence on the resulting dynamics, because the motion crosses the regularization zones for three of them. For a complete correspondence with NNM17, the two axial connections NC2-Z and NC3-Z must remain quiescent. This happens at point E, but NC4-Z has been activated between points D and E. It is only at point F that the axial connections are no longer active; the MAC with mode 17 is 0.99. From point F to point J, a reverse scenario for evolving from NNM17 back to NNM6 is observed in Table 2.3. Axial connections are again activated, and lateral connections become quiescent. We note that all these results hold for different sizes of the regularization intervals, as shown in Figure 2.20.

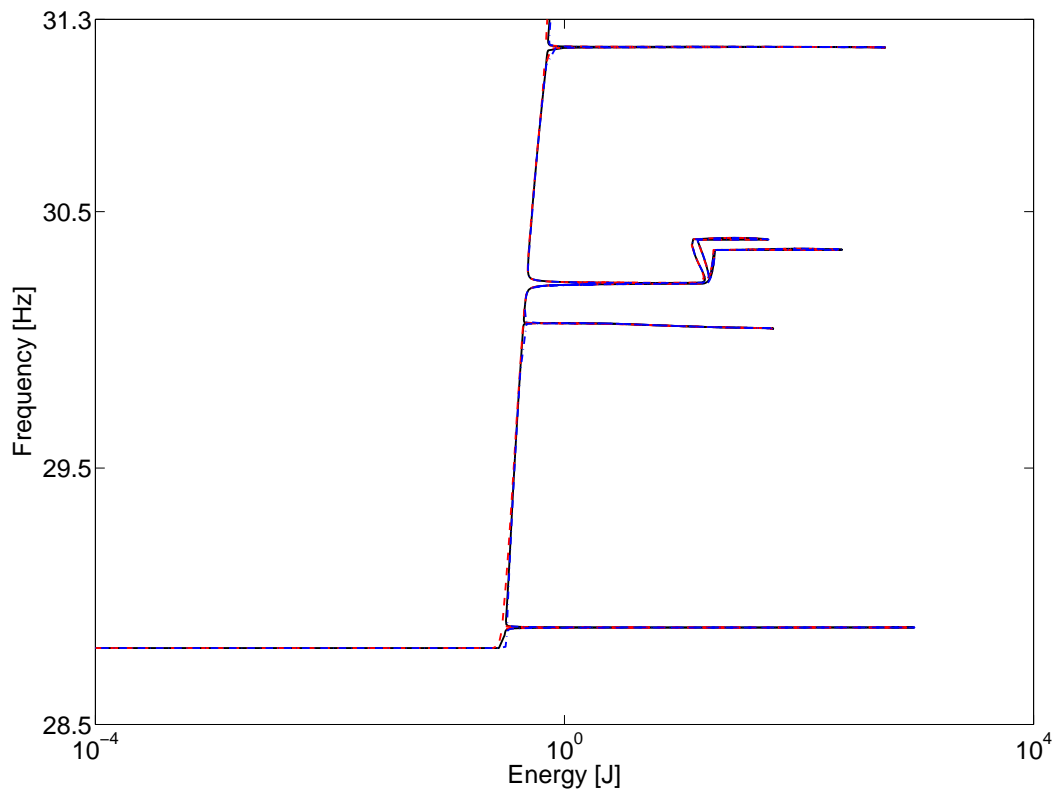


Figure 2.20: Influence of the size of the regularization interval on the FEP of NNM6. The nominal interval considered throughout the paper is equal to 5% of the clearance size (-); (-) 1%, and (-) 10%.

Another interesting nonlinear phenomenon that the SmallSat satellite exhibits is the so-called localization phenomenon [50, 155, 157] during which new nonlinear modes with deformation localized to specific components of the structure appear. Figure 2.21 presents the FEP of NNM 7. Unlike previously described NNMs, NNM7 frequency remains identical to the linear natural frequency until energies greater than  $10^2 J$ . Then, the backbone undergoes a bifurcation and bends backwards. Important modifications of the modal shapes are observed along the backbone branch. The linear-like modal shape only involves instrument panel motion. After the bifurcation, a markedly different ( $MAC < 0.5$ ) modal shape involving significant WEMS motion is produced. Progressing on the backbone, the WEMS deformation is further enhanced whereas instrument panel motion disappears, giving rise to a localized mode possessing some similarities with LNM6 ( $MAC = 0.85$ ). Finally, a motion of the instrument panel, different from the motion at low energy, reappears further on the branch. We note that the localization phenomenon is different from modal interactions. For instance, very little harmonic components are generated along the backbone in Figure 2.21.

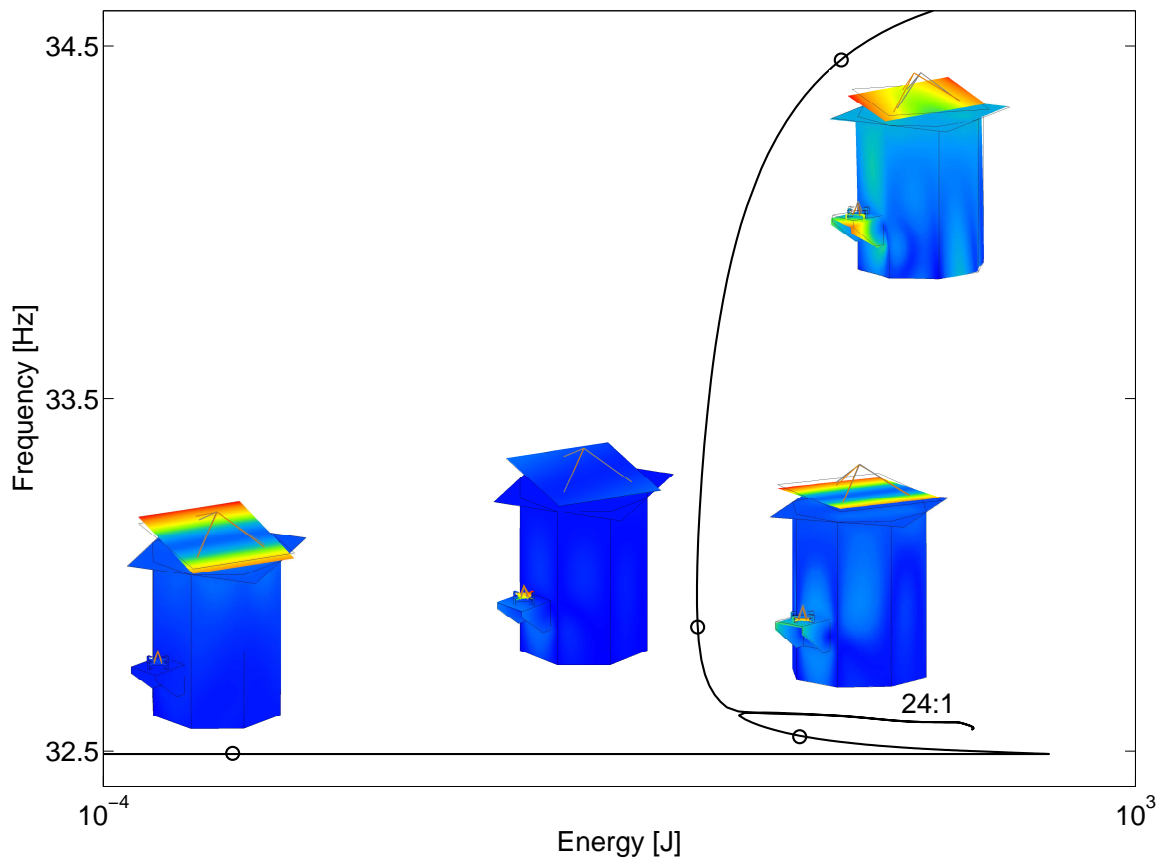


Figure 2.21: FEP of the seventh NNM with different modal shapes inset.

Finally, the NNMs computed in the present section are related to the forced continuation curves discussed in Section 2.4. The satellite response in the vicinity of the sixth resonance computed through forced numerical continuation is represented in solid line in Figure 2.22. The external forcing is a stepped sine with different amplitudes, namely 20, 55, 60, 75, 80 and 100 N. In view of the sudden skewness of the resonance peaks, the nonsmooth character of the WEMS nonlinearities is evident. The frequency-energy dependence of NNM6 in Figure 2.17 is also depicted in dashed line in Figure 2.22. Clearly, the backbone branch computed in the undamped, unforced case coincides with the locus of the resonance peaks of the damped, forced response. This confirms the well-known result that nonlinear resonances occur in the neighborhood of NNMs [157]. Unlike the backbone branch, the 2:1 modal interaction, represented by a vertical dashed line in Figure 2.22, could not be reproduced in the forced continuation curves.

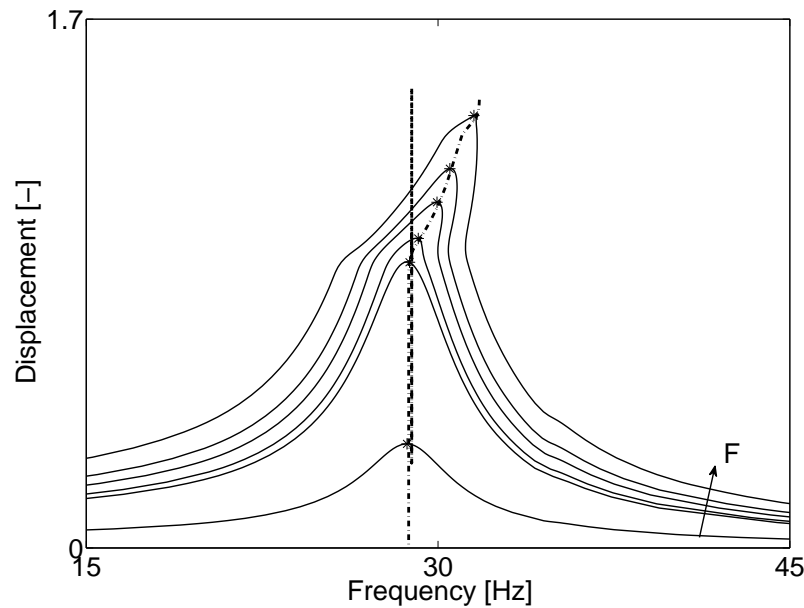


Figure 2.22: Undamped/unforced (dashed line) vs. damped/forced (solid line) response at the WEMS (NC4-Z) in the vicinity of the sixth resonance.

## 2.6 Concluding Remarks

In this chapter, the dynamics of a strongly nonlinear aerospace structure was studied. The application posed several challenges due to the presence of multiple strongly nonlinear components, closely-spaced modes and relatively high damping. This work revealed that the complex phenomena usually observed for numerical simulations of low-dimensional nonlinear systems can also be observed in the experimental conditions commonly endured by engineering structures in industry. The advanced investigations carried out confirmed that the satellite can not only exhibit jumps and a rich frequency content, but also a wide variety of nonlinear phenomena such as quasiperiodic motion and modal interactions. An important observation is the generic character of interactions between modes with noncommensurate linear frequencies even for this complex spacecraft. The ability to understand and reliably predict such interactions is of utmost importance as they may involve energy transfer between modes and, in turn, jeopardize the structural integrity. A specific contribution of this work was thus to reproduce with great fidelity interactions that were observed experimentally. And, overall, a very good qualitative agreement between numerical and experimental results was obtained.

In summary, the work performed in this chapter demonstrates that there now exist rigorous mathematical concepts and effective numerical methods, such as nonlinear normal modes, numerical continuation and the wavelet transform, for addressing the dynamics of complex, real-life engineering structures possessing strongly nonlinear components.

The SmallSat also pointed out some of the remaining challenges for the future developments of nonlinear modal analysis. In particular, throughout the numerical investigations, a great number of modal interactions was encountered by the continuation algorithm. As a result, this complicates the computation of NNMs. For instance, Figure 2.17 shows that the NNM computation was carried out up to 31.3 Hz whereas the time simulations clearly showed that the NNM frequency was shifted up to 35 Hz (Figure 2.9). Moreover, although low-order interactions are often the only ones of interest, the continuation algorithm has to pass through high-order interactions (e.g., the 15:1 and 120:1 in Figure 2.15), which are increasingly present as the dimensionality of the system increases. As illustrated in Figure 2.23, one solution to this issue is the harmonic balance method which allows to truncate the high-frequency content [37].

Another important research direction is to consider the presence of (nonlinear) damping in the structural model. Indeed, although the present study neglects its presence for the computation of NNMs, the SmallSat structure possesses an important amount of damping introduced by the elastomeric plots of the WEMS. The next chapters investigate the concept of NNMs for nonconservative systems and bring numerical tools for dealing with nonlinearly-damped structures.

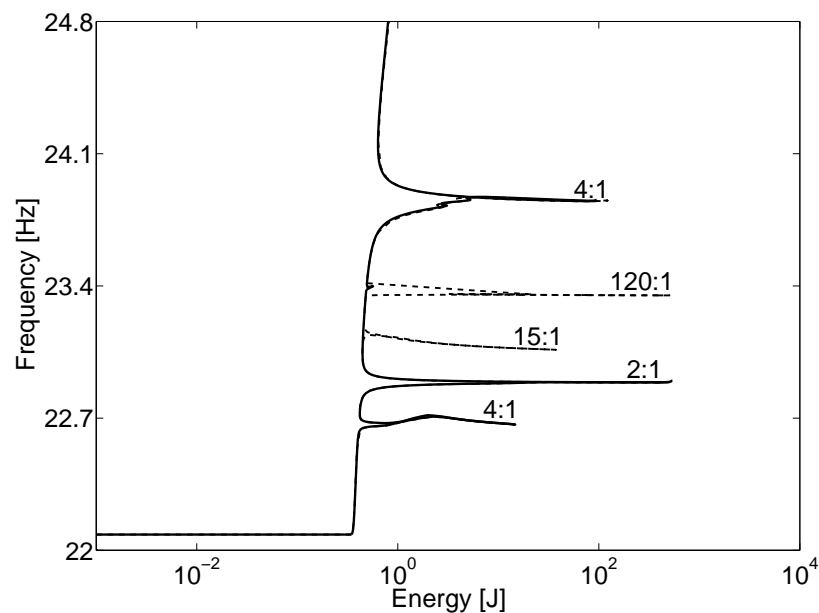


Figure 2.23: Fifth NNM of the SmallSat computed using the method of Chapter 1 (—) and the harmonic balance method (---) whose frequency content is truncated after the fifth harmonic.



## Chapter 3

# A Finite Element Approach to Compute NNMs of Nonconservative Systems

---

### Abstract

This chapter aims at developing a finite-element-based method for solving the partial differential equations governing the geometry of an invariant manifold. The hyperbolic character of the equations is rigorously addressed using a Petrov-Galerkin formulation. Appropriate boundary conditions are also considered by using an annular resolution strategy which progressively grows the manifold. The algorithm is applicable to both conservative and nonconservative systems.

---

## 3.1 Introduction

In Chapter 2, the dynamics of a strongly nonlinear spacecraft was discussed. In this example, and, as frequently reported in the literature, the damped dynamics of the nonlinear system could be interpreted based on the topological structure and bifurcations of the nonlinear normal modes (NNMs) of the underlying Hamiltonian system. However, “simple” viscous damping may sometimes drastically alter the dynamics, e.g., by turning hardening nonlinear behavior into softening behavior [151]. Moreover, complex damping mechanisms are present in all engineering applications. For illustration, the frequency response function of the Morane Saulnier MS-760 Paris aircraft (Figure 3.1(a)) is plotted in Figure 3.1(b) for low and high excitation amplitudes. The response amplitude decreases as the force level increases, a clear sign of the presence of nonlinear damping mechanisms. The development of a nonconservative framework for NNMs can help rigorously understand and predict such effects.

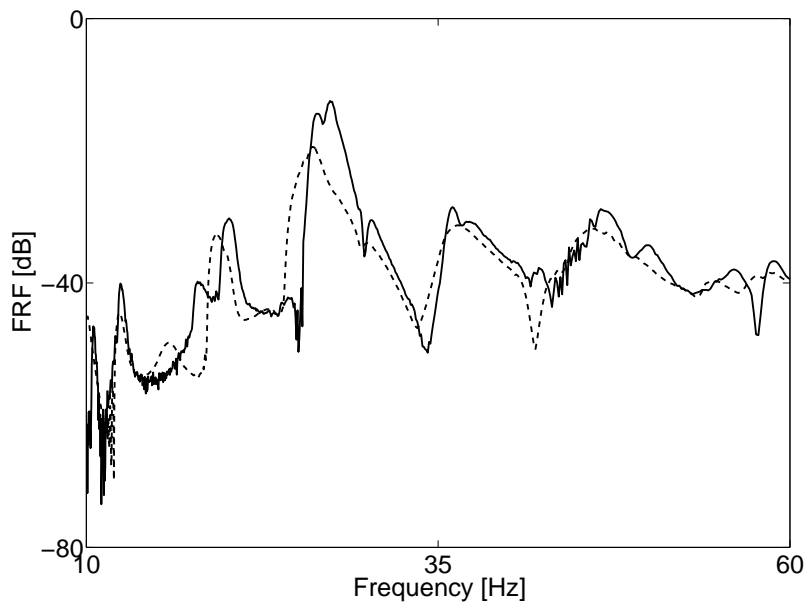
For nonconservative systems, nonlinear normal modes (NNMs) are defined as two-dimensional invariant manifolds which can, in turn, be described using partial differential equations (PDEs) (cf. Chapter 1). Although there exist two numerical methods that can accurately solve these PDEs, several challenges remain to be addressed. The method of Pesheck et al. [124] is computationally expensive, and, in spite of its improvement with simpler shape functions for the amplitude variable, progress for considering larger dimensional systems have still to be made. Moreover, to our knowledge, the method was applied for computing the NNMs of a nonconservative system only in [96]. Finally, the method proposed by Blanc et al. [13] is, as of now, not applicable to nonconservative systems.

The objective of this chapter is therefore to develop a method that can efficiently and accurately compute NNMs of nonconservative systems. Targeting high-dimensional mechanical systems, the idea of reducing the shape function complexity is followed and the recourse to the finite element method (FEM) appears naturally. An important observation of this chapter that was not recognized in the work of Pesheck et al. [124] is to identify the hyperbolic nature of the PDEs, which requires the use of appropriate numerical methods. This interpretation is actually similar to the interpretation of Blanc et al. [13] who interpreted the PDEs as transport equations.

The chapter is organized as follows. Section 3.2 discusses the hyperbolic nature of the PDEs. In Section 3.3, the finite element method is presented and each step of the resolution strategy is detailed. However, for clarity, the discussion focuses first on conservative systems. It is then extended to nonconservative systems in Section 3.4. Section 3.5 stresses the importance of taking into account the hyperbolic character of the PDEs for accurately solving them. The proposed method is also briefly compared to the finite difference method (FDM) proposed in [13]. Finally, the key points about the developments are summarized in Section 3.6.



(a)



(b)

Figure 3.1: Morane-Saulnier 760 Paris aircraft. (a) Aircraft in the ONERA’s laboratory; (b) frequency response function (FRF) for low (—) and high (---) excitation amplitudes.

### 3.2 The Manifold-Governing PDEs

The approach of Shaw and Pierre presented in Chapter 1 describes a NNM in terms of  $2N - 2$  PDEs

$$\begin{aligned}
 Y_i(u, v) &= \frac{\partial X_i(u, v)}{\partial u} v + \frac{\partial X_i(u, v)}{\partial v} f_k, \\
 f_i &= \frac{\partial Y_i(u, v)}{\partial u} v + \frac{\partial Y_i(u, v)}{\partial v} f_k,
 \end{aligned} \tag{3.1}$$

where  $i = 1, \dots, N$ ;  $i \neq k$ ,  $f_i = f_i(u, \mathbf{X}(u, v), v, \mathbf{Y}(u, v))$  are the components of  $\mathbf{f}$  (cf. Equation (1.14)) with  $\mathbf{X} = \{X_j : j = 1, \dots, N ; j \neq k\}$  and  $\mathbf{Y} = \{Y_j : j = 1, \dots, N ; j \neq k\}$ .

Interestingly, Equations (3.1) can be recast into a form similar to [13]:

$$\begin{cases} \mathbf{V} \cdot \nabla X_i(u, v) - Y_i(u, v) = 0, \\ \mathbf{V} \cdot \nabla Y_i(u, v) - f_i(u, v) = 0, \end{cases} \quad \mathbf{V}^T = \{V_1 \ V_2\} = \{v \ f_k(u, v)\} \quad (3.2)$$

$$i = 1, \dots, N; i \neq k.$$

where  $\nabla$  stands for the gradient operator and  $(\cdot)^T$  for the transpose operation. These equations are quasilinear first-order hyperbolic PDEs that bear a resemblance to flow equations encountered in fluid dynamics. Following this interpretation, the streamlines of the velocity field  $\mathbf{V}$  are given by the so-called characteristic curves  $(u(s), v(s))$  which are governed by [70]:

$$\frac{du}{ds} = V_1 = v, \quad \frac{dv}{ds} = V_2 = f_k, \quad (3.3)$$

where  $s$  is the curvilinear coordinate which parametrizes a given characteristic curve. These curves correspond to the system's dynamics projected onto the  $(u, v)$  plane. Figure 3.2 shows the flow of the 2DOF conservative system considered in Section 1.5.2, which possesses a cubic spring attached to its first mass. The flow was computed after solving the manifold-governing PDEs with the proposed method. Characteristics curves (or characteristics) are known to illustrate the propagation of the “information” into the domain. In the conservative framework, the characteristics coincide with the closed iso-energy curves of the system, i.e., the isolated periodic solutions of the NNM.

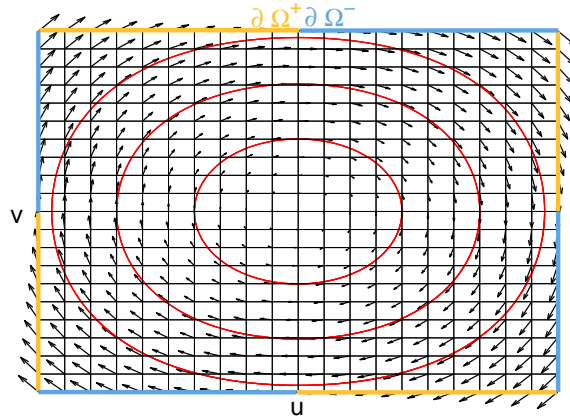


Figure 3.2: Flow  $\mathbf{V}$  of the manifold-governing PDEs for the 2DOF nonlinear conservative system considered in Section 4.2 and for a finite domain  $\Omega$ . The velocity field ( $\rightarrow$ ) is tangent to iso-energy curves ( $-$ ). The inflow and outflow boundaries,  $\partial\Omega^-$  and  $\partial\Omega^+$ , are underlined in blue and orange, respectively.

Along a characteristic, the derivatives of the unknown fields are:

$$\begin{aligned}\frac{dX_i(u(s), v(s))}{ds} &= \frac{\partial X_i}{\partial u} \frac{du}{ds} + \frac{\partial X_i}{\partial v} \frac{dv}{ds} = \mathbf{V} \cdot \nabla X_i, \\ \frac{dY_i(u(s), v(s))}{ds} &= \frac{\partial Y_i}{\partial u} \frac{du}{ds} + \frac{\partial Y_i}{\partial v} \frac{dv}{ds} = \mathbf{V} \cdot \nabla Y_i,\end{aligned}\quad (3.4)$$

with  $i = 1, \dots, N; i \neq k$ . Comparing with Equations (3.1), one has the following correspondence:

$$\frac{\partial X_i}{\partial s} = Y_i, \quad \frac{\partial u}{\partial s} = v, \quad \frac{\partial v}{\partial s} = f_k, \quad \frac{\partial Y_i}{\partial s} = f_i. \quad (3.5)$$

Characteristics are thus curves along which the PDEs becomes ordinary differential equations (ODEs) with appropriate initial conditions. Interestingly, the set of ODEs (3.5) is exactly the original system governing the dynamics of the system where  $s$  plays the role of time. As a result, any attempt to solve the manifold-governing PDEs using the so-called method of characteristics would result in the original problem of solving the ODE. The reader can refer to references [88, 135] for further details about hyperbolic PDEs.

### 3.3 Computation of NNMs Using the Finite Element Method

This section presents a rigorous and effective methodology for computing NNMs which exploits the interpretation of the PDEs as fluid flow equations. The conservative case is considered in this section, whereas the computational method is extended to nonconservative systems in Section 3.4.

Targeting a solution for finite amplitudes, the PDEs are solved in a finite domain  $\Omega \subset \mathbb{R}^2$  whose boundary is denoted  $\partial\Omega$ . As illustrated in Figure 3.2, this boundary may comprise inflow and outflow regions

$$\begin{aligned}\partial\Omega^- &: \{\mathbf{u} = (u, v) \in \Omega : \mathbf{V}(\mathbf{u}) \cdot \mathbf{n}(\mathbf{u}) < 0\} \\ \partial\Omega^+ &: \{\mathbf{u} = (u, v) \in \Omega : \mathbf{V}(\mathbf{u}) \cdot \mathbf{n}(\mathbf{u}) > 0\},\end{aligned}\quad (3.6)$$

respectively.  $\mathbf{n}(\mathbf{u})$  is the outward normal vector to  $\partial\Omega$ .

Solving hyperbolic PDEs requires boundary conditions (BCs) at inflow where the velocity vector  $\mathbf{V}$  points inward the domain. Indeed, even if there are no BCs in Equations (3.2), the solution along the incoming characteristic depends mathematically on the solution outside the domain. This is why the unknown field values  $(X_i, Y_i)$  have to be imposed on  $\partial\Omega^-$ . The mathematical problem to solve becomes

$$\begin{cases} \mathbf{V} \cdot \nabla X_i - Y_i = 0, \\ \mathbf{V} \cdot \nabla Y_i - f_i = 0, \\ X_i|_{\partial\Omega^-} = X_i^-, \\ Y_i|_{\partial\Omega^-} = Y_i^-, \end{cases} \quad \mathbf{V}^T = \{v \ f_k\}, \quad \text{in } \Omega, \quad (3.7)$$

$$i = 1, \dots, N; \ i \neq k,$$

A difficulty is that BCs at  $\partial\Omega^-$  cannot be set before the actual solution is known. One interesting observation in Figure 3.2 is that the flow is tangent to the iso-energy curves, i.e., there is no inflow if the computation domain coincides with an iso-energy curve. Indeed, on the one hand, based on Hamilton's principle, the power balance for a conservative system writes

$$\frac{d}{dt}\mathcal{E} = \frac{d}{dt}(\mathcal{K} + \mathcal{V}) = 0 \quad (3.8)$$

where  $\mathcal{E}$ ,  $\mathcal{K}$ , and  $\mathcal{V}$  are the total, kinetic, and potential energy, respectively. On the other hand,  $\mathcal{E} = \mathcal{E}(\mathbf{u})$  on the invariant manifold describing the NNM. This leads to

$$\frac{d}{dt}\mathcal{E}(\mathbf{u}) = \nabla\mathcal{E} \cdot \frac{d\mathbf{u}}{dt} = \nabla\mathcal{E} \cdot \mathbf{V}. \quad (3.9)$$

This last expression equals zero if and only if the flow is locally everywhere tangent to the iso-energy curve defined by  $\mathcal{E}$ . In this case, no BCs have to be imposed. In addition, two iso-energy curves form the inner and outer boundaries of an annular domain in which no inflow exists. The invariant manifold can therefore be computed considering subsequent annular domains, which substantially reduces the computational burden.

The computational method proposed herein exploits this strategy and is represented schematically in Figure 3.3. It starts in a small domain centered around the origin in which the system is assumed to behave linearly. A first guess of the iso-energy curve that realizes the domain boundary is obtained based on the corresponding LNM (see Section 3.3.1). To compute the invariant manifold in this domain, the boundary is first corrected to better fit the actual iso-energy curve. This is carried out thanks to a mesh-moving technique discussed in Section 3.3.2. Then, an iteration of a specific FE method described in Section 3.3.3 is performed. The mesh-moving and FE methods are applied sequentially until the solution is computed with a given accuracy. A new annular domain is predicted based on the computed solution, as presented in Section 3.3.4, and the PDEs are solved in this new computational domain following the same procedure. The algorithm is stopped after a user-defined number of regions ( $N_{max}$ ), at a user-defined energy ( $E_{max}$ ), or when the manifold parameterization fails (cf. discussion in Chapter 4). Eventually, the different annular domains are merged to form a single domain by defining a global mesh that interpolates over all the local meshes.

### 3.3.1 Initial Domain and First Guess

The algorithm starts by solving the equations in a small domain around the origin. The initial shape of the domain is computed using an iso-energy curve traced by a low-energy ( $\mathcal{E}_0$ ) periodic solution of the underlying conservative LNM. In the  $(u, v)$  plane, this curve is defined by

$$\begin{aligned} u_0 &= \delta\psi_k^m \cos(\omega_m t), \\ v_0 &= -\delta\omega_m \psi_k^m \sin(\omega_m t), \end{aligned} \quad (3.10)$$

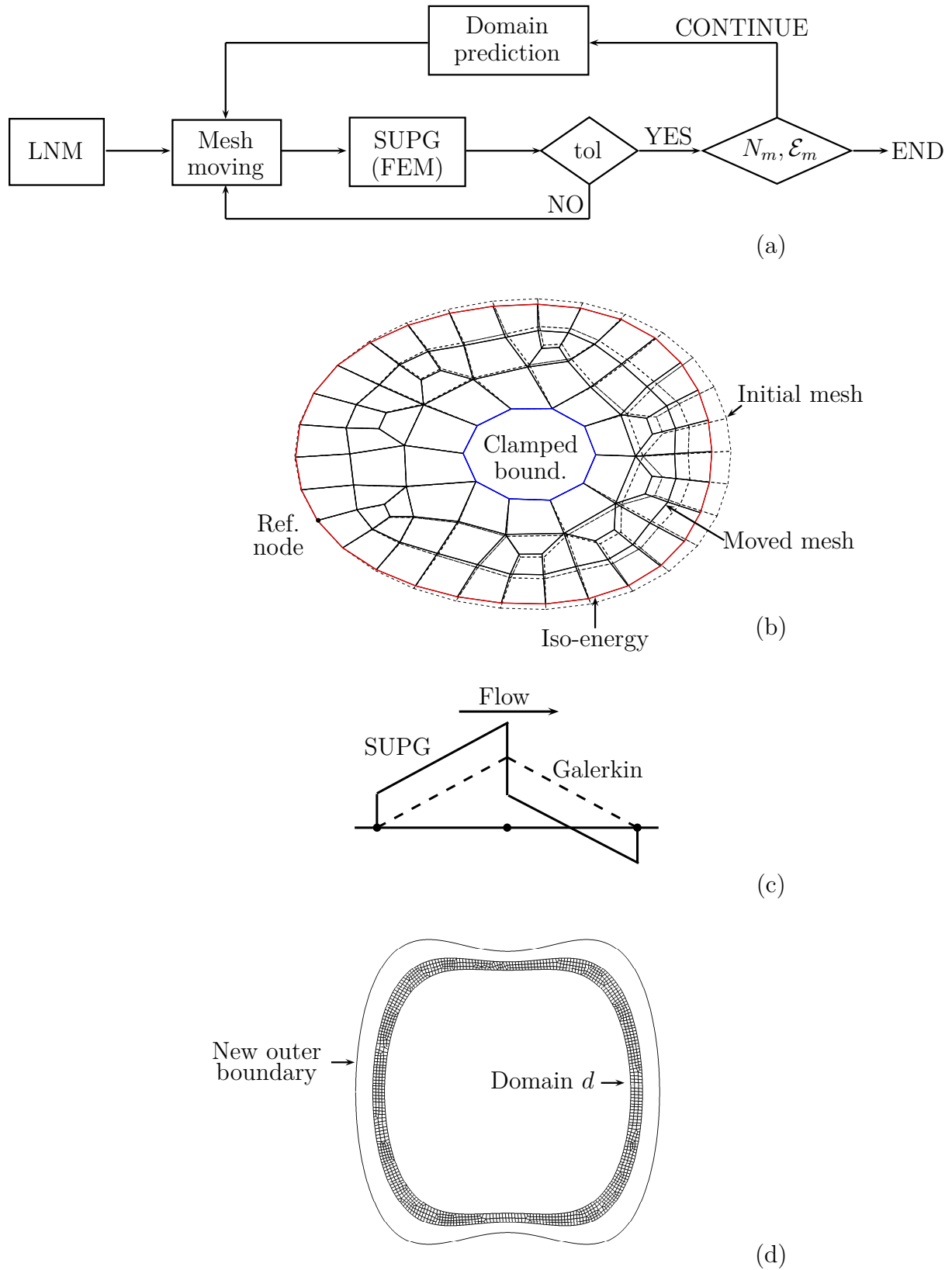


Figure 3.3: Schematics of the algorithm resolution strategy (a) including the mesh moving operation (b), the finite element formulation using SUPG (c), and the domain prediction (d).

where  $t = \{t_0 = 0, \dots, t_F = t_0 + F \cdot \Delta T = T_m\}$ ,  $\boldsymbol{\psi}^m$  is the  $m^{\text{th}}$  normalized LNM and  $\psi_k^m$  its  $k^{\text{th}}$  component,  $\omega_m$  its natural frequency, and  $T_m$  the corresponding period. The scaling factor  $\delta$  is given by:

$$\delta = \left( \frac{2\mathcal{E}_0}{(\boldsymbol{\psi}^m)^T \mathbf{K} \boldsymbol{\psi}^m} \right)^{\frac{1}{2}}, \quad (3.11)$$

where  $\mathbf{K}$  is the linear stiffness matrix. For solving the PDEs, the domain is discretized into a set of finite elements  $\Omega^e$ . In order to have elements whose size is not influenced by the non-regular spacing between the points defining the domain boundary, boundary points are first interpolated using splines. The domain is then meshed according to a user-defined characteristic length and using algorithms implemented in METAFOR [1] or GMSH [52] if quadrangular or triangular elements are needed, respectively.

For this initial mesh, a first guess of the solution is defined equal to the two-dimensional invariant plane of the linear system (i.e., the LNM). Accordingly, each pair of unknown fields  $i$  is computed at node  $j$  using

$$X_i(u_j, v_j) = a_{1i}u_j + a_{2i}v_j, \quad Y_i(u_j, v_j) = b_{1i}u_j + b_{2i}v_j, \quad (3.12)$$

where the linear coefficients are obtained as in Chapter 1. To improve this first approximation, the full third- or fifth-order polynomial expansion developed in Chapter 1 could have been employed. However, generally speaking, as the convergence domain of this polynomial series is *a priori* unknown, nothing guarantees an actual improvement of the first guess over the entire domain  $\Omega$ .

In mechanical systems, there often exist several orders of magnitude between displacements and velocities (see, for instance, the beam example in Chapter 4). This difference results in a disproportionate computational domain whose accurate meshing requires many elements. To circumvent this issue, all variables are scaled using two transformations. A first dimensionless scalar parameter,  $\beta$ , rescales time in order to obtain similar displacement and velocity magnitudes. A new time scale, slow if ( $\beta < 1$ ) or fast if ( $\beta > 1$ ), is thus introduced by the change of variable  $\tau = \beta t$  where  $\tau$  is the new time. The parameter  $\beta$  is estimated at the linear natural frequency  $\omega_l$ . The second transformation further improves numerical performance by individually rescaling all displacements in order to obtain, at the linear level, order 1 quantities. The displacements and velocities become  $\mathbf{x} = \mathbf{S}\tilde{\mathbf{x}}$  and  $\mathbf{y} = \mathbf{S}\tilde{\mathbf{y}}$ , where  $\mathbf{S}$  is a diagonal matrix whose elements are  $S_{ii} = \delta\psi_i^m, \forall i = 1, \dots, N$ . For clarity, scaled variables are not further considered in the mathematical developments of the chapter. The reader should however remember that PDEs are solved in the scaled variables and that the change of coordinates from and to the scaled quantities is performed for every evaluation of the nonlinear terms and of their derivatives.

### 3.3.2 Domain Correction Using a Mesh-Moving Technique

The next step of the algorithm corrects the assumed domain boundary such that it follows an iso-energy curve. To this end, the boundary is moved according to the energy difference

$\Delta\mathcal{E}_n$  between a reference node and each other boundary node  $n$ . The reference node is defined as the boundary node with the smallest energy. As shown in Figure 3.3(b), this ensures that the corrected boundary is enclosed into the initial boundary so that delicate extrapolation between meshes is avoided.

The corrections  $\Delta\mathbf{u}^n = [\Delta u^n \quad \Delta v^n]^T$  to the boundary node  $n$  are calculated by linearizing the energy around this node considering that  $u$  and  $v$  are independent

$$\begin{aligned}\Delta\mathcal{E}^n = \mathcal{E}^{\text{ref.}} - \mathcal{E}^n &= \left. \frac{d\mathcal{E}}{du} \right|^n \Delta u^n + \left. \frac{d\mathcal{E}}{dv} \right|^n \Delta v^n \\ \Rightarrow \Delta\mathcal{E}^n &= \begin{bmatrix} \left. \frac{d\mathcal{E}}{du} \right|^n & \left. \frac{d\mathcal{E}}{dv} \right|^n \end{bmatrix}^T \Delta\mathbf{u}^n\end{aligned}\quad (3.13)$$

The total derivatives of the energy with respect to the master coordinates are derived using the chain rule for differentiation

$$\begin{aligned}\frac{d\mathcal{E}^n}{du} &= \left. \frac{\partial\mathcal{E}}{\partial u} \right|^n + \left. \frac{\partial\mathcal{E}}{\partial\mathbf{X}} \right|^n \left. \frac{\partial\mathbf{X}}{\partial u} \right|^n + \left. \frac{\partial\mathcal{E}}{\partial\mathbf{Y}} \right|^n \left. \frac{\partial\mathbf{Y}}{\partial u} \right|^n, \\ \frac{d\mathcal{E}^n}{dv} &= \left. \frac{\partial\mathcal{E}}{\partial v} \right|^n + \left. \frac{\partial\mathcal{E}}{\partial\mathbf{X}} \right|^n \left. \frac{\partial\mathbf{X}}{\partial v} \right|^n + \left. \frac{\partial\mathcal{E}}{\partial\mathbf{Y}} \right|^n \left. \frac{\partial\mathbf{Y}}{\partial v} \right|^n.\end{aligned}\quad (3.14)$$

The partial derivatives of the unknown fields  $(\mathbf{X}, \mathbf{Y})$  with respect to  $(u, v)$  are obtained through the finite element interpolation (see Section 3.3.3) whereas the partial derivatives of the energy with respect to  $(\mathbf{X}, \mathbf{Y})$  almost reduce to the equations of motion (1.2). Indeed, the expression of the energy is given by

$$\mathcal{E}^n = \mathcal{E}^n(u, v, \mathbf{X}(u, v), \mathbf{Y}(u, v)) = \frac{1}{2} (\mathbf{x}^T \mathbf{K} \mathbf{x} + \dot{\mathbf{x}}^T \mathbf{M} \dot{\mathbf{x}}) + \mathcal{V}_{\text{nl}}, \quad (3.15)$$

where  $\mathcal{V}_{\text{nl}}$  defines the potential energy of the nonlinear stiffness terms. The partial derivatives with respect to state-space variables reads

$$\frac{\partial\mathcal{E}^n}{\partial x_j} = \mathbf{K}_{ji} \mathbf{x}_i + \frac{\partial\mathcal{V}_{\text{nl}}}{\partial x_j} = \mathbf{K}_{ji} \mathbf{x}_i + \mathbf{f}_{\text{nl},j} \quad (3.16)$$

$$\frac{\partial\mathcal{E}^n}{\partial y_j} = \mathbf{M}_{ji} \mathbf{x}_i + \frac{\partial\mathcal{V}_{\text{nl}}}{\partial y_j} = \mathbf{K}_{ji} \mathbf{x}_i + \mathbf{f}_{\text{nl},j} \quad (3.17)$$

where summation for repeated indices is assumed. Eventually, the variations  $\frac{\partial\mathcal{E}^n}{\partial u}$  and  $\frac{\partial\mathcal{E}^n}{\partial v}$  are obtained for  $j = k$  and  $\frac{\partial\mathcal{E}^n}{\partial\mathbf{X}}$  and  $\frac{\partial\mathcal{E}^n}{\partial\mathbf{Y}}$  for  $j = 1, \dots, N; j \neq k$ . Solving Equations (3.13) for  $(\Delta u, \Delta v)$  requires the use of the Moore-Penrose pseudo-inverse since the system is under determined.

To preserve a well-shaped mesh during boundary corrections, the annular domain is viewed as a pseudo-elastic medium for which the nodes follow the solution of an in-plane linear elasticity problem [150, 167]. This is illustrated in Figure 3.3(b). The main advantage of mesh-moving techniques is that remeshing operations are not necessary, which decreases the computational cost.

The equations governing the nodal displacements  $\Delta \mathbf{u}$  are

$$\nabla \cdot \boldsymbol{\sigma} = \mathbf{0}, \quad \boldsymbol{\sigma} = \mathbf{D} : \boldsymbol{\epsilon}, \quad \boldsymbol{\epsilon} = \frac{1}{2}(\nabla \Delta \mathbf{u} + \nabla \Delta \mathbf{u}^T), \quad (3.18)$$

$$\mathbf{D}_{ijkl} = \frac{E\nu}{(1+\nu)(1-2\nu)}\delta_{ij}\delta_{kl} + \frac{E}{1+\nu} \left( \frac{1}{2}\delta_{ik}\delta_{jl} + \frac{1}{2}\delta_{il}\delta_{jk} \right). \quad (3.19)$$

The operator  $\nabla(\cdot)$  denotes the divergence operator,  $\boldsymbol{\sigma}$  the Cauchy stress tensor,  $\mathbf{D}$  the Hooke tensor,  $\boldsymbol{\epsilon}$  the strain tensor,  $E$  Young's modulus,  $\nu$  Poisson's ratio, and  $\delta_{ij}$  the Kronecker delta. The parameter values are not critical and are set to  $E = 10^8 \text{ Pa}$ ,  $\nu = -0.25$  throughout this study. However, to preserve element aspect ratios,  $\nu$  must be negative.

After discretization using the finite element method, a linear algebraic problem,  $\mathbf{K}^{\text{elast}} \Delta \mathbf{u} = \mathbf{0}$ , is obtained where  $\mathbf{K}^{\text{elast}}$  denotes the stiffness matrix of the discretized annular domain. The nodes are partitioned into three sets, namely clamped (inner), interior and outer nodes

$$\begin{bmatrix} \mathbf{K}_{cc} & \mathbf{K}_{ci} & \mathbf{K}_{co} \\ \mathbf{K}_{ic} & \mathbf{K}_{ii} & \mathbf{K}_{io} \\ \mathbf{K}_{oc} & \mathbf{K}_{oi} & \mathbf{K}_{oo} \end{bmatrix}^{\text{elast}} \begin{bmatrix} \Delta \mathbf{u}_c \\ \Delta \mathbf{u}_i \\ \Delta \mathbf{u}_o \end{bmatrix} = \mathbf{0} \quad (3.20)$$

The inner nodes are clamped (i.e.,  $\Delta \mathbf{u}_c = \mathbf{0}$ ), and the outer nodes follow the corrections computed through Equations (3.13). The displacements of the interior nodes are then computed through

$$\Delta \mathbf{u}_i = -\mathbf{K}_{ii}^{-1} \mathbf{K}_{io} \Delta \mathbf{u}_o \quad (3.21)$$

Domain corrections are recursively applied until the mean and standard deviation of the energy difference of all outer-boundary nodes are below a certain tolerance.

### 3.3.3 Streamline Upwind Petrov-Galerkin (SUPG)

Standard Galerkin FE formulations use identical shape and test functions. They are known to exhibit poor performance in the case of first-order hyperbolic PDEs, such as those encountered in fluid dynamics [19, 41, 44]. Specifically, a suboptimal convergence rate as well as spurious oscillations in the solutions were observed. As a remedy, numerous stabilization methods, based on alternative test functions, were introduced. Among the many techniques introduced, the streamline upwind Petrov-Galerkin (SUPG) method proved to be effective and is considered herein. It falls within the family of Petrov-Galerkin formulations where test and shape functions are taken in different spaces and which overweight test functions that are upstream. The approach is rather standard in computational mechanics, and the interested reader can refer to [19] for a detailed description of SUPG method.

Applying a weighted residual approach to Equations (3.2) where the variations  $\delta\tilde{Y}_i$  and  $\delta\tilde{X}_i$  are applied to preserve consistent units yields

$$\begin{aligned} \int_{\Omega} [\mathbf{V} \cdot \nabla X_i(u, v) - Y_i(u, v)] \delta\tilde{Y}_i d\Omega &= 0, \\ \int_{\Omega} [\mathbf{V} \cdot \nabla Y_i(u, v) - f_i(u, v, \mathbf{X}, \mathbf{Y})] \delta\tilde{X}_i d\Omega &= 0, \end{aligned} \quad (3.22)$$

with  $i = 1, \dots, N; i \neq k$ .

The weak form (3.22) over  $\Omega$  is evaluated by summing the integrals over each element  $e$  which pave the domain:

$$\begin{aligned} \sum_e \int_{\Omega_e} [\mathbf{V} \cdot \nabla X_i^e(u, v) - Y_i^e(u, v)] \delta\tilde{Y}_i^e d\Omega^e &= 0, \\ \sum_e \int_{\Omega_e} [\mathbf{V} \cdot \nabla Y_i^e(u, v) - f_i(u, v, \mathbf{X}^e, \mathbf{Y}^e)] \delta\tilde{X}_i^e d\Omega^e &= 0 \end{aligned} \quad (3.23)$$

where unknown and virtual fields within an element  $e$  are expressed as

$$X_i^e = \sum_{b=1}^{\tilde{n}} N^b(u, v) X_i^{e,b} \quad Y_i^e = \sum_{b=1}^{\tilde{n}} N^b(u, v) Y_i^{e,b} \quad (3.24)$$

$$\delta\tilde{X}_i^e = \sum_{b=1}^{\tilde{n}} \tilde{N}^b(u, v) \delta\tilde{X}_i^{e,b} \quad \delta\tilde{Y}_i^e = \sum_{b=1}^{\tilde{n}} \tilde{N}^b(u, v) \delta\tilde{Y}_i^{e,b} \quad (3.25)$$

where  $\tilde{n}$  equals to 3 or 4 for linear triangular or linear quadrangular elements, respectively. The shape functions are first-order Lagrange shape functions,  $N^b \in \mathbb{P}^1$ :  $N^b(u, v) = \frac{1}{4}(1 + u_b u)(1 + v_b v)$  with  $u_b$  and  $v_b$  the values of the coordinates at node  $b$ . The test functions are  $\tilde{N}^b = N^b + \tau^e \mathbf{V} \cdot \nabla N^b$  where  $\tau^e \mathbf{V} \cdot \nabla N^b$  is the upstream overweighting. As a consequence, discontinuous test functions are employed, as illustrated in Figure 3.3(c) [60]. In fluid dynamics, the parameter  $\tau^e$  is defined on the basis of the element-Peclet number, which is a measure element by element of the ratio between convection and diffusion in the flow. In the present study, taking the limit for pure convection,  $\tau^e = h^e / (2\|\tilde{\mathbf{V}}\|_2)$  where  $h^e$  is the characteristic size of mesh elements and  $\tilde{\mathbf{V}}$  is the velocity vector evaluated at the center of the element  $(u_c, v_c)$ .

Each element-integral is evaluated with the so-called Gauss quadrature rule which estimates an integral  $I$  as

$$I = \int_{-1}^{+1} \int_{-1}^{+1} f(\xi, \eta) d\xi d\eta = \sum_{i=1}^{N_g} \sum_{j=1}^{N_g} f(\xi_i, \eta_j) w_i w_j \quad (3.26)$$

where  $w_i$  and  $w_j$  are the Gauss weights associated to the  $N_g^2$  Gauss points  $(\xi_i, \eta_j)$  defined in a system of coordinates of a reference elements. Gauss-point coordinates and weights are tabulated in many standard text-books about the FEM [171]. In the present work,  $N_g$  was considered equal to two.

For each element, the linear mapping from the reference element to the actual element in the physical coordinates  $(u, v)$  is given by

$$\begin{pmatrix} u \\ v \end{pmatrix} = \begin{pmatrix} g_u(\xi, \eta) \\ g_v(\xi, \eta) \end{pmatrix} = \begin{pmatrix} \sum_i^{\tilde{n}} N^b(\xi, \eta) u_b \\ \sum_i^{\tilde{n}} N^b(\xi, \eta) v_b \end{pmatrix} \quad (3.27)$$

where the functions  $N^b$  are identical to the shape functions of the finite element interpolation. Accordingly, the derivatives in Equations (3.23) follow

$$\begin{bmatrix} \frac{\partial N^a}{\partial \xi} \\ \frac{\partial N^a}{\partial \eta} \end{bmatrix} = \begin{bmatrix} \frac{\partial u}{\partial \xi} & \frac{\partial v}{\partial \xi} \\ \frac{\partial u}{\partial \eta} & \frac{\partial v}{\partial \eta} \end{bmatrix} \begin{bmatrix} \frac{\partial N^a}{\partial u} \\ \frac{\partial N^a}{\partial v} \end{bmatrix} = \mathbf{J} \begin{bmatrix} \frac{\partial N^a}{\partial u} \\ \frac{\partial N^a}{\partial v} \end{bmatrix}, \quad (3.28)$$

$$\Rightarrow \begin{bmatrix} \frac{\partial N^a}{\partial u} \\ \frac{\partial N^a}{\partial v} \end{bmatrix} = \mathbf{J}^{-1} \begin{bmatrix} \frac{\partial N^a}{\partial \xi} \\ \frac{\partial N^a}{\partial \eta} \end{bmatrix} \quad (3.29)$$

where the matrix  $\mathbf{J}$  is the Jacobian matrix of the mapping.

The inverse transformation is useful not only for computing  $\tau^e$  but also for the post-processing of the dynamics on the NNM. This transformation is defined as

$$\begin{pmatrix} u \\ v \end{pmatrix} = \begin{pmatrix} a_0 + a_1\xi + a_2\eta + a_3\xi\eta \\ b_0 + b_1\xi + b_2\eta + b_3\xi\eta \end{pmatrix} \quad (3.30)$$

where the coefficients  $a$  and  $b$  are determined using the four nodes of the element since their  $(\xi, \eta)$  coordinates are known. The system of equations is then solved for the point  $(u, v)$  of interest.

After FE discretization, the PDEs are transformed into a set of coupled nonlinear algebraic equations possessing a sparse tri-band-diagonal structure. This is a distinct advantage over the formulation in [126]. These algebraic equations are solved using a Newton-Raphson procedure where the Jacobian matrix is provided analytically. Despite the PDEs possess  $N$  distinct solutions (i.e., one for each mode), only one is relevant for the current shape of the domain and is close to the first guess obtained from the previous domain (see next section). If BCs are well set and the manifold parametrization is still valid (see Section 4.2), the Newton-Raphson procedure converges within 2 or 3 iterations. In this study, the convergence criterion *tol* is satisfied when the  $L^2$  norm of the residue is below  $10^{-7}$ . We note that the PDEs to solve remain nonlinear even if the considered mechanical system is linear.

*Remark:* As the size of the discretized problem increases, Matlab direct solver requires important memory resources. As a consequence, the recourse to iterative solvers (e.g., the generalized minimal residual (GMRes)) was sometimes mandatory. To avoid a slow convergence of these solvers, preconditioners computed from incomplete LU factorization (ILU) were considered. However, no dedicated investigations for defining a general and effective preconditioner were conducted.

### 3.3.4 Domain Prediction

Once the solution for the current annular domain is computed, a new annular domain can be predicted, as illustrated in Figure 3.3(d). Its inner boundary is defined as the previous outer boundary, whereas its outer boundary is determined by applying an energy increment  $\Delta\mathcal{E}$  to the previous outer boundary. The new increment  $\Delta\mathcal{E}_{d+1}$  is determined so that the SUPG method requires on average a user-specified number  $N^*$  of iterations. It follows that

$$\Delta\mathcal{E}_{d+1} = \left(\frac{N^*}{N_d}\right) \Delta\mathcal{E}_d \quad (3.31)$$

where  $N_d$  is the actual number of iteration require for the previous domain.

Similarly to the first step of the algorithm, Equation (3.13) can be used to compute the corresponding nodal displacements  $\Delta u^n$  and  $\Delta v^n$ . The solution at each outer-boundary node of the new domain is computed as follows

$$X_i(u^n + \Delta u^n, v^n + \Delta v^n) = X_i(u^n, v^n) + \left.\frac{\partial X_i}{\partial u}\right|^n \Delta u^n + \left.\frac{\partial X_i}{\partial v}\right|^n \Delta v^n, \quad (3.32)$$

$$Y_i(u^n + \Delta u^n, v^n + \Delta v^n) = Y_i(u^n, v^n) + \left.\frac{\partial Y_i}{\partial u}\right|^n \Delta u^n + \left.\frac{\partial Y_i}{\partial v}\right|^n \Delta v^n, \quad (3.33)$$

with  $i = 1, \dots, N$ ;  $i \neq k$ . The new annular domain is meshed, and the solution for all internal nodes is approximated using linear interpolation. Eventually, a complete guess for the solution in the new annular domain is obtained, and the mesh-moving technique of Section 3.3.2 can be applied.

## 3.4 Extension to Nonconservative Systems

All the previous developments considered the conservative case. This section aims at showing that the method can be naturally extended to nonconservative systems. Figure 3.4 presents the flow field of the 2DOF nonconservative system considered in Chapter 1. This system includes cubic hardening nonlinearity and nonproportional linear damping. Generally speaking, the flow spirals down to the equilibrium point of the system. Unlike the conservative case, the flow now crosses the iso-energetic boundaries, which means that BCs are required at the outer, yet unknown, boundary. A graphical depiction is provided in Figure 3.5(a).

Mathematically, the flow can be “reversed” by changing the sign of the test functions. Doing so, inflow/outflow boundaries are swapped, as illustrated in Figure 3.5(b). There is now inflow at the inner boundary. Because the solution in the previous annular domain is available, BCs can be easily imposed at this boundary for solving the PDEs in the current annular domain. As a consequence, the recursive strategy developed for conservative

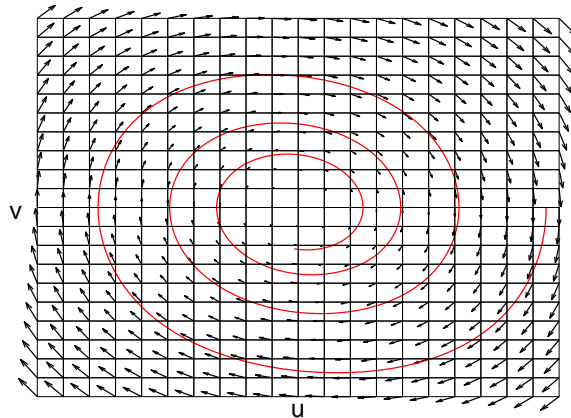


Figure 3.4: Trajectory (—) and velocity vector  $\mathbf{V}$  ( $\rightarrow$ ) of the manifold-governing PDEs for a 2DOF nonconservative system.

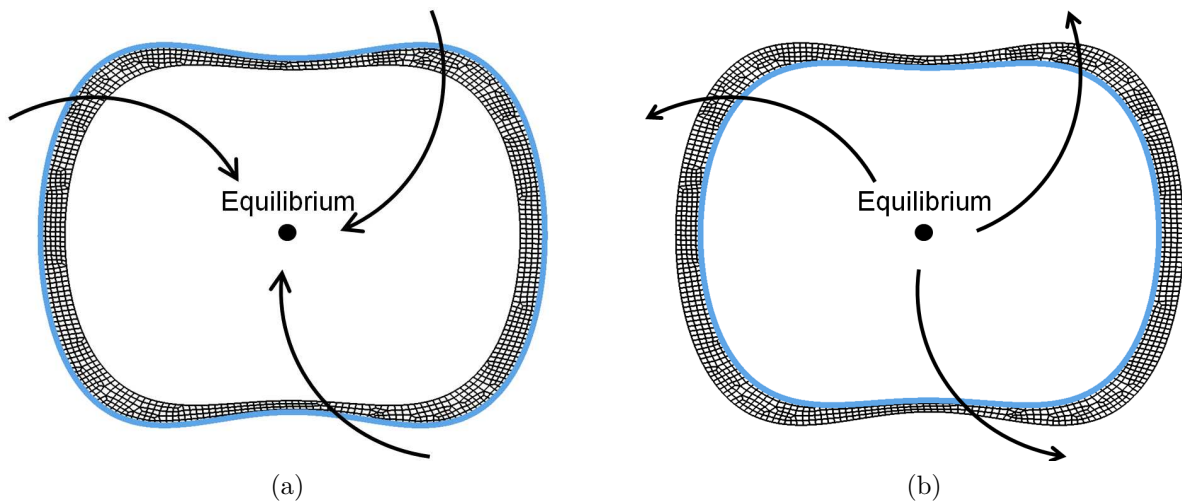


Figure 3.5: Schematics of the extension of the algorithm to nonconservative systems. BCs are required at the inflow boundary  $\partial\Omega^-$  depicted in light blue. (a) Original problem; (b) Problem with reversed flow.

systems can be applied as such in the nonconservative case, providing a straightforward extension of our algorithm to damped nonlinear systems.

The choice of an iso-energy curve for defining an inflow boundary appears natural because damping decreases energy. Although rigorous in many circumstances, Chapter 5 will show that this choice is not always adequate in the presence of nonlinear damping. This particular aspect of the method will be revised in Chapter 5.

## 3.5 Discussion

### 3.5.1 Comparison with the Transport Method

As mentioned at several instances, Blanc et al. [13] recently regarded the manifold-governing PDEs as transport equations. This interpretation is, in essence, similar to the interpretation made in this thesis. The hyperbolic nature of the equations was rigorously addressed using an off-centered finite difference scheme and appropriate BCs updated using an adjoint method (cf. Chapter 1). Thanks to its solid theoretical foundations, the method provided accurate reduced-order models capturing the frequency-energy dependence of a conservative system.

The FEM proposed in this chapter is now briefly compared to the finite difference method (FDM). For this comparison, the 2DOF conservative system presented in Chapter 1 is considered without damping.

The slave coordinate  $Y_2(u, v)$  of the in-phase NNM is plotted in Figure 3.6. The results obtained with the FEM and the FDM are presented in Figure 3.6(a) and (b), respectively. A preliminary observation shows that both surfaces have a similar aspect with an increasing curvature for large amplitudes of the master velocity. In this area, the surfaces become almost vertical which indicates that both methods computed the manifold close to the theoretical limit imposed by the parametrization (cf. Chapter 4). The agreement between the FEM and FDM is confirmed by an almost perfect overlap of the two surfaces in Figure 3.6(c).

The out-of-phase NNM of the same 2DOF system is now computed and investigated for high vibration amplitudes. The slave displacement  $X_2$  obtained by the FEM is presented in Figure 3.7(a). In contrast to the in-phase NNM, the overall shape strongly deviates from a flat surface and presents a peak and a dip on either side of the zero-displacement line. This illustrates the localization phenomenon during which the energy of the system localizes to some DOFs (here, the master one) while the amplitude of the others is strongly reduced. The surface computed using the FDM is presented in Figure 3.7(b). Although the overall shape is similar to the FEM, the manifold appears elongated. The superposition of both surfaces in Figure 3.7(c) shows that, in spite of similar maximum amplitudes for  $x_1$ , the domains where the solution was computed are different in both methods. Moreover, whereas the agreement between both methods is excellent along the zero-velocity line, a deviation is noticed elsewhere. Figure 3.7(c) shows that the solution of the FEM is in better agreement with the reference solution (in orange) obtained using continuation (1).

In order to understand the differences observed between the FEM and FDM results, both resolution methods and, in particular, their treatment of BCs are discussed. Figure 3.8 presents the amplitude-phase domain considered by the FDM for solving the manifold-governing PDEs. Inside this domain, the characteristics of the PDEs (or, equivalently, the

periodic orbits of the NNM) are represented by continuous curves. For low amplitudes, nonlinearities are negligible and characteristics are straight lines. However, as amplitude increases, nonlinear effects come into play and the straight lines are distorted. The PDEs are solved in a domain of fixed maximum amplitude  $a$ ; say, e.g.,  $a = 2$ . This choice has two consequences:

1. The characteristics leave and enter into the domain which introduces regions of inflow and outflow. The transport method thus identifies and imposes BCs on the inflow parts of the boundary  $a = 2$ . As this boundary is at high amplitude, no information about the incoming flow is available. To overcome this issue, a technique based on the smoothness of the invariant manifold is used to extrapolate the solution computed inside the domain [13]. This treatment of BCs is essentially different from the FEM which considers a domain whose boundary follows the periodic orbit and where no inflow is present.
2. A direct exploitation of the NNM for model reduction is not possible for motion amplitudes close to the boundary  $a = 2$  because, during the time integration of the equations of motion, the dynamics of the system leaves the computational area. The recourse to global shape functions (as in Pesheck et al. [126]) or to an interpolation function computed a posteriori (as in the FDM [13]) is thus mandatory. A classical finite element approach (with local interpolation) would be ineffective as a part of the rectangular domain would be unexploitable.

In summary, while the difference in the computational domain arises from the amplitude-phase domain of the FDM that does not cover the high-velocity region of the periodic orbits (i.e., at  $\phi = \frac{\pi}{2}$  and  $\phi = \frac{3\pi}{2}$ ), the differences that exist between the two surfaces are explained by the treatment of BCs.

We believe that, in view of its rigorous theoretical foundations, the deviation of the FDM from the reference solution can actually be resolved by simply changing the domain discretization and accuracy tolerances. As a computational method, the accuracy of the solution is reduced to a computational effort (contrary to analytical methods). This example was however the opportunity to further explain and illustrate our computational strategy and to show its major differences with an existing method.

### 3.5.2 Hyperbolicity

The specific treatment of the hyperbolicity, simultaneously through the imposition of BCs and the consideration of the SUPG formulation, is necessary. Figure 3.9 compares the solution obtained with a classical Galerkin formulation (blue) and a reference solution obtained using continuation (orange). In the absence of the two elements mentioned above, the FE solution deviates substantially from the reference. The importance of the SUPG method will be further stressed in the first application of Chapter 4.

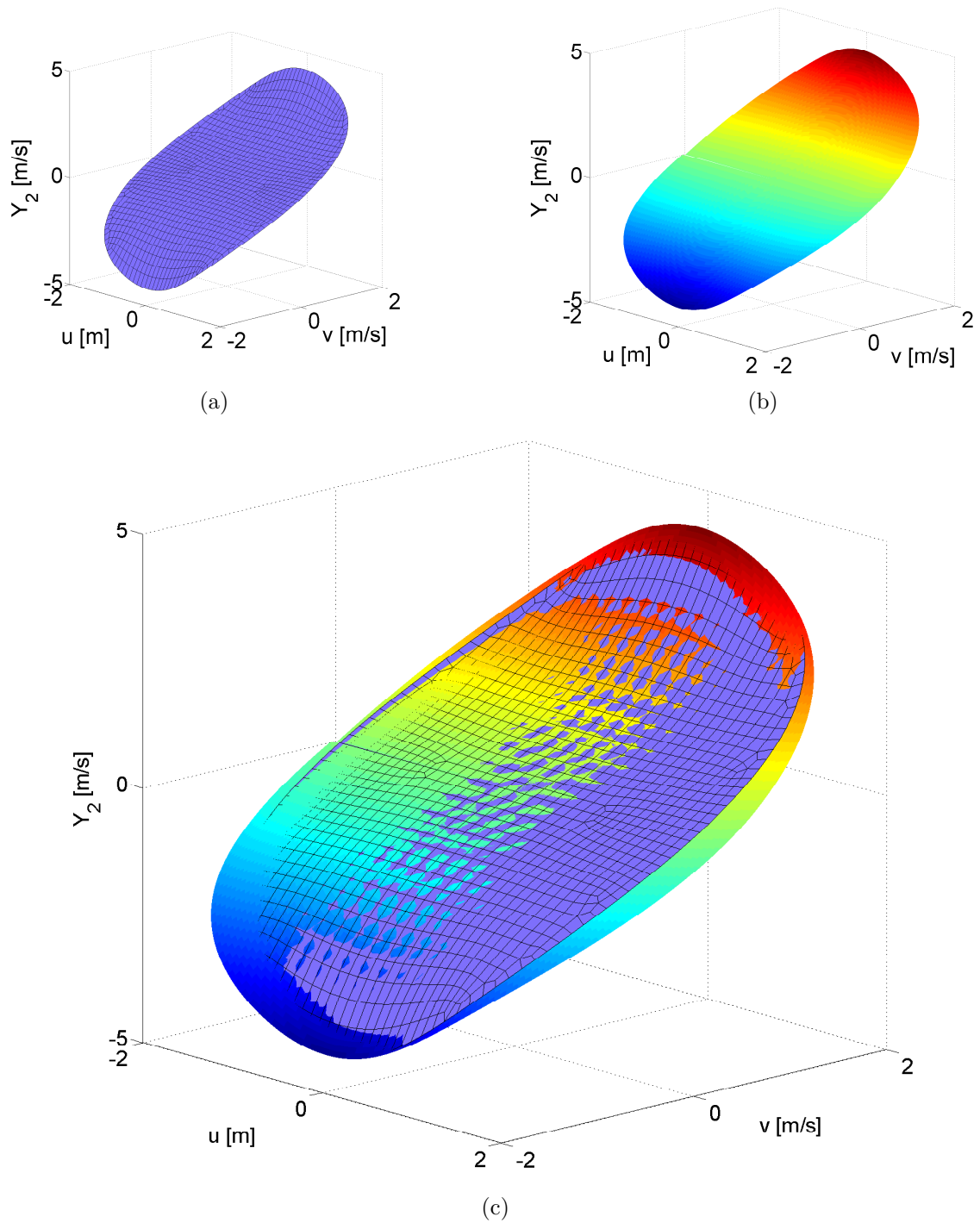


Figure 3.6: Slave velocity  $Y_2$  of the in-phase NNM of the 2DOF (1.1). (a) The manifold computed using the FEM; (b) the manifold computed using the FDM [13]; (c) comparison of both surfaces.

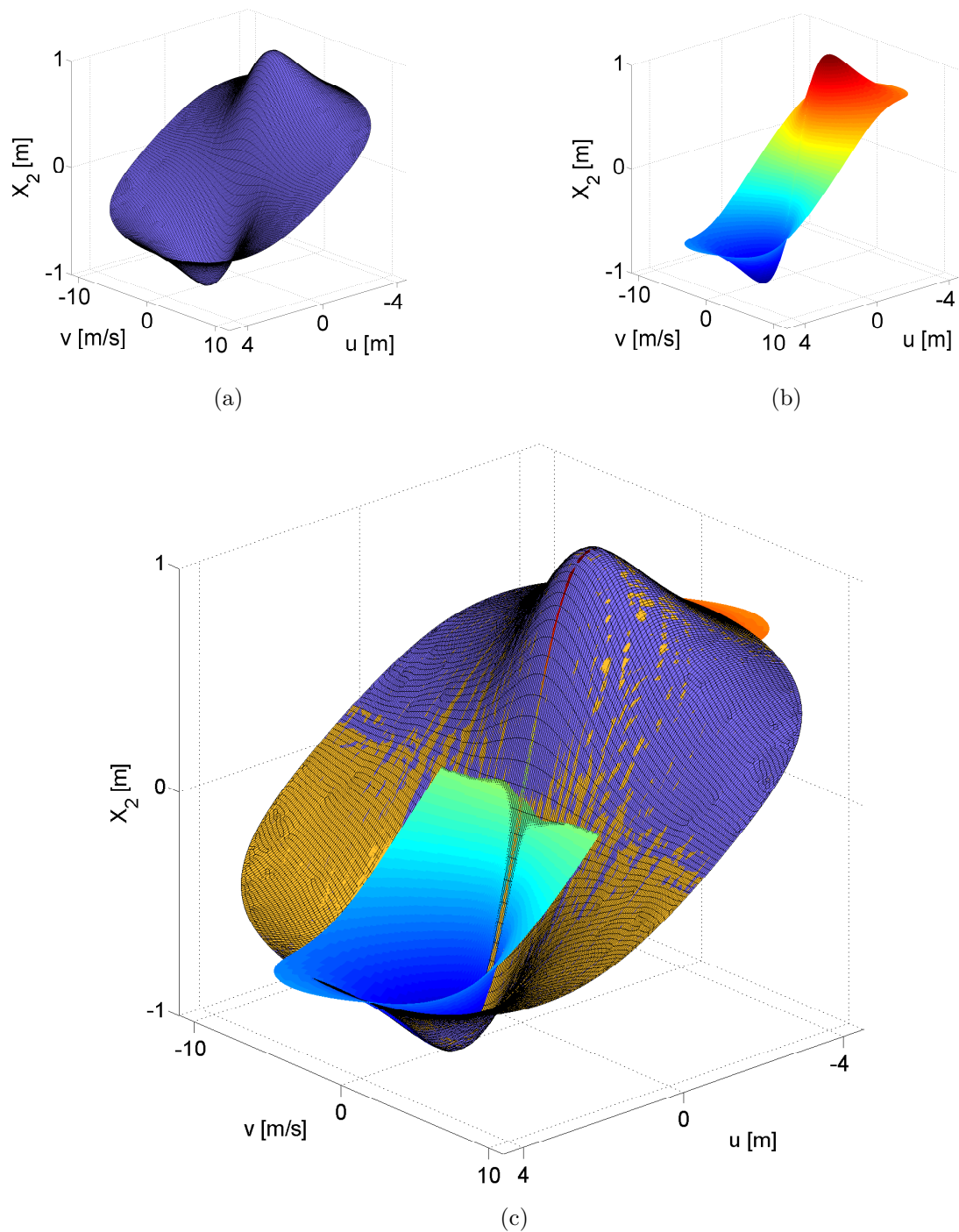


Figure 3.7: Slave displacement  $X_2$  of the out-of-phase NNM of the 2DOF (1.1). (a) The manifold computed using the FEM; (b) the manifold computed using the FDM [13]; (c) comparison of both surfaces with a reference solution obtained from a continuation algorithm (orange).

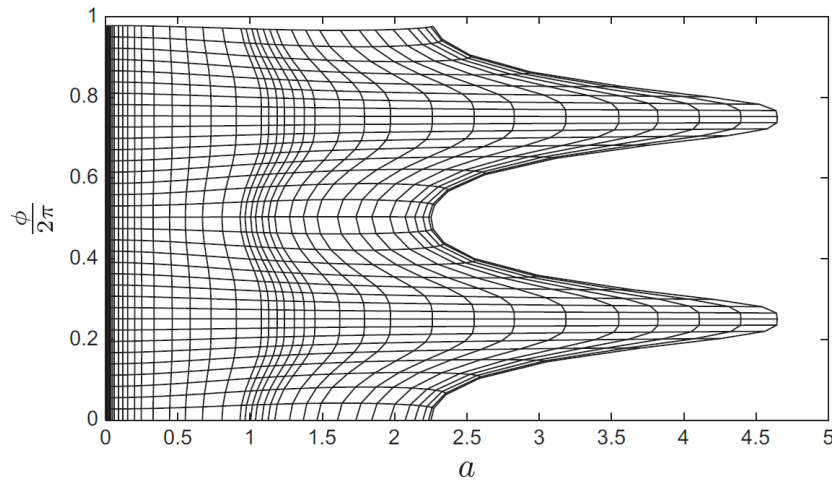


Figure 3.8: Characteristics of the manifold-governing PDEs in the amplitude-phase domain used by the FDM. Taken from [13].

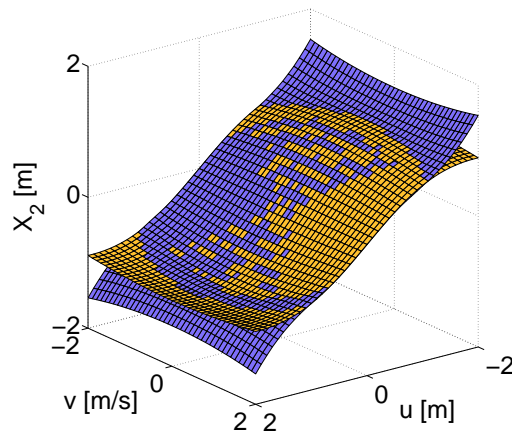


Figure 3.9: Comparison between the reference manifold (orange) and the manifold computed using a classical Galerkin formulation without BCs (blue).

## 3.6 Conclusions

In this chapter, a new finite-element-based method for calculating NNMs defined as two-dimensional invariant manifolds is established. The challenges that we had to address were the high dimensionality of the problem (i.e.,  $2N - 2$  equations), the hyperbolic character of the governing PDEs and the applicability to both conservative and nonconservative systems. To resolve the first issue, a resolution strategy which grows the invariant manifold in small annular strips was used. The method was also carefully implemented in Matlab exploiting its parallel computing capabilities. The second challenge was addressed by imposing BCs on the inflow boundary, as required by hyperbolic PDEs, and by utilizing an

appropriate finite-element scheme, the SUPG formulation. While there exist other methods such as Galerkin least-squares (GLS) FEM [14] or the discontinuous Galerkin (DG) methods which can deal with hyperbolic PDEs, the SUPG formulation was considered as a simple and effective choice. Finally, by simply reversing the flow, a scheme that can tackle both undamped and damped systems was obtained. The next chapter demonstrates the proposed method on different conservative and nonconservative examples.

We note that the PDEs obtained from the approach of modal quantities in Section 1.4.2 are similar to the PDEs considered in this chapter. We therefore believe that the developments presented in this thesis could also be useful in the context of this approach.

# Chapter 4

## Numerical Demonstration of the Proposed Algorithm

---

### Abstract

In this chapter, the accuracy and effectiveness of the proposed algorithm for computing NNMs as two-dimensional invariant manifolds is demonstrated using four examples. First, a two-degree-of-freedom system demonstrates the general applicability of the method. A cantilever beam with nonlinear boundary conditions is then considered to show the effectiveness of the method for mechanical systems with increased dimensionality. Another example considers the presence of nonlinear damping in a system composed of two coupled Van der Pol oscillators. Finally, the last example investigates a full-scale aircraft, the Morane-Saulnier 760, and demonstrates the applicability of the algorithm to high-dimensional systems.

---

## 4.1 Introduction

The accuracy and effectiveness of the method is demonstrated using four examples. A two-degree-of-freedom (2DOF) system with quadratic and cubic nonlinearities is investigated in Section 4.2. A method for estimating the motion frequency as a byproduct of the algorithm is also presented. The NNMs of a cantilever beam with nonlinear boundary conditions are computed in Section 4.3. Both examples are first considered in their conservative configuration, and linear damping is then introduced. Section 4.4 shows the general applicability of the method to systems including nonlinear damping and studies a system of two coupled Van der Pol oscillators. Finally, the Morane-Saulnier aircraft whose model includes cubic nonlinearities and linear damping is studied in Section 4.5.

## 4.2 2DOF System With Geometric Nonlinearities

The 2DOF system presented in Figure 4.1 contains quadratic and cubic nonlinearities arising from second-order terms in the strain tensor. It is an interesting example, because it can exhibit both softening and hardening behaviors. This example was previously studied in references [8, 13, 151]. The motion-governing ordinary differential equations (ODEs) are

$$\begin{aligned} \ddot{\hat{x}}_1 + 2\omega_1\zeta_1\dot{\hat{x}}_1 + \omega_1^2\hat{x}_1 + \frac{\omega_1^2}{2}(3\hat{x}_1^2 + \hat{x}_2^2) + \omega_2^2\hat{x}_1\hat{x}_2 + \frac{\omega_1^2 + \omega_2^2}{2}\hat{x}_1(\hat{x}_1^2 + \hat{x}_2^2) &= 0, \\ \ddot{\hat{x}}_2 + 2\omega_2\zeta_2\dot{\hat{x}}_2 + \omega_2^2\hat{x}_2 + \frac{\omega_2^2}{2}(3\hat{x}_2^2 + \hat{x}_1^2) + \omega_1^2\hat{x}_1\hat{x}_2 + \frac{\omega_1^2 + \omega_2^2}{2}\hat{x}_2(\hat{x}_1^2 + \hat{x}_2^2) &= 0, \end{aligned} \quad (4.1)$$

where  $\hat{x}_{1,2} = x_{1,2}/l_0$ ,  $l_0$  is the spring's natural length,  $\zeta_1$  and  $\zeta_2$  are the damping ratios. The system is completely parametrized by the two natural frequencies  $\omega_1 = \sqrt{k_1/m}$  and  $\omega_2 = \sqrt{k_2/m}$  [153]. They are chosen equal to 1 *rad/s* and  $\sqrt{3}$  *rad/s*, respectively.

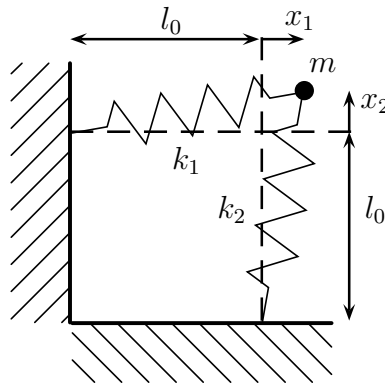


Figure 4.1: Schematic representation of the 2DOF example.

### 4.2.1 Conservative Case

The 2DOF system is first considered in its conservative configuration, i.e.,  $\zeta_1 = \zeta_2 = 0$ . Figure 4.2 presents the results for the first NNM of the system. The displacement–velocity pair of the first DOF was considered as master coordinates  $(u, v) = (u_1, v_1)$ . The invariant manifold corresponding to the constraint relation  $X_2(u, v)$  is presented in phase space in Figure 4.2(a). Four annular regions were considered for the computation of this manifold, leading to a computational time of 3 minutes in Matlab on a standard laptop computer. The annular approach which consists in progressively growing the manifold is computationally interesting. Indeed, solving the PDEs directly on a global mesh with a number of element similar to that in Figure 4.2(a) requires 2 iterations of the Newton-Raphson (NR) algorithm for a total computational time of 5 minutes. Conversely, although the resolution of each annular domain also requires 2 NR iterations, the computational problems are much smaller, leading to a lower computational time.

Using numerical continuation, a reference manifold of the considered NNM can be built by gathering in phase space all computed periodic orbits. The global mesh built from the different annular domains is compared to the reference manifold in Figure 4.2(b). The two manifolds overlay almost perfectly. In addition, Figure 4.2(c) shows that a classical Galerkin formulation is associated with spurious element-wise oscillations around the SUPG solution. Interestingly, due to these oscillations, the flow lines can clearly be distinguished. This confirms that the hyperbolic PDEs require specific numerical treatment.

Further validation can be achieved by investigating the nonlinear modal dynamics, i.e., the system’s dynamics on the manifold. Initial conditions (ICs) on the first mode in modal space  $(u, v)$  are considered, and Equations (1.18) are integrated over time using a fourth-order Runge-Kutta method. The modal time series are then projected back to the physical space using Equations (1.15). The ICs are also transformed back to physical space, and a second time integration of the full system’s equations (4.1) is performed considering these ICs. The resulting time series for  $\hat{x}_2(t)$  are displayed in Figure 4.3(a) and agree to the point where the difference between the signals is not visible. The presence of an important second harmonic component in the time series is the sign of a strongly nonlinear regime of motion. A more quantitative comparison is achieved using the normalized mean-square error (NMSE). This indicator is considered as very good below 1% (cf. Chapter 1). For the present example, the NMSE is  $10^{-7}\%$ . This NMSE value is particularly low, and one might want to trade off this accuracy for gaining computational efficiency. The computation of the first NNM for a total number of 110 elements (instead of 967 as presented in Figure 4.2(a)) was performed in only 22 seconds. The accuracy of the time series  $\hat{x}_2(t)$  (presented in Figure 4.3(b)) is still acceptable with a NMSE of  $10^{-1}\%$ . Contrary to Figure 4.3(a), small differences with respect to the reference solution are observable.

Due to the frequency-energy dependence of nonlinear oscillations, an appropriate graphical depiction of NNMs is a frequency-energy plot (FEP) in which the NNM frequency is represented at different energy levels [75, 94]. However, because the invariant manifold

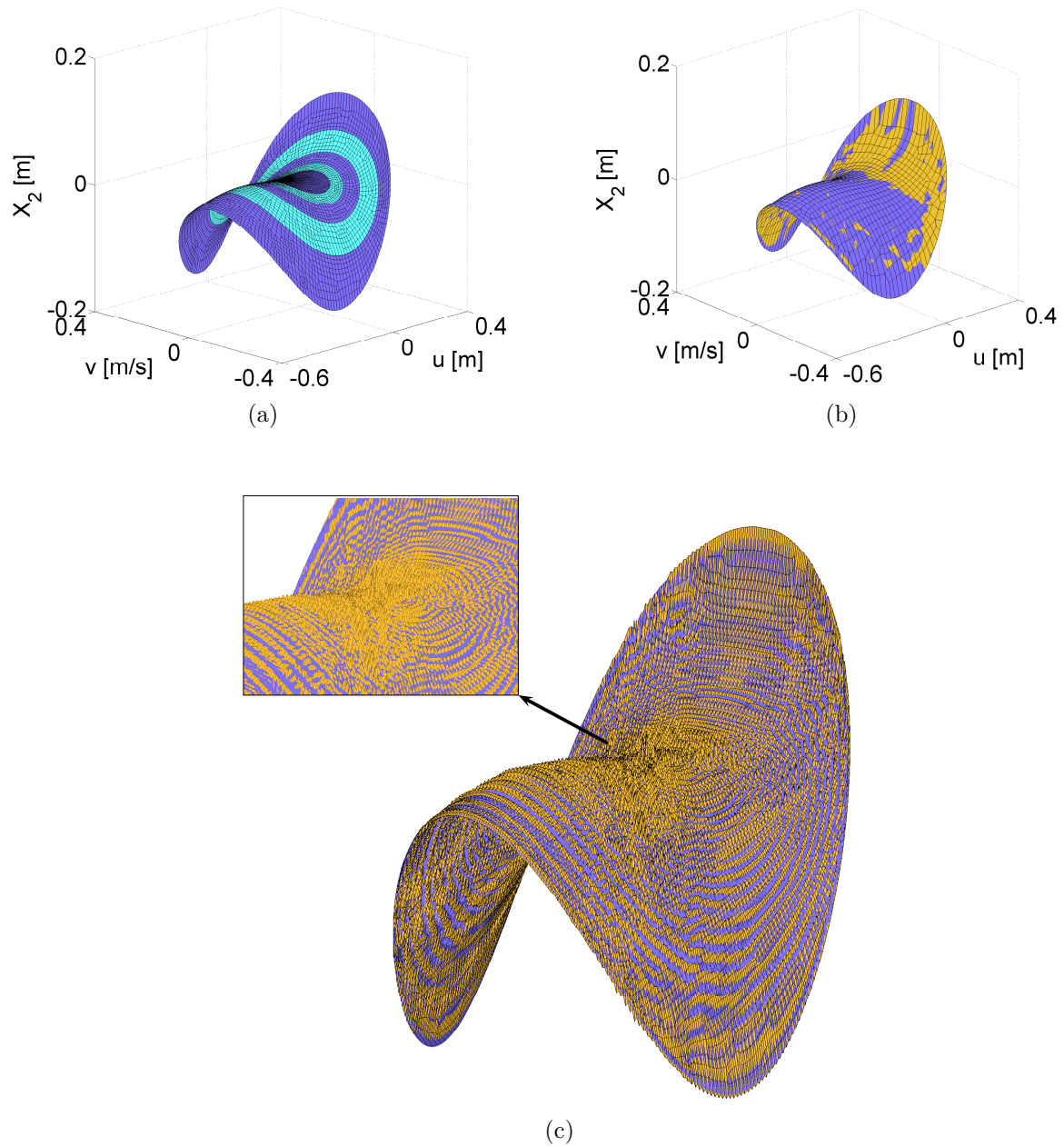


Figure 4.2: First NNM of the 2DOF system. (a) Invariant manifold  $X_2$  in phase space with the different annular domains; (b) invariant manifold  $X_2$  in phase space (blue: FE method, orange: numerical continuation); (c) comparison between SUPG (blue) and a classical Galerkin approach (orange).

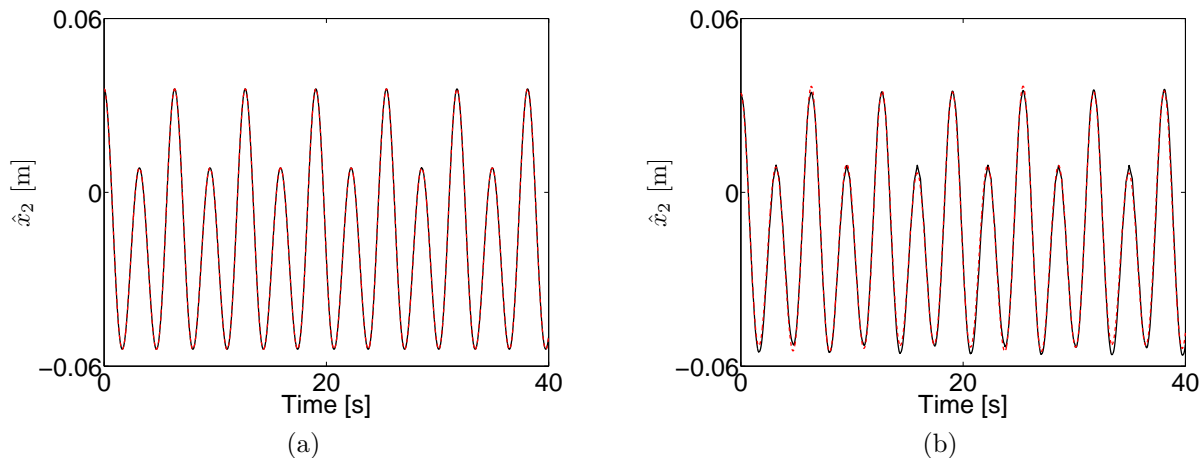


Figure 4.3: Validation of the results obtained on the first NNM of the 2DOF system. (a) Solution computed with 967 mesh elements; (b) 110 elements. Comparison between reduced- and full-system dynamics in black and red, respectively. Initial conditions corresponding to the red marker in Figure 4.4.

approach is geometric by nature, the frequency is not a direct by-product of the method. The approach followed here is to estimate, for each iso-energy curve, the NNM period as the sum over each boundary edge of the ratio between the edge length and the norm of the velocity vector  $\mathbf{V}$  along the edge. Figure 4.4 presents the FEP of the first NNM as computed by the FE method and by numerical continuation [120]. Blue circles discretize the frequency-energy curve according to the energy increments performed by the FE algorithm while growing the manifold. The softening behavior of the first NNM is perfectly well reproduced by the FE method. Another observation is that the FE method provides accurate results, even for unstable regimes of motion. Note that the red marker corresponds to the energy of ICs considered in Figure 4.3

The convergence of the FE method is now demonstrated on this first mode. The manifold is computed for different meshes of the same global domain  $\Omega$ . The domain corresponds to an iso-energy boundary in order to remove the influence of the mesh-moving technique. As no exact analytical solution exists, a solution  $\mathbf{Z}$  is compared to the solution  $\mathbf{Z}^{\text{ref}}$  obtained with the finest mesh. Because the different meshes have no common nodes, a direct  $L^2$  measure of the solution error cannot be used. Instead, non-overlapping regions are ignored, and a simple Euclidean vector norm ( $\|\cdot\|_2$ ) is employed. The convergence rate in Figure 4.5 is clearly observed for decreasing element characteristic sizes  $h_e$  and is close to the theoretically expected value of  $O(h_e^{3/2})$  [71].

The results for the second NNM are presented in Figure 4.6. As for the first NNM, the invariant manifold and FEP computed by the FE and continuation methods overlay very well. Figure 4.7 compares the dynamics of the slave velocity  $y_1$  reduced on the

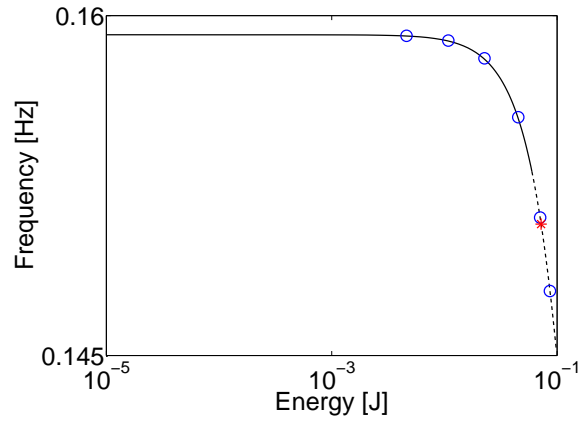


Figure 4.4: FEP (blue circles: FE method, black solid line: stable branch computed using numerical continuation, black dashed line: unstable branch computed using numerical continuation).

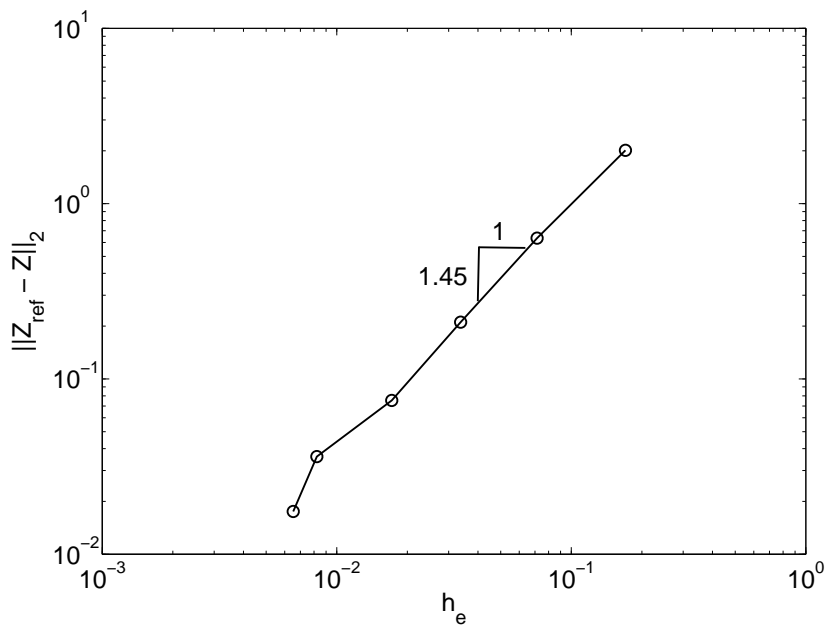


Figure 4.5: Convergence of the SUPG method.

invariant manifold with the full-system dynamics for the points corresponding to the two red markers in Figure 4.6(b). In Figure 4.7(a), there is a good correspondence between both time series; the NMSE is  $3 \times 10^{-2}\%$ . However, a slight discrepancy is observed for values of  $y_1$  around 0, which is due to a too coarse mesh for small displacements. Decreasing the characteristic size  $h_e$  from 0.0198 in Figure 4.7(a) to 0.0149 in Figure 4.7(b) resolves this issue; the NMSE reduces to  $4 \times 10^{-4}\%$ . Figure 4.7(c) performs the same comparison for initial conditions in the unstable region. Despite the unstable character of the dynamics, both time series match over more than 8 periods and then drift apart. The finer mesh considered in Figure 4.7(d) can delay this drift.

To conclude the study of this conservative 2DOF system, the first NNM is computed for alternative parameters,  $(\omega_1^2, \omega_2^2) = (1.7, 6) \text{ rad}^2/\text{s}^2$ . Figure 4.8 shows that the system has first a hardening behavior, which is then transformed into softening behavior as energy increases. This interesting dynamics is accurately reproduced by our method.

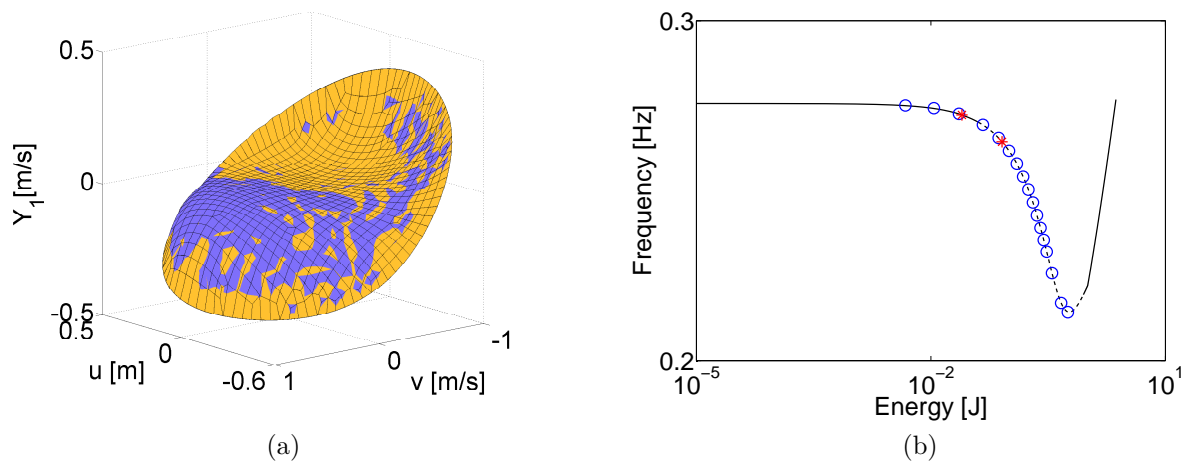


Figure 4.6: Second NNM of the 2DOF system. (a) Invariant manifold  $Y_1$  in phase space (blue: FE method, orange: numerical continuation); (b) FEP (blue circles: FE method, black solid line: stable branch computed using numerical continuation, black dashed line: unstable branch computed using numerical continuation).

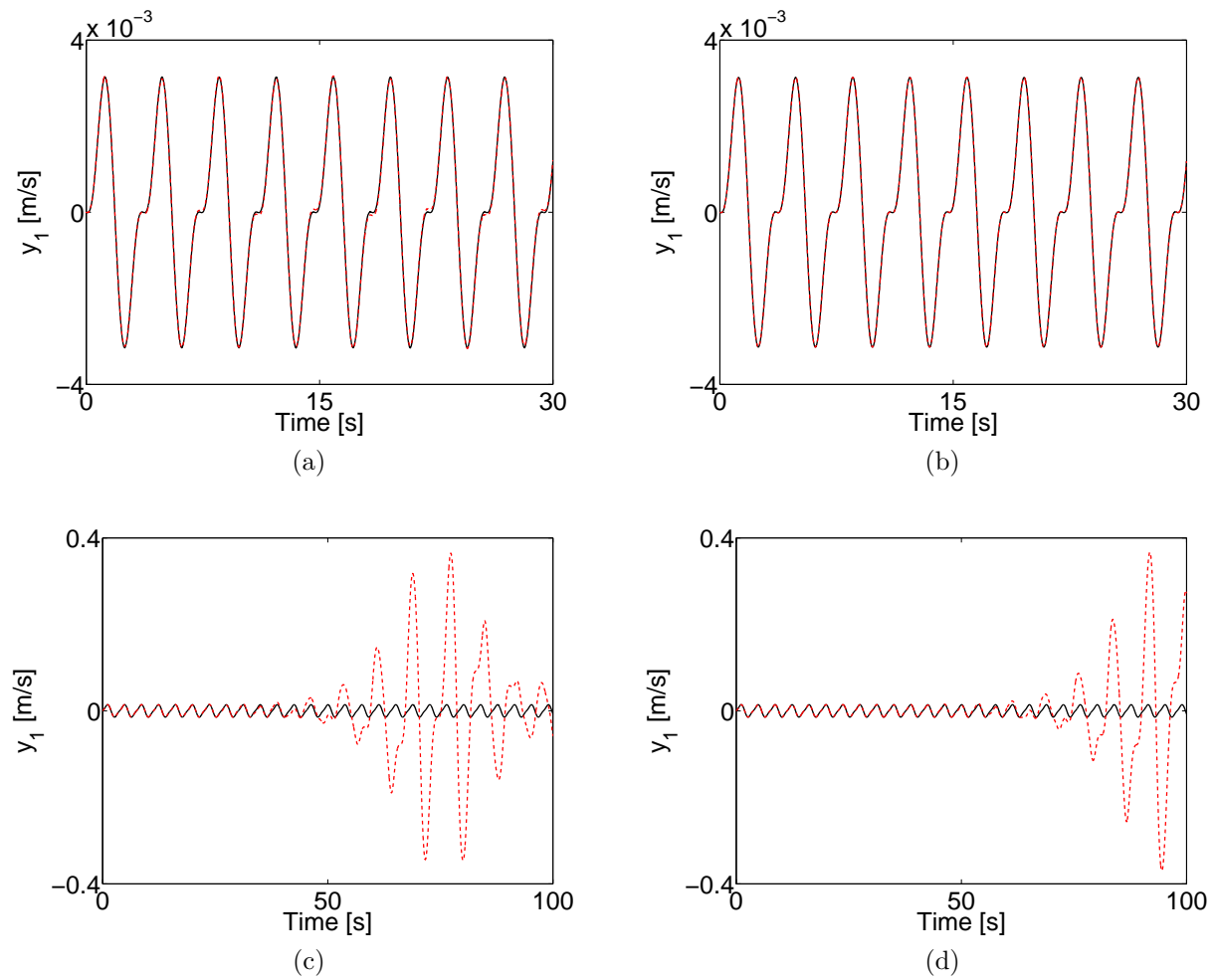


Figure 4.7: Second NNM of the 2DOF system: comparison between reduced- and full-system dynamics in black and red, respectively. (a, b) Initial conditions in the stable region with  $h_e = 0.0198$  and  $h_e = 0.0149$ , respectively; (c, d) Initial conditions in the unstable region with  $h_e = 0.0198$  and  $h_e = 0.0149$ , respectively.

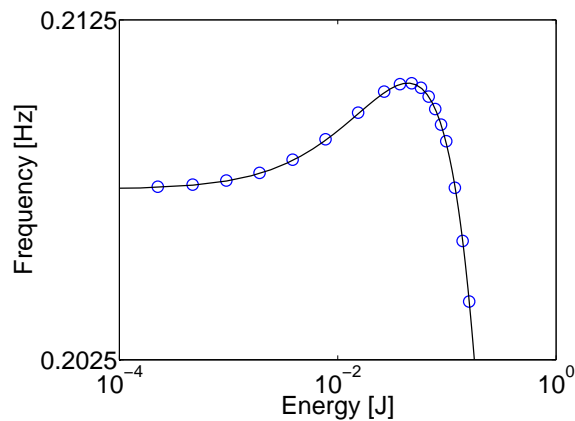


Figure 4.8: FEP of the first NNM of the 2DOF system for  $(\omega_1^2, \omega_2^2) = (1.7, 6) \text{ rad}^2/\text{s}^2$ . Blue circles: FE method, black line: numerical continuation.

## 4.2.2 Nonconservative Case

The 2DOF example where  $(\omega_1^2, \omega_2^2) = (1.8, 6) \text{ rad}^2/\text{s}^2$  is now considered with linear damping. The first NNM is computed for a lightly damped and a strongly damped case with  $(\zeta_1, \zeta_2) = (0.001, 0.005)$  and  $(\zeta_1, \zeta_2) = (0.001, 0.2)$ , respectively. The results are presented in Figure 4.9. In the presence of weak damping, the invariant manifold in Figure 4.9(a) possesses the same characteristic shape as for the conservative system (Figure 4.2). However, the introduction of strong damping dramatically modifies its structure as illustrated in Figure 4.9(b). The surface now presents a plateau around the origin and then suddenly bends. The dynamics of the slave velocity  $y_2$  reduced on the invariant manifold is compared to the full-system's dynamics for both damping cases in Figures 4.9(c, d). The ICs considered for the lightly and strongly damped cases are  $(u, v) = (0.225, 0)$  and  $(u, v) = (0.24, 0)$ , respectively. Each time series is in excellent agreement with its reference solution, and the NMSE values equal to  $4 \times 10^{-4}\%$  and  $3 \times 10^{-6}\%$ , respectively. One can note that, due to damping, the presence of harmonics that indicates a strongly nonlinear regime of motion gradually decreases with time. Another observation is that, although ICs in amplitude are considered, the slave velocity of the strongly damped system starts from a non-zero value indicating clearly a phase lag between the master and slave coordinates of the system.

Figures 4.10(a, b) present the system's frequency response to harmonic excitation computed for different forcing amplitudes. The computations are carried out using a numerical continuation algorithm (as in Chapter 2). For  $(\zeta_1, \zeta_2) = (0.001, 0.005)$ , a clear hardening behavior is observed, whereas softening behavior is present for  $(\zeta_1, \zeta_2) = (0.001, 0.2)$ . It is interesting that simple viscous damping can lead to such fundamental changes in the dynamics [151]. As nonlinear resonances occur in the neighborhood of NNMs [158], this behavior can also be predicted by the damped NNMs. Based on the dynamics integrated in time on the computed manifolds, the frequency-amplitude dependence was extracted from the free-decay response and the backbone curves shown in dashed lines in Figure 4.10(a, b) were obtained. The computed backbones accurately draw the resonance locus of the system and thus are in perfect agreement with numerical continuation. This further validates the proposed algorithm in the damped case.

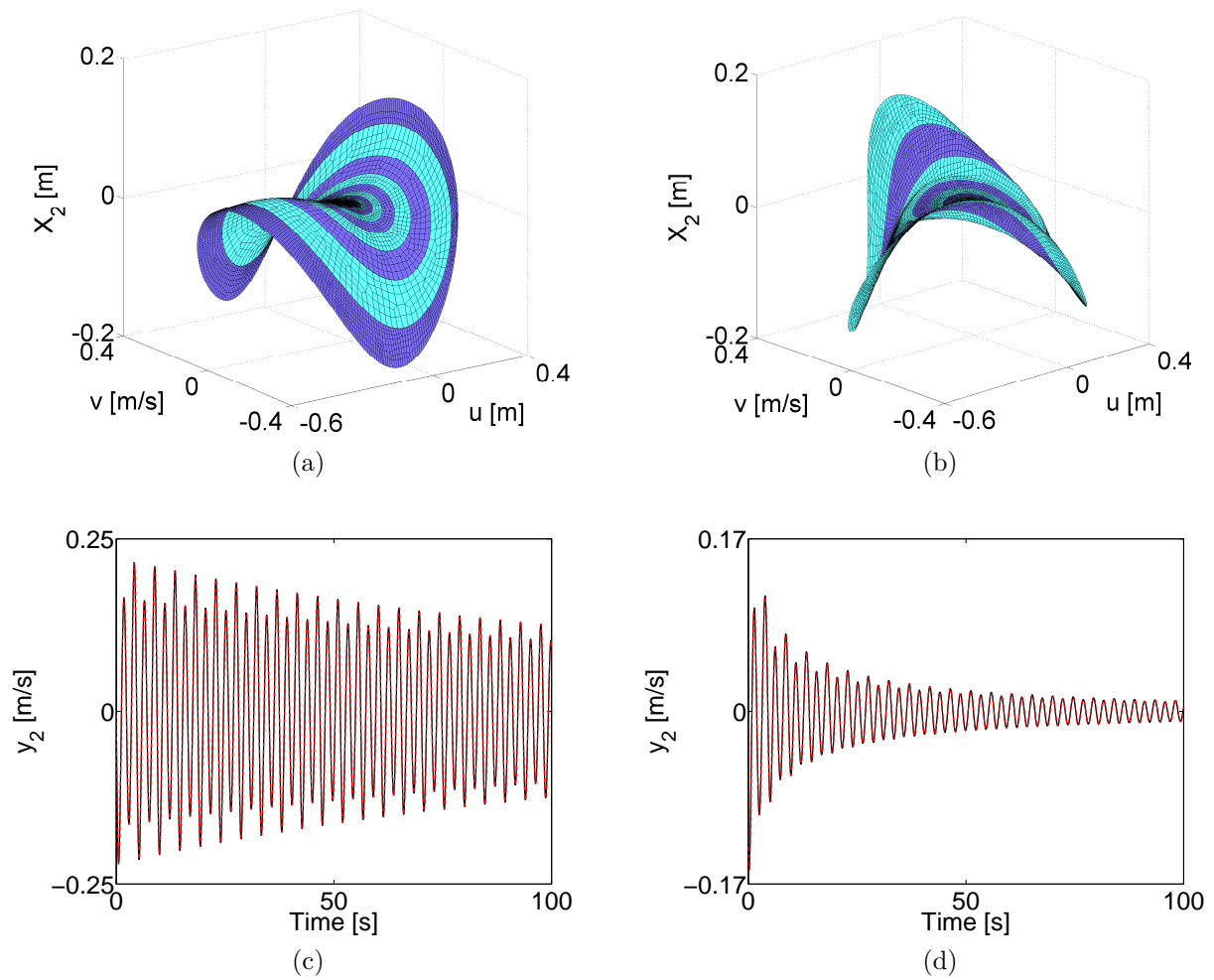


Figure 4.9: First NNM of the damped 2DOF system. (a, c)  $(\zeta_1, \zeta_2) = (0.001, 0.005)$ ; (b, d)  $(\zeta_1, \zeta_2) = (0.001, 0.2)$ . (c, d) Comparison between reduced- and full-system dynamics in black and red, respectively.

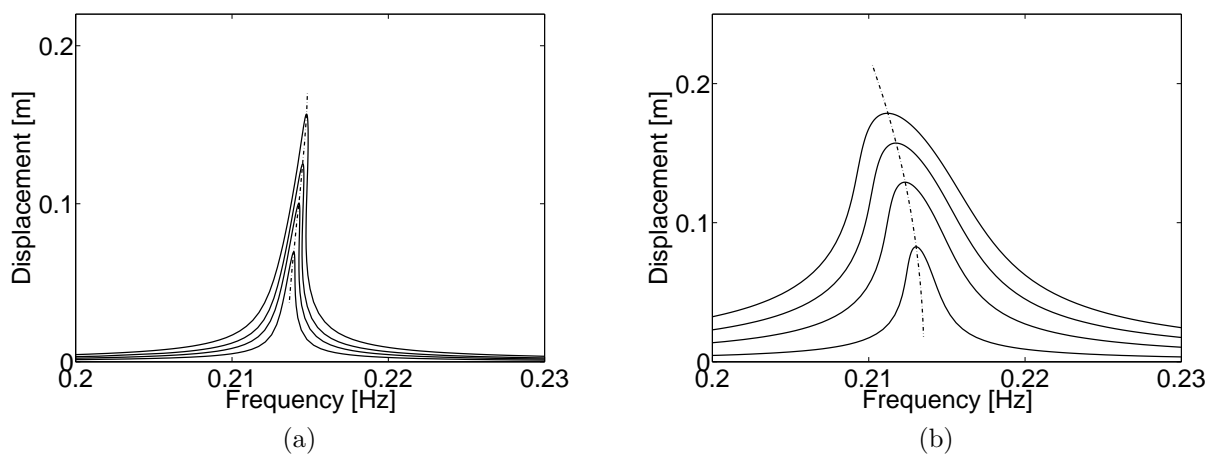


Figure 4.10: Frequency response of the damped 2DOF system to harmonic forcing. (a)  $(\zeta_1, \zeta_2) = (0.001, 0.005)$ ; (b)  $(\zeta_1, \zeta_2) = (0.001, 0.2)$ . Solid line: numerical continuation; dashed line: backbone curves extracted from damped NNMs.

### 4.3 Cantilever Beam With Nonlinear Boundary Conditions

The algorithm is now validated using a higher-dimensional system, a cantilever steel beam with a cubic spring attached at its tip (see Figure 4.11). The nonlinear stiffness coefficient equals to  $10^9 \text{ N/m}^3$ . The beam is discretized using 10 linear beam elements resulting in a system of 20 second-order ODEs.

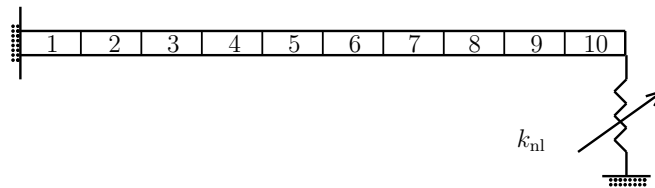


Figure 4.11: Nonlinear beam: length =  $0.7 \text{ [m]}$ , width =  $0.014 \text{ [m]}$ , height =  $0.014 \text{ [m]}$ ,  $k_{nl} = 10^9 \text{ N/m}^3$ .

#### 4.3.1 Conservative Case

The 38 unknown, coupled PDEs are solved by considering the displacement and velocity of the first beam element as master coordinates. Figure 4.12(a) represents the invariant manifold of the second NNM for the constraint relation  $Y_8(u_1, v_1)$ . Overall, this represents a very large problem with 334.400 nodal unknowns ( $38 \times 8.800$  nodes). However, thanks to the partition in annular domains, only ten minutes were needed for the computation of the first eight domains. Due to the folding of the manifold at higher energies, it took 20 minutes for the last two annular domains. For this example, the growing strategy is even more important than in the 2DOF example. Indeed, the algorithm cannot converge on a global mesh because the initial guess of the iso-energy boundary and of the solution (i.e., the LNM) are too far from the actual solution. Numerical experimentation also demonstrated that, as the number of degrees of freedom of the mechanical system increases, the most effective approach to compute the NNM is to use small annular domains combined with a small number of finite elements. However, a sufficient number of element is required to allow convergence up to the desired accuracy *tol*.

As confirmed in Figure 4.12(b), the manifold computed by the FE method is in excellent agreement with that computed using numerical continuation. Figure 4.13(a) compares the reduced and full-system dynamics for the point depicted by a red marker in Figure 4.13(b); the NMSE is  $10^{-2}\%$ . One notes the presence of a very strong third harmonic component, which is the sign of a strongly nonlinear regime of motion.

Figure 4.12(c) depicts the invariant manifold computed for larger energies using numerical continuation. The manifold starts to fold and appears to intersect itself but this can be explained by the fact that it is embedded in the full phase space. As mentioned in

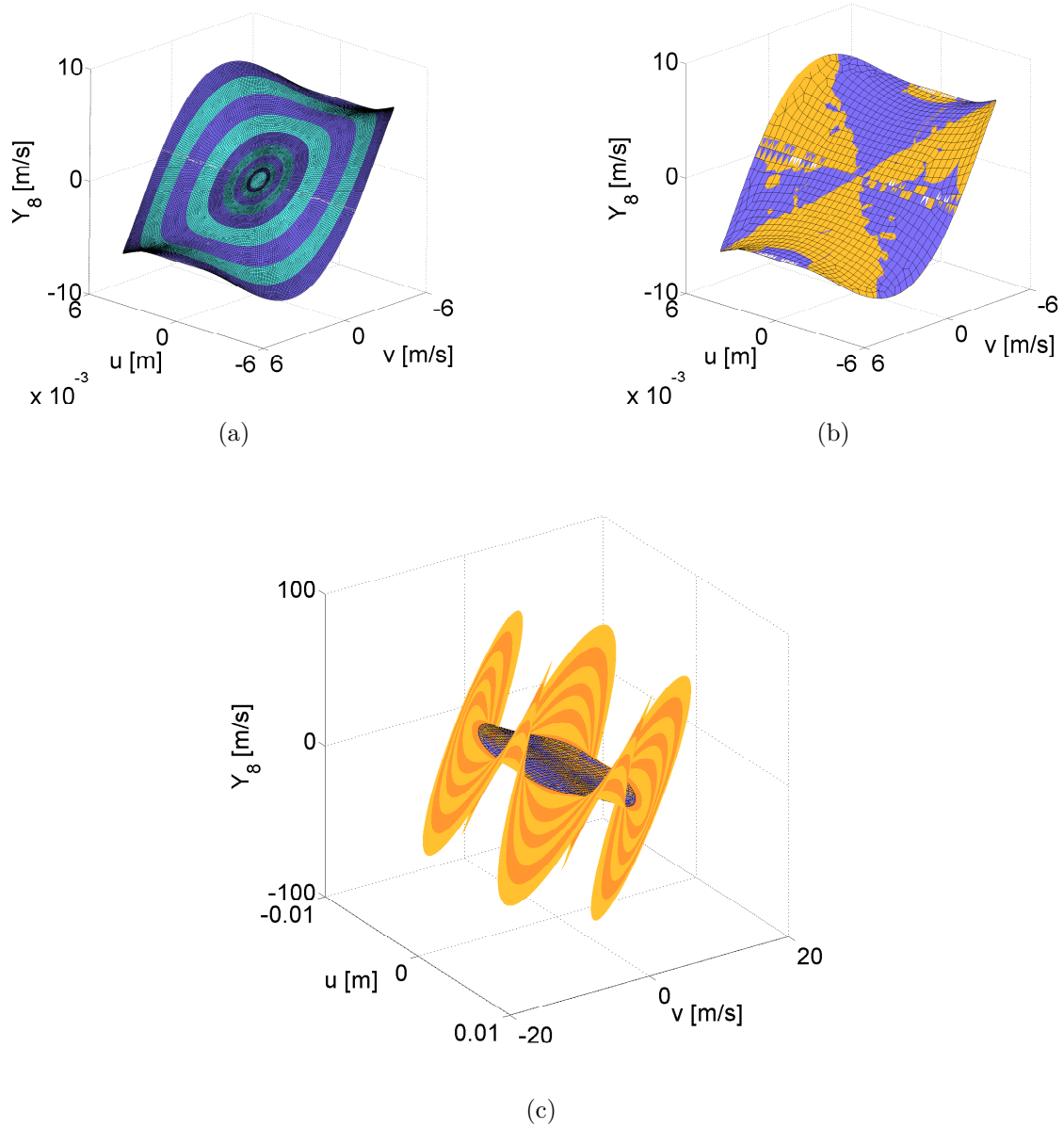


Figure 4.12: Second bending mode of the nonlinear beam. (a) Invariant manifold  $Y_8$  in phase space with the different annular domains; (b) invariant manifold  $Y_8$  in phase space (blue: FE method, orange: numerical continuation). For clarity, only 1.212 nodes out of the 8.800 used for the computation are represented. (c) Invariant manifold computed for larger energies (blue: FE method, orange: numerical continuation).

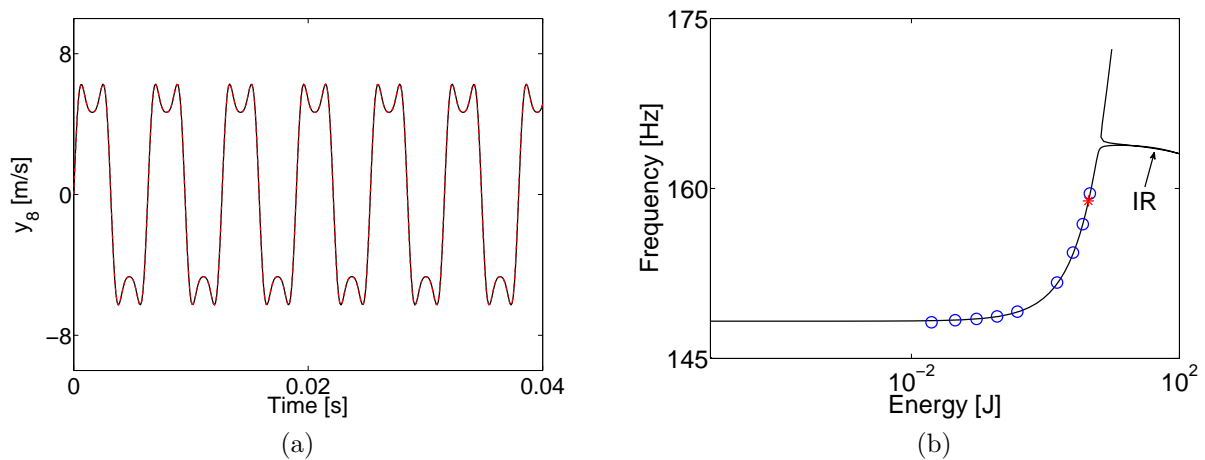


Figure 4.13: Second bending mode of the nonlinear beam. (a) Comparison between reduced- and full-system dynamics in black and red, respectively; (b) FEP (blue circles: FE method, black line: numerical continuation).

[13, 16, 66, 124], this folding often arises when a nonlinear coupling, i.e., an internal resonance, between two NNMs exists, but it can also occur in the presence of localization or multiple fixed points. The FEP of Figure 4.13(b) shows that a tongue of internal resonance indeed appears for high energies. This highlights one intrinsic limitation of the two-dimensional explicit parameterization of the dynamics, which cannot deal with folding of the manifolds. However, as shown in Figure 4.12(c), our method managed to get very close to this theoretical limit. To circumvent this issue, Shaw and Pierre introduced multi-modal NNMs where the invariant manifold is described by multiple pairs of master variables [16, 66, 124]. This generalization is not considered in this thesis, but an alternative is explored in Chapter 6. Note that all the results presented in this chapter are computed up to the limits of the parameterization.

In the FE method, we remark that a typical sign of the parameterization failure is the derivatives of constraint relations which become large, and the Jacobian matrix of the Newton-Raphson scheme that becomes badly conditioned (due to the presence of large-value elements).

### 4.3.2 Nonconservative Case

Proportional damping with  $\mathbf{C} = \alpha\mathbf{M} + \beta\mathbf{K}$  where  $\alpha = 5$  and  $\beta = 5 \times 10^{-6}$  is introduced in the cantilever beam example. The (linear) damping ratio for the first mode is 1%. The slave velocity  $Y_{19}$  obtained for this damped system is displayed in Figure 4.14(a). In the presence of damping, no reference manifold computed using a well-established method exists, and results validation relies on time integration. Figure 4.14(b) compares the

reduced and full dynamics. They agree very well with an NMSE value of  $7 \times 10^{-3}\%$ . Figure 4.14(c) examines the invariant manifold computed for the undamped (blue) and lightly damped (orange) cases. First, both surfaces appear identical. It is explained by the proportional character of the damping which does not modify the LNM underlying the NNM. Only the dynamics on the invariant manifold is modified whereas its geometry is unchanged. Second, it appears that the presence of damping has slightly shortened the region where the manifold parameterization is valid. The manifold was therefore computed in a smaller domain.

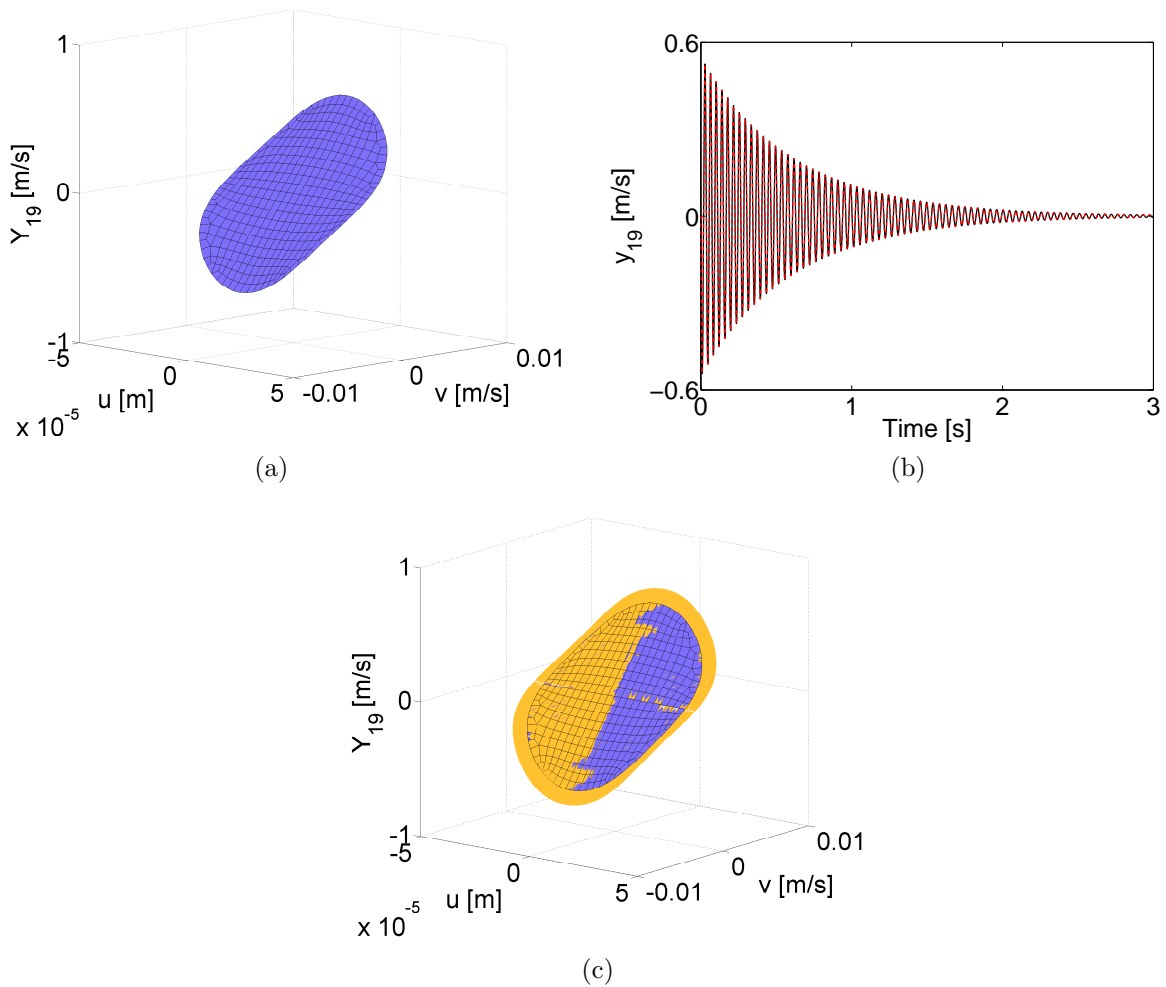


Figure 4.14: First NNM of the nonconservative nonlinear beam. (a) Invariant manifold  $Y_{19}$ ; (b) comparison between reduced- and full-system dynamics in black and red, respectively; (c) comparison between the invariant manifold  $Y_{19}$  for the damped (blue) and undamped (orange) systems.

## 4.4 Two Coupled Van Der Pol Oscillators

A system of two coupled Van der Pol oscillators is now considered for demonstrating the method in the presence of nonlinear damping. This example was already presented by Bellizzi et al. in [9]. The equations of motion are

$$\begin{aligned}\ddot{x}_1 + c_{11}\dot{x}_1 + c_{12}\dot{x}_2 - \epsilon_1 \left(1 - x_1^2 - \delta_1 x_2^2\right) \dot{x}_1 + x_1 &= 0, \\ \ddot{x}_2 + c_{21}\dot{x}_1 + c_{22}\dot{x}_2 - \epsilon_2 \left(1 - x_2^2 - \delta_2 x_1^2\right) \dot{x}_2 + 4x_2 &= 0,\end{aligned}\tag{4.2}$$

where  $c_{11} = c_{22} = 0$ ,  $c_{12} = -c_{21} = 0.8$ ,  $\epsilon_1 = \epsilon_2 = 0.5$ ,  $\delta_1 = \delta_2 = 1$ . Gathering together all the linear velocity-dependent terms, it appears that the linear damping matrix possesses a skew-symmetric contribution which is thus conservative. This gyroscopic-like term is accounted for in the definition of the energy of the system, and the algorithm is simultaneously generalized to handle such cases.

Figures 4.15(a, b) show the slave coordinates  $X_2$  and  $Y_2$  associated with the first NNM, respectively. This NNM was computed in 4 minutes with 19 annular domains. The dynamics on the NNM is validated in Figure 4.15(c) using  $(u, v) = (0.1, 0)$  as initial conditions. The agreement with respect to the full-system dynamics is excellent with a NMSE  $\approx 10^{-5}\%$ . Due to the negative linear damping present for low-amplitude oscillations, the displacement  $x_2(t)$  increases with time. As the (positive) nonlinear damping terms come into play, negative and positive damping contributions counterbalance each other, and  $x_2(t)$  describes a periodic solution. This periodic solution, also called limit cycle oscillation (LCO), is traced in Figure 4.15(d) using initial condition on either side. The observation of LCO using NNMs was reported in, e.g., [42, 163].

The second NNM is investigated in Figures 4.16. Similarly to the first NNM, the manifold was computed using 19 domains but a larger number of elements per domain was however needed. This leads to a total computational time of 10 minutes. Figures 4.16(a) and (b) show the slave displacement  $X_2$  and velocity  $Y_2$ , respectively. While the surface describing  $X_2$  is only slightly deformed, the surface for  $Y_2$  presents clear deformations inside the domain. The study of the dynamics for this second NNM also reveals, as for the first NNM, the presence of a LCO (not represented). Figures 4.16(c) and (d) compare the reduced- and full-system dynamics for initial conditions on either side of this LCO. At the beginning of the time series, an excellent agreement is observed. However, after about forty seconds and owing to the unstable character of the LCO, the small numerical errors rapidly grow and the dynamics leaves the region of the manifold. Interestingly, after that the dynamics escapes from the LCO, a transient regime of motion is observed during about another forty second. Then, the dynamics reaches a steady-state solution of constant frequency and amplitude (after about  $t = 80$  s). For illustration, the time series of Figure 4.16(c) is plotted in the  $(x_1, y_1, x_2)$  space in Figure 4.17. The trajectory is colored according to the time elapsed with dark blue for  $t = 0$  s and red for  $t = 100$  s. The figure clearly shows that the steady-state response observed after 80 seconds corresponds to the stable LCO captured by the first NNM.

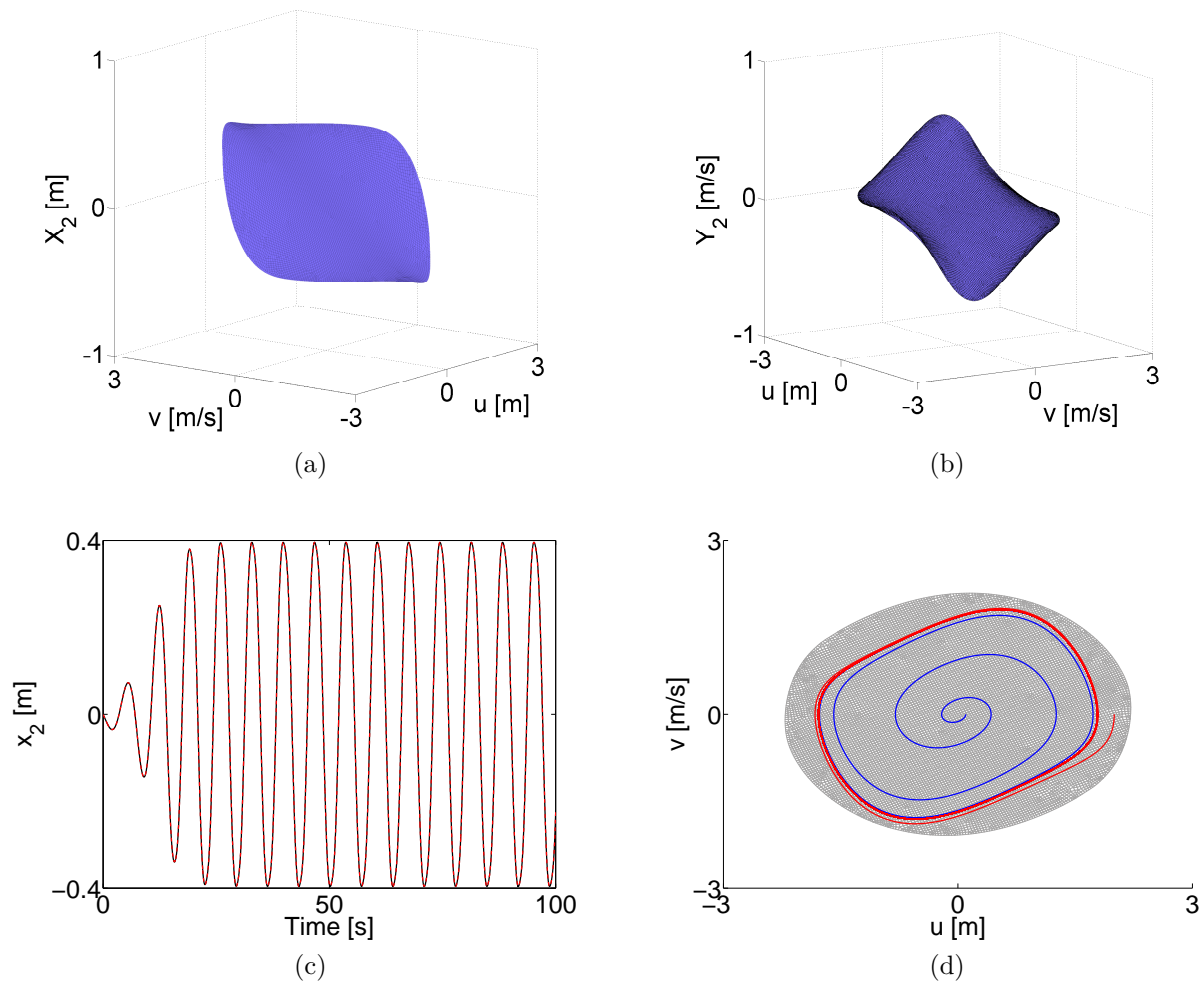


Figure 4.15: First NNM of the system of two coupled Van der Pol oscillators. (a, b) Invariant manifold  $X_2$  and  $Y_2$ . (c) Comparison between reduced- and full-system dynamics in black and red, respectively.  $\text{NMSE} \approx 10^{-5}\%$ . (d) Projection of the dynamics onto the  $(x_1, y_1)$  plane for initial conditions on either sides of the limit cycle.

Finally, a shooting algorithm (cf. Chapter 1) was used to accurately capture the initial conditions and periods of the detected LCOs. The periods are 6.9 s and 2.9 s for the LCOs on the first and second NNM, respectively. The sensitivity analysis included in the shooting procedure also confirmed the stable (resp. unstable) character of the LCO on the first (resp. second) NNM. Note that a larger number of elements was needed to accurately capture the LCOs.

Clearly, this example shows that NNMs can not only reduce the dynamics of the system on SDOF oscillators, but can also capture particular steady state solutions (LCO), allowing thus to interpret the transient dynamics of the system.

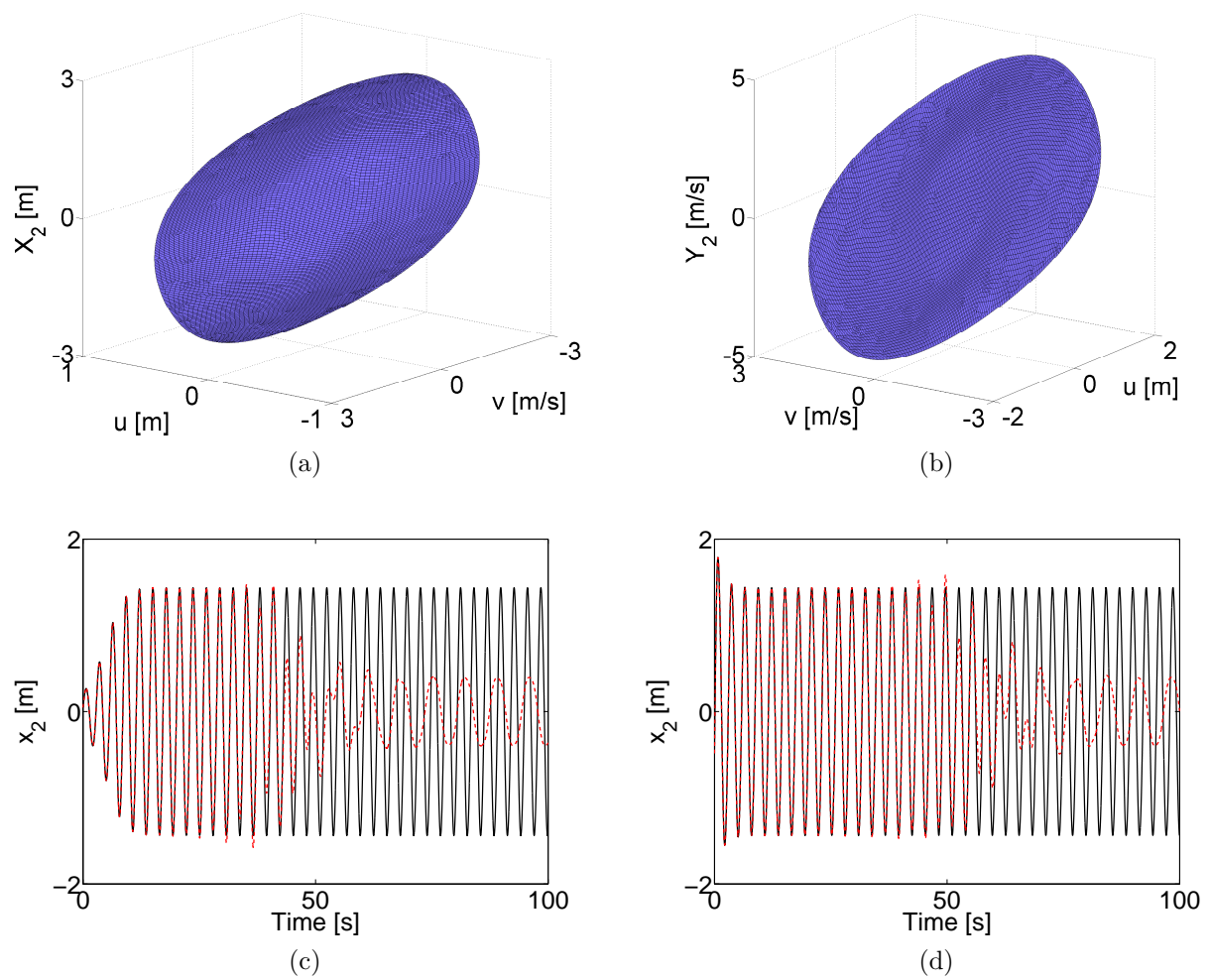


Figure 4.16: Second NNM of the system of two coupled Van der Pol oscillators. (a, b) Invariant manifold  $X_2$  and  $Y_2$ . (c, d) Comparison between reduced- and full-system dynamics in black and red, respectively. Initial conditions on either sides of the limit cycle.

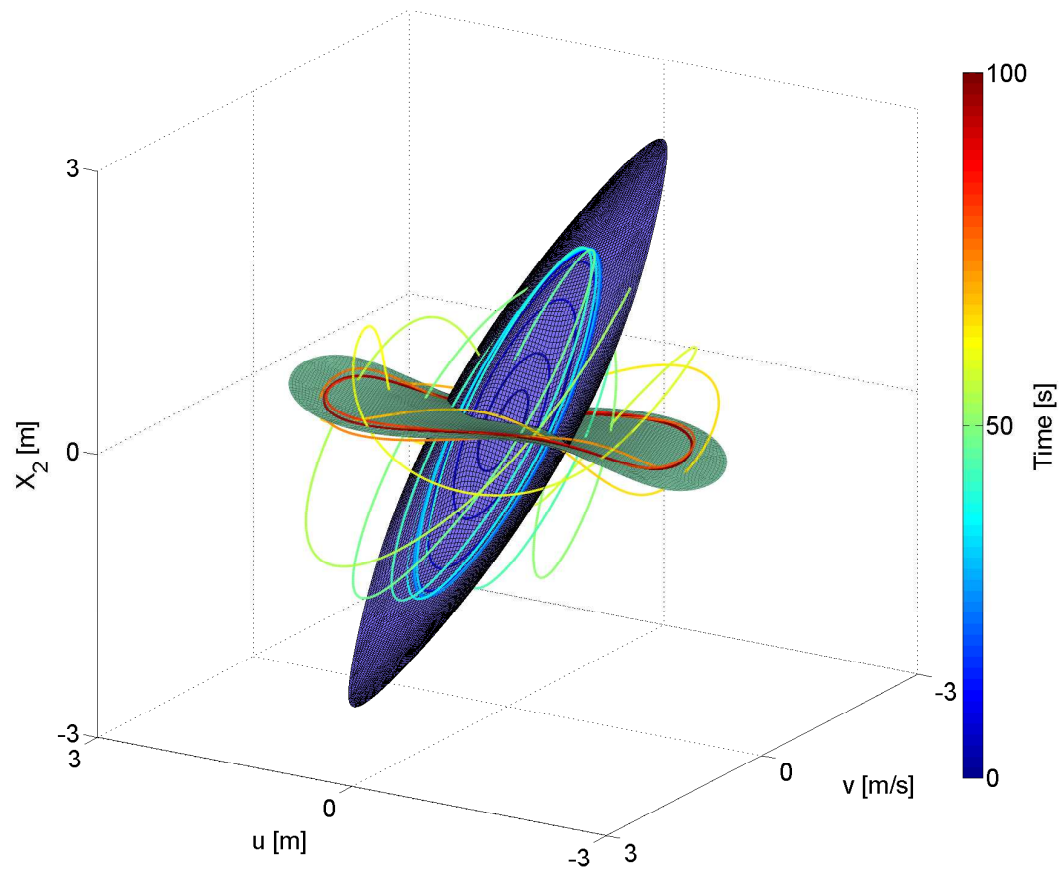


Figure 4.17: Invariant manifold  $X_2$  for the first (green) and second (blue) NNM. The time series of Figure 4.16(c) is represented with a curve whose color evolves from blue at  $t = 0$  s to red at  $t = 100$  s.

## 4.5 A Full-Scale Aircraft

As a final example, the numerical computation of the NNMs of a complex real-world structure, the Morane-Saulnier Paris aircraft, is addressed. A picture of the structure present in ONERA's laboratory (the French aerospace laboratory) was presented in Figure 3.1.

During ground vibration tests, nonlinear behaviors in the bolted connections between the wing and the external fuel tanks located at wing tips were reported [119]. A photograph of these connections is given in Figure 4.18. Based on experimental time series obtained with a swept sine excitation, the restoring force surface (RFS) method was applied to characterize the nonlinearities. As it is frequently reported in the literature [15, 43, 48, 61, 129], the bolted connections introduce a softening behavior. Accordingly, each connection was modeled using a vertical cubic spring defined between the nodes on either side of the connection, and whose coefficients were approximated as  $k_{nl} = -10^{13} \text{N/m}^3$ . We refer to [74, 119] for further details about this model.

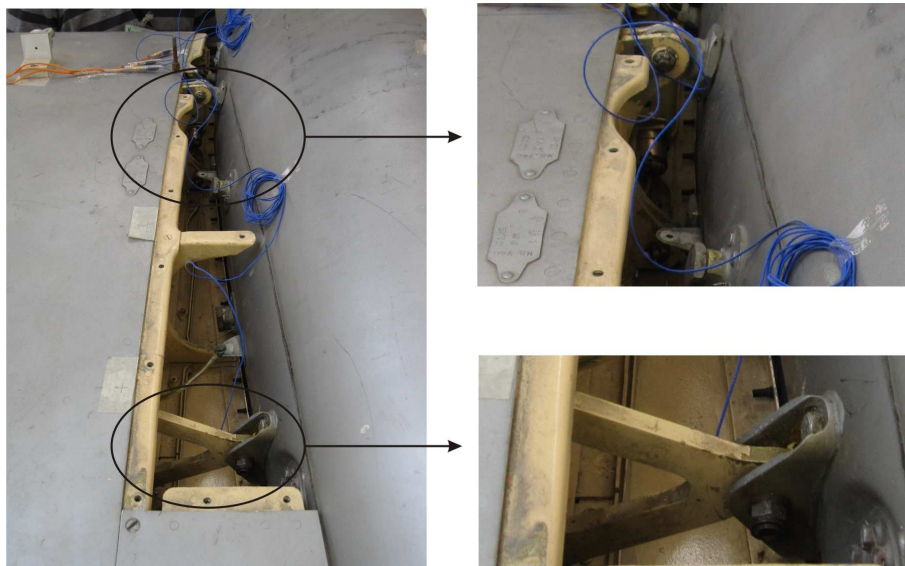


Figure 4.18: Bolted connections between the external fuel tanks and the wing tips. (a) Top view; (b) close-up of front and (c) rear attachments.

The linear finite element model of the full-scale aircraft is illustrated in Figure 4.19(a). Originally created in the Nastran software, it contains more than 80,000 DOFs. It was converted and exploited in the LMS-SAMTECH SAMCEF software in [119]. Although the complete model provides a detailed geometry of the structure, an accurate reproduction of its dynamical behavior in the 0 – 100 Hz frequency range of interest can be obtained with a lower-dimensional model. Therefore, similarly to the SmallSat application of Chapter 2 and because the nonlinearities are spatially localized, the Craig-Bampton method [7] is used for reducing the linear components of the model. The reduced-order model (ROM)

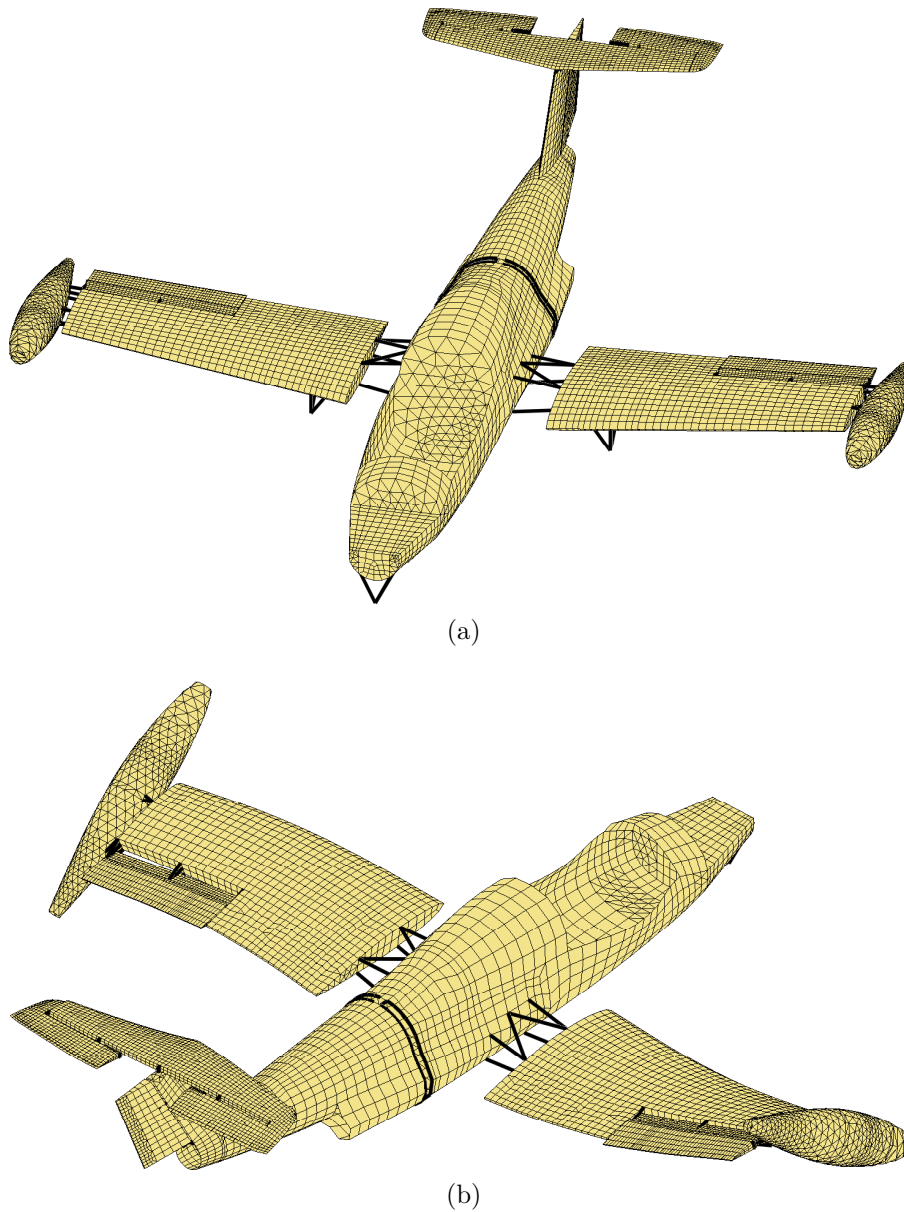


Figure 4.19: Morane-Saulnier 760. (a) Finite element model; (b) antisymmetric wing-torsion LNM.

considered herein includes one node on either side of the bolted connections and a total of 100 internal LNMs. The resulting ROM comprises 124 DOFs: 3 translations per retained node and 1 per internal mode. It is generated using the SAMCEF software and next imported in the MATLAB environment.

The investigation of the conservative model in [74, 119] showed that only the modes

including a motion of the wing were affected by the nonlinearities. The present study focuses on the first antisymmetric torsion mode of the wing (at  $\approx 34$  Hz) which is strongly affected due to important relative displacements at the connections (see the illustration of the mode in Figure 4.19(b)). Targeting the computation of NNMs for nonconservative systems, linear proportional damping is introduced into the model. The linear damping matrix  $\mathbf{C}$  is given by the relation  $\mathbf{C} = \alpha\mathbf{M} + \beta\mathbf{K}$  where  $\alpha$  and  $\beta$  were determined so as to have 0.5% of damping on the mode of interest. This value is arbitrary since no experimental identification of the damping was carried out. However, the value remains realistic for aerospace applications.

Figure 4.20 presents the first antisymmetric torsion mode of the aircraft. The different annular regions computed by the algorithm are presented in Figure 4.20(a) for the slave velocity  $Y_{56}$ . Close to the origin, the surface is flat, an indication of a linear regime of motion. Then, the surface deforms and becomes almost vertical over a single annular region. This observation is also confirmed by the slave velocity coordinate  $Y_{124}$  presented in Figure 4.20(b). It turns out that the validity limit of the parameterization occurs for very low motion amplitudes with the consequence that the FEM algorithm could not progress further. The integration of the dynamics on the invariant manifold is presented in Figure 4.21. The presence of strong harmonics at the beginning of the time series indicates the strongly nonlinear character of the vibrations. These harmonics disappear as damping decreases the energy present in the system. The comparison of the reduced- and full-system dynamics over about 18 periods shows very good correlation with a NMSE of  $10^{-2}\%$ .

In conclusion, although the presented results are still very preliminary and would deserve more attention, they show that the proposed algorithm can address the computation of NNMs for large-scale structures.

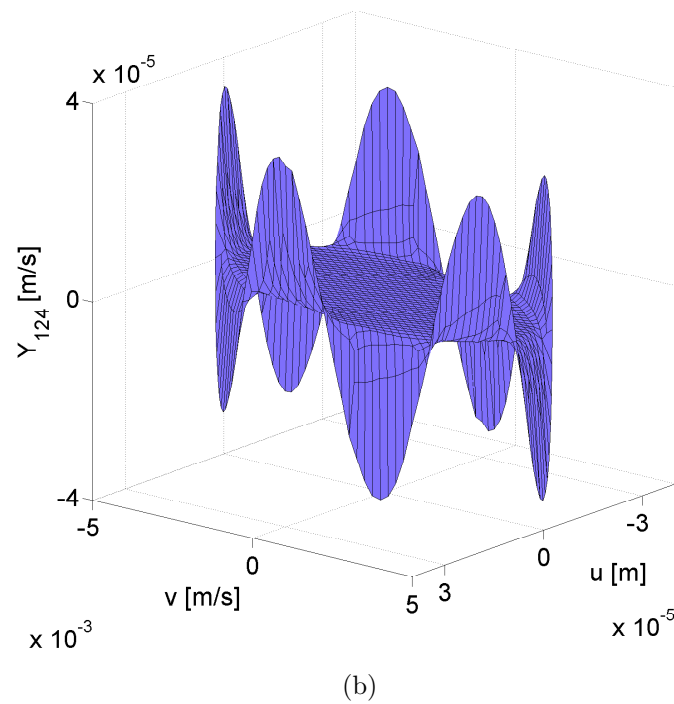
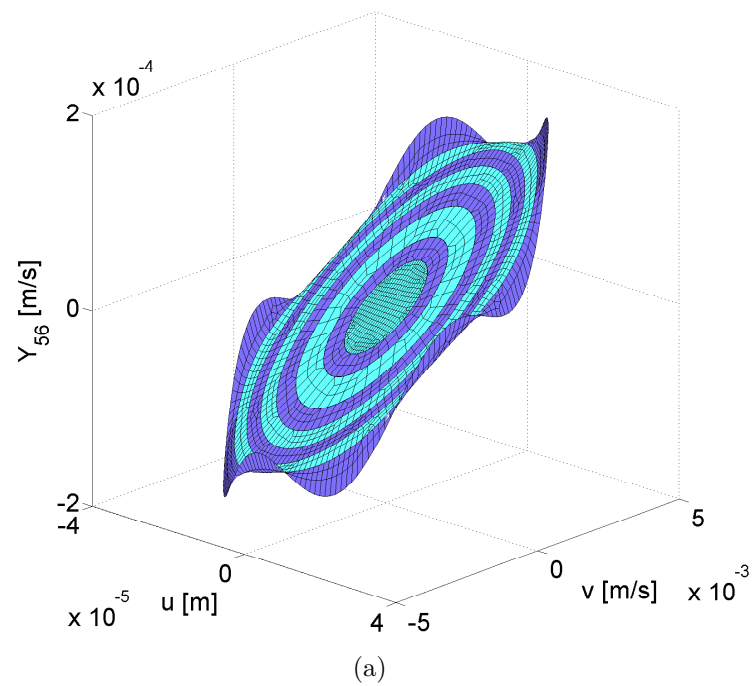


Figure 4.20: Antisymmetric wing-torsion NNM of the Paris Aircraft. (a) Slave velocity  $Y_{56}$  in phase space with the different annular domains; (b) slave velocity  $Y_{124}$  in phase space.

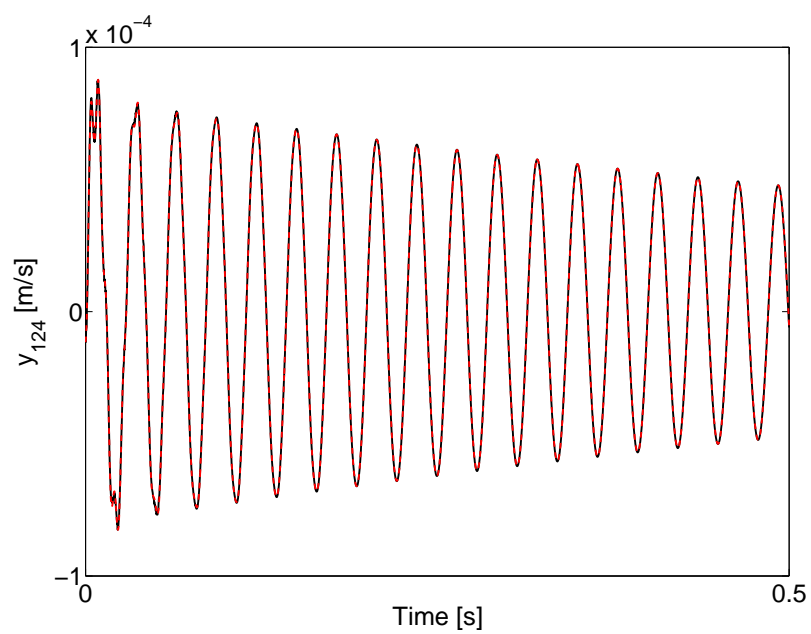


Figure 4.21: Validation of the results obtained for the antisymmetric torsion NNM of the Paris Aircraft. Comparison between reduced- and full-system dynamics in black and red, respectively.

## 4.6 Conclusions

In the present chapter, the algorithm developed in Chapter 3 was demonstrated using several examples. The annular resolution strategy proved to be effective and simultaneously applicable to conservative and nonconservative systems. For all examples, the method gave accurate results which, in addition, were not restricted to small-amplitude vibrations. Moreover, the method has several interesting features. First, thanks to the definition of the computational domain in terms of iso-energy curves, the computed solution is entirely available for time integration. Second, thanks to the recourse to shape functions, the dynamics on the invariant manifold results directly from the interpolation with finite element bases and thus perfectly reflects the geometric approximation of the invariant surface. In the conservative case, the frequency was estimated as a byproduct of the FE method using the boundary of the different annular domains.

Alike any other algorithm based on the PDEs of Shaw and Pierre, the method is inherently limited to the regions of phase space where the two-dimensional explicit parameterization of the manifold remains valid. The method cannot, for instance, handle internal resonances between the modes.

Besides the validation of our computational method, this chapter also showed that the concept of NNMs can play an important role for interpreting the dynamics of damped nonlinear systems. The 2DOF including quadratic and cubic stiffness demonstrated that damping can dramatically change the system's behavior, which cannot be inferred from conservative NNMs. The system with coupled Van der Pol oscillators also showed that NNMs can be used for capturing important dynamical phenomena such as LCOs and for understanding the transient dynamics.

# Chapter 5

## Application to More Complex Damping Models

---

### Abstract

This chapter investigates the computation of nonlinear normal modes for systems possessing more complex damping models, and, hence, more general flows. In this context, the need for a numerically-robust boundary of the annular domains of our finite-element-based method is discussed, and the recourse to Lyapunov functions is made. The new methodology is illustrated using a two-degree-of-freedom system with regularized friction.

---

## 5.1 Introduction

The finite-element-based method (FEM) developed in Chapter 3 was demonstrated on several examples possessing linear or nonlinear damping. However, damping arises from many physical mechanisms, and its description often requires more complex mathematical models than the polynomials considered in Chapter 4. One of the most important dissipation mechanisms in mechanical engineering is friction. Friction is present in virtually all mechanical systems encountered in practice as, e.g., bladed disks, bearings, brakes, joints, and, more generally, at the interfaces between structural components. Friction can play a significant role in the dynamical behavior of a structure and introduce, for instance, softening nonlinearity [90], bifurcations [47, 63, 142], and even chaos [46, 47]. Under some circumstances, friction can also generate dynamical instabilities [12].

Since Coulomb's original work in 1785 [30], the modeling of the friction mechanism led to numerous physical and phenomenological models which vary according to the micro- and macro-scale physics that is accounted for. Existing models can be classified in two categories, namely static and dynamic models. Static models define a direct relation between the friction force and the relative velocity. An example is the classical Coulomb friction model. Conversely, dynamic models relate the friction force and the relative velocity through an additional variable playing the role of memory. This internal variable is described by a differential equation. One of the first dynamic models is Dahl's model [31]. Since then, several other models were introduced as the LuGre [34], Dankowicz [32], and Bouc-Wen models [62]. A detailed discussion of these models is beyond the scope of the present thesis, and we refer to [3, 165] for further details.

In this chapter, we limit our investigations to the computation of nonlinear normal modes (NNMs) for a system including regularized Coulomb (RC) friction. Although the algorithm developed in Chapter 3 can account for damping, a slow convergence is observed. This issue is addressed in Section 5.2 where the methodology is generalized using domain boundaries defined as Lyapunov functions. The effectiveness of the novel algorithm is demonstrated in Section 5.3 using a two-degree-of-freedom (2DOF). The system is investigated for several parameter sets.

## 5.2 Lyapunov-Based Domains

### 5.2.1 A Case Study

The methodology proposed in Chapter 3 is now applied to a 2DOF system including RC friction. The governing equations of motion are

$$\begin{aligned} \ddot{x}_1 + (2x_1 - x_2) + F_{\max} \tanh(R\dot{x}_1) &= 0, \\ \ddot{x}_2 + (2x_2 - x_1) &= 0. \end{aligned} \tag{5.1}$$

As illustrated in Figure 5.1,  $F_{\max}$  defines the maximum friction force (at high velocity), and  $R$  determines the degree of regularization (i.e., the slope) introduced by the hyperbolic tangent function. The parameters considered are  $F_{\max} = 1.3$  N and  $R = 1$  rad.s/m.

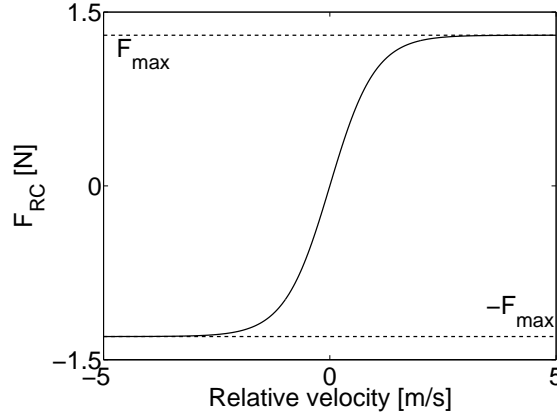


Figure 5.1: Restoring force for the RC friction:  $f_{RC}(x) = F_{\max} \tanh(Rx)$  with  $F_{\max} = 1.3$  N and  $R = 1$  rad.s/m.

The algorithm developed in Chapter 3 grows the invariant surface defining a NNM using successive annular regions whose boundaries are defined as iso-energy curves of the underlying conservative system. The basic idea is that the iso-energy curves should describe inflow boundaries so that the flow can be reversed and boundary conditions (BCs) imposed at inner boundaries. In the case of linear damping, we can demonstrate that this requirement is satisfied. Indeed, the time derivative of the total energy  $\mathcal{E}$  is given by

$$\dot{\mathcal{E}} = \frac{d}{dt} (\mathcal{K} + \mathcal{V}) = -\mathcal{D}. \quad (5.2)$$

where  $\mathcal{K}$  and  $\mathcal{V}$  are the kinetic and potential energies, respectively, and  $\mathcal{D}$  is Rayleigh's dissipation function [51]. This function is a nonnegative quantity as it takes the form

$$\mathcal{D} = \frac{1}{2} \dot{\mathbf{x}}^T \mathbf{C} \dot{\mathbf{x}} \quad (5.3)$$

where  $\mathbf{C}$  is the definite-positive linear damping matrix. Equation (5.2) guarantees that

$$\dot{\mathcal{E}} = \nabla \mathcal{E} \cdot \frac{d\mathbf{u}}{dt} < 0 \quad (5.4)$$

and thus the inflow character of the iso-energy boundaries. For (non-regularized) Coulomb friction, a similar demonstration is possible and was carried out, e.g., in [159]. Clearly, the choice of the energy to define domain boundaries is adequate. However, as it will be shown later, this definition is not necessarily optimal for the inflow.

Indeed, starting from the conservative case where the flow is tangent to the iso-energy boundary, the introduction of small damping still leads to regions where the flow is almost

tangent to the boundary. Small numerical “perturbations” as, for instance, boundary points that do not lie exactly on the same iso-energy curve, can thus turn a part of the boundary either into inflow or outflow. This is illustrated in Figure 5.2. The domain centered at the origin is the initial domain computed with an iso-energy curve. The flow of the equations for the first NNM of system (5.1) is represented by arrows with normalized amplitudes. Outflow regions are noticed around  $(u, v) = (-0.3, 0)$  and  $(u, v) = (0.3, 0)$ . As a result, the inner boundary of the next domain will contain both inflow and outflow regions. In the conservative case, this is not a problem because no BC is imposed when growing the manifold. Conversely, in the nonconservative case, the setting of BCs on the entire inner boundary can introduce numerical difficulties.

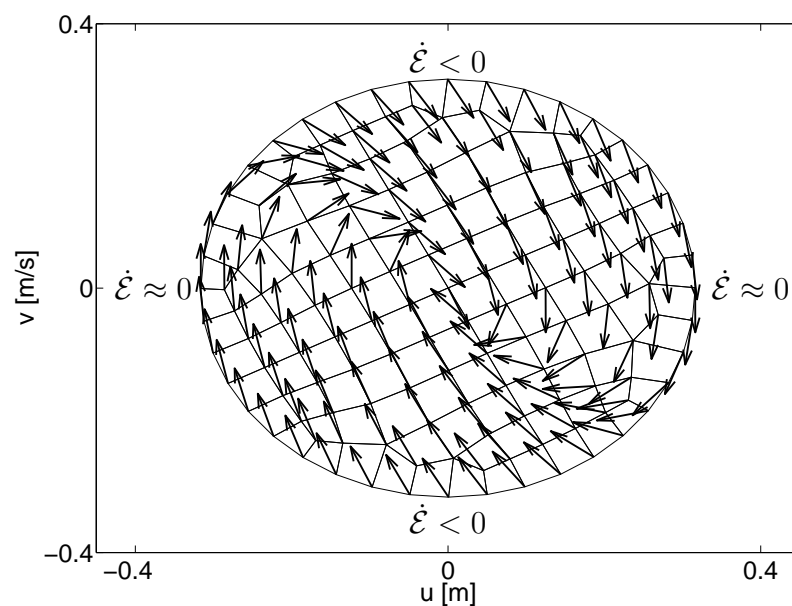


Figure 5.2: Flow of the equations of the 2DOF system (5.1) in a domain defined with an iso-energy boundary. For clarity, arrows are normalized.

For this example, the BC problem led to a slow convergence of the algorithm presented in Chapter 3. The computation of the first NNM required 18 annular domains for a total computational time of 60 minutes. On average, each annular domain required eight iterations of the Newton-Raphson algorithm whereas previous examples required only two or three iterations. Finally, in spite of the important computational resources that were used, the reduced dynamics presented a normalized mean-square error (NMSE) of only 0.5% with respect to the full-system dynamics.

To address this issue, the central idea is to find boundaries presenting more inflow so that the BCs remain always well-established. This chapter develops this idea through the definition of numerically robust domain boundaries. As we shall see, Lyapunov functions are particularly suited for this purpose.

## 5.2.2 Definition of New Domain Boundaries

To maximize inflow, a new boundary  $V(\mathbf{u})$  should be defined such that  $\dot{V} = \nabla V \cdot d\mathbf{u}/dt$  is as negative as possible. This problem bears strong resemblance with the definition of a Lyapunov function. A Lyapunov function  $V = V(\mathbf{u})$  is a scalar definite positive function:

$$V(\mathbf{0}) = 0, \quad (5.5)$$

$$V(\mathbf{u}) > 0 \quad \forall \mathbf{u} \neq \mathbf{0} \in X^0. \quad (5.6)$$

The compact and connected region  $X^0 \subset \mathbb{R}^2$  includes the equilibrium point of the system (here, the origin). The existence of a Lyapunov function for which

$$\dot{V} = \frac{dV}{dt} = \frac{dV}{d\mathbf{u}} \frac{d\mathbf{u}}{dt} = \nabla V \cdot \frac{d\mathbf{u}}{dt} < 0 \quad (5.7)$$

in the region  $X^0$ , guarantees the local asymptotic stability of the equilibrium.

The computational approach described below constructs such Lyapunov function automatically, allowing to define a domain boundary that is suitable for the problem at hand. In particular, the search for a this Lyapunov function targets large values of  $\gamma$ , a quantity treated as decay rate, in order to have  $\dot{V}$  strongly negative:  $\dot{V} \leq -\gamma V(\mathbf{u})$ . Figure 5.3 illustrates the domain obtained with the approach described herein. Clearly, the outflow regions noticed in Figure 5.2 have disappeared. One should also note that the function  $V$  is confined to the two-dimensional space of the master coordinates  $\mathbf{u}$ , regardless of the dimensionality of the mechanical system.

## 5.2.3 Computing Lyapunov Functions

In view of their interesting properties, there exist numerous techniques for computing a Lyapunov function (if there exists one) [53, 68, 69, 118]. In this thesis, the method proposed by Johansen in [68] is considered. The method is a priori applicable to generic, yet smooth, nonlinear systems. The problem of finding a Lyapunov function is regarded as an optimization problem including linear inequalities and can be solved effectively using quadratic programming.

### Parameterization of Lyapunov Function Candidates

The method considers a Lyapunov function candidate under the form:

$$V(\mathbf{u}) = \mathbf{u}^T \mathbf{P}(\mathbf{u}) \mathbf{u}, \quad (5.8)$$

where  $\mathbf{P}(\mathbf{u})$  is a matrix-valued function defined by the linear parameterization

$$\mathbf{P}(\mathbf{u}) = \sum_{i=1}^{N_L} \mathbf{P}_i \rho_i(\mathbf{u}) \quad (5.9)$$

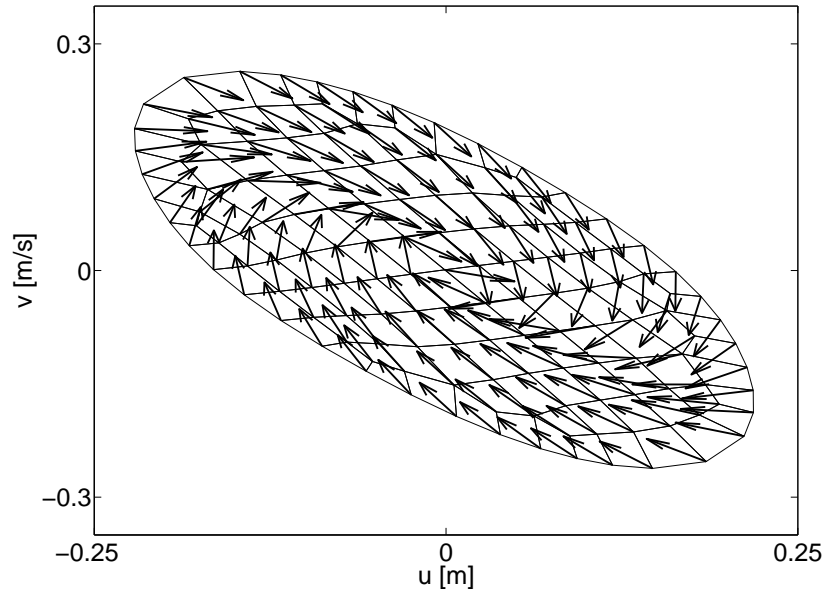


Figure 5.3: Flow of the equations of the 2DOF system (5.1) in a domain defined with a Lyapunov function. For clarity, arrows are normalized.

where the matrices  $\mathbf{P}_i$  contain the unknown parameters defining the Lyapunov function,  $N_L$  is the number of smooth basis functions  $\rho_i$  that form a partition of unity, i.e.,

$$\sum_i^{N_L} \rho_i(\mathbf{u}) = 1 \quad \forall \mathbf{u} \in X^0. \quad (5.10)$$

For our investigations, the normalized Gaussian basis functions are considered [68]. They are defined as

$$\rho_i(\mathbf{u}) = \frac{\mu_i(\mathbf{u})}{\sum_{j=1}^{N_L} \mu_j(\mathbf{u})}, \quad \mu_i(\mathbf{u}) = e^{-\frac{1}{2} \sum_{k=1}^2 (u_k - \bar{u}_{i,k})^2 / s_{i,k}^2}, \quad (5.11)$$

where the parameters  $\bar{u}_{i,k}$  and  $s_{i,k}$  define the position and the spread (or smoothness) of the basis function  $\rho_i$ , respectively.

### Linear Inequalities

By construction, the function  $V$  satisfies  $V(\mathbf{0}) = 0$ , but to be positive definite, the function has to verify  $V(\mathbf{u}) > 0$ . This condition is expressed using the (stricter) inequality

$$V(\mathbf{u}) \geq c_1 \|\mathbf{u}\|_2^2 \quad \forall \mathbf{u} \in X^0 \quad (5.12)$$

for some small  $c_1 > 0$ . Moreover, for  $V$  to be a Lyapunov function, its time derivative has to be negative. This condition on the function candidate writes

$$L(\mathbf{u}) \leq -\gamma V(\mathbf{u}) \quad (5.13)$$

for some  $\gamma > 0$ , where

$$L(\mathbf{u}) = \dot{V} = \frac{dV}{d\mathbf{u}}(\mathbf{u}) \frac{d\mathbf{u}}{dt}. \quad (5.14)$$

The derivative of the master coordinates is  $\frac{d\mathbf{u}}{dt} = (\dot{u}, \dot{v}) = (v, f_k)$  (cf. Section 1.4.2). Johansen proved that Equation (5.13) in conjunction with Equation (5.12) ensures that  $V$  is a Lyapunov function [68].

The derivative of  $V$  with respect to  $\mathbf{u}$  is determined using Equation (5.8), which gives:

$$\frac{dV}{d\mathbf{u}}(\mathbf{u}) = \sum_{i=1}^{N_L} \left( \mathbf{u}^T \mathbf{P}_i \mathbf{u} \frac{d\rho_i(\mathbf{u})}{d\mathbf{u}} + (\mathbf{P}_i^T \mathbf{u} + \mathbf{P}_i \mathbf{u}) \rho_i(\mathbf{u}) \right). \quad (5.15)$$

Although the inequalities are nonlinear in the coordinates  $\mathbf{u}$ , one notes that they are linear in the parameters  $P_i^{j,k}$ . Grouping the elements of the matrices  $\mathbf{P}_i$  in the vector  $\mathbf{p}$  as

$$\mathbf{p}^T = [P_1^{1,1}, P_1^{1,2}, P_1^{2,1}, P_1^{2,2}, \dots, P_{N_L}^{2,2}], \quad (5.16)$$

the inequalities (5.12) and (5.13) write

$$\begin{aligned} \mathbf{p}^T \mathbf{v}(\mathbf{u}) &\geq c_1 \|\mathbf{u}\|_2^2, \\ \mathbf{p}^T \mathbf{l}(\mathbf{u}) &\leq -\gamma \mathbf{p}^T \mathbf{v}(\mathbf{u}). \end{aligned} \quad (5.17)$$

where  $\mathbf{p}$  contains  $m = 4N_L$  elements and the functions  $\mathbf{v} : X^0 \rightarrow \mathbb{R}^m$  and  $\mathbf{l} : X^0 \rightarrow \mathbb{R}^m$  are determined from Equations (5.8) and (5.14), respectively.

Equations (5.17) must hold for every  $\mathbf{u}$  in  $X^0$  and represent thus an infinite set of linear inequalities. When discretizing the domain, this infinite set is reduced to a finite number of inequalities that write

$$\begin{aligned} \tilde{\mathbf{V}} \mathbf{p} &\geq \tilde{\mathbf{c}}, \\ (\tilde{\mathbf{L}} + \gamma \tilde{\mathbf{V}}) \mathbf{p} &\leq \mathbf{0}, \end{aligned} \quad (5.18)$$

where the rows of matrix  $\tilde{\mathbf{V}}$  correspond to  $\mathbf{v}^T(\mathbf{u})$  evaluated at each point discretizing  $X^0$ . Similarly, the elements of  $\tilde{\mathbf{c}}$  correspond to  $c_1 \|\mathbf{u}\|_2^2$ , and the rows of  $\tilde{\mathbf{L}}$  correspond to  $\mathbf{l}^T(\mathbf{u})$ .

## 5.2.4 The Modified Algorithm for NNM Computation

The strategy for solving the manifold-governing PDEs using annular domains defined with Lyapunov functions is schematically presented in Figure 5.4. The original algorithm

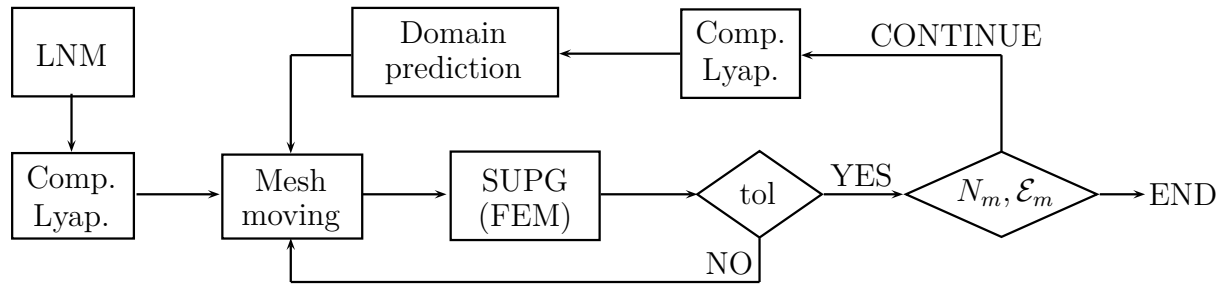


Figure 5.4: Schematics of the algorithm's resolution strategy including the computation of Lyapunov functions after the initial domain and before each domain prediction.

presented in Figure 3.3 requires only minor modifications. In particular, a Lyapunov-based domain boundary definition step (denoted *Comp. Lyap.*) is introduced after the computation of the initial domain from the linear normal mode (LNM) and after the convergence of the FE algorithm on an annular domain.

The first Lyapunov function is thus determined for the initial domain computed using the equations of motion linearized at the origin. The computational domain  $\Omega$  plays the role of  $X^0$  and its discretization into finite elements is considered for defining the finite set of inequalities. For the next domains, the set  $X^0$  is considered as the collection of previous domains  $\Omega$  in order to always include the origin in the problem.

In the case where inequalities (5.18) are impossible to satisfy, the parameter  $\gamma$  is decreased and the optimization problem is restarted. Conversely, if successful, an iterative procedure tries to maximize the decay rate by increasing  $\gamma$  (cf. Equation 5.13). Contrary to Chapter 3 where the shape of iso-energy curves is similar from one annular domain to the next, the Lyapunov functions may strongly vary. To guarantee the robustness of the subsequent mesh-moving and domain-prediction steps, the search for the Lyapunov function is combined with an objective function that aims at minimizing its complexity. To this end, the objective is formulated as [68]:

$$\phi(\mathbf{p}) = \sum_i^{N_L} \sum_l^{N_L} \sum_j^2 \sum_k^2 \left( P_i^{j,k} - P_l^{j,k} \right)^2 w_{i,l}. \quad (5.19)$$

The  $w_{i,l}$ 's represent weights that are considered, in the present case, equal to one for all  $(i, l)$ .  $\phi(\mathbf{p})$  can be written in quadratic form  $\phi(\mathbf{p}) = \mathbf{p}^T \mathbf{Q} \mathbf{p}$  where  $\mathbf{Q}$  is a definite positive matrix determined from Equation (5.19). The *quadprog* function of MATLAB is considered for minimizing  $\phi(\mathbf{p})$  under the constraints (5.18).

Once a Lyapunov function is available, the equations derived for the mesh-moving step in Section 3.3.2 and for the domain-prediction step in Section 3.3.4 remain applicable, replacing  $\mathcal{E}$  by  $V$ . In particular, to follow an iso-value of a Lyapunov function, each boundary node is moved to equal a reference value  $V^{\text{ref}}$  of the function. The corrections

$\Delta \mathbf{u}^n = [\Delta u^n \quad \Delta v^n]^T$  to the node  $n$  are calculated by solving

$$\Delta V^n = V^{\text{ref.}} - V^n = \left[ \frac{dV}{d\mathbf{u}} \right]^{nT} \Delta \mathbf{u}^n. \quad (5.20)$$

where  $V^n = V(\mathbf{u}^n)$ ,  $V^{\text{ref.}} = \inf_n \{V(\mathbf{u}^n)\}$  and where  $\frac{dV}{d\mathbf{u}}$  is given by Equation (5.15). The result of the mesh-moving procedure is illustrated with the evolution of the outer boundary presented in Figure 5.5. The initial domain is represented with a dashed line. Based on the flow in this domain, a Lyapunov function is computed and its level sets are represented by the color lines. After mesh moving, the new domain matches one of the level sets of the Lyapunov function (solid black line).

As the Lyapunov function changes from domain to domain, the domain-prediction step cannot rely on a prescribed increment in the Lyapunov function value. Contrary to Chapter 3, relative increments with respect to the maximum value of the current Lyapunov function are considered.

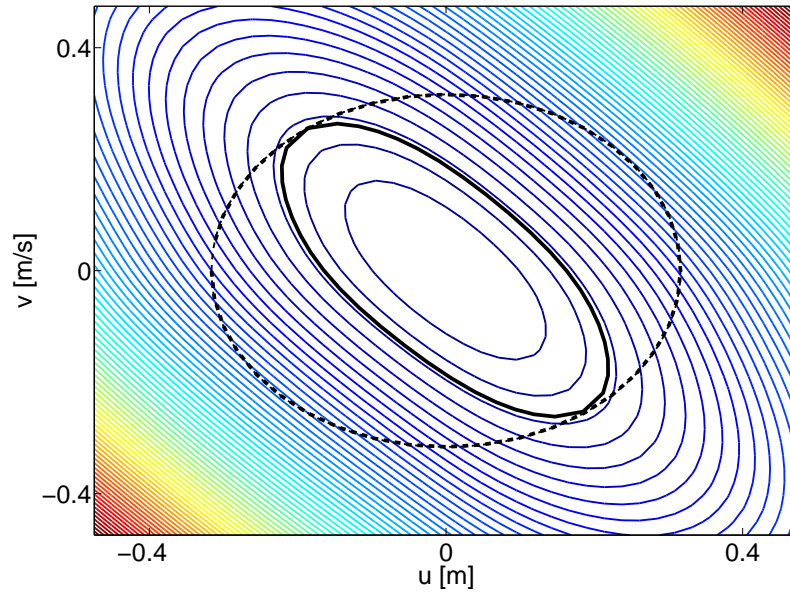


Figure 5.5: Novel approach for defining the domain boundary. (– –) Boundary defined using the equations of motion linearized at the origin; (–) final boundary that matches a iso-value of the Lyapunov function; (color lines) level sets of the Lyapunov function.

### 5.3 Revisiting the 2DOF System with Regularized Friction

The Lyapunov-based methodology is now applied to the 2DOF system (5.1) including RC friction. In a first step, the parameters  $F_{\max} = 1.3$  N and  $R = 1$  rad.s/m considered in Section 5.2.1 are used.

The computation of the in-phase NNM now requires seven annular regions for a total computational time of 6 minutes. This represents a significant improvement with respect to the previous computation time of 60 minutes. Each annular region is defined with a different Lyapunov function. Four basis functions  $\rho_i$  were considered ( $N_L = 4$ ), each of them centered at a constant distance  $r$  from the origin and equally distributed in  $\theta \in [0 - 2\pi]$ . The parameter  $c_1$  was considered equal to  $10^{-3}$ . The total cost of the procedure, i.e., the computation of the terms involved in the inequalities and the optimization problem, is typically 0.4 s for 10,000 points. The different boundaries obtained for this NNM are presented in Figure 5.6. The boundaries are different from each other, but they possess however a simple shape (as it was required during the optimization procedure). Overall, the boundaries form ellipses whose main axes are not horizontal.

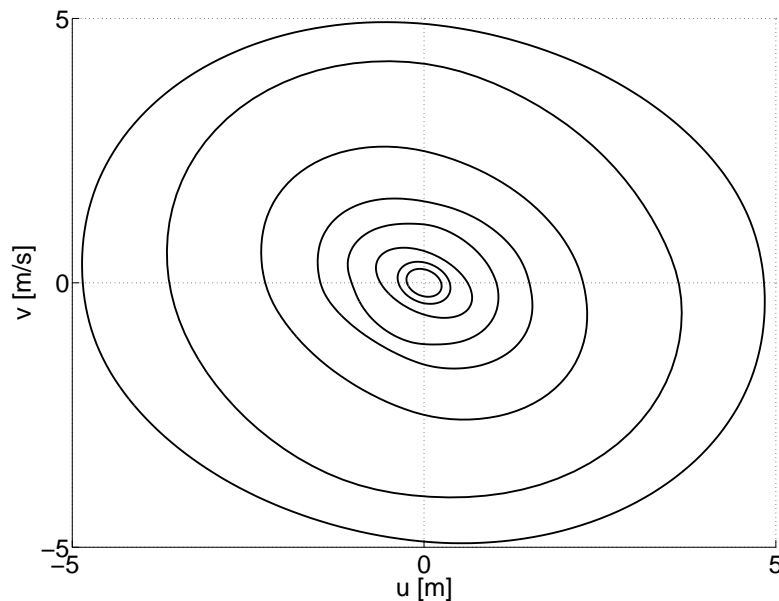


Figure 5.6: Domain boundaries which follow the different Lyapunov functions computed. System parameters are  $F_{max} = 1.3$  N and  $R = 1$  rad.s/m.

The slave velocity  $Y_1$  is illustrated in Figure 5.7(a). The manifold presents a wavy shape that strongly deviates from a flat surface. These effects are attributable to RC friction which is the only nonlinearity introduced into the system. The validation of the results

is presented in Figures 5.7(b) and (c) where the time series of slave coordinates  $x_1$  and  $y_1$  are depicted. Due to the strong character of the damping, only three oscillations are observed. The comparison between the reduced and full dynamics reveals an excellent agreement with a normalized mean-square error (NMSE) of  $9 \times 10^{-4}\%$ . This is a significant improvement with respect to the 0.5% obtained with the iso-energy domain.

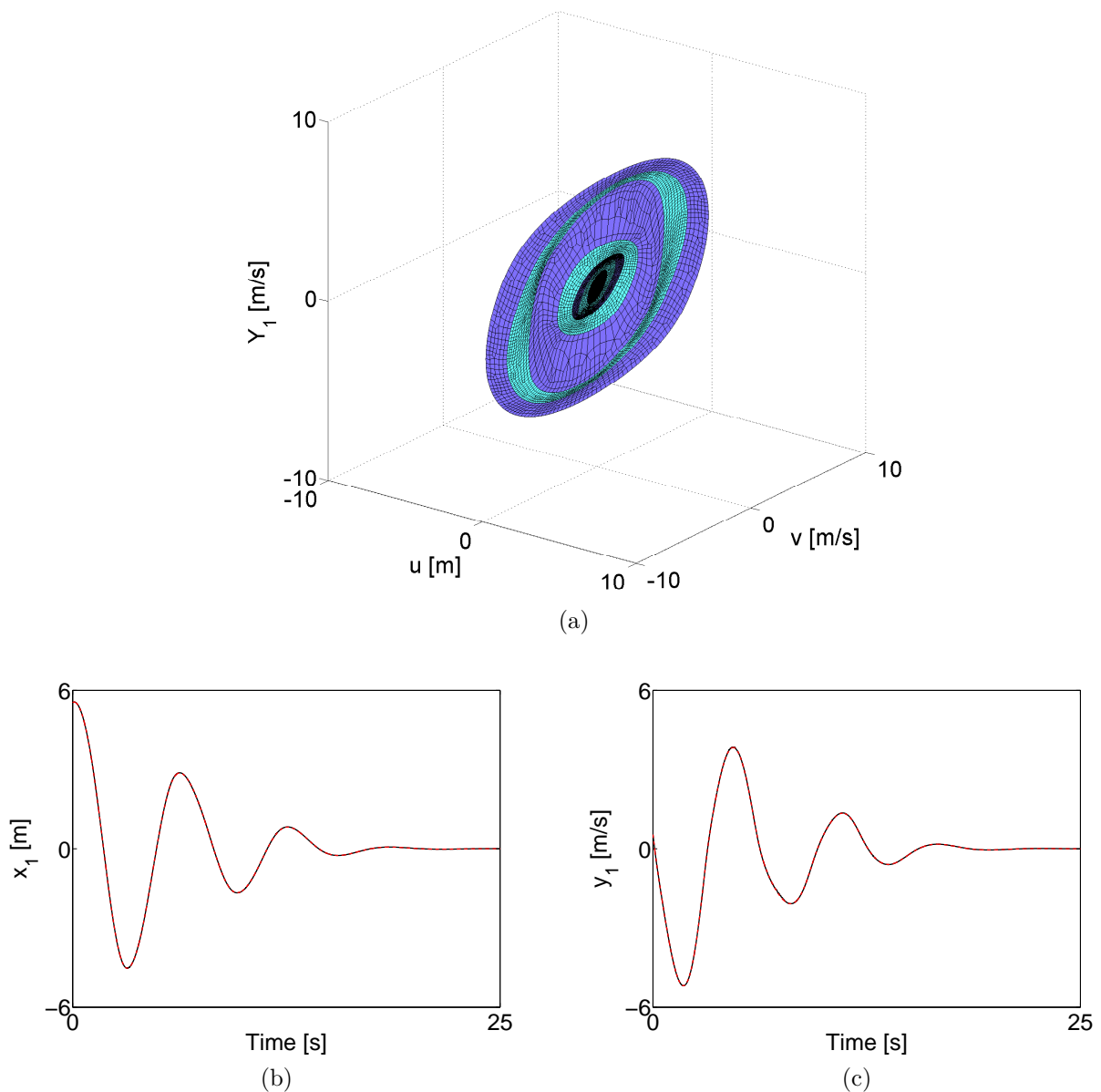


Figure 5.7: First NNM of the 2DOF system with RC. (a) Invariant surface computed for  $Y_1$  with seven annular domains; (b, c) comparison between reduced- and full-system dynamics in black and red for  $x_1$  and  $y_1$ , respectively.

The out-of-phase NNM of system (5.1) is presented in Figure 5.8. The 8 domains were computed by the algorithm in 9 minutes and are presented in Figure 5.8(a) for the slave displacement  $X_1$ . Overall, the manifold is less deformed than for the first NNM. The wavy shape is however clearly distinguished in Figure 5.8(b) where all the annular domains were grouped to form a single global mesh. The time series for the slave displacement  $x_1$  and slave velocity  $y_1$  are given in Figures 5.8(c) and (d), respectively. As more than ten oscillations are visible, the typical linear decay rate introduced by friction damping is noticeable. The validation of the dynamics reduced on the manifold indicates a NMSE value of  $7 \times 10^{-4}\%$  with respect to the full-system dynamics.

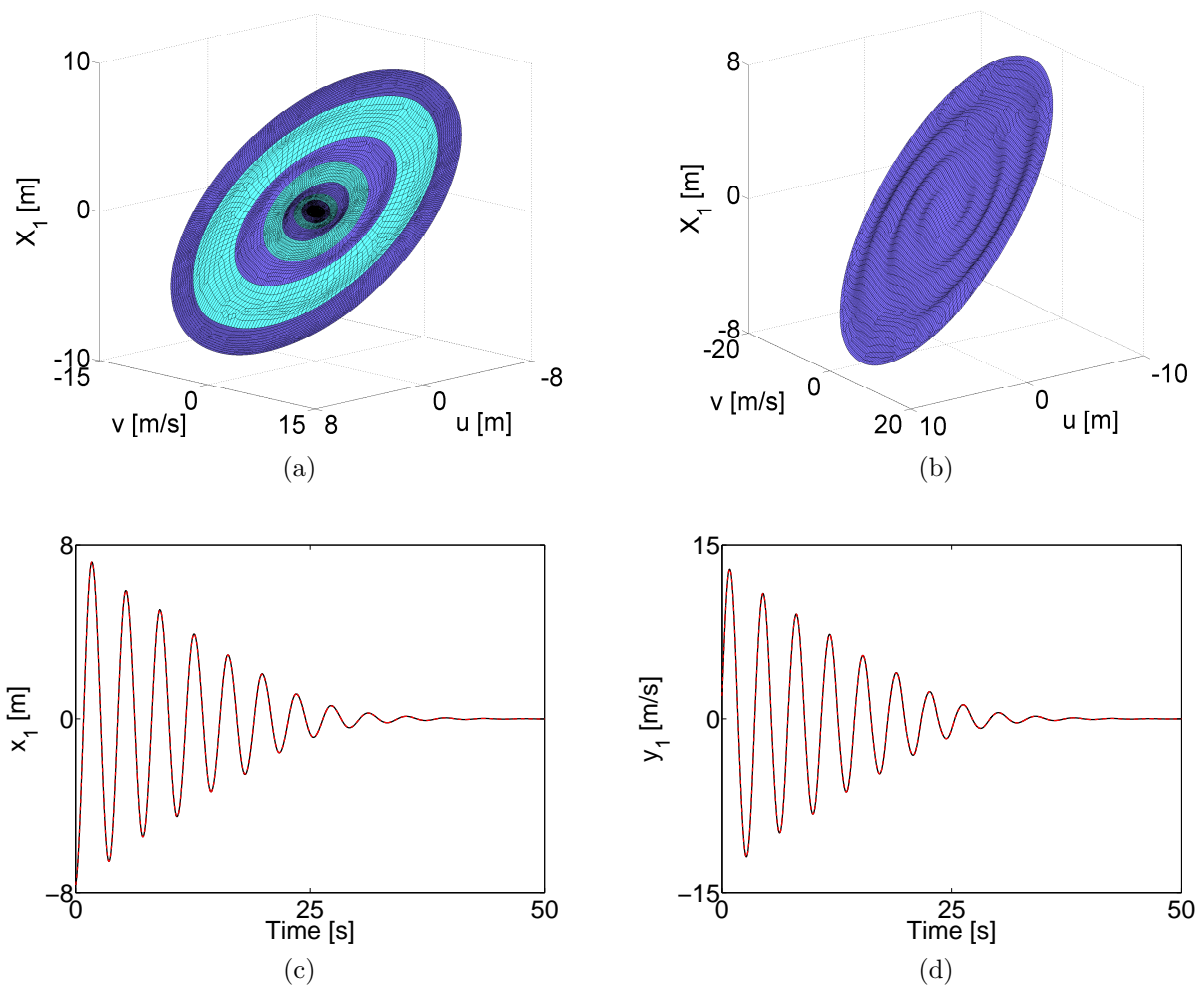


Figure 5.8: Second NNM of the 2DOF system with RC. (a) Invariant surface computed for  $Y_2$  with the annular domains; (b, c) comparison between reduced- and full-system dynamics in black and red for  $x_1$  and  $y_1$ , respectively.

Whereas the out-of-phase NNM can be computed for higher amplitudes, the computation of the first NNM was interrupted because the algorithm could not progress further. To

extract the frequency amplitude dependence over a very large range of amplitudes, the 2DOF system is now considered with a lower maximum friction force,  $F_{\max} = 1.0$  N. Figure 5.9 presents the frequency response of the 2DOF system for harmonic forcing of different amplitudes. At low vibration amplitudes, the nonlinear effects play a great role, and the resonance frequency strongly varies with motion amplitude. The first mode presents a softening behavior (as frequently reported in the literature [80, 89, 91]) whereas the second mode presents a hardening behavior. At higher vibration amplitudes, the resonance peaks narrow, and the resonance frequencies do no longer evolve. The region of maximum friction force is reached, and the nonlinearity introduced by the RC friction element does not play an important role, as it was the case for low amplitudes. Similarly to Chapter 4, the behavior along the backbone is a direct by-product of our method. After computing the invariant surfaces for both NNMs, the amplitude-frequency dependence of the oscillations is extracted from the time series integrated on the manifolds. The result is presented in Figure 5.9 using dashed-dotted lines. The NNMs accurately capture the system's backbones.

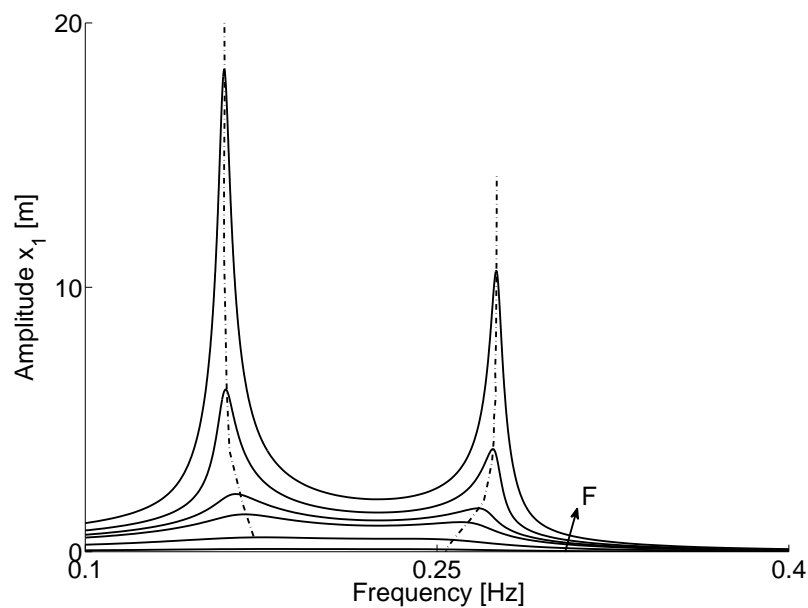


Figure 5.9: Response of the 2DOF system with RC friction to harmonic excitations with different amplitudes (–). Backbone curve traced by the NNMs (dashed - dotted line). System parameters are  $F_{\max} = 1$  N and  $R = 1$  rad.s/m.

As final example, the system is considered for a larger value of the maximum friction force, i.e.,  $F_{\max} = 1.5$  N. The in-phase NNM of the system was computed using 9 annular regions for a total computational time of 15 minutes. The annular domains obtained for the slave velocity  $Y_1$  are presented in Figure 5.10(a). Overall, the surface looks different from the reference case  $F_{\max} = 1.3$  N, and, in particular, the wavy shape is no longer

present. This observation will find an explanation in Chapter 6. Finally, the dynamics on the invariant surface is computed and compared to the full-system dynamics. The two time series of the velocity  $y_1(t)$  are presented in Figure 5.10(b). Their NMSE is  $5 \times 10^{-5}\%$ . For the last annular domain, the surface becomes almost vertical in the zero-displacement high-velocity regions, which indicates a failure of the parameterization. Due to this folding, it is not possible to choose high-amplitude initial conditions and to observe more oscillations. This observation will also be confirmed in Chapter 6.

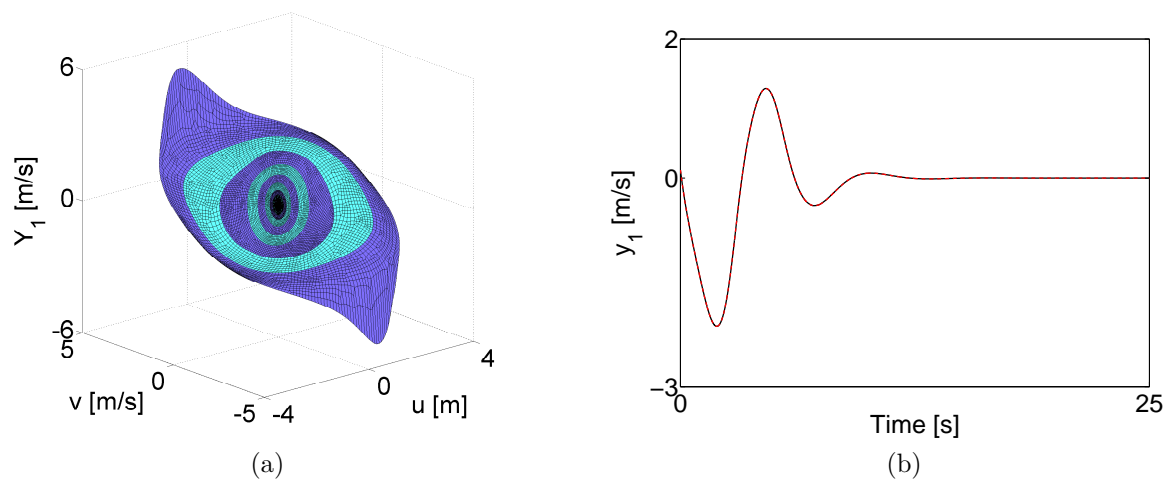


Figure 5.10: In-phase NNM of the 2DOF system with RC. Parameters  $F_{\max} = 1.5$  N and  $R = 1$  rad.s/m. (a) Invariant surface computed for  $Y_1$  with the annular domains; (b) comparison between reduced- and full-system dynamics in black and red, respectively.

## 5.4 Conclusions

This chapter has revealed the important role played by domain boundaries. If iso-energy curves represent a theoretically-sound solution for these boundaries, they may not always be numerically robust. To guarantee and maximize inflow at the domain boundary, a methodology that exploits general Lyapunov functions was proposed herein and successfully validated using a 2DOF system with RC friction. The performance and accuracy of the NNM computation algorithm were both found to be significantly improved with respect to the original algorithm developed in Chapter 3. However, more complex case studies considering dynamic friction models, such as, e.g., Bouc-Wen models, are still to be investigated to fully assess the potential of the modified algorithm. The influence of regularization should also be studied.

# Chapter 6

## Computation of Damped NNMs Using Boundary Value Problems

---

### Abstract

An important assumption in the description of nonlinear normal modes (NNMs) proposed by Shaw and Pierre is that there must exist an explicit parameterization of the invariant manifold, which is not the case when folding of the manifold occurs. This chapter investigates an alternative method for the computation of damped NNMs that does not rely on a predefined parameterization. The two-dimensional manifold is computed as a one-parameter family of trajectories calculated using a boundary value problem. It is illustrated with two different two-degree-of-freedom systems possessing a cubic spring and Coulomb friction, respectively. In view of the complex and interesting dynamics observed, the work presented in this chapter should be viewed as exploratory research; it, however, clearly demonstrates the interest of these methods for the computation of NNMs.

---

## 6.1 Introduction

The finite-element-based method (FEM) presented in Chapter 3 and generalized in Chapter 5 resolves a number of issues in the computation of nonlinear normal modes (NNMs) defined as two-dimensional invariant manifolds. The method is based on partial differential equations (PDEs) which were obtained by assuming that it is possible to globally describe the invariant manifold. An explicit parameterization was thus considered. As a result, the method is applicable only to regions of the phase space where this parameterization remains valid. In practice, this validity range may be limited for several reasons including internal resonances and localization. For instance, in the presence of an internal resonance, the manifold appears to fold, as illustrated in the nonlinear beam and Morane-Saulnier aircraft examples (Figures 4.12 and 4.20).

This is why the concept of multi-modal NNMs was introduced by Boivin et al. in [16]. Multi-modal NNMs were presented as a means to create multi-mode reduced-order models (ROMs) for which the coupling that exists between the individual NNMs of interest is considered while the influence of other modes is discarded. As mentioned in [16], the approach is naturally suitable for addressing the presence of internal resonances. The mathematical description of these NNMs is obtained by following the single-mode approach. The state space variables are partitioned into master and slave coordinates, the latter being functionally related to the former. The difference with the earlier approach is that  $M$  pairs of variables are taken as master pairs leading to  $2N - 2M$  slave variables described as

$$x_i = X_i(\mathbf{u}_m, \mathbf{v}_m), \quad y_i = Y_i(\mathbf{u}_m, \mathbf{v}_m), \quad (6.1)$$

where  $\mathbf{u}_m$  and  $\mathbf{v}_m$  represent the vectors of the nonlinear modal coordinates [16]. Similarly to the derivation presented in Chapter 1, the PDEs governing the geometry of the invariant manifold are obtained by removing the explicit time dependence of the equations. After solving the equations in  $\mathbb{R}^{2M}$ , the constraint functionals (6.1) allow to reduce the dynamics to  $M$  coupled nonlinear oscillators. The effectiveness of obtained ROMs was presented in [124] using a nonlinear beam example. A method for computing multi-mode NNMs was presented by Jiang et al. in [66] and is an elegant extension of the method proposed by Pesheck et al. [126] to higher-dimensional PDEs. While effective for reduced-order modeling, this method still assumes an explicit and global description of the NNM which does not completely solve the intrinsic parameterization problem.

In this chapter, we propose to address this issue by exploiting a method that was presented in the general context of two-dimensional (un)stable invariant manifold calculation. Indeed, there exist several methods which consist in locally growing the invariant surface without assuming any global parameterization. A comprehensive review of all methods existing in the literature is beyond the scope of the present thesis, but we can for instance mention the method of Krauskopf and Osinga [81, 82] which grows the manifold as a sequence of discretized geodesic level sets. The method proposed by Henderson [57, 58] paves the manifold surface using a collection of spherical balls centered on well-distributed points, forming so-called fat trajectories. Another interesting approach is the method of

Dellnitz and Hohmann [35, 36] where the manifold is covered with boxes. Similar in many regards with the other methods, it however approximates the invariant manifold using elements with the same dimension as the phase space. We refer to the survey paper of Krauskopf et al. [84] for additional details.

Herein, we investigate the method proposed by Doedel et al. [84], which locally covers the invariant surface using successive trajectories. No parameterization is assumed which allows to compute the NNM a priori without any limit and, therefore, possibly in the presence of nonlinear modal interactions. The method is presented in Section 6.2, and, to fit within its framework, only damped systems are considered. The method is also interesting because it considers continuation techniques for computing the invariant surface and gives, as a byproduct, access to the dynamics on the manifold. This represents valuable information, e.g., for analyzing the frequency-amplitude dependence of the oscillations. A two-degree-of-freedom (2DOF) system with a cubic-spring nonlinearity (cf. Chapter 1) and a 2DOF with regularized Coulomb (RC) friction (cf. Chapter 5) are considered to examine the performance of the method.

## 6.2 A Boundary Value Approach

In contrast with the geometrical approach presented in Chapter 3, the method proposed by Doedel et al. [39, 40, 84] computes a two-dimensional invariant manifold as a one-parameter family of trajectories which are defined as boundary value problems (BVPs). In this section, the method is exploited for the computation of NNMs. For simplicity, the discussion is limited to stable systems, i.e., systems whose dynamics is attracted to the equilibrium point around which the invariant manifold is computed. The method is however applicable to unstable systems.

Using the general first-order form of the equation of motion,  $\dot{\mathbf{z}} = \mathbf{g}(\mathbf{z})$ , a trajectory on the invariant manifold (i.e., the NNM) is defined as

$$\mathbf{z}'(t) = T\mathbf{g}(\mathbf{z}(t)), \quad (6.2)$$

$$\mathbf{z}(0) = \mathbf{z}_0 + r_0(\cos(\theta)\boldsymbol{\psi}_1 + \sin(\theta)\boldsymbol{\psi}_2), \quad (6.3)$$

where  $(\cdot)'$  denotes the first derivative with respect to the normalized time  $t \in [0, 1]$ ,  $r_0$  is a small parameter, and  $T$  is the final time. Equations (6.2)-(6.3) parameterize using  $\theta$  a family of trajectories that start on a small ellipse around the equilibrium point  $\mathbf{z}_0$ . If the vectors  $\boldsymbol{\psi}_1$  and  $\boldsymbol{\psi}_2$  are chosen so as to define the eigenspace of the linearized system (at  $\mathbf{z}_0$ ), the trajectories will describe the corresponding NNM. An alternative to the eigenvectors of Equation (6.3) is to use the linear coefficients  $(a_{ji}, b_{ji})$  introduced by Shaw and Pierre (see Chapter 1, Section 1.5).

A first trajectory on the manifold is grown using continuation with  $T$  as free parameter and  $\theta$  arbitrarily fixed at  $\theta = \theta_0$  [83]. In this problem, Equations (6.2) and (6.3) are solved

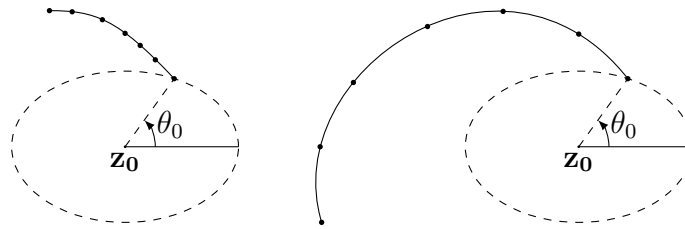


Figure 6.1: Schematics of the first continuation step used in the BVP approach. A first trajectory is grown for  $\theta = \theta_0$ .

for  $\mathbf{Z}$  which groups all the points that discretize the trajectory. This step is illustrated in Figure 6.1 where, although they can be equally distributed in time, the points along the trajectory are not necessarily equally distributed in space. During the continuation process, a function measuring the arclength of the trajectory as

$$L = \int_0^1 T \|\mathbf{g}(\mathbf{z})\| ds. \quad (6.4)$$

is monitored by the algorithm, and the continuation is stopped when the trajectory reaches a user-defined length  $\bar{L}$ . Equation (6.3) together with the condition  $L = \bar{L}$  define a BVP that constrains the initial and final conditions of the trajectory. A second continuation step, with  $\theta$  as parameter, is then performed. As illustrated in Figure 6.2, all the points that discretize the trajectory are continuously varied to cover the complete invariant manifold. For this last step,  $T$  is free to vary. Other stopping criteria than the arclength of the trajectory can be employed. We refer to [83] for additional details about the original method.

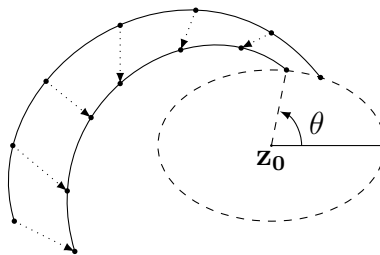


Figure 6.2: Schematics of the second step used in the BVP approach. Trajectories are continued with respect to  $\theta$  to cover the entire invariant surface.

The different continuation steps are performed with the software AUTO [40] which solves BVPs using the method of orthogonal collocation with piecewise polynomials [38].

For a stable system,  $T < 0$ , and the computation of the first trajectory is similar to backward time integration. The recourse to the BVP approach has however the advantage of being compatible with the subsequent continuation steps. The latter are important because trajectories can be very sensitive with respect to the parameter  $\theta$ . A continuation approach which controls the step size in  $\theta$  with respect to the variation of all the trajectory (i.e.,  $\mathbf{Z}$ ) guarantees a nice covering of the invariant surface. Moreover, stable manifolds become unstable in backward time, and the recourse to BVP approach is thus arguably more robust than direct time integration.

### 6.2.1 The 2DOF System With Cubic Spring

The BVP method is now applied to a 2DOF system possessing a cubic spring and linear nonproportional damping. The equation of motion are

$$\begin{aligned}\ddot{x}_1 + 0.3(\dot{x}_1 - \dot{x}_2) + (2x_1 - x_2) + 0.5x_1^3 &= 0, \\ \ddot{x}_2 + 0.3\dot{x}_2 + 0.3(\dot{x}_2 - \dot{x}_1) + (2x_2 - x_1) &= 0.\end{aligned}\tag{6.5}$$

The out-of-phase NNM of this system was computed using polynomial series expansions and compared to the FEM results in Chapter 1. This mode is now studied for larger vibration amplitudes. Figure 6.3 presents a three-dimensional view of the NNM. The invariant manifold computed with the BVP approach is represented by the blue surface that was obtained by constructing a mesh between adjacent trajectories. The manifold is covered with a total of 2012 trajectories of arclength  $L = 150$ . The initial ellipse was computed for  $r_0 = 10^{-3}$  and each trajectory is computed with  $\text{NTST} = 300$  time steps and  $\text{NCOL} = 4$  collocation points in each time interval, for a total of 1200 points per trajectory.

In order to analyze the complex shape of the surface, two trajectories in the set of coordinates  $(x_1, y_1, x_2)$  are reported in Figures 6.4(a) and (b), respectively. Close to the origin, the trajectories spiral out of the system's equilibrium point and form an almost planar surface. Then, as the motion amplitude increases, the trajectories start to describe a more complex shape and the linear ratio between their amplitudes is lost. The projection of the trajectories in the  $(x_1, x_2)$  plane shows that the out-of-phase motion that was present at the origin is now lost for some parts of the trajectory. It is inferred that both coordinates start to oscillate at different frequencies.

The time series  $y_1(t)$  and  $y_2(t)$  computed for an arclength of 5000 are presented in Figure 6.5. For high vibration amplitudes, the difference between the oscillation frequency of the first and second DOFs is clearly visible. For low amplitudes, a linear regime with a classical out-of-phase motion and a phase lag between the coordinates due to damping is recovered. In order to validate the time series of Figure 6.5, a forward time integration is performed with a fourth-order Runge-Kutta method for initial conditions defined as the final point of the trajectory. The comparison leads to a normalized mean-square error (NMSE) equal to  $10^{-8}\%$ .

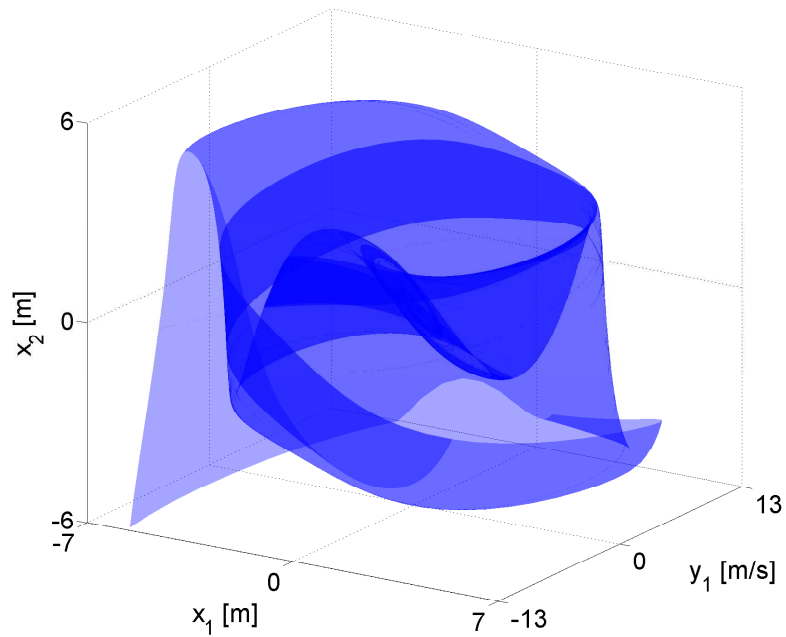


Figure 6.3: Out-of-phase NNM of the 2DOF system (6.5). The blue surface is a mesh built with the trajectories computed by the BVP approach.

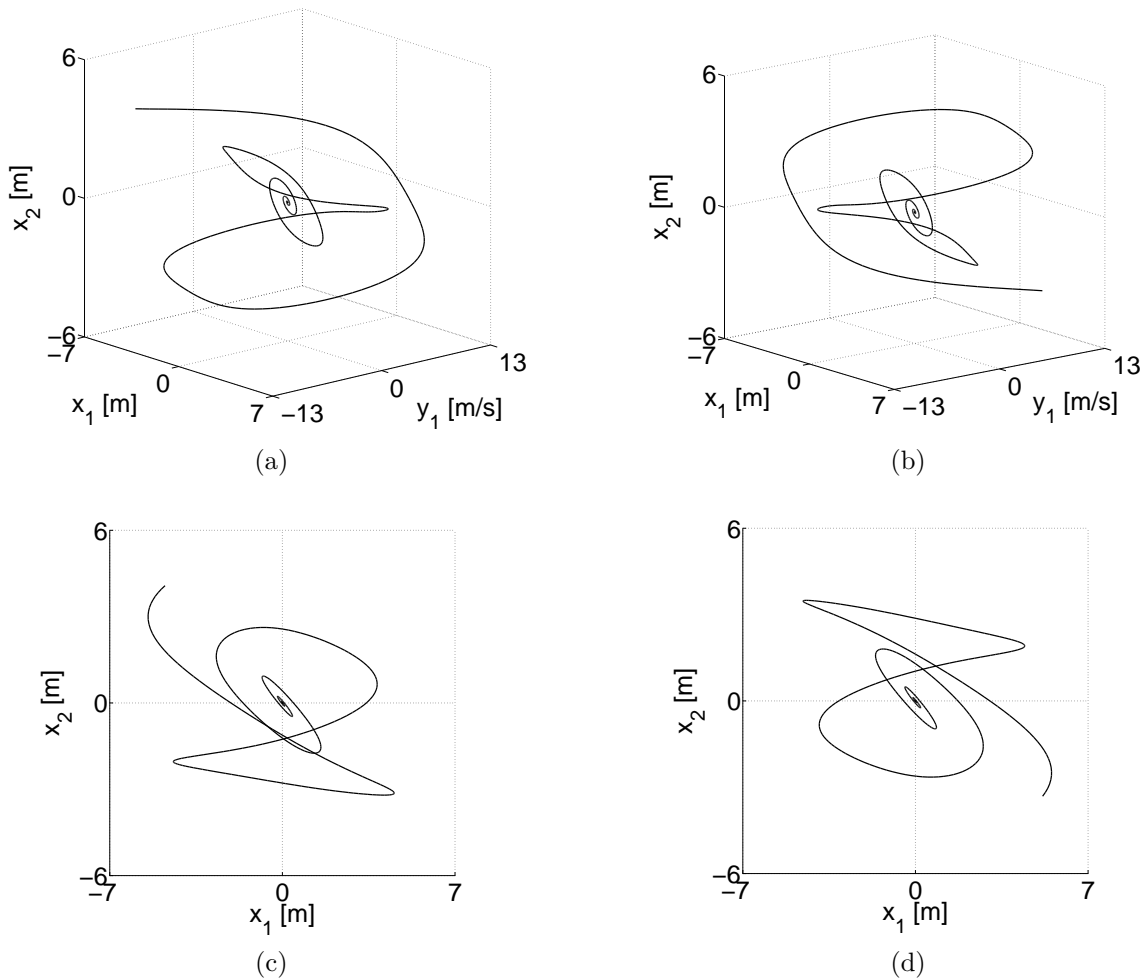


Figure 6.4: Out-of-phase NNM of the 2DOF system (6.5). (a, b) Two trajectories computed using the BVP approach; (c, d) side view of the trajectories (a) and (b), respectively.

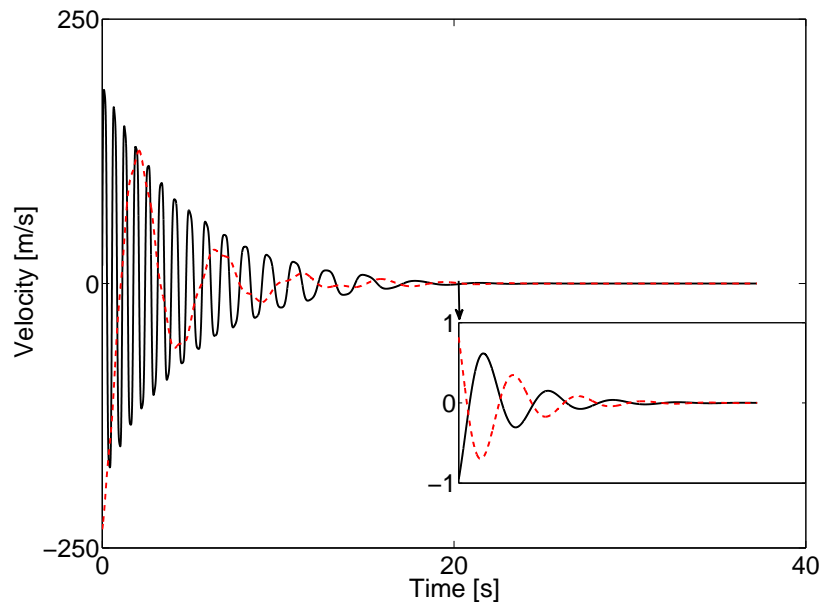
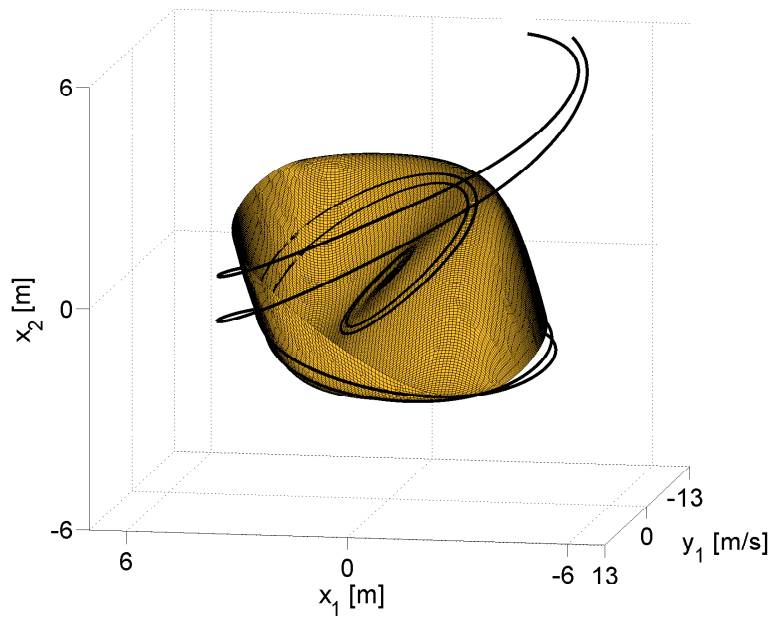


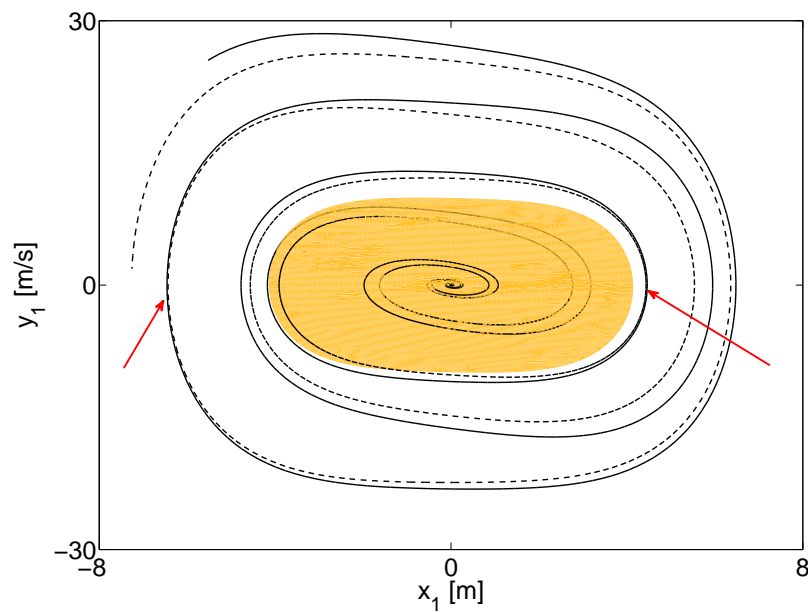
Figure 6.5: Dynamics in forward time for the out-of-phase NNM for  $y_1$  (—) and  $y_2$  (---). Trajectory computed for an arclength of  $L = 5000$ .

In view of the amplitudes reached, the regime of motion is very strongly nonlinear. The dynamics looks complex and would clearly deserve a dedicated study. Due to time constraints, a deeper analysis was however not feasible.

The invariant manifold obtained with the FEM algorithm is presented in Figure 6.6(a). The FEM algorithm was stopped after a dramatic decrease in the energy steps. Two trajectories obtained with the BVP approach are also depicted. For  $x_1 < 5$ , the trajectories follow to the FEM surface which shows that the results of both methods are consistent. For higher vibration amplitudes, the failure of the FEM is explained by the  $(x_1, y_1)$  parameterization that is no longer adequate. Indeed, to continue to follow the trajectories, the FEM surface has to simultaneously change its slope and to become almost vertical. In particular,  $x_2$  has to severely decrease and to become negative for  $x_1 > 0$ . Similarly,  $x_2$  has to become positive for  $x_1 < 0$ . Another illustration of this sharp transition is presented in Figure 6.6(b) which shows a projection of the trajectories onto the master coordinates plane. The two orbits are getting very close to each other in two specific regions pointed out by arrows. Although they do not cross each other, all the trajectories stack in these regions where the invariant surface becomes almost vertical (cf. Figure 6.3). Finally, for higher vibration amplitudes (as, e.g., in Figure 6.5), the projections of the trajectories onto the plane  $(x_1, y_1)$  cross each other. Although the exact reason for the folding of the manifold is not clearly identified and would certainly deserve more investigations, it is interesting to note that the second NNM of the underlying conservative system does not fold.



(a)



(b)

Figure 6.6: Out-of-phase NNM of the 2DOF system (6.5). Comparison between the FEM (orange) and two trajectories computed using the BVP approach: (a) three-dimensional view of the NNM in the  $(x_1, y_1, x_2)$  space; (b) top view in the master coordinates' plane of the FEM. Solid and dashed lines are used to distinguish both trajectories.

## 6.2.2 The 2DOF System With Regularized-Coulomb Friction

A 2DOF system including RC friction is now investigated. The equations of motion are

$$\begin{aligned}\ddot{x}_1 + (2x_1 - x_2) + F_{\max} \tanh(R\dot{x}_1) &= 0, \\ \ddot{x}_2 + (2x_2 - x_1) &= 0.\end{aligned}\tag{6.6}$$

The case where  $F_{\max} = 1.3$  N and  $R = 1$  rad.s/m was studied in Chapter 5 and is again considered here. Figure 6.7(a) illustrates the in-phase NNM obtained by the BVP approach. The manifold is computed using 1,000 trajectories of arclength  $L = 200$ . The elements that form the mesh of the invariant surface are represented in order to illustrate the structure of the manifold. The surface possesses a wavy shape as it was reported in Chapter 5. A trajectory is presented in Figure 6.7(b). It spirals to the equilibrium point and, as it approaches the origin, rapid direction changes occur when the trajectory leaves the top of a “wave”. The time history of the trajectory is given in Figure 6.7(c). The classical linear decay rate already observed in Chapter 5 is recovered.

Figure 6.8(a) compares the NNM obtained by the FEM (orange) and the BVP approach (blue). Both surfaces agree very well around the origin. Figure 6.8(b) presents the absolute error between the two methods. Specifically, for each point belonging to a trajectory computed by the BVP method, the error is computed by comparing the  $y_1$  value obtained by the BVP and by the FEM for each set of coordinates  $(x_2, y_2)$  of the trajectory. There exist at least two orders of magnitudes between the error and the values of  $y_1$ . In the BVP approach, several parameters can influence this error as, for instance, the initial radius  $r_0$  and the number of time intervals considered in the collocation method. Similarly, for the FEM algorithm, the size of the initial domain, the size of the annular regions, and the number of finite elements play a role on this error. Figure 6.8(c) shows that the error globally decreases as smaller elements are considered.

The case where  $F_{\max} = 1.5$  N is now considered. The first mode of this system is illustrated in Figure 6.9. The invariant manifold computed with the BVP approach is presented in Figure 6.9(a). The wavy character of the surface that was not observable in Chapter 5 is recovered and the surface is, in essence, similar to the reference test case with  $F_{\max} = 1.3$  N. One can however note that the deformation of the invariant surface is more pronounced. In the center of the figure, the solution obtained with the FEM (in orange) perfectly overlaps the BVP results. The blue mesh also appears to fold in several regions recognizable by the darker blue color. The projection in Figure 6.9(b) of three trajectories onto the master’s coordinate plane used by the FEM confirms this observation. The trajectories appear to intersect each other in two different regions around  $(u, v) = (-5, 2)$  and  $(u, v) = (2, 5)$ . Clearly, the FEM algorithm is limited by an inappropriate manifold’s parameterization in these regions.

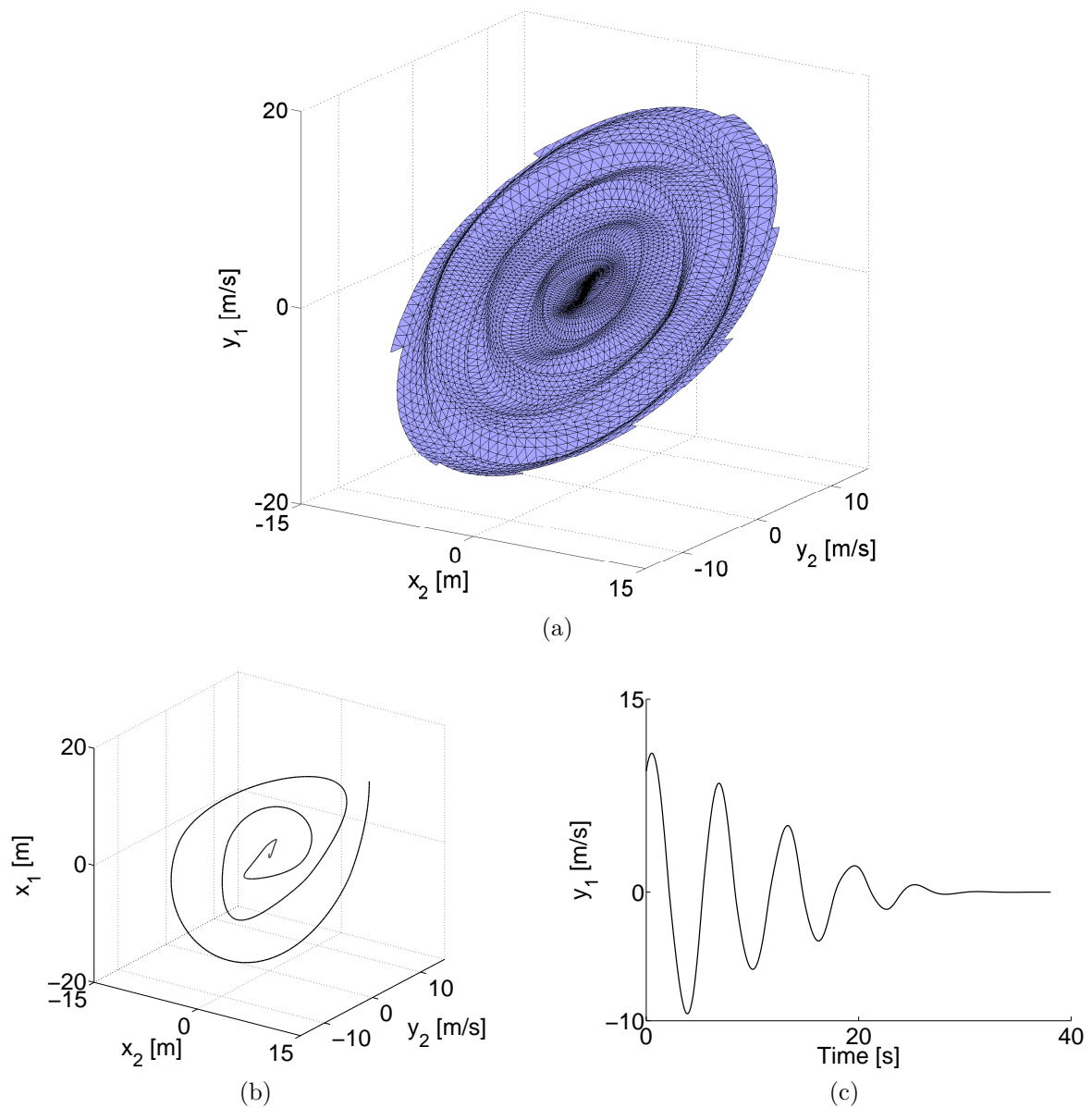


Figure 6.7: First NNM of the 2DOF system (6.6). (a) Invariant surface obtained with the BVP approach; (b) one trajectory on the invariant surface; (c) time series  $y_1(t)$  for the trajectory in (b).

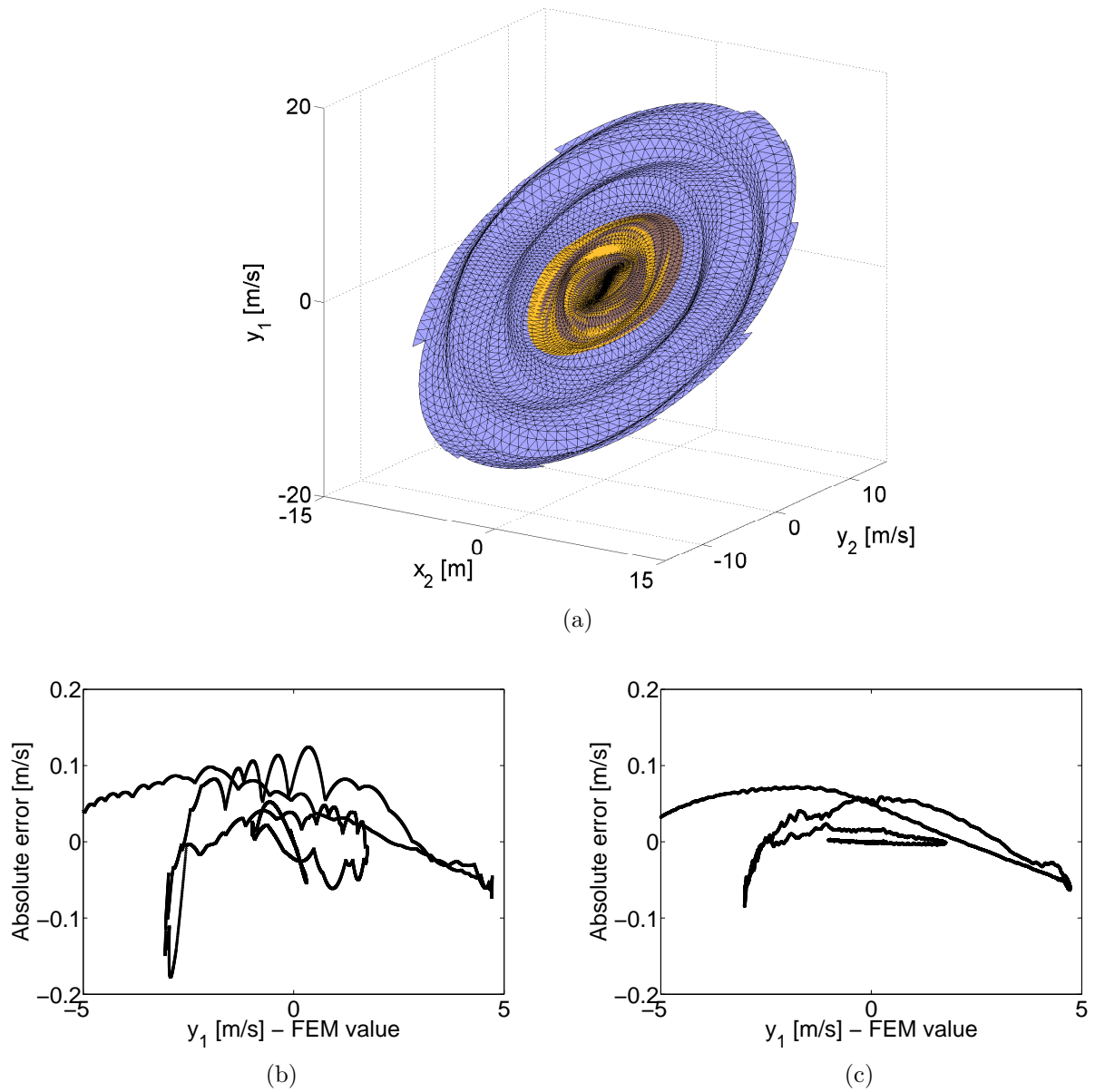


Figure 6.8: Distance along  $y_1$  between a trajectory computed using the BVP approach and the FEM surface. (a) Global mesh with 1,000 elements; (b) global mesh with 10,000 elements.

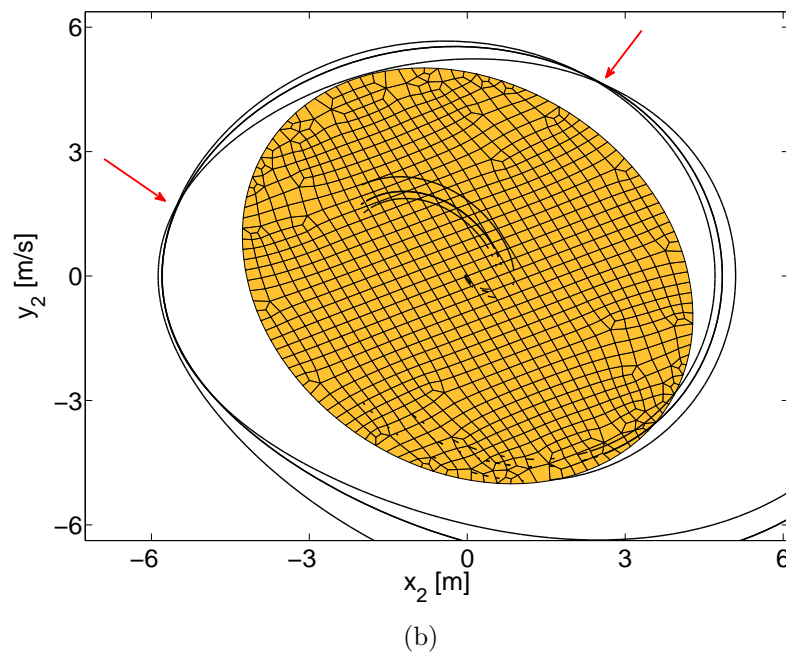
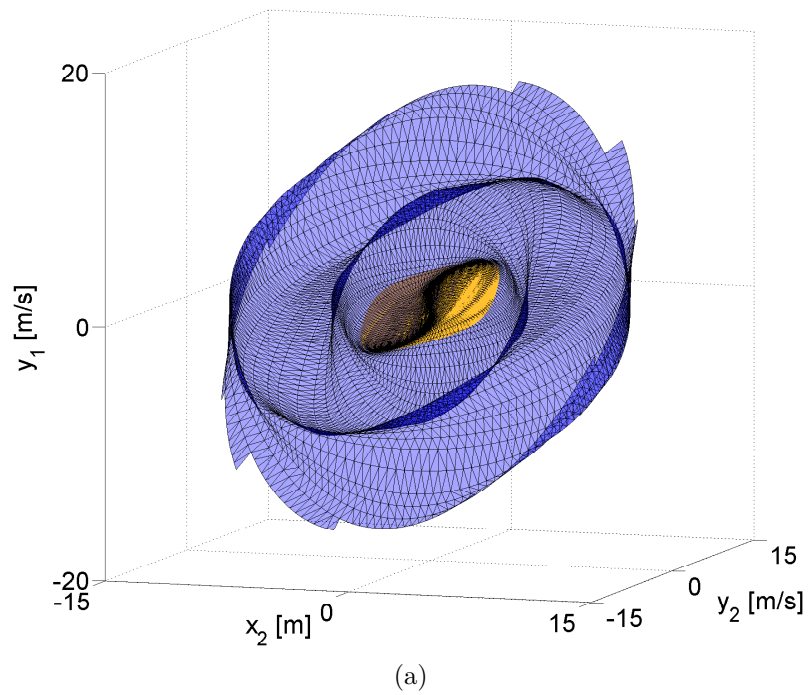


Figure 6.9: First NNM of the 2DOF system with regularized Coulomb friction and  $F_{max} = 1.5$  N. (a) Comparison between the BVP results (blue mesh) and the FEM results (orange mesh). (b) Projection of three trajectories (black curves) computed with the BVP approach onto the master plane considered by the FEM.

### 6.3 Conclusions

In this chapter, we explore an alternative method for computing NNMs of nonconservative systems. Originally proposed by Doedel in the context of (un)stable invariant manifold calculation, the method considers successive BVPs to (i) compute a trajectory on the invariant manifold, (ii) continue the trajectory to cover the manifold. The method does not rely on a parameterization of the NNM, and can a priori deal with the presence of internal resonances. In particular, it allows to compute NNMs in regions where the explicit parameterization used by the FEM fails. The method was shown to be accurate and provided invariant surfaces in very good agreement with those computed by the FEM. Moreover, a trajectory computed by the method corresponds directly to the dynamics on the invariant manifold and can be exploited for dynamical analysis. We note that the method is not applicable to conservative systems.

In conclusion, we believe that this method, and more generally the methods which locally grow invariant surfaces, paves the way for a completely new approach to the calculation of NNMs defined as two-dimensional invariant manifolds. These methods, which are a priori applicable in presence of internal resonances, provide a more profound understanding of the dynamics and, in particular, of the influence of damping. Finally, the applicability of the method to higher-dimensional mechanical systems is still to be investigated. In particular, in the presence of weak damping, the method might require an important number of points along the first trajectory in order to reach large amplitude vibrations, which, in turn, would make the subsequent continuation steps of this trajectory computationally more intensive.



# Conclusions

The objective of this doctoral thesis is to contribute to the development of a practical analog of modal analysis for nonlinear systems. Specifically, three numerical methods were considered in this manuscript for the effective computation of nonlinear normal modes (NNMs) of both conservative and nonconservative systems. Table 6.1 presents a summary of their main characteristics.

The first algorithm that was considered combines a shooting method with the pseudo-arclength continuation technique. Based on the extension of Rosenberg’s definition, the method computes periodic solutions of nonlinear conservative systems. The algorithm is computationally effective so that it was applied in Chapter 2 to investigate the dynamics of a real-life aerospace structure, the SmallSat spacecraft. The method can handle internal resonances (IR), which enabled us to study some specific modal interactions of the satellite. An important result of the thesis is that, thanks to the NNM theory and the algorithm, we were able to reproduce numerically and explain the modal interactions identified experimentally. Such results demonstrate, if it was still necessary, that NNMs represent a very useful concept for the interpretation of nonlinear oscillations.

The second algorithm was developed within the framework of this thesis and solves the manifold-governing partial differential equations (PDEs) obtained from Shaw and Pierre’s definition. It relies on the finite element (FE) method, and combines a streamline up-

	Definition	Conservative	Nonconservative	IR	By-product
Shooting-based method	Rosenberg extended	Yes.	No.	Yes.	Dynamics on NNM FEP
FE-based method	Shaw & Pierre	Yes.	Yes.	No.	Dynamics on NNM ROM
Trajectory-based method	Shaw & Pierre	No.	Yes.	Yes.	Dynamics on NNM

Table 6.1: Features of the different methods exploited in this thesis.

wind Petrov-Galerkin (SUPG) formulation with a resolution strategy based on annular domains. As a result, the manifold is grown sequentially, which leads to a significant decrease in computational time. In view of the hyperbolic nature of the governing PDEs, specific attention has to be paid to the definition of the computational domain boundaries. Eventually, the domains were defined using Lyapunov functions, which were found to be particularly helpful for this purpose. One significant advantage of this FE method over the shooting method is that both conservative and nonconservative systems can be studied. However, although the method was applied to a relatively large-scale problem (i.e., the Paris aircraft), the resolution of the PDEs is computationally more demanding than the boundary value problem (BVP) of the shooting method. Because it is geometric by nature, the FE method has the distinctive feature to provide a reduced-order model (ROM) of the dynamics. Conversely, since time is eliminated when constructing the manifold, a direct access to motion frequency is not available. The main limitation of the FE method is certainly the fact that it relies on an explicit parameterization of the invariant manifold. Such parameterization no longer exists when folding of the manifold occurs, e.g., when an internal resonance is encountered.

The third algorithm for the computation of NNMs addresses the latter limitation of the FE method and exploits a technique proposed by Doedel. Also based on Shaw and Pierre's definition, the method covers the two-dimensional invariant manifold that represents a NNM with a collection of trajectories. Similarly to the shooting-based method, the trajectories are defined using BVP problems, but the method is naturally applicable to nonconservative systems. However, the effectiveness of the method for lightly-damped systems for which trajectories slowly spiral out of the equilibrium point is more questionable as a large number of collocation points can be required. Another drawback is that the absence of parameterization complicates the construction of a ROM.

In conclusion, it turns out that there is not yet an universal method that can compute the NNMs of large-scale, damped and undamped nonlinear mechanical systems featuring modal interactions. However, we believe that by combining the respective strengths and characteristics of the three methods studied in this thesis the dynamics of a relatively large class of nonlinear systems can be adequately addressed.

## Directions for Future Work

Since we devoted the vast majority of our efforts to the numerical computation of nonlinear normal modes, a detailed analysis and interpretation of the dynamics on the computed manifolds could not be performed during this research. Yet, the results obtained herein, particularly in Chapters 5 and 6, show that the manifolds carry important and relevant information. An immediate perspective of this research is therefore the direct exploitation of the numerical tools, developed to uncover the role played by (linear and nonlinear) damping in the systems dynamics. This makes even more sense when one considers that even viscous damping can, for instance, turn hardening nonlinear behavior into softening

behavior.

In addition, realizing that a seemingly simple two-degree-of-freedom system can possess a countable infinity of modal interactions, a fundamental question is how these modal interactions survive damping. Starting from the conservative system and increasing damping gradually would allow to identify the dynamical mechanisms that lead to the persistence or elimination of modal interactions. More generally, the presence of mode bifurcations leads to the existence of new NNMs which cannot be regarded as the direct extension of a linear normal mode. These modes can convey important dynamics as, e.g., modal interactions. The importance of these supernumerary families of periodic solutions in complex systems remains an open question [26, 160].

Besides progressing toward a more fundamental understanding of nonlinear oscillations, the algorithms developed in this thesis can also find other applications in structural dynamics. A first example is the construction of reduced-order models. The FE method could be used to capture the essential damped dynamics of complex nonlinear systems and, therefore, facilitate their dynamical analysis. Another field of application is the design of nonlinear vibration absorbers and energy harvesters where damping plays a central role [23, 56, 156]. The algorithms could help validate the theoretical developments, further investigate the damped dynamics and better characterize the performance of the devices. Finally, a finite element model updating methodology that would rely on the comparison between experimentally-identified and theoretically-predicted NNMs was not yet proposed in the literature. There is no doubt that NNMs provide a sound basis for improving and validating the mathematical models developed by engineers. For instance, NNMs could be very useful during ground vibration testing of aircraft and during the subsequent model validation effort.



# Appendix A

## Bifurcation Analysis

In the continuation algorithm presented in Chapter 1, the monodromy matrix was introduced as an essential component of the linearization of the shooting function. This  $2N \times 2N$  matrix was defined as

$$\Phi = \frac{\partial \mathbf{z}_p(T, \mathbf{z}_{p0})}{\partial \mathbf{z}_{p0}}, \quad (\text{A.1})$$

where  $\mathbf{z}_p(T, \mathbf{z}_{p0})$  is a periodic solution of period  $T$  corresponding to initial conditions  $\mathbf{z}_{p0}$ . The monodromy matrix represents the sensitivity of the solution at time  $T$  with respect to initial conditions. It determines whether a small initial perturbation decays or grows. In the present continuation algorithm, the monodromy matrix is computed using a sensitivity analysis embedded into the time integration procedure of the shooting method.

The eigenvalues  $\mu_i$  of the monodromy matrix are the so-called Floquet multipliers which determine the stability of a periodic orbit. If an eigenvalue is larger than one (i.e.,  $|\mu_i| > 1$ ), the orbit is said unstable. Conversely, the periodic orbit is stable if  $|\mu_i| < 1, \forall i$ . As demonstrated, e.g., in [141], one multiplier always equals +1. The notion of stability is closely related to the notion of bifurcation because stability changes occur through bifurcations. Periodic solutions often encounter one of the three following bifurcations:

1. the saddle-node (SN) or fold bifurcation, where a Floquet multiplier crosses the unit circle through +1. This bifurcation is also called limit-point (LP) bifurcation in Chapter 2.
2. the period-doubling (PD) or flip bifurcation, where a Floquet multiplier crosses the unit circle through -1.
3. the Neimark-Sacker (NS) or torus bifurcation, where a pair of (complex conjugate) Floquet multipliers crosses simultaneously the unit circle.

During the continuation of a family of periodic solutions, a convenient way to detect the presence of bifurcations and to analyze their nature is to rely on so-called test functions.

A test function is scalar function  $\psi(\mathbf{z})$  whose zero corresponds to a bifurcation point. A bifurcation is therefore detected as a change of sign of the test function between two successive periodic solutions  $\mathbf{z}_p^k$  and  $\mathbf{z}_p^{k+1}$ :

$$\psi(\mathbf{z}_p^k)\psi(\mathbf{z}_p^{k+1}) < 0. \quad (\text{A.2})$$

The test functions that were introduced in the continuation algorithm are [10, 85]:

$$\psi_{\text{LP}} = \det(\mathbf{P}_{\mathbf{z}} - \mathbf{I}_{2N}), \quad (\text{A.3})$$

$$\psi_{\text{PD}} = \det(\mathbf{P}_{\mathbf{z}} + \mathbf{I}_{2N}), \quad (\text{A.4})$$

$$\psi_{\text{NS}} = \det(\mathbf{P}_{\mathbf{z}} \odot \mathbf{P}_{\mathbf{z}} - \mathbf{I}_m), \quad (\text{A.5})$$

where  $\mathbf{I}_m$  is an identity matrix,  $m = \frac{1}{2}N(N-1)$ ,  $\mathbf{A} \odot \mathbf{B}$  denotes the bialternate product of the two matrices  $\mathbf{A}$  and  $\mathbf{B}$ , and the matrix  $\mathbf{P}_{\mathbf{z}}$  is the linearization of the Poincaré map  $\mathbf{P}$ .

In the presence of harmonic excitation, as in Chapter 2, the autonomous character of the system is preserved by introducing an artificial state-space variable, increasing therefore the system's dimensionality of 1. Simultaneously, in the presence of harmonic forcing, a Poincaré map reducing the system's dimensionality of 1 is easily constructed by taking snapshots of the dynamics every time interval  $T$  (where  $T$  is the forcing period). The resulting Poincaré section is thus  $2N$ -dimensional and its linearization corresponds to  $\Phi$ .

Ultimately, in order to accurately identify a bifurcation point, a standard secant method is considered in order to efficiently reach the actual zero of the test function.

# Bibliography

- [1] Metafor. <http://metafor.ltas.ulg.ac.be/dokuwiki/start>, 02/2014.
- [2] M. Amabili and C. Touzé. Reduced-order models for nonlinear vibrations of fluid-filled circular cylindrical shells: Comparison of pod and asymptotic nonlinear normal modes methods. *Journal of Fluids and Structures*, 23(6):885–903, 2007.
- [3] S. Andersson, A. Söderberg, and S. Björklund. Friction models for sliding dry, boundary and mixed lubricated contacts. *Tribology International*, 40(4):580–587, 2007.
- [4] P. Apiwattanalungarn, S. W. Shaw, and C. Pierre. Component mode synthesis using nonlinear normal modes. *Nonlinear Dynamics*, 41:30, 2005.
- [5] R. Arquier, S. Bellizzi, R. Bouc, and B. Cochelin. Two methods for the computation of nonlinear modes of vibrating systems at large amplitudes. *Computers & Structures*, 84(24-25):1565–1576, 2006.
- [6] K. V. Avramov and Y. V. Mikhlin. Review of applications of nonlinear normal modes for vibrating mechanical systems. *Applied Mechanics Reviews*, 65(2):020801–020801, 2013.
- [7] M. C. C. Bampton and Jr. R. R. Craig. Coupling of substructures for dynamic analyses. *AIAA Journal*, 6(7):1313–1319, 1968.
- [8] S. Bellizzi and R. Bouc. A new formulation for the existence and calculation of nonlinear normal modes. *Journal of Sound and Vibration*, 287(3):545–569, 2005.
- [9] S. Bellizzi and R. Bouc. An amplitude-phase formulation for nonlinear modes and limit cycles through invariant manifolds. *Journal of Sound and Vibration*, 300(3-5):896–915, 2007.
- [10] W.-J. Beyn, A. Champneys, E. Doedel, W. Govaerts, Y. A. Kuznetsov, and B. Sandstede. *Chapter 4 Numerical continuation, and computation of normal forms*, volume Volume 2, pages 149–219. Elsevier Science, 2002.
- [11] R. Bhattacharyya, P. Jain, and A. Nair. Normal mode localization for a two degrees-of-freedom system with quadratic and cubic non-linearities. *Journal of Sound and Vibration*, 249(5):909–919, 2002.

- [12] D. Bigoni and G. Noselli. Experimental evidence of flutter and divergence instabilities induced by dry friction. *Journal of the Mechanics and Physics of Solids*, 59(10):2208–2226, 2011.
- [13] F. Blanc, C. Touzé, J. F. Mercier, K. Ege, and A. S. Bonnet Ben-Dhia. On the numerical computation of nonlinear normal modes for reduced-order modelling of conservative vibratory systems. *Mechanical Systems and Signal Processing*, 36(2):520–539, 2013.
- [14] P. B. Bochev and M. D. Gunzburger. *Least-Squares Finite Element Methods*, volume 166 of *Applied Mathematical Sciences*. Springer, 2009.
- [15] S. Bograd, P. Reuss, A. Schmidt, L. Gaul, and M. Mayer. Modeling the dynamics of mechanical joints. *Mechanical Systems and Signal Processing*, 25(8):2801–2826, 2011.
- [16] N. Boivin, C. Pierre, and S. W. Shaw. Non-linear modal analysis of structural systems featuring internal resonances. *Journal of Sound and Vibration*, 182:6, 1995.
- [17] N. Boivin, C. Pierre, and S. W. Shaw. Nonlinear normal modes, invariance, and modal dynamics approximations of nonlinear systems. *Nonlinear Dynamics*, 8:32, 1995.
- [18] N. Boivin, C. Pierre, and S. W. Shaw. Non-linear modal analysis of the forced response of structural systems. *AIAA Journal*, page 22, 1996.
- [19] A. N. Brooks and T. J. R. Hughes. Streamline upwind/Petrov-Galerkin formulations for convection dominated flows with particular emphasis on the incompressible Navier-Stokes equations. *Computer Methods in Applied Mechanics and Engineering*, 32(1-3):199–259, 1982.
- [20] T. D Burton. Numerical calculation of nonlinear normal modes in structural systems. *Nonlinear Dynamics*, 49(3):425–441, 2007.
- [21] E. A. Butcher and R. Lu. Order reduction of structural dynamic systems with static piecewise linear nonlinearities. *Nonlinear Dynamics*, 49(3):375–399, 2007.
- [22] P. Camarasa and S. Kiryenko. Shock attenuation system for spacecraft and adaptor (SASSA). In *European Conference on Spacecraft Structures, Materials and Mechanical Testing*, Toulouse, France, 2009.
- [23] A. Cammarano, S. G. Burrow, and D. A. W. Barton. Modelling and experimental characterization of an energy harvester with bi-stable compliance characteristics. *Proceedings of the Institution of Mechanical Engineers, Part I: Journal of Systems and Control Engineering*, 225(4):475–484, 2011.
- [24] N. Carpineto, W. Lacarbonara, and F. Vestroni. Hysteretic tuned mass dampers for structural vibration mitigation. *Journal of Sound and Vibration*, 333(5):1302–1318, 2014.

- [25] J. Carr. *Applications of Centre Manifold Theory*, volume 35 of *Applied Mathematical Sciences*. Springer-Verlag, 1981.
- [26] P. Casini, O. Giannini, and F. Vestroni. Effect of damping on the nonlinear modal characteristics of a piecewise-smooth system through harmonic forced response. *Mechanical Systems and Signal Processing*, 36(2):540–548, 2013.
- [27] S.-L. Chen and S. W. Shaw. Normal modes for piecewise linear vibratory systems. *Nonlinear Dynamics*, 10:135–164, 1996.
- [28] B. Cochelin, N. Damil, and M. Potier-Ferry. *Méthodes Asymptotiques Numériques*. Lavoisier, Paris, 2007.
- [29] B. Cochelin and C. Vergez. A high order purely frequency-based harmonic balance formulation for continuation of periodic solutions. *Journal of Sound and Vibration*, 324(1-2):243–262, 2009.
- [30] C. A. Coulomb. *Théorie des machines simples*. Mémoires de Mathématique et de Physique de l’Académie des Sciences, 1785.
- [31] P. Dahl. A solid friction model. In *Technical Report TOR-0158(3107-18)-1, The Aerospace Corporation, El Segundo, CA*, 1968.
- [32] H. Dankowicz. On the modeling of dynamic friction phenomena. *ZAMM - Journal of Applied Mathematics and Mechanics / Zeitschrift für Angewandte Mathematik und Mechanik*, 79(6):399–409, 1999.
- [33] H. Dankowicz and F. F. Schilder. *Recipes for Continuation*. Computational Science and Engineering 11, SIAM, 2013.
- [34] C. C. de Wit, H. Olsson, K. J. Astrom, and P. Lischinsky. A new model for control of systems with friction. *Automatic Control, IEEE Transactions on*, 40(3):419–425, 1995.
- [35] M. Dellnitz and A. Hohmann. *The Computation of Unstable Manifolds Using Subdivision and Continuation*, volume 19 of *Progress in Nonlinear Differential Equations and Their Applications*, chapter 21, pages 449–459. Birkhäuser Basel, 1996.
- [36] M. Dellnitz and A. Hohmann. A subdivision algorithm for the computation of unstable manifolds and global attractors. *Numerische Mathematik*, 75(3):293–317, 1997.
- [37] T. Detroux, L. Renson, and G. Kerschen. The harmonic balance method for advanced analysis and design of nonlinear mechanical system. In *Proceedings of the International Modal Analysis Conference, Orlando, USA*, 2014.
- [38] E. J. Doedel. *Lecture Notes on Numerical Analysis of Nonlinear Equations*, chapter 1, pages 1–49. Springer Netherlands, 2007.

- [39] E. J. Doedel, B. Krauskopf, and H. M. Osinga. Global bifurcations of the lorenz manifold. *Nonlinearity*, 19, 2006.
- [40] E. J. Doedel, R. C. Paffenroth, A. R. Champneys, T. F. Fairgrieve, Y. A. Kuznetsov, B. E. Oldeman, B. Sandstede, and X. J. Wang. Auto2000: Continuation and bifurcation software for ordinary differential equations, 2000. available via <http://cmvl.cs.concordia.ca/>.
- [41] J. Donea and A. Huerta. *Steady Transport Problems*. Finite Element Methods for Flow Problems. John Wiley & Sons, Ltd, 2005.
- [42] C. W. Emory and M. J. Patil. Predicting limit cycle oscillation in an aeroelastic system using nonlinear normal modes. *Journal of Aircraft*, 50(1):73–81, 2013.
- [43] M. Eriten, M. Kurt, G. Luo, D. M. McFarland, L. A. Bergman, and A. F. Vakakis. Nonlinear system identification of frictional effects in a beam with a bolted joint connection. *Mechanical Systems and Signal Processing*, 39(1-2):245–264, 2013.
- [44] A. Ern and J.-L. Guermond. *Theory and Practice of Finite Elements*, volume 159 of *Applied Mathematical Sciences*. Springer New York, 2004.
- [45] D. J. Ewins. *Modal Testing: Theory, Practice and Application, 2nd Edition*. John Wiley, 2009.
- [46] B. Feeny and F. Moon. Empirical dry-friction modeling in a forced oscillator using chaos. *Nonlinear Dynamics*, 47(1):129–141, 2007.
- [47] B. F. Feeny and F. C. Moon. Bifurcation sequences of a coulomb friction oscillator. *Nonlinear Dynamics*, 4(1):25–37, 1993.
- [48] L. Gaul and J. Lenz. Nonlinear dynamics of structures assembled by bolted joints. *Acta Mechanica*, 125(1-4):169–181, 1997.
- [49] O. V. Gendelman. Bifurcations of nonlinear normal modes of linear oscillator with strongly nonlinear damped attachment. *Nonlinear Dynamics*, 37(2):115–128, 2004.
- [50] F. Georgiades, M. Peeters, G. Kerschen, J. C. Golinval, and M. Ruzzene. Modal analysis of a nonlinear periodic structure with cyclic symmetry. *AIAA Journal*, 47(4):1014–1025, 2009.
- [51] M. Géradin and D. Rixen. *Mechanical Vibrations: Theory and application to structural dynamics*. John Wiley, 1997.
- [52] C. Geuzaine and J.-F. Remacle. Gmsh: a three-dimensional finite element mesh generator with built-in pre- and post-processing facilities. *International Journal for Numerical Methods in Engineering*, 79(11):1309–1331, 2009.

- [53] P. A. Giesl and S. F. Hafstein. Revised CPA method to compute lyapunov functions for nonlinear systems. *Journal of Mathematical Analysis and Applications*, 410(1):292–306, 2014.
- [54] D. E. Gilsinn. Asymptotic approximations of integral manifolds. *SIAM Journal on Applied Mathematics*, 47(5):929–940, 1987.
- [55] A. Grolet and F. Thouverez. Free and forced vibration analysis of a nonlinear system with cyclic symmetry: Application to a simplified model. *Journal of Sound and Vibration*, 331(12):2911–2928, 2012.
- [56] G. Habib, T. Detroux, and G. Kerschen. Generalization of Den Hartog’s equal-peak method for nonlinear primary systems. In *Proceedings of International Conference on Structural Nonlinear Dynamics and Diagnosis*, Agadir, Marocco, 2014.
- [57] M. E. Henderson. Computing invariant manifolds by integrating fat trajectories. *SIAM Journal on Applied Dynamical Systems*, 4(4):832–882, 2005.
- [58] M. E. Henderson. *Covering an Invariant Manifold with Fat Trajectories*, chapter 3, pages 39–54. Springer Berlin Heidelberg, 2006.
- [59] M. W. Hirsch, S. Smale, and R. L. Devaney. *Differential equations, dynamical systems, and an Introduction to Chaos, Third Edition*. Academic Press, 2012.
- [60] T. J. R. Hughes and T. E. Tezduyar. Finite element methods for first-order hyperbolic systems with particular emphasis on the compressible Euler equations. *Computer Methods in Applied Mechanics and Engineering*, 45(1-3):217–284, 1984.
- [61] M. Iranzad and H. Ahmadian. Identification of nonlinear bolted lap joint models. *Computers & Structures*, 96-97:1–8, 2012.
- [62] M. Ismail, F. Ikhouane, and J. Rodellar. The hysteresis Bouc-Wen model, a survey. *Archives of Computational Methods in Engineering*, 16(2):161–188, 2009.
- [63] A. P. Ivanov. Bifurcations in systems with friction: Basic models and methods. *Regular and Chaotic Dynamics*, 14(6):656–672, 2009.
- [64] L. Jezequel and C. H. Lamarque. Analysis of non-linear dynamical systems by the normal form theory. *Journal of Sound and Vibration*, 149(3):429–459, 1991.
- [65] D. Jiang, C. Pierre, and S. W. Shaw. Large-amplitude non-linear normal modes of piecewise linear systems. *Journal of Sound and Vibration*, 272(3-5):869–891, 2004.
- [66] D. Jiang, C. Pierre, and S. W. Shaw. The construction of non-linear normal modes for systems with internal resonance. *International Journal of Non-Linear Mechanics*, 40(5):729–746, 2005.
- [67] D. Jiang, C. Pierre, and S. W. Shaw. Nonlinear normal modes for vibratory systems under harmonic excitation. *Journal of Sound and Vibration*, 288(4-5):791–812, 2005.

- [68] T. A. Johansen. Computation of Lyapunov functions for smooth nonlinear systems using convex optimization. *Automatica*, 36(11):1617–1626, 2000.
- [69] M. Johansson and A. Rantzer. Computation of piecewise quadratic lyapunov functions for hybrid systems. *IEEE Transactions on Automatic Control*, 43(4):555–559, 1998.
- [70] C. Johnson. *Numerical Solution of Partial Differential Equations by the Finite Element Method*. Dover Publications, 2012.
- [71] C. Johnson, U. Nävert, and J. Pitkäranta. Finite element methods for linear hyperbolic problems. *Computer Methods in Applied Mechanics and Engineering*, 45(1-3):285–312, 1984.
- [72] A. Kelley. On the liapounov subcenter manifold. *Journal of Mathematical Analysis and Applications*, 18(3):472–478, 1967.
- [73] G. Kerschen, J. J. Kowtko, D. M. McFarland, L. A. Bergman, and A. F. Vakakis. Theoretical and experimental study of multimodal targeted energy transfer in a system of coupled oscillators. *Nonlinear Dynamics*, 47(1-3):285–309, 2006.
- [74] G. Kerschen, M. Peeters, J. C. Golinval, and C. Stéphan. Nonlinear modal analysis of a full-scale aircraft. *Journal of Aircraft*, 50(5):1409–1419, 2013.
- [75] G. Kerschen, M. Peeters, J. C. Golinval, and A. F. Vakakis. Nonlinear normal modes, part I: A useful framework for the structural dynamicist. *Mechanical Systems and Signal Processing*, 23(1):170–194, 2009.
- [76] M. E. King and A. F. Vakakis. An energy-based formulation for computing nonlinear normal modes in undamped continuous systems. *Journal of Vibration and Acoustics*, 116(3):332–340, 1994.
- [77] M. E. King and A. F. Vakakis. A very complicated structure of resonances in a nonlinear system with cyclic symmetry - nonlinear forced localization. *Nonlinear Dynamics*, 7:20, 1995.
- [78] J. A. C. Knowles, B. Krauskopf, and M. H. Lowenberg. Numerical continuation applied to landing gear mechanism analysis. *Journal of Aircraft*, 48:1254–1262, 2011.
- [79] M. Krack, L. Panning-von Scheidt, and J. Wallaschek. A method for nonlinear modal analysis and synthesis: Application to harmonically forced and self-excited mechanical systems. *Journal of Sound and Vibration*, 332(25):6798–6814, 2013.
- [80] M. Krack, L. Panning-von Scheidt, and J. Wallaschek. On the computation of the slow dynamics of nonlinear modes of mechanical systems. *Mechanical Systems and Signal Processing*, 42(1-2):71–87, 2014.

- [81] B. Krauskopf and H. Osinga. Two-dimensional global manifolds of vector fields. *Chaos: An Interdisciplinary Journal of Nonlinear Science*, 9(3):768–774, 1999.
- [82] B. Krauskopf and H. Osinga. Computing geodesic level sets on global (un)stable manifolds of vector fields. *SIAM Journal on Applied Dynamical Systems*, 2(4):546–569, 2003.
- [83] B. Krauskopf and H. M. Osinga. *Computing Invariant Manifolds via the Continuation of Orbit Segments*, chapter 4, pages 117–154. Springer Netherlands, 2007.
- [84] B. Krauskopf, H. M. Osinga, E. J. Doedel, M. E. Henderson, J. Guckenheimer, A. Vladimirov, M. Dellnitz, and O. Junge. A survey of methods for computing (un)stable manifolds of vector fields. *International Journal of Bifurcation and Chaos*, 15(3):763–791, 2005.
- [85] Y. A. Kuznetsov. *Elements of Applied Bifurcation Theory*, volume 112 of *Applied Mathematical Sciences*. Springer New York, 2004.
- [86] W. Lacarbonara and G. Rega. Resonant non-linear normal modes. part II: activation/orthogonality conditions for shallow structural systems. *International Journal of Non-Linear Mechanics*, 38(6):873–887, 2003.
- [87] W. Lacarbonara, G. Rega, and A. H. Nayfeh. Resonant non-linear normal modes part I: analytical treatment for structural one-dimensional systems. *International Journal of Non-Linear Mechanics*, 38:22, 2003.
- [88] S. Larsson and V. Thomée. *Partial Differential Equations with Numerical Methods*, volume 45. Springer Berlin Heidelberg, 2003.
- [89] D. Laxalde, J.-P. Lombard, and F. Thouverez. Forced response analysis of integrally bladed disks with friction ring dampers. *Journal of Vibration and Acoustics*, 132(1):011013–011013, 2010.
- [90] D. Laxalde, L. Salles, L. Blanc, and F. Thouverez. Non-linear modal analysis for bladed disks with friction contact interfaces. In *Proceedings of GT2008, ASME Turbo Expo 2008: Power for Land, Sea and Air, Berlin, Germany*, 2008.
- [91] D. Laxalde and F. Thouverez. Complex non-linear modal analysis for mechanical systems: Application to turbomachinery bladings with friction interfaces. *Journal of Sound and Vibration*, 322(4-5):1009–1025, 2009.
- [92] D. Laxalde, F. Thouverez, and J. J. Sinou. Dynamics of a linear oscillator connected to a small strongly non-linear hysteretic absorber. *International Journal of Non-Linear Mechanics*, 41(8):969–978, 2006.
- [93] D. Laxalde, F. Thouverez, J. J. Sinou, and J. P. Lombard. Qualitative analysis of forced response of blisks with friction ring dampers. *European Journal of Mechanics A/Solids*, 26:676–687, 2007.

- [94] Y. S. Lee, G. Kerschen, A. F. Vakakis, P. Panagopoulos, L. Bergman, and D. M. McFarland. Complicated dynamics of a linear oscillator with a light, essentially nonlinear attachment. *Physica D: Nonlinear Phenomena*, 204(1-2):41–69, 2005.
- [95] Y. S. Lee, F. Nucera, A. F. Vakakis, D. M. McFarland, and L. A. Bergman. Periodic orbits, damped transitions and targeted energy transfers in oscillators with vibro-impact attachments. *Physica D: Nonlinear Phenomena*, 238(18):1868–1896, 2009.
- [96] M. Legrand, D. Jiang, C. Pierre, and S. W. Shaw. Nonlinear normal modes of a rotating shaft based on the invariant manifold method. *International Journal of Rotating Machinery*, 10(4):319–335, 2004.
- [97] S. Lenci and G. Rega. Dimension reduction of homoclinic orbits of buckled beams via the non-linear normal modes technique. *International Journal of Non-Linear Mechanics*, 42(3):515–528, 2007.
- [98] H.-G. Li and G. Meng. Nonlinear dynamics of a SDOF oscillator with Bouc-Wen hysteresis. *Chaos, Solitons and Fractals*, 34:337–343, 2007.
- [99] J.-L. Lions. *Optimal Control of Systems Governed by Partial Differential Equations*. Springer-Verlag, 1971.
- [100] A. M. Lyapunov. *The general problem of the stability of motion*. Princeton University Press, 1947.
- [101] L. I. Manevich and Y. V. Mikhlin. On periodic solutions close to rectilinear normal vibration modes. *Journal of Applied Mathematics and Mechanics*, 36(6):988–994, 1972.
- [102] L. I. Manevitch. *Complex Representation of Dynamics of Coupled Oscillators in Mathematical Models of Nonlinear Excitations, Transfer Dynamics and Control in Condensed Systems*. Kluwer Academic/Plenum Publishers, New York, 1999.
- [103] S. F. Masri and T. K. Caughey. A nonparametric identification technique for nonlinear dynamic problems. *Journal of Applied Mechanics*, 46(2):433–447, 1979.
- [104] C. E. N. Mazzilli and O. G. P. Neta. Evaluation of non-linear normal modes for finite element models. *Computers and Structures*, 80:9, 2002.
- [105] T. McKelvey, H. A. Cay, and L. Ljung. Subspace-based multivariable system identification from frequency response data. *IEEE Transactions on Automatic Control*, 41:960–979, 1996.
- [106] Y. V. Mikhlin and K. V. Avramov. Nonlinear normal modes for vibrating mechanical systems. review of theoretical developments. *Applied Mechanics Reviews*, 63(6):060802–21, 2010.

- [107] F. J. Muñoz Almaraz, E. Freire, J. Galán, E. Doedel, and A. Vanderbauwhede. Continuation of periodic orbits in conservative and hamiltonian systems. *Physica D: Nonlinear Phenomena*, 181(1-2):1–38, 2003.
- [108] A. H. Nayfeh. *Nonlinear Interactions: Analytical, Computational and Experimental Methods*. Wiley-Interscience, New York, 2000.
- [109] A. H. Nayfeh. *The Method of Normal Forms*. Wiley-VCH Verlag GmbH & Co. KGaA, 2011.
- [110] A. H. Nayfeh and T. D. Mook. *Nonlinear Oscillations*. Wiley Interscience, New York, 1979.
- [111] A. H. Nayfeh and S. A. Nayfeh. On nonlinear modes of continuous systems. *Journal of Vibration and Acoustics*, 116(1):129–136, 1994.
- [112] A. H. Nayfeh and S. A. Nayfeh. Nonlinear normal modes of a continuous system with quadratic nonlinearities. *Journal of Vibration and Acoustics*, 117(2):199–205, 1995.
- [113] S. A. Neild and D. J. Wagg. Applying the method of normal forms to second-order nonlinear vibration problems. *Proceedings of the Royal Society A: Mathematical, Physical and Engineering Science*, 467(2128):1141–1163, 2011.
- [114] T. M. Nguyen. *Dynamique non linéaire des systèmes mécaniques couplés : Réduction de modèle et Identification*. PhD thesis, École nationale des ponts et Chaussées, Paris, 2007.
- [115] J.-P. Noël, L. Renson, and G. Kerschen. Complex dynamics of a nonlinear spacecraft structure: experimental identification and modal interactions. *Journal of Sound and Vibration, in press*, 2014.
- [116] J. P. Noël, L. Renson, G. Kerschen, B. Peeters, S. Manzato, and J. DeBille. Non-linear dynamic analysis of an F-16 aircraft using GVT data. In *Proceedings of the International Forum on Aeroelasticity and Structural Dynamics, Bristol, UK*, 2013.
- [117] D. Noreland, S. Bellizzi, C. Vergez, and R. Bouc. Nonlinear modes of clarinet-like musical instruments. *Journal of Sound and Vibration*, 324(3-5):983–1002, 2009.
- [118] A. Papachristodoulou and S. Prajna. On the construction of lyapunov functions using the sum of squares decomposition. In *Proceedings of the 41st IEEE Conference on Decision and Control*, volume 3, pages 3482–3487, 2002.
- [119] M. Peeters. *Theoretical and Experimental Modal Analysis of Nonlinear Vibrating Structures using Nonlinear Normal Modes*. PhD thesis, University of Liège, 2010.
- [120] M. Peeters, R. Vigiúí, G. Sérandour, G. Kerschen, and J. C. Golinval. Nonlinear normal modes, part II: Toward a practical computation using numerical continuation techniques. *Mechanical Systems and Signal Processing*, 23(1):195–216, 2009.

- 
- [121] F. Pellicano and F. Mastroddi. Applicability conditions of a non-linear superposition technique. *Journal of Sound and Vibration*, 200(1):3–14, 1997.
- [122] N. V. Perepelkin, Y. V. Mikhlin, and C. Pierre. Non-linear normal forced vibration modes in systems with internal resonance. *International Journal of Non-Linear Mechanics*, 57(0):102–115, 2013.
- [123] E. Pesheck. *Reduced order modeling of nonlinear structural systems using nonlinear normal modes and invariant manifolds*. PhD thesis, University of Michigan, 2000.
- [124] E. Pesheck, N. Boivin, C. Pierre, and S. W. Shaw. Nonlinear modal analysis of structural systems using multi-mode invariant manifolds. *Nonlinear Dynamics*, 25, 2001.
- [125] E. Pesheck, C. Pierre, and S. W. Shaw. Accurate reduced-order models for a simple rotor blade model using nonlinear normal modes. *Mathematical and Computer Modelling*, 33(10-11):1085–1097, 2001.
- [126] E. Pesheck, C. Pierre, and S. W. Shaw. A new Galerkin-based approach for accurate non-linear normal modes through invariant manifolds. *Journal of Sound and Vibration*, 249(5):971–993, 2002.
- [127] E. P. Petrov and D. J. Ewins. Advanced modeling of underplatform dampers for analysis of bladed disk vibration. *Journal of Turbomachinery*, 129:143–150, 2007.
- [128] C. Pierre, D. Jiang, and S. W. Shaw. Nonlinear normal modes and their application in structural dynamics. *Mathematical Problems in Engineering*, 2006:1–16, 2006.
- [129] D. D. Quinn. Modal analysis of jointed structures. *Journal of Sound and Vibration*, 331(1):81–93, 2012.
- [130] R. H. Rand. A higher order approximation for non-linear normal modes in two degree of freedom systems. *International Journal of Non-Linear Mechanics*, pages 545–547, 1971.
- [131] R. H. Rand. Nonlinear normal modes in two-degree-of-freedom systems. *Journal of Applied Mechanics*, 38(2):561, 1971.
- [132] R. H. Rand. The geometrical stability of non-linear normal modes in two degree of freedom systems. *International Journal of Non-Linear Mechanics*, 8:161–168, 1973.
- [133] R. H. Rand. A direct method for non-linear normal modes. *International Journal of Non-Linear Mechanics*, 9:363–368, 1974.
- [134] R. H. Rand, C. H. Pak, and A. F. Vakakis. *Bifurcation of nonlinear normal modes in a class of two degree of freedom systems*, volume 3 of *Acta Mechanica*, chapter 10, pages 129–146. Springer Vienna, 1992.

- [135] M. Renardy and R. Rogers. *An Introduction to Partial Differential Equations*, volume 13. Springer Berlin Heidelberg, 2004.
- [136] R. M. Rosenberg. Normal modes of nonlinear dual-mode systems. *Journal of Applied Mechanics*, 27(2):263–268, 1960.
- [137] R. M. Rosenberg. The normal modes of nonlinear n-degree-of-freedom systems. *Journal of Applied Mechanics*, 29(1):7–14, 1962.
- [138] R. M. Rosenberg. On nonlinear vibrations of systems with many degrees of freedom. *Advances in Applied Mechanics*, 9:155–242, 1966.
- [139] A. G. Russell. Thick skin, faceted, CFRP, monocoque tube structure for smallsats. In *European Conference on Spacecraft Structures, Materials and Mechanical Testing*, Noordwijk, The Netherlands, 2000.
- [140] E. Sarrouy, A. Grolet, and F. Thouverez. Global and bifurcation analysis of a structure with cyclic symmetry. *International Journal of Non-Linear Mechanics*, 46(5):727–737, 2011.
- [141] R. Seydel. *Practical Bifurcation and Stability Analysis*, volume 5 of *Interdisciplinary Applied Mathematics*. Springer New York, 2010.
- [142] S. W. Shaw. On the dynamic response of a system with dry friction. *Journal of Sound and Vibration*, 108(2):305–325, 1986.
- [143] S. W. Shaw. An invariant manifold approach to nonlinear normal modes of oscillation. *Nonlinear Science*, 4:30, 1994.
- [144] S. W. Shaw and C. Pierre. Non-linear normal modes and invariant manifolds. *Journal of Sound and Vibration*, 150(1):170–173, 1991.
- [145] S. W. Shaw and C. Pierre. Normal modes for non-linear vibratory systems. *Journal of Sound and Vibration*, 164:40, 1993.
- [146] S. W. Shaw and C. Pierre. Normal modes of vibration for non-linear continuous systems. *Journal of Sound and Vibration*, 169(3):319–347, 1994.
- [147] J. C. Slater. A numerical method for determining nonlinear normal modes. *Nonlinear Dynamics*, 10(1):19–30, 1996.
- [148] M. E. S. Soares and C. E. N. Mazzilli. Nonlinear normal modes of planar frames discretised by the finite element method. *Computers and Structures*, 77:9, 2000.
- [149] N. Srinil, G. Rega, and S. Chucheepsakul. Two-to-one resonant multi-modal dynamics of horizontal/inclined cables. part I: Theoretical formulation and model validation. *Nonlinear Dynamics*, 48(3):231–252, 2007.

- [150] K. Stein, T. E. Tezduyar, and R. Benney. Automatic mesh update with the solid-extension mesh moving technique. *Computer Methods in Applied Mechanics and Engineering*, 193(21-22):2019–2032, 2004.
- [151] C. Touzé and M. Amabili. Nonlinear normal modes for damped geometrically nonlinear systems: Application to reduced-order modelling of harmonically forced structures. *Journal of Sound and Vibration*, 298(4-5):958–981, 2006.
- [152] C. Touzé, M. Amabili, and O. Thomas. Reduced-order models for large-amplitude vibrations of shells including in-plane inertia. *Computer Methods in Applied Mechanics and Engineering*, 197(21-24):2030–2045, 2008.
- [153] C. Touzé, O. Thomas, and A. Chaigne. Hardening/softening behaviour in non-linear oscillations of structural systems using non-linear normal modes. *Journal of Sound and Vibration*, 273(1-2):77–101, 2004.
- [154] C. Touzé, O. Thomas, and A. Huberdeau. Asymptotic non-linear normal modes for large-amplitude vibrations of continuous structures. *Computers & Structures*, 82(31-32):2671–2682, 2004.
- [155] A. F. Vakakis. Non-linear normal modes (NNMs) and their applications in vibration theory: An overview. *Mechanical Systems and Signal Processing*, 11(1):3–22, 1997.
- [156] A. F. Vakakis, O. Gendelman, L. A. Bergman, D. M. McFarland, G. Kerschen, and Y. S. Lee. *Nonlinear Targeted Energy Transfer in Mechanical and Structural Systems*. Springer, Series: Solid Mechanics and Its Applications, Vol. 156, 2009.
- [157] A. F. Vakakis, L. I. Manevitch, Y. V. Mikhlin, V. N. Pilipchuk, and A. A. Zevin. *Normal Modes and Localization in Nonlinear Systems*. Wiley-VCH Verlag GmbH, 2008.
- [158] A. F. Vakakis, L. I. Manevitch, Y. V. Mikhlin, V. N. Pilipchuk, and A. A. Zevin. *Normal Modes and Localization in Nonlinear Systems*. Wiley-VCH Verlag GmbH, 2008.
- [159] N. van de Wouw and R. I. Leine. Attractivity of equilibrium sets of systems with dry friction. *Nonlinear Dynamics*, 35(1):19–39, 2004.
- [160] F. Vestroni, A. Luongo, and A. Paolone. A perturbation method for evaluating nonlinear normal modes of a piecewise linear two-degrees-of-freedom system. *Nonlinear Dynamics*, 54(4):379–393, 2008.
- [161] C. Viana Serra Villa, J.-J. Sinou, and F. Thouverez. The invariant manifold approach applied to nonlinear dynamics of a rotor-bearing system. *European Journal of Mechanics - A/Solids*, 24(4):676–689, 2005.
- [162] F. Wang and A. Bajaj. Nonlinear normal modes in multi-mode models of an inertially coupled elastic structure. *Nonlinear Dynamics*, 47(1):25–47, 2007.

- 
- [163] J. Warminsky. Nonlinear normal modes of coupled self-excited oscillators in regular and chaotic vibration regimes. *Journal of Theoretical and Applied Mechanics*, 46:693–714, 2008.
- [164] F. Wei, L. Liang, and G. T. Zheng. Parametric study for dynamics of spacecraft with local nonlinearities. *AIAA Journal*, 48:1700–1707, 2010.
- [165] J. Wojewoda, A. Stefanski, M. Wiercigroch, and T. Kapitaniak. Hysteretic effects of dry friction: modelling and experimental studies. *Philosophical Transactions of the Royal Society A: Mathematical, Physical and Engineering Sciences*, 366(1866):747–765, 2008.
- [166] K. Worden and G. R. Tomlinson. *Nonlinearity in Structural Dynamics: Detection, Identification and Modelling*. Taylor & Francis, 2000.
- [167] Z. Xu and M. Accorsi. Finite element mesh update methods for fluid-structure interaction simulations. *Finite Elements in Analysis and Design*, 40(9-10):1259–1269, 2004.
- [168] P. Yu. Computation of normal forms via a perturbation technique. *Journal of Sound and Vibration*, 211(1):19–38, 1998.
- [169] W. Zhang, K. Huseyin, and M. I. N. Ye. On the computation of the coefficients associated with high order normal forms. *Journal of Sound and Vibration*, 232(3):525–540, 2000.
- [170] X. Zhang. Geodesics, nonlinear normal modes of conservative vibratory systems and decomposition method. *Journal of Sound and Vibration*, 282(3-5):971–989, 2005.
- [171] O. C. Zienkiewicz, R. L. Taylor, and J. Z. Zhu. *The Finite Element Method: Its Basis and Fundamentals, 6th Edition*. Elsevier, 2005.

# List of Journal Publications

1. L. Renson, G. Deliége, G. Kerschen. An effective finite-element-based method for the computation of nonlinear normal modes of nonconservative systems. *Meccanica*, DOI 10.1007/s11012-014-9875-3, 2014.
2. J.-P. Noël, L. Renson, G. Kerschen. Complex dynamics of a nonlinear aerospace structure: experimental identification and modal interactions. *Journal of Sound and Vibration*, DOI 10.1016/j.jsv.2014.01.024, 2014.
3. L. Renson, J.-P. Noël, G. Kerschen. Complex dynamics of a nonlinear aerospace structure: numerical continuation and normal modes. *Nonlinear Dynamics*, In review.

# List of Conference Publications

1. T. Detroux, L. Renson, G. Kerschen. The harmonic balance method for advanced analysis and design of nonlinear mechanical systems. *Proceedings of the SEM IMAC XXXII*, Orlando, FL, USA, 2014.
2. J.-P. Noël, L. Renson, G. Kerschen. Experimental identification of the complex dynamics of a strongly nonlinear spacecraft structure. *Proceedings of the ASME IDETC/CIE*, Portland, OR, USA, 2013.
3. L. Renson, G. Kerschen. Numerical computation of nonlinear normal modes of nonconservative systems. *Proceedings of the ASME IDETC/CIE*, Portland, OR, USA, 2013.
4. J.-P. Noël, L. Renson, G. Kerschen, B. Peeters, S. Manzato, J. Debille. Nonlinear dynamic analysis of an F-16 aircraft using GVT data. *Proceedings of the International Forum on Aeroelasticity and Structural Dynamics*, Bristol, UK, 2013.
5. L. Renson, G. Kerschen. A new computational method for nonlinear normal modes of nonconservative systems. *Proceedings of the Euromech Colloquium n. 541 - New Advances in the Nonlinear Dynamics and Control of Composites for Smart Engineering Design*, Senigallia, Italy, 2013.
6. L. Renson, G. Kerschen. Nonlinear Normal Modes of Nonconservative Systems. *Proceedings of the SEM IMAC XXXI Conference*, Orange County, CA, USA, 2013.
7. L. Renson, G. Deliège, G. Kerschen. Finite element computation of nonlinear normal modes of nonconservative systems. *Proceedings of the ISMA conference*, Leuven, Belgium, 2012.
8. J.-P. Noël, L. Renson, G. Kerschen, A. Newerla. Experimental identification of a nonlinear space structure. *Proceedings of the 12th European Conference on Spacecraft Structures, Materials and Environmental Testing*, Noordwijk, The Netherlands, 2012.
9. L. Renson, J.-P. Noël, G. Kerschen, A. Newerla. Nonlinear Modal Analysis of the SmallSat Spacecraft. *Proceedings of the European Conference on Spacecraft Structures, Materials & Environmental Testing*, Noordwijk, The Netherlands, 2012.

10. A. Cammarano, A. Carrella, L. Renson, G. Kerschen. Identifying and computing nonlinear normal modes. *Proceedings of the SEM IMAC XXX Conference*, Jacksonville, FL, USA, 2012.
11. L. Renson, G. Kerschen, A. Newerla. Nonlinear modal analysis of the SmallSat spacecraft. *Proceedings of the SEM IMAC XXX Conference*, Jacksonville, FL, USA, 2012.
12. M. Peeters, L. Renson, G. Kerschen, J.-C. Golinval, C. Stéphan, P. Lubrina. Computation of nonlinear normal modes of large structures: application to a full-scale aircraft. *Proceedings of the 7th European Nonlinear Dynamics Conference*, Rome, Italy, 2011.
13. L. Renson, G. Deliége, L. Noels, G. Kerschen. Finite Element Computation of Nonlinear Normal Modes. *Fifth International Conference on Advanced Computational Methods in ENgineering*, Liège, Belgium, 2011.